



The
University
Of
Sheffield.

A Novel Design Development for Piezoelectric Energy Harvesting Device

Zongyou ZUO

A thesis submitted in partial fulfilment of the requirements for the degree of
Doctor of Philosophy

The University of Sheffield
Faculty of Engineering
Department of Mechanical Engineering

January 2023

Acknowledgements

First, I would like to thank my supervisor, Professor Bill Nimmo. Without his careful guidance and help, I would not have been able to complete my thesis. During my PhD studies, I faced many setbacks and my physical condition also had problems. During these times, he continuously gave me encouragement and support, allowing me to continue my research and ultimately complete my thesis. He is the best supervisor I have ever met, and it is my luck to have met him. Professor Bill is not only my teacher in learning but also my teacher for life.

Thank you to Dr. Robert Howell for providing me with the wind tunnel laboratory that allowed me to complete my experiments. I also want to thank Dmitry Govorukhin and Oliver Copper for their help during my experiments.

My mother and my father, thank you for your concern and support throughout my studies. After graduating from my master's degree, it was them who gave me the confidence to continue my PhD. As an international self-funded student, they lived frugally these past few years to provide me with more living expenses so that I could better complete my studies. They made me a confident and brave person, and I am proud to be a son of them.

I also want to thank my friends, Dr. Huanrong Lei, Tianyi Sha, Linyi Xiao, Jiabao Xiu and so on, thank you for your companionship these past few years. Finally, I want to thank Sheffield Chinese Students and Scholars Association, and thank the over 200 fellow students of CSSA Sheffield for their trust in me as the president; it is you who made me a better person.

Abstract

As more and more small electronic equipment enters people's lives, the power supply demand for these small electronic devices is also increasing. For small electronic devices, batteries are usually used for power supply, but for remote areas, frequently changing batteries is a complex job. Energy harvesting is a good way to solve this problem, such as photovoltaic batteries. Piezoelectric energy harvesting, as a method of energy harvesting, can generate unconventional clean energy through mechanical vibrations present in the environment. Due to the advantages of simplicity in structure, and low manufacturing and maintenance costs, piezoelectric energy harvesting holds great potential, especially for developing countries.

Firstly, the thesis summarizes and analyses various types of existing piezoelectric energy harvester designs, identifying their shortcomings and potential areas for development. This provides a theoretical foundation for future research. Secondly, a novel galloping piezoelectric energy harvesting design, "a reverse C shape with a tail design," is proposed. Experimental and simulation analysis in a wind tunnel demonstrates that this design achieves a 25-fold increase in power output compared to existing designs at a wind speed of 5m/s. Furthermore, at a wind speed of 7m/s, the power output reaches 2.15mW, which can effectively meet the daily power requirements of specific electronic devices, such as hearing aids. In addition, this thesis also studied each parameter of the design, such as the length of the tail, the thickness of the "C shape", the selection of the cantilever beam, etc., which determine the impact of each parameter on the power output. The end of this thesis provides theoretical support through simulation studies, and suggestions for future research are provided.

Overall, this thesis provides a new design for piezoelectric energy harvesters and also provides a broader perspective and theoretical support for the future development of this type of energy harvester.

Declaration

As the author, I hereby affirm that the contents of this thesis are entirely my own original work. I am well-informed about the University's regulations regarding the Use of Unfair Means (www.sheffield.ac.uk/ssid/unfair-means). This thesis has not been previously submitted for any academic award at this or any other institution.

Journal Publication

Chapter 5 include the following publication

- Z. Zuo and W. Nimmo, "A Curved Body with Tail Design for Piezoelectric Energy Harvesting," *Int. J. Sustain. Energy Dev.*, vol. 9, no. 1, pp. 427–430, 2021, doi: 10.20533/ijsted.2046.3707.2021.0051.
- Z. Zuo, W. Nimmo and R. Howell, "A Reverse C Shape with a Tail Design for Galloping-based Piezoelectric Energy Harvesting," [Submitted.]

Conference Presentation

- Z. Zuo and W. Nimmo, (2021) "A Novel Design Development for Piezoelectric Energy Harvesting Devices," *World Congress on Sustainable Technologies (WCST-2021)*, London, UK, 9th December 2021.
- Z. Zuo, (2022) "A Novel Design Development for Piezoelectric Energy Harvesting Device," *MEC PhD Poster Presentation*, Sheffield, UK, 14th June 2022.

CONTENTS

Acknowledgements.....	I
Abstract.....	II
Declaration.....	III
Contents.....	IV
List of Tables.....	IX
List of Figures	XI
CHAPTER 1. INTRODUCTION.....	1
1.1 Thesis Overview	1
1.2 Power Supply	2
1.3 Energy Harvesting	3
1.3.1 Photovoltaic Modules Energy Harvesting.....	7
1.3.2 Thermoelectric Energy Harvesting.....	8
1.3.3 Wind Energy Harvesting.....	10
1.3.4 Vibration Energy Harvesting	12
1.4 Aim and Objectives	14
CHAPTER 2. LITERATURE REVIEW	16
2.1 Introduction	16
2.1.1 Review Scope	16
2.2 Type of Vibration Energy Harvesting	16
2.2.1 Electromagnetic Harvesting Method.....	16
2.2.2 Electrostatic Harvesting Method	17
2.2.3 Piezoelectric Harvesting Method.....	19
2.2.3.1 Piezoelectric Effect and Inverse Piezoelectric Effect	19
2.2.3.2 Piezoelectric Material Properties	21
2.2.3.3 Piezoelectric Material	24

2.2.3.4	Devices of Piezoelectric Vibration Energy Harvesting	28
2.2.4	Comparison of Three Methods	33
2.3	Flow-induced Vibration Energy Harvesting	35
2.3.1	Vortex-induced vibration	36
2.3.2	Galloping	44
2.3.3	Flutter.....	53
2.3.4	Buffeting.....	56
2.3.5	Summary of Flow-induced Energy Harvesting.....	59
2.4	The Study of Cantilever Beam.....	64
2.4.1	The Natural Frequency	65
2.4.2	The Internal Moment.....	67
2.5	Conclusion and Research Gaps	68
CHAPTER 3.	METHODOLOGY	70
3.1	Introduction	70
3.2	Design.....	70
3.2.1	Novel Design Idea	71
3.2.2	Prototype	71
3.2.3	Variables.....	72
3.3	Experiment.....	76
3.3.1	Piezoelectric Layer	76
3.3.2	Wind Tunnel.....	79
3.3.3	Measure Devices.....	81
3.4	Modelling	85
3.4.1	Geometry	85
3.4.2	Mesh Generation	87
3.4.3	Solver Settings.....	88
3.4.4	Validation	90

3.5	Mechanical and Electrical Circuit Coupling Equation	92
CHAPTER 4. EXPERIMENT		96
4.1	Introduction	96
4.2	Effect of Tail	97
4.2.1	Experimental purpose and requirements.....	97
4.2.2	Experimental Device and Setup.....	97
4.2.3	Experimental Steps	98
4.2.4	Experimental results and Phenomenon	99
4.2.5	Conclusion.....	100
4.3	Effect of Varies Tail Length	101
4.3.1	Experimental Purpose and Requirements	101
4.3.2	Experimental Device and Setup.....	103
4.3.3	Experimental Steps	104
4.3.3.1	First Stage: The Lift Force.....	104
4.3.3.2	Second Stage: The Power Output.....	105
4.3.4	Experimental Results and Phenomenon of the A Series Models	105
4.3.5	Experimental Results and Phenomenon of the S Series Models.....	110
4.3.6	Discussion.....	116
4.3.7	Conclusion.....	118
4.4	Effect of Thickness of the Curved Body	118
4.4.1	Experimental Purpose and Requirements	118
4.4.2	Experimental Device and Setup.....	119
4.4.3	Experimental results and Phenomenon	119
4.4.4	Conclusion.....	121
4.5	Effect of Cantilever Beam Material.....	121
4.5.1	Experimental Purpose and Requirements.....	121
4.5.2	Experimental Device and Setup.....	122

4.5.3	Experimental results and Phenomenon	122
4.5.4	Discussion.....	125
4.5.5	Conclusion.....	128
4.6	Effect of Different Piezoelectric Layer	128
4.6.1	Experimental Purpose and Requirements	128
4.6.2	Experimental Device and Setup	129
4.6.3	Experimental results and Phenomenon	129
4.6.4	Conclusion.....	130
4.7	Conclusion.....	130
CHAPTER 5. SIMULATION.....		132
5.1	Introduction	132
5.2	Simulation of the S Series Models	133
5.2.1	Geometry	133
5.2.2	Mesh Generation	134
5.2.3	Solver Setting	136
5.2.4	Result	136
5.2.4.1	Fluid Movement Analysis.....	136
5.2.4.2	Lift Coefficient Curve Analysis	140
5.2.4.3	S Series Model Comparison Analysis	143
5.2.4.4	Responding time Analysis	145
5.2.5	Discussion and Conclusion.....	146
5.3	Study of Tail.....	147
5.3.1	Geometry and Other Setting	147
5.3.2	Result	148
5.3.3	Discussion and Conclusion.....	150
5.4	Effect of Thickness of Curved Body.....	151
5.4.1	Geometry and Other Setting	151

5.4.2	Result	152
5.4.3	Discussion and Conclusion	154
5.5	Conclusion	154
CHAPTER 6. SIMULATION/EXPERIMENT EVALUATION.....		156
6.1	Introduction	156
6.2	Comparison the Result.....	156
6.2.1	Lift Force	156
6.2.2	Frequency.....	160
6.3	Power Output Analysis.....	163
6.4	Piezoelectric Energy Harvesters in Real Application	164
6.5	Conclusion.....	167
CHAPTER 7. CONCLUSION.....		169
7.1	Experimental Findings.....	169
7.1.1	Conclusion.....	169
7.1.2	Suggestions for Future Work	170
7.2	Simulated Findings	171
7.2.1	Conclusion.....	171
7.2.2	Suggestions for Future Work	172
7.3	Validating Findings	172
7.3.1	Conclusion.....	172
7.3.2	Suggestions for Future Work	173
REFERENCES		175
APPENDICES		184

List of Tables

Table 1-1 - The Minimum Power Required of a Number of Common Devices [2].....	5
Table 2-1 – Four Piezoelectric Coefficients.....	22
Table 2-2 – Comparison of Different Piezoelectric Material.	27
Table 2-3 – Properties of Commonly Used Materials [2].	27
Table 2-4 – Comparison of Three Vibration Energy Harvester [2].	34
Table 2-5 – Other Bluff Body Novel Design for Galloping in Recent Years.....	52
Table 2-6 Comparison of Flow-induced Vibration	59
Table 2-7 - Summary of Recent Flow-induced Vibration Energy Harvesters	61
Table 3-1 - Experimental Models Specifications.....	74
Table 3-2 - Cantilever Beams Specifications	75
Table 3-3 - The Dimension Comparison of LDT0 and LDT4.	76
Table 3-4 - Parameters of Two Piezoelectric Kits.	78
Table 3-5 - Specifications of Axial Flow Fan and Wind Tunnel	80
Table 3-6 - Key Performance Specifications for TBS 1072B Oscilloscope.....	82
Table 3-7 - Nano43 Transducer Specifications	84
Table 3-8 - Parameter of Simulation Models and Fluid	86
Table 3-9 - Comparison of Various Viscous Models	89
Table 3-10 - The Simulation Solution Method.....	90
Table 4-1 - Gravity Point of the A Series Models.....	109
Table 4-2 - Power Output for S Series Models with Aluminium Cantilever Beam and LDT0- 28K Piezoelectric Kit.....	116
Table 4-3 - Power Output for R1 and R2 Models (mW).....	120
Table 4-4 - The First Natural Frequency Parameter for Two Beams (S3 model).....	126
Table 4-5 - Frequency of Models with an Aluminium Cantilever Beam	127

Table 4-6 - Frequency of Models with a Plastic Cantilever Beam	127
Table 4-7 - Power Output for S Series Models with Aluminium Cantilever Beam and M-2807-P2 Piezoelectric Kit	130
Table 5-1 - The Parameters of the Simulation Models and the Fluid	133
Table 5-2 - Evaluation of Mesh Quality for S0 Model	135
Table 5-3 - The Geometric Parameters for the P Series Models Simulation	147
Table 5-4 - The Parameters of the Models Geometry and Simulation	151
Table 6-1 - Lift Force (N) of Simulation Result for S Series Models	157
Table 6-2 - Lift Force (N) of Experiment Result for S Series Models (Aluminium)	157
Table 6-3 - Frequency (Hz) of Simulation Result for S Series Models	161
Table 6-4 - Frequency (Hz) of Experiment Result for S Series Models	161

List of Figures

Figure 1.1 - MEMs Applications for the Human Body [1].	3
Figure 1.2 - Various Energy Harvesting Source from the Environment [5].	4
Figure 1.3 - Small-scale Solar Cell.	7
Figure 1.4 – Solar Cell Efficiency [18].....	8
Figure 1.5 - (a) Schematic Representation of Thermoelectric Power Generator (b) Micor Thermoelectric Generator form D.T.S Company [21].....	9
Figure 1.6 - The Waste Heat Potential of Different Sectors [22].	9
Figure 1.7 - Annual Mean Wind Speed in UK (at 25m above ground level) [25].....	11
Figure 1.8 - (a) A Typical WPEH (b) A Non-contact WPEH[26], [27].	12
Figure 1.9 – Potential Vibration Sources	13
Figure 1.10 - Vibration Energy Harvesting System [2].	13
Figure 1.11 - A Reverse C shape with a Tail Design.	15
Figure 2.1 - Block Diagram of Electromagnetic Energy Harvesting System [2].	17
Figure 2.2 - Block Diagram of Electrostatic Energy Harvesting System [2].	18
Figure 2.3 – Two Types of Electrostatic Generators.....	19
Figure 2.4 - Internal Structure of Piezoelectric Material in Positive Piezoelectric Effect.	20
Figure 2.5 - Internal Structure of Piezoelectric Material in Inverse Piezoelectric Effect.	21
Figure 2.6 – Direction of Both Related Quantities for Piezoelectric Coefficients.	23
Figure 2.7 - Piezoelectric Material Classification.....	25
Figure 2.8 - Domain Direction of the Piezoelectric Ceramics.	25
Figure 2.9 - Piezoelectric Ceramics Polarization Process.....	26
Figure 2.10 – The Diagram of PVEHS [61].	29
Figure 2.11 - Energy Flow of the Piezoelectric Energy Harvesting System [47].	30

Figure 2.12 – Applications Based on Piezoelectric Effect [64], [65].31

Figure 2.13 - A Diode Bridge Rectifier.....32

Figure 2.14 - Different Categories of Aeroelastic Energy Harvesters [75].....36

Figure 2.15 - The Effect of Reynolds Number on the Fluid Flowing through the Bluff Body [76]......37

Figure 2.16 - The Relationship between Re Number and Strouhal Number [81].38

Figure 2.17 - The Three Regions for VIV [81].38

Figure 2.18 – (a)A Typical VIV Energy Harvester (b) A Bending and Torsion Piezoelectric Energy Harvester [83].39

Figure 2.19 - Different Cantilever Configurations [86].41

Figure 2.20 - Power Output for Four Cantilever Configurations [86].41

Figure 2.21 - Two-cylinder and Three-cylinder Energy Harvester [87], [88].42

Figure 2.22 - Hybrid Wind Energy Harvester [89]......43

Figure 2.23 - (a) Cylinder with Splitter Plate (b) Cross-section of Bluff Bodies Created [91].44

Figure 2.24 - (a) Typical Galloping Piezoelectric Energy Harvester (b) The Governing Equation of Galloping Motion (c) Typical Curve of Galloping Vibration Amplitude VS Fluid Velocity [83].46

Figure 2.25 - Fluid Pass Square and Triangle Shape [96].49

Figure 2.26 - (a) A Funnel-shape Design (b) T-shaped Structure [96].50

Figure 2.27 - T-shaped Energy Conversion System [97].50

Figure 2.28 - A Comb-like Beam Design [99].50

Figure 2.29 - Removable Cuboid Design [100]......51

Figure 2.30 - (a)Wing-shaped Structure (b) A Typical Wing-shaped Movement [103], [104]......53

Figure 2.31 - A typical Flutter Amplitude [105].54

Figure 2.32 - Novel Flutter Energy Harvesting Design [106].....	55
Figure 2.33 - Higher Attack Angel Futter Energy Harvester [108].	56
Figure 2.34 - Adaptive Flutter Piezoelectric Energy Harvester [110].	56
Figure 2.35 - Computational Process of Coupling [109].	58
Figure 2.36 - D-shaped Cylinder WIV [111].	58
Figure 2.37 - Triangularly Shaped Leaf Futter Design [113].	59
Figure 2.38 - A Typical Structure of the Aeroelastic Energy Harvester	64
Figure 3.1 - Top View of the Prototype.....	72
Figure 3.2 - Different Series Model for the Experiment	74
Figure 3.3 - LDT0-028K Structure.....	76
Figure 3.4 - Relationship of Tip Deflection and Voltage (LDT0-0.28K).	77
Figure 3.5 - M-2807-P2 Structure.	78
Figure 3.6 - Wind Tunnel.....	79
Figure 3.7 - Digital Oscilloscope and Screen	82
Figure 3.8 - Nano43 Transducer System.....	83
Figure 3.9 - The Operation Screen of the Transducer System.....	85
Figure 3.10 - Four Design of Initial Simulation Verification	86
Figure 3.11 - The 2D Simulation Models.....	87
Figure 3.12 - Important Criteria Spectrum (Skewness and Orthogonality).....	88
Figure 3.13 - Lift Coefficient of Rectangular, Cycle and Curved Plate at 4m/s.....	91
Figure 3.14 - Lift Coefficient of Curved Plate and New Design at 4m/s	92
Figure 4.1 - A Mounting Interface Plate for Connecting Transducer and Cantilever Beam	98
Figure 4.2 - Lift Force for T1 and T0 at 5m/s	99
Figure 4.3 - Peak Lift Force for the T1 and T2 Models.....	100

Figure 4.4 - Voltage Generated (RMS) for the T1 and T2 Models	100
Figure 4.5 - R Series Models Design.....	102
Figure 4.6 - The Broken R Series Models	102
Figure 4.7 - Experimental Setups for A Series Models.....	104
Figure 4.8 - Lift Force for A1-A5 at 6m/s	106
Figure 4.9 - Peak Value of Lift Force for A1-A5 Models at 3m/s-7m/s.....	107
Figure 4.10 - Average Lift Force for A1-A5 Models at 3m/s-7m/s.....	108
Figure 4.11 – (a) Broken Cantilever Beam (b) The A Series Model X Axis Schematic Diagram.....	108
Figure 4.12 - The S Series Models	111
Figure 4.13 - Experimental Setup for S Series Models (Aluminium Cantilever Beam)..	111
Figure 4.14 - The Lift Force of the S0 and S5 Model at 3m/s	112
Figure 4.15 - Peak Lift Force for S Series Models.....	113
Figure 4.16 - Average Frequency for S Series Models	114
Figure 4.17 - Voltage Generated for the S Series Models	115
Figure 4.18 - The External Resistance Box.....	115
Figure 4.19 - Lift Force for S0 model at 3m/s	117
Figure 4.20 - Voltage Generated Comparison (R1-S4 & R2-S5) (LDT0-028K)	120
Figure 4.21 - Average Frequency Comparison (R1-S4 & R2-S5)	120
Figure 4.22 - The Cantilever Beams Used in the Experiment	122
Figure 4.23 - Average Lift Force for the S0 and S5 Models at 3m/s (Plastic Cantilever Beam)	123
Figure 4.24 - Peak Lift Force for the S Series Models (Plastic Cantilever Beam)	124
Figure 4.25 - Average Frequency for the S Series Models (Plastic Cantilever Beam) ...	125
Figure 4.26 - RMS Voltage for the S Series Models (Plastic Cantilever Beam)	125

Figure 4.27 - Voltage Generated for the S Series Models (M-2807-P2)	129
Figure 5.1 - The Simulation Geometry for the S Series Models.....	133
Figure 5.2 - Mesh Generated for S0 Model	134
Figure 5.3 - Mesh Independent Study for the S Series Models	136
Figure 5.4 - Lift Coefficient for S0 Model at 7m/s	137
Figure 5.5 - Representative Lift Coefficient Cycle for the S0 Model.....	137
Figure 5.6 - Vector and Contour Plots for S0 Model at Key Points.....	138
Figure 5.7 - Vector and Contour Plots for S1 Model at Key Points.....	139
Figure 5.8 - Velocity Streamline Diagram of the S1 Model at 1.526s.....	140
Figure 5.9 - Lift Coefficient for S1 Model at 7m/s	141
Figure 5.10 - Lift Coefficient for S5 Model at 7m/s	141
Figure 5.11 - Representative Cycles of S5 Model	142
Figure 5.12 - Streamline Plot for S5 Model at Key Points.....	142
Figure 5.13 - Vector Plot for S5 Model at Key Points	143
Figure 5.14 - The Peak Lift Coefficient Simulation Results of the S Series Models	144
Figure 5.15 - Frequency Simulation Results of the S Series Models.....	145
Figure 5.16 - Response Time Analysis.....	145
Figure 5.17 - Vector and Contour Plots for P10 Model at Key Points	149
Figure 5.18 - Effect of Tail Length on Lift Coefficient (The P Series Models)	150
Figure 5.19 - Effect of Tail Length on Frequency (The P Series Models)	150
Figure 5.20 - Lift Coefficient Comparison for First Group (S5&R2)	152
Figure 5.21 - Vector plot Comparison for First Group (S5&R2).....	153
Figure 5.22 - Lift Coefficient Comparison for Second Group (S4&R1).....	153
Figure 6.1 - The Ratio of Experimental to Simulated Lift Force.....	158

Figure 6.2 - Model Deflection Simulation Diagram159

Figure 6.3 - The Lift Force of the S0 and S1 Model at 7m/s (Aluminium)162

Figure 6.4 - Power Output Trend with Increased Tail Length.....164

Figure 6.5 - Cantilever Beam with Mass Block [2]165

Figure 6.6 – Tail Structure with Grooves166

Figure 6.7 - Illustration of a Cantilever Beam Covered with Piezoelectric Films on Both Sides167

CHAPTER 1. INTRODUCTION

1.1 Thesis Overview

With the development of technology, more and more electronic devices appear in people's lives. The power supply problem of these devices has also become a field that needs to be studied, especially for some electronic devices in remote areas. Piezoelectric energy harvesters are expected to harvest energy from the wind and supply it to small electronic devices. In the current research, further improving the energy conversion efficiency of harvesters has become a popular topic. This thesis will try to propose a novel piezoelectric energy harvester that vibrates in the galloping mode in order to improve the energy conversion efficiency and provide power for small electronic devices.

This thesis is divided into seven chapters, in the introduction section, it will start from the current background, identify the current problems, introduce different energy harvesting methods, and introduce the vibration energy in nature. Chapter two will review the literature, compare and determine the advantages and limitations of different types of vibration energy harvesters, and introduce how piezoelectric energy harvesters work. In addition, it will also review and classify the four primary vibrations used in piezoelectric energy harvesters, in order to be able to compare and analyse the differences between them. In chapter three, it will begin to introduce the prototype of the novel piezoelectric energy harvester designed, and also introduce various equipment that will be used in subsequent experiments. At the end of this chapter, the model will be initially simulated and verified before the experiment begins.

Chapter four mainly focuses on the experimental verification of the model. Through experiments, in addition to verifying the effectiveness of the model, the experimental study of various parameters of the model will also be conducted, such as the influence of the front-end curved body thickness on the performance of the model, etc. The simulation study will be used in chapter five to study the model. By simulating the study, the flow of the fluid around the model will be determined, in order to analyse the principle of the model's vibration. The simulation results and experimental results will be compared in chapter six to analyse the differences between the two results, providing ideas and inspiration for design in

real-world applications. Finally, chapter seven will summarize the main findings of this thesis and make suggestions for future work.

1.2 Power Supply

With the development of science and technology in recent years, people's demand for various electronic devices has become increasingly extensive. Electronic device provides information and services for people and is everywhere in people's lives. The need for multiple types of mobile devices used in daily communication, sensor devices used to provide information, and intelligent devices used for supporting work is still increasing [1]. At present, electronic devices are becoming lighter and miniaturized in size, such as microelectromechanical systems. Microelectromechanical systems (MEMs) are high-tech devices with a few millimetres or smaller dimensions. MEMs are Miniature devices or systems which combine Micro-sensor, micromechanical structures, micro-power sources, signal processing, control circuits, high-performance integrated electronic device, interface, and communication parts. Because of their small physical size, MEMs are widely used in different fields [2]. There already has many MEMs applications for the human body, as shown in Figure 1.1. Moreover, it also has many other applications. For example, it could accurately measure stability for building [3], deliver drugs inside a living organism safely [4], eliminate additional noise from the signal [5], monitor body movements by biomedical sensors [6], etc. As a result, these devices occupy a high proportion of people's lives. However, since MEMs are usually embedded in the structure, they mainly rely on batteries for power supply, and almost all devices require frequent charging or replacing batteries.

The battery could convert electric energy and chemical energy, and store converted energy. Although the efficiency and performance of the battery have been developed year by year, there are still some limitations. First, because of its finite electricity storage and shelf life, it must be frequently replaced. In some remote areas, that will be costly and complicated work. Moreover, even for a rechargeable battery, repeated charging is not only a tedious task, but the number of times the battery is charged and discharged is inversely proportional to the efficiency of the battery.

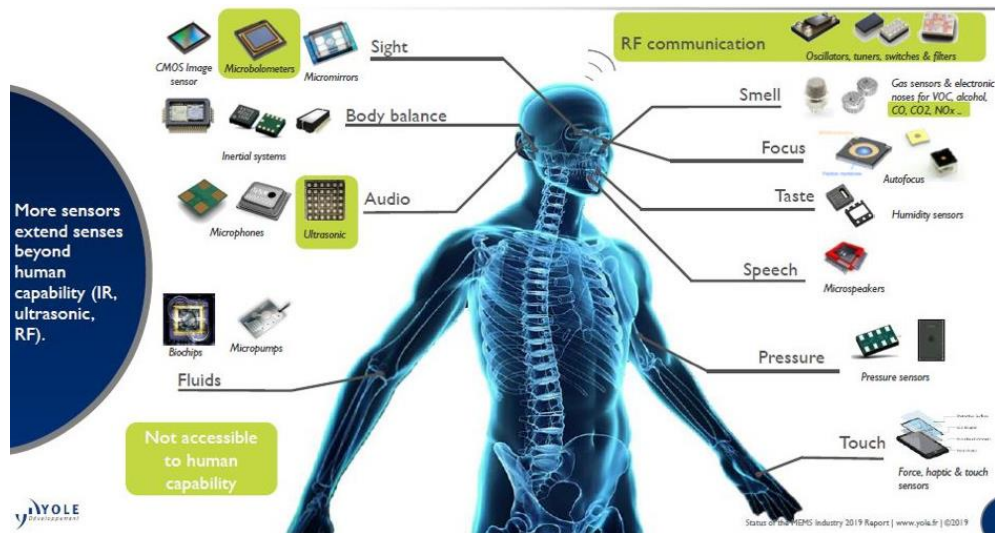


Figure 1.1 - MEMS Applications for the Human Body [7].

Also, to increase the capacity of the battery, the volume of the battery will also increase, and the bulky battery is obviously not the best choice for micro-electro-mechanical systems and portable devices. In addition, if the battery is used outdoors, it must cover the surface with a coating or protective cover to protect it from natural erosion, increasing the battery's installation cost and maintenance cost. Finally, because different types of batteries contain various chemicals, they are particularly susceptible to damage when subjected to external forces, and leaked chemicals may damage devices, operators, or the natural world [8]. Therefore, it is crucial to find a stable alternative energy supply.

1.3 Energy Harvesting

Due to the demand for energy supply for devices, in recent years, energy harvesting has attracted people's attention, and it has become a promising solution for small power devices by obtaining ambient energy. Energy harvesting is the process of capturing energy from the ambient and then converting it to electricity or other suitable forms of energy to support power to other equipment or batteries. Some large-scale energy harvesting technologies have matured and are widely used, such as wind farms, hydropower plants and solar battery arrays.

These energy harvesting methods usually power the grid. Nowadays, micro energy harvesting gradually focuses, which is not a new concept. As the power consumption of the sensor and other devices has decreased, the system energy consumption and energy acquisition

gradually become balanced, and micro energy harvesting will become a potential technology. In general, the power generated by micro energy harvesting is usually between 10-100s of Microwatts and the overall size of micro energy harvester is generally in millimetres or centimetre levels. In summary, micro energy harvesters have better adaptability to MEMS or portable equipment.

So that energy harvesting may become a practical approach to solving battery shortcomings. Using energy harvesting to power the battery ensures that batteries do not need to be changed frequently, even in remote locations. Also, energy harvesting could become the main power supply for the devices if it has a higher efficiency of harvesting [2],[3].

In general, the benefits of energy harvesting are as follows. First, energy harvesting has a high degree of flexibility, especially for devices that cannot use an external power supply. The energy harvesting device can be placed inside the device for power supply. In addition, maintenance costs are significantly reduced due to the endurance of the energy harvesting device. And because the energy source comes from the natural environment, no chemical treatment is required, and no chemical reaction is involved, the energy collection equipment is safer. Figure 1.2 indicates the various energy harvesting sources from the ambient, including solar radiation, water flow, wind, radio waves, mechanical vibration, etc.

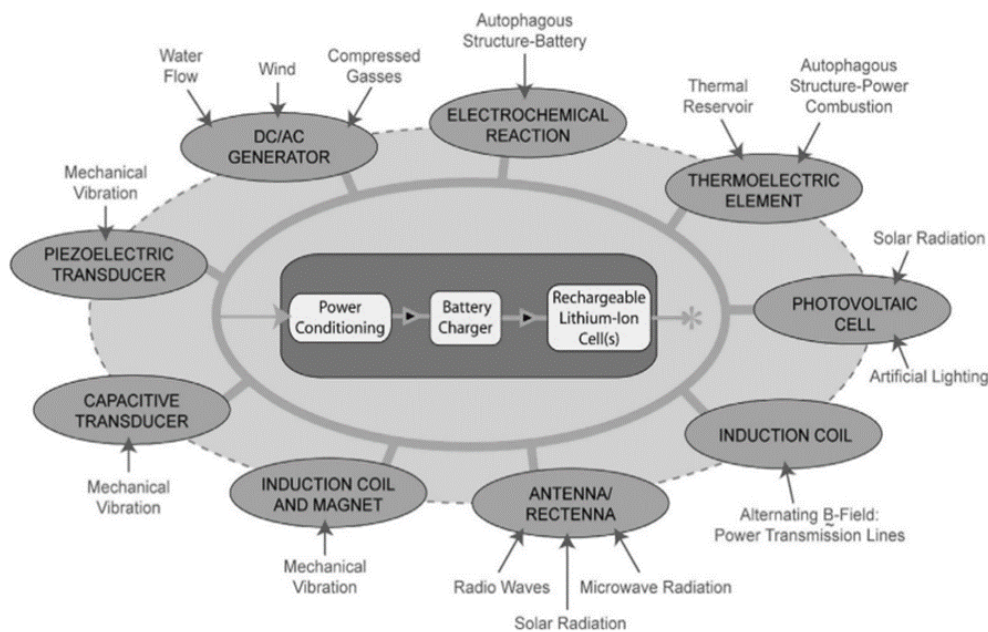


Figure 1.2 - Various Energy Harvesting Source from the Environment [9].

The energy harvesting system is usually composed of four parts. First, various types of transducers (e.g., a thermoelectric element, photovoltaic cell, piezoelectric transducer) are used to harvest different forms of energy (e.g., solar radiation, thermal energy, mechanical vibration) from the environment. After that, the transducer's signal is adjusted through power conditioning. Due to the different transducers and the changes in the background, the signal is usually unpredictable. It is taking the piezoelectric vibration energy harvesting system as an example. The oscillator is placed in a fluid to capture vibration energy, and the piezoelectric kit converts the vibration energy into electrical energy output. However, the output is unstable and depends mainly on environmental factors. The output is affected by the frequency and amplitude of the oscillator, and it may generate a high voltage power output. Moreover, the piezoelectric kit will generate AC outputs; however, the storage requires a stable DC. At this time, power conditioning could convert the output current into a steady and continuous DC. Finally, the excess DC is stored to ensure continuous power output. The key component of a small-scale energy harvesting system is the energy capture component and transducer, which determine the efficiency of the whole system.

Energy harvesting has better performance in powering ultra-lower-power devices. In some remote areas, the devices may not need too much power to drive, and the micro-level energy harvested is enough to fulfil power requirements at a lower cost. In that case, energy harvesting may substitute the battery and become the device's only power supply. The minimum power required for some common devices is shown in

Table 1-1.

Table 1-1 - The Minimum Power Required of a Number of Common Devices [8].

NO.	Devices	Power	References
1	Quartz oscillator (32kHz)	100nW	[10]
2	Electronic watch or calculator	1 μ W	[10]
3	RFID Tag / Implanted medical device	10 μ W	[11]
4	Hearing aid	100 μ W	[10]
5	Short range (~30mm) proximity sensor, model SFH 7741 (OSRAM)	270 μ W	[12]

6	Automotive light sensor, model SFH 5711 supplied from 2.5V (OSRAM)	1.03mW	[13]
7	The sunflower miniature computing system	1.75mW	[14]
8	An ultra-wide-band (UWB) transmitter developed in 0.18m CMOS for body area networks	2mW	[15]
9	Accelerometer, model ADXL103 supplied from 5V (Analog Devices)	3.35mW	[16]
10	A transmitter (model RFM HX1003) working at 418MHz with a range of 50ft	7.5mW	[17]
11	Potential needs of a WSN working Zigbee circuits	10mW	[18]
12	A custom-designed radio operating at 1.9GHz with a range of 10m	12mW	[19]
13	A bulk acoustic wave-based transceiver for a tyre pressure observing sensor module	18.6mW	[20]
14	Autonomous sensor module	20mW	[20]
15	Berkeley's Telos Mote	36mW	[21]
16	Bluetooth Transceiver	45mW	[10]
17	PALM, MP3	100mW	[10]

In many applications, a micro energy harvester as a power source becomes an attractive alternative to a battery, and these harvesters have some characteristics as follows.

- Long lifespan and high reliability
- be competitive on size and cost
- No need for regular maintenance
- Continuously power supply
- No emissions in operation

Currently, micro energy harvesting methods mainly have photovoltaic modules, thermoelectric, wind, and piezoelectric energy harvesting methods. The background of these harvesters is provided in the following subsections.

1.3.1 Photovoltaic Modules Energy Harvesting

According to the Photo-electric effect, photovoltaic modules energy harvesting is a harvesting method that converts sunlight into electricity. When a photon is irradiated onto a light-sensitive substance (such as selenium), its energy can be absorbed by electrons of the materials. After the electron absorbs the photon's energy, the kinetic energy increases immediately and becomes a photoelectron, forming an optical current.

Solar radiation energy harvesting is more and more mature technology, and the electricity is generated from sunlight by photo-electric effect and harvested by solar cells or solar arrays. As one form of energy harvesting, the solar array has been arranged in many cities and connected to the power grid. In addition, some small-scale or micro solar cells are also developed for portable devices, as shown in Figure 1.3. Furthermore, the advantages of solar batteries are apparent. For example, there is no release of pollution substances, including noise pollution, during operation, the solar cells' size could be optimized depending on the need, and the efficiency of the solar cell has significant increase in recent years, with the highest reaching 47.1%, as shown in Figure 1.4.

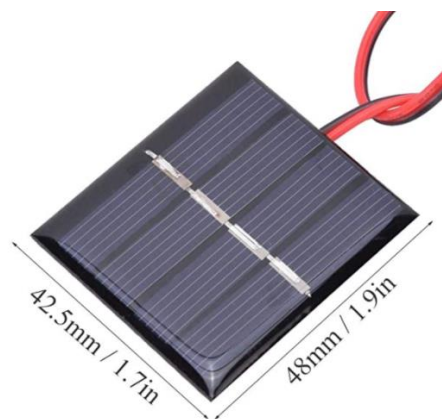


Figure 1.3 - Small-scale Solar Cell.

However, there still has some limitations for small-scale or micro solar cells. Solar radiation is not stable [22] ; for example, at night or on cloudy days, the intensity of solar radiation becomes extremely weak. Although solar radiation can be predicted, providing smooth and reliable energy for small-scale solar cells for small equipment may be challenging. Moreover, the energy output of solar cells is directly proportional to the area receiving solar radiation, and the cell requires a relatively large surface area to meet energy demands for devices, so it

is difficult to be used for some embedded devices. In terms of cost, photovoltaic cells require frequent maintenance to ensure that the surface is clean to maintain high efficiency; otherwise, efficiency will continue to decrease. Therefore, using photovoltaic cells instead of batteries to power MEMs or wireless devices or power batteries does not necessarily reduce installation and maintenance costs [18], [19].

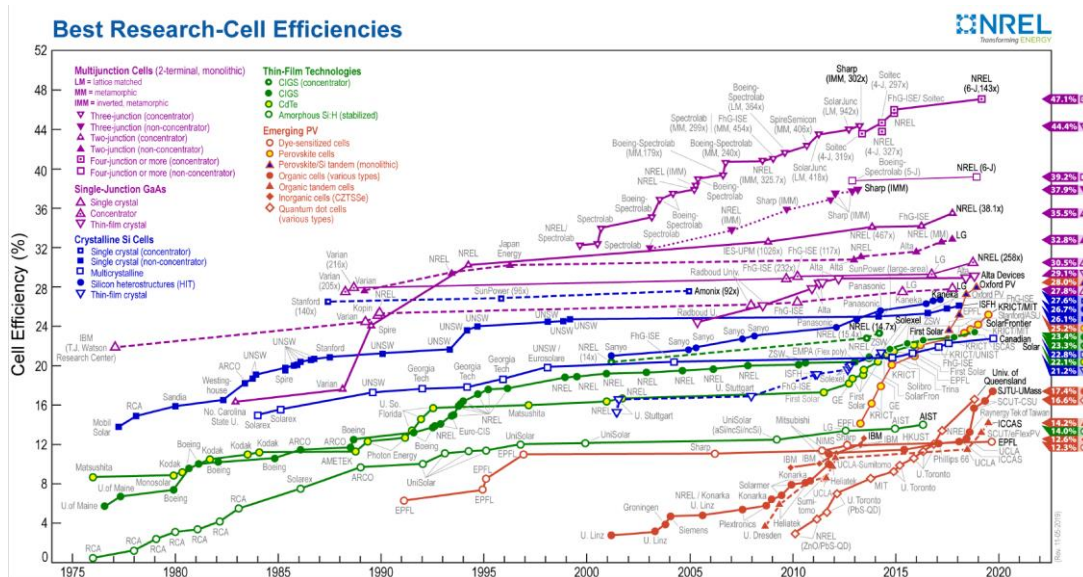


Figure 1.4 – Solar Cell Efficiency [22].

1.3.2 Thermoelectric Energy Harvesting

A schematic representation of a thermoelectric energy harvester is shown in Figure 1.5(a); it consists of two semiconductors, negative and positive charge carriers (n-doped and p-doped, respectively). The current flow is in series, and the heat flow is parallel in semiconductors. According to the Seebeck effect, the current it produces is proportional to the temperature difference between the heat source and the heat sink. In general, the temperature of a heat sink is the temperature of outdoor air. Therefore, as long as there is a temperature difference, it can be used, such as waste heat, living body, solar heat, etc. In addition, its size is flexible and can be mounted in some miniature devices.

Since a large amount of thermal energy is wasted, the thermoelectric energy harvester is widely concerned. Forman et al. pointed out that about 72% of global energy is lost by first direct energy conversion, which includes 63% of the energy loss in the form of waste heat.

The waste heat potential of different sectors is shown in Figure 1.6, and Carnot's potential (efficiency) is the upper limit of thermal energy to be converted.

It can be seen from the figure that although the thermal energy loss from the electricity loss is high, the convertible heat energy is negligible. Therefore, only Carnot's potential for industrial and transportation show a better value, 34% and 35%, respectively. However, due to the temperature difference and the conversion efficiency of the thermal generator, only 5% of waste heat can be converted into electrical energy for these two sectors.

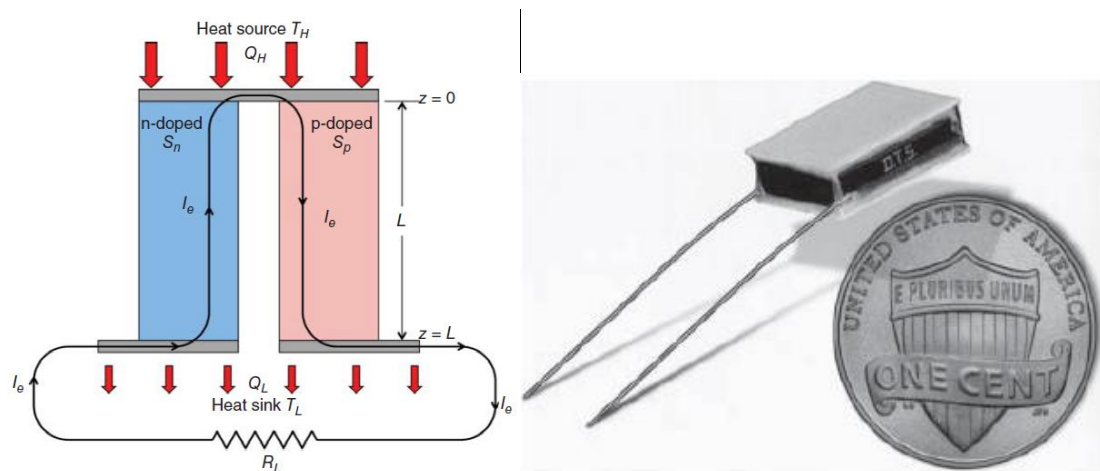


Figure 1.5 - (a) Schematic Representation of Thermoelectric Power Generator (b) Micror Thermoelectric Generator form D.T.S Company [25].

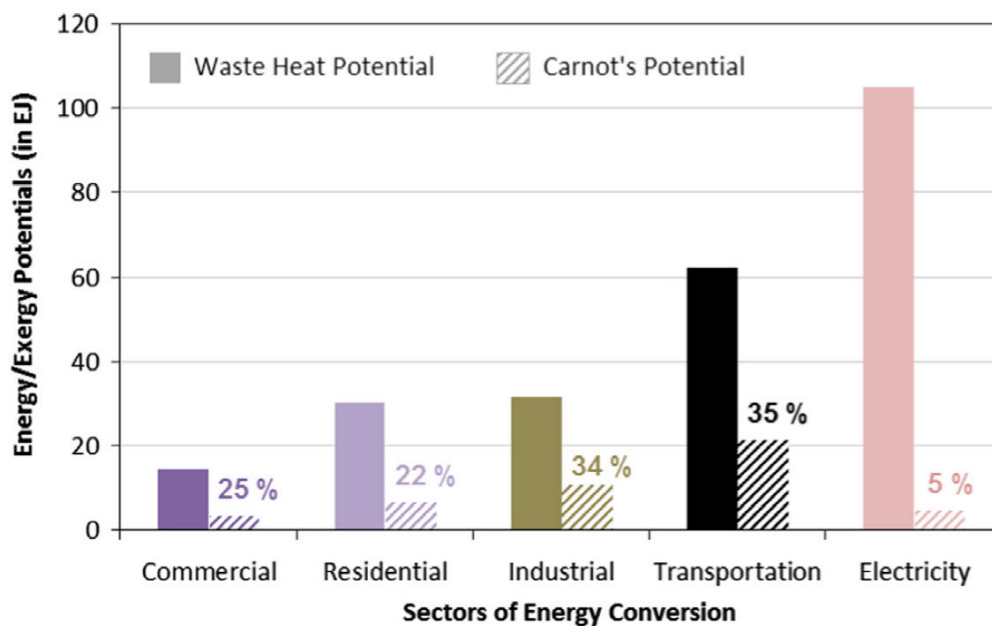


Figure 1.6 - The Waste Heat Potential of Different Sectors [26].

There are also many breakthroughs in the field of micro-thermal power generators. In 1997, D.T.S launched the first commercial micro-thermal generator (Figure 1.5(b)), with only one coin size. At present, various micro-thermal energy harvesting devices are continuously reduced in size and improved in efficiency. Compared with other micro-energy harvesting devices, the micro-thermal energy harvesting device has the following benefits:

- The device's size can be used in micro-electro-mechanical systems (MEMs).
- Its shape can be adjusted according to specific needs, and its materials and design are highly flexible.
- The cost of this device is low.

In summary, the size of the thermal energy harvester can meet most of the MEMs demands. Still, its energy output depends primarily on temperature difference, which leads to its application being mainly limited to industry and transportation. In addition, since the human skin has low thermal conductivity, thermal resistance is about 200 to over 1000 cm² KW⁻¹. The application of a thermal energy harvester for a living body still needs more research to increase efficiency. This also adds to its difficulty for installation and use in MEMs and wireless devices [22], [23].

1.3.3 Wind Energy Harvesting

Wind energy, as one of the clean energy sources, has great potential, especially for the United Kingdom. As shown in Figure 1.7, the United Kingdom has sufficient wind energy resources, and the average annual wind speed can reach more than 5m/s at 25m above ground level. In addition, wind energy has many other natural advantages that are not available in clean energy, compared to photovoltaic power and hydropower; for example, wind energy has lower dependence on geographical position and weather. General, the capture device of wind energy is a wind farm for large-scale energy harvesting; giant wind turbines can be placed offshore and connected to the grid. Some small wind turbines are also used to power small devices, such as traffic lights. The micro wind energy harvester mainly comprises wind turbines and a power generator. Large wind turbines typically use a permanent magnet generator, while micro wind energy harvester has different generator designs, such as piezoelectric thin film harvesting energy, etc.

At present, more wind power farms have been established worldwide, but the efficiency of wind power generators is related to the size of their blades. For micro wind energy harvesters, the shorter wind blades lower the efficiency. When the wind speed changes, the micro wind harvester cannot adjust its fan deflection angle or automatically shut down according to the wind speed. The micro wind harvester is easily damaged at a high wind speed.

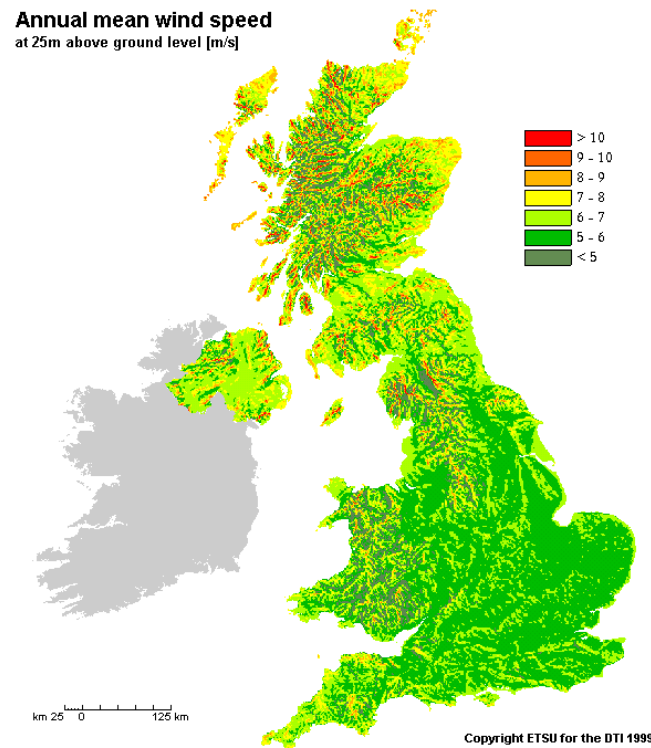


Figure 1.7 - Annual Mean Wind Speed in UK (at 25m above ground level) [29].

A typical micro wind energy harvesting device is rotating piezoelectric energy harvesters, also called windmill piezoelectric energy harvesters (WPEH). Wind turbines have been developed for years and used in commercial applications. Like a wind turbine, WPEH usually uses the wind flow to drive the fan blades to rotate and place objects or magnets behind the rotating shaft to make the piezoelectric device bend continuously with the rotation of the fan blades to generate electricity.

A rotating piezoelectric energy harvesters is shown in Figure 1.8(a)[30]. The back of the rotating shaft is fixed with a turntable. When the shaft rotates, the turntable will continuously hit the piezoelectric device to make it bend. The design can produce a maximum power output of 2566.4uW at 15m/s. But the cut-in wind speed of this design is 4m/s. Therefore, the friction of the design through a turntable in contact with the piezoelectric device may

affect the power output. Another common way is to bend the piezoelectric material in a non-contact manner by fixing the magnet behind the rotating shaft and on the piezoelectric device. This type of design is shown in Figure 1.8 (b)[26], [27].

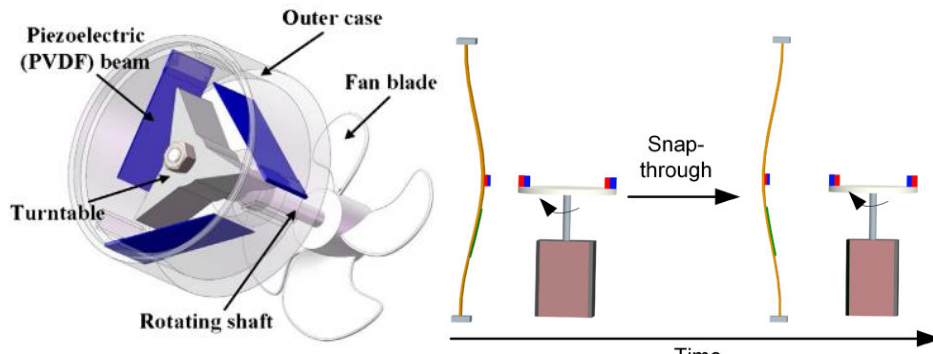


Figure 1.8 - (a) A Typical WPEH (b) A Non-contact WPEH[26], [27].

In recent years, most of the design concepts for WPEH have been contactless, using magnets to make piezoelectric devices bend under "contactless" conditions. This way does increase the power output, but it is still inevitable that friction is generated when the blades rotate. In addition, WPEH also has a relatively high cut-in wind speed, which makes it difficult for this type of energy harvester to operate under low wind speed conditions. Finally, the problem of WPEH is the large physical size. Since the area of the fan, the blade is proportional to the energy conversion efficiency, but the large fan blade causes the portability of the energy harvester to decrease, so developing the new fan blade shape to increase the energy conversion efficiency may be a key point for reducing WPEH physical size.

Another application of wind energy is to use aeroelastic instability to harvest energy. This harvester will be specifically discussed in the next subsection, vibration energy harvest.

1.3.4 Vibration Energy Harvesting

The vibration is anywhere in the ambient, such as the vehicle (trains, ships, etc.), machinery (pumps, rotation, etc.) and so on as shown in Figure 1.9. Vibration energy harvesting is able to transfer mechanical vibration to electric power, and vibration energy harvesting has huge potential. In addition, the study of flow-induced vibration is popular, the different design of oscillator was proposed, they vibrate when wind or fluid passes them, and then different method was used to harvest the vibration. Vibration energy harvesting system normally

consists of four sections, as shown in Figure 1.10, the energy harvester, the circuit system, storage and the load (devices) [28]–[30].

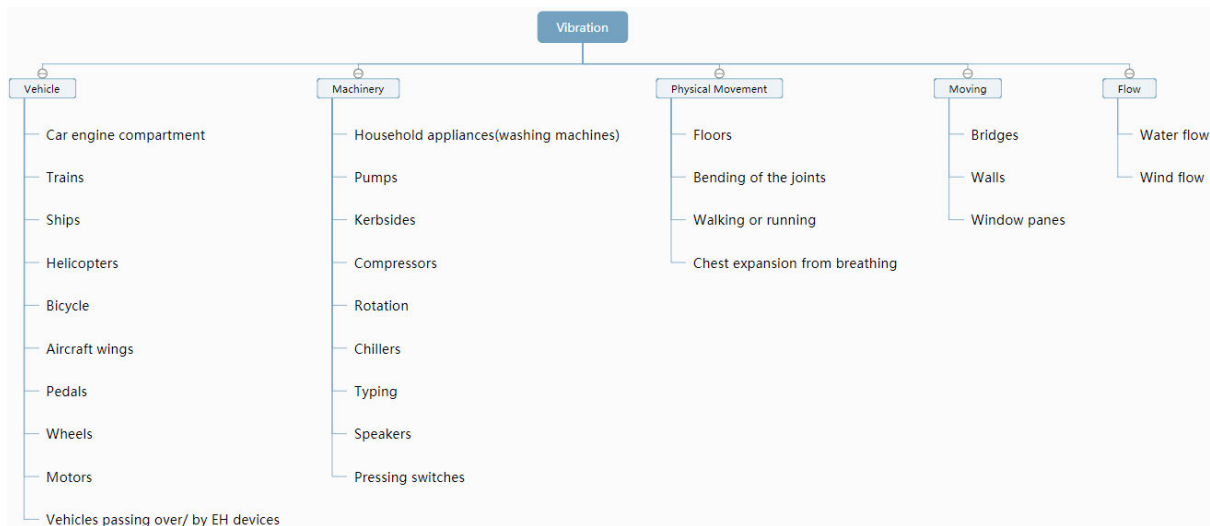


Figure 1.9 – Potential Vibration Sources.

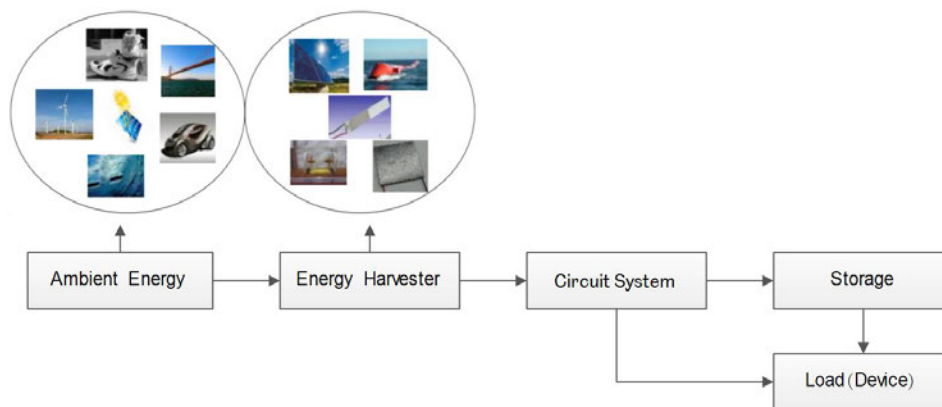


Figure 1.10 - Vibration Energy Harvesting System [8].

The circuit system is used to process signals from harvester to accepted electric power, and the common components include the filter, which could filter the signals to eliminate power signals in unwanted frequencies, an AC-DC converter and so on. There are three most common types of vibration energy harvester, which depends on different mechanical methods, electromagnetic, electrostatic and piezoelectric harvester [31]–[33]. In the following part of this section, a brief description of these three harvesting methods is provided and compared.

The power output of the vibration energy harvester is usually relatively small, not enough to be connected to the grid. Existing research is mainly in the laboratory test stage, improving energy conversion efficiency by changing the design to maximize vibration frequency and

amplitude. The evaluation of various vibration energy harvesters and various types of flow-induced vibration will be introduced in detail in the next chapter.

1.4 Aim and Objectives

Energy harvesting is a future trend with the implementation of policies such as reducing emissions. For large-scale energy harvesting devices such as hydroelectric power stations, it has already been used as one of the main power supply facilities in many countries. However, the demand for power supply for small devices in remote areas is increasing. Vibration energy harvesting is also considered as one of the future mainstream directions for small device power supply. Vibration energy is widely present in nature, and wind energy, as one of the widely used clean energy, is also attracting attention. By using some models, wind energy that is widely present in nature can be converted into the vibration of the model, and then harvested by vibration energy harvesters for small device power supply. The power output of existing designs is still at a low level and its research is still in the experimental stage. As one of the most important components of vibration energy harvesters, the design of the front-end model is currently mainly based on several mainstream models (cylinder, cube, etc.). Therefore, the design of the front-end model can greatly affect the power output of the vibration energy harvester, thus enabling energy harvesters to move from the laboratory to people's lives.

The aim of this thesis is as follows.

This thesis aims to design and experiment with a novel model (a reverse C shape with a tail design), as shown in Figure 1.11, that can be used at the front end of a piezoelectric energy harvester, based on existing theories and models of vibration energy harvesting. The model is expected to have a higher energy conversion efficiency and be able to provide a greater power output for the harvester.

In order to achieve this aim, the following objectives are defined:

- By reviewing the literature and theories of various types of vibrations, summarize and compare existing designs of various types of vibrations, design a front-end model that can provide greater lift force.

- Through experimentation, research the effects of each component of the model on the performance of the model in order to optimize the model design.
- Use simulation software to investigate the fluid behaviour around the model to provide theoretical support for the vibration of the model.
- Compare experimental and simulation results, further optimize the model design, and provide optimization solutions and suggestions for the use of the model in practical applications.



Figure 1.11 - A Reverse C shape with a Tail Design.

CHAPTER 2. LITERATURE REVIEW

2.1 Introduction

This chapter conducts a comprehensive review of the current literature on vibration energy harvesting, starting with the three types of vibration energy harvesting methods. The literature is summarized, and the current mainstream three vibration energy harvesting methods are introduced and compared. The main focus is on the literature related to piezoelectric energy harvesters, which includes a review of piezoelectric materials. In addition, the literature on fluid-induced vibration energy harvesting is also reviewed, and four different vibration types are summarized according to the literature, and the application, challenges, and future development directions of each vibration type are analysed. Furthermore, an essential component of vibration energy harvesters, cantilever beams, is reviewed in the literature. Finally, the current gaps are identified in this field based on existing literature.

2.1.1 Review Scope

This chapter is divided into three review sections:

- Three types of vibration energy harvesting
- Four types of flow-induced vibration energy harvesting
- The study of cantilever beam

2.2 Type of Vibration Energy Harvesting

2.2.1 Electromagnetic Harvesting Method

Electromagnetic Vibration Energy Harvester (EVEH) is used to convert mechanical vibration energy to electric energy by magnetic field. This method could convert energy by Faraday's law of induction as shown in Equation 2.1 and maximum open-circuit voltage is as shown in Equation 2.2.

$$\varepsilon = -\frac{d\Phi_B}{dt}$$

Equation 2.1

$$V_{OC} = NBl \frac{dx}{dt}$$

Equation 2.2

Which ε is the electromotive force (EMF); Φ_B is the magnetic flux; N is the number of the coil wire; B is the strength of the magnetic field; l is the length of a winding and x is the relative displacement distance between the coil wire and magnet.

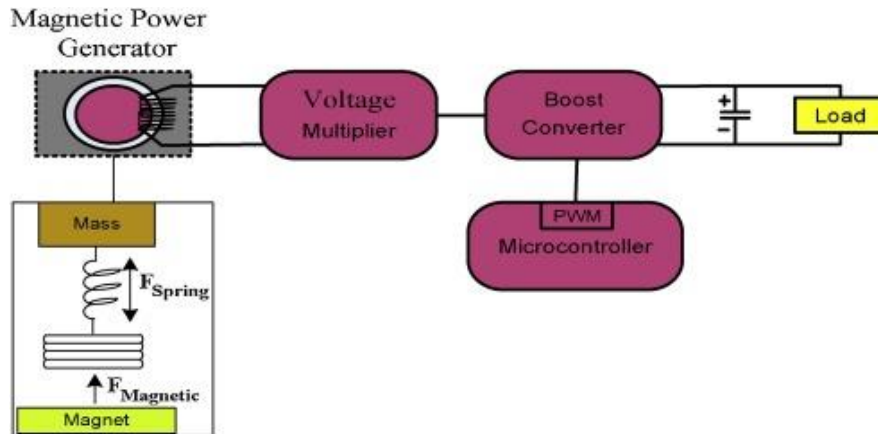


Figure 2.1 - Block Diagram of Electromagnetic Energy Harvesting System [8].

According to the Faraday's law, the electromotive force (EMF) will be generated on the conductive loop, when the magnetic flux through the surface enclosed changes by time. Vibration is changed to the comparative motion between the coil and mass in the EVEH system, at the same time, the coil will continuously cut the magnetic induction field and generate current in the coil. As shown in Figure 2.1, the magnet offers a strong magnetic induction field, and the voltage multiplier and boost converter are used to increase the voltage generated, meantime, the output current will decrease due to the law of conservation of energy. Some DC-DC boost converters have been developed to reduce energy loss and increase the power output of the system to 58mW [39].

Some researchers suggested that using EVEH as a sensor to drives the devices [40]. Some authors discussed a model based on the simulation design that stated the wireless device could obtain the power of $46.2 \mu W$ from EVEH, and the excitation frequency is 5 Hz [41].

2.2.2 Electrostatic Harvesting Method

Electrostatic energy harvesting technology converts mechanical vibration to electric power by electrostatic effect. Electrostatic vibration energy harvester (EtAWAH) needs some

preparations before harvesting energy; EtAWAH requires an external power supply to create the original voltage difference between the variable capacitors, and the energy conversion happens when the value of the variable capacitor changes due to vibration[36],[42].

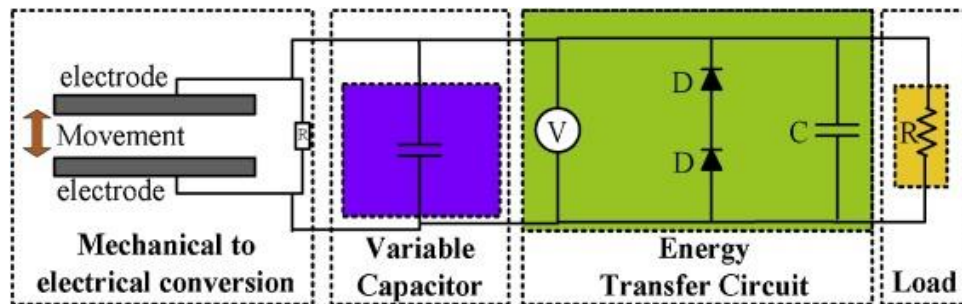


Figure 2.2 - Block Diagram of Electrostatic Energy Harvesting System [8].

Normally, a capacitive structure prepared consists of two adjacent conductor's electrode plates and the gap of the structure is filled with air, dielectric materials or vacuum as shown in Figure 2.2. Moreover, EtAWAH also includes a variable capacitor and an energy transfer circuit to adjust and control energy output. In order to maximize the efficiency of converting, a whole EtAWAH may have several capacitive structures[43].

$$E = \frac{1}{2}V^2C = \frac{1}{2}V^2(\epsilon_0 \frac{S}{d})$$

Equation 2.3

Which E is the energy stored within capacitor; V is the voltage between the plates; C is the capacitance; ϵ_0 is the electric constant; S is the area of overlap of the plates and d is the separation between the plates. As shown in Equation 2.3, there are two parameters that are decisive for the electrostatic energy stored within the capacitor, the separation between the plates and the area of overlap of the plates. Therefore, there are two different types of electrostatic generators, which are in Figure 2.3, In-plane generators by changing the overlapping area and out-of-plane generators by changing the separation.

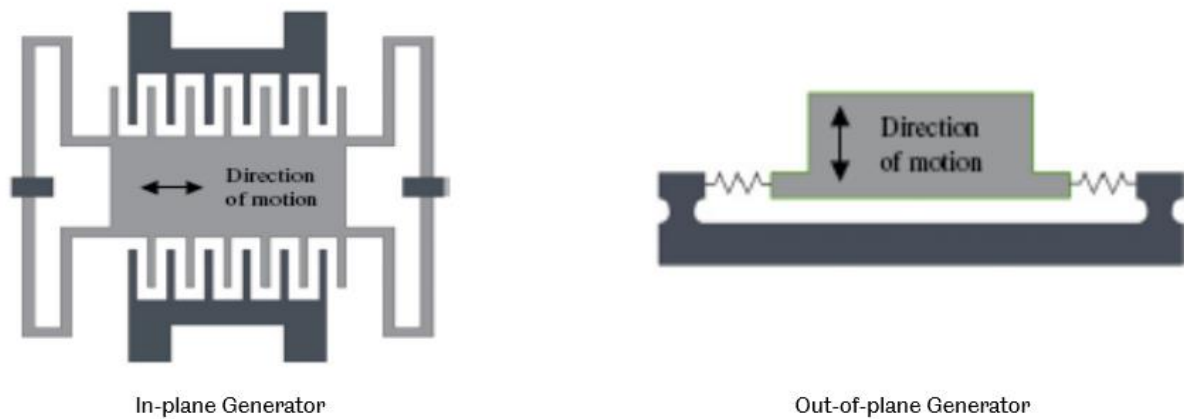


Figure 2.3 – Two Types of Electrostatic Generators.

The EtAWAH has already been used in MEMs in some applications, although it is difficult to have power output for MEMs, because of miniaturization [8]. For example, the research in [44] states the harvester could generate high power output $1 \mu W$ in MEMs. And in [45], the voltage generated is more than 3V when an external free-rolling proof mass is selected to be the experiment object, and it also pointed out that the energy harvester is only suitable for small frequency motion sources. The device of EtAWAH could be easily smaller than other vibration harvester, however, large frequency and external sources required, and the lower conversion efficiency are still the main limitations.

2.2.3 Piezoelectric Harvesting Method

Piezoelectric energy harvest as a popular way to harvest vibration, could transfer vibration energy to electricity. Piezoelectric transducers are widely used in small vibration energy harvesting field, due to their ease of miniaturization, high power density, compatibility with integrated circuit technology, and various general structural shapes. Using the output energy of the piezoelectric vibration energy harvesting to power wireless sensors has become a hot issue of concern to industry and academia [46].

2.2.3.1 Piezoelectric Effect and Inverse Piezoelectric Effect

The word Piezo is from the Greek, which means to squeeze or press [47]. In the early 1880s, the piezoelectric effect was founded by Curie Brother who were French physicists. Generally speaking, the piezoelectric material will generate the electric charge, when its surface is stressed. Later, the inverse piezoelectric effect was also discovered, which means the shape of piezoelectric material will change by applying in an electric field [48]. Piezoelectricity is a

coupling property that occurs between mechanical and electrical behaviour on certain crystals. The piezoelectric effect exhibited by these piezoelectric materials changes with time, withstand the pressure and the temperature of the surrounding environment, especially when the temperature exceeds the Curie temperature (magnetic transition point), the piezoelectricity will disappear [49].

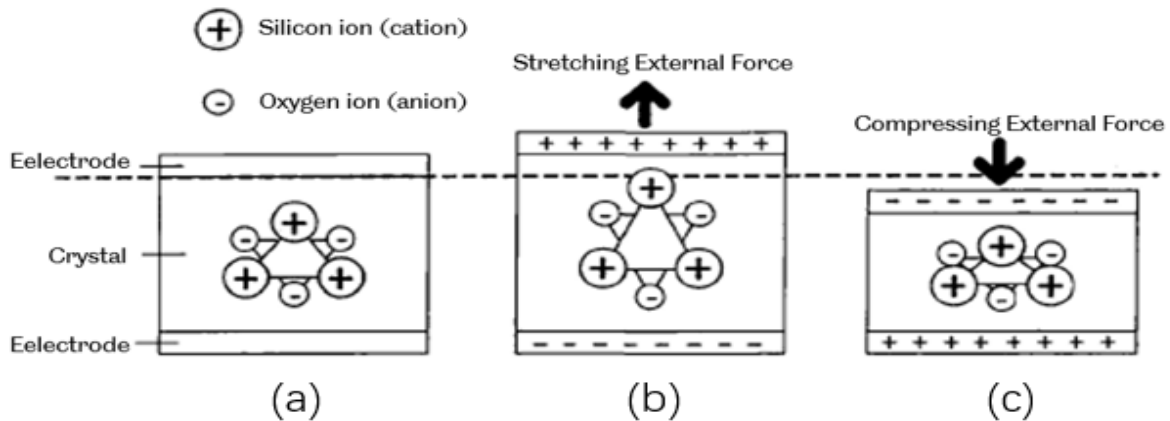


Figure 2.4 - Internal Structure of Piezoelectric Material in Positive Piezoelectric Effect.

As mentioned before, piezoelectric materials have piezoelectric effects, and piezoelectric effects can be divided into positive piezoelectric effects and negative piezoelectric effects (inverse piezoelectric effect). The positive piezoelectric effect is the conversion of the mechanical strain or stress applied by the piezoelectric material into electrical energy. The positive piezoelectric effect is to produce an equal amount of positive and negative charges on the opposite surface of the material, thereby producing an electrode polarization effect proportional to the strain force. Figure 2.4 shows a crystal structure in a piezoelectric material as a basic reference to illustrate the basic principle of the positive piezoelectric effect. When the piezoelectric material receives mechanical strain, the electrical neutral balance of the crystal in the piezoelectric material is destroyed, and the internal charge centre will be relatively shifting. This shift will create an electrical potential on the surface of the piezoelectric material that varies with the mechanical strain and the amount of charge produced is related to the direction of the shifting and the level of strain [50], [51]. As shown in Figure 2.4b, when the piezoelectric material receives the tensile external force indicated by the direction of the arrow, the crystal is pulled up in the vertical direction. Since the density of the negative ions near the upper plate becomes larger, the upper plate will correspond to it and generate a positive charge, while the lower plate generates an equal amount of

negative charge at the same time. Similarly, when the piezoelectric material is subjected to a compressive external force, the charge generation of the two plates is as shown in **Figure 2.4c**.

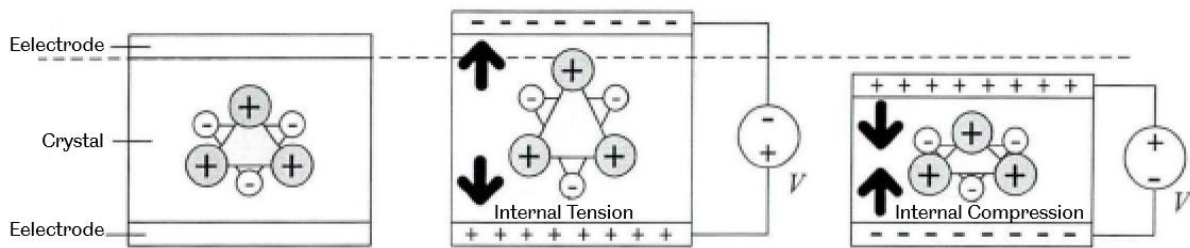


Figure 2.5 - Internal Structure of Piezoelectric Material in Inverse Piezoelectric Effect.

Figure 2.5 shows a diagram of the inverse piezoelectric effect of a piezoelectric material, that is, if an electric field is applied in the direction of polarization of the piezoelectric material, and the piezoelectric material will produce mechanical deformation in a directly proportional to the intensity of polarization. When the potential of the lower electrode plate is higher than that of the upper electrode plate, the negative ions that are out of equilibrium gather near the upper plate in order to attempt to restore the electrical neutral balance, while the positive ions gather in the lower plate. This forces the material to stretch and induces a corresponding positive and negative charge near the upper and lower plates to resist the applied electric field.

2.2.3.2 Piezoelectric Material Properties

The property that some dielectrics are polarized under pressure and a potential difference occurs at both end surfaces is called piezoelectricity. Also, some materials with piezoelectricity are called piezoelectric materials. There are several types of material nowadays, including man-made and natural material and composite material, etc. Different piezoelectric material is suitable for various applications depending on their piezoelectric parameters; therefore, the comparison and analysis of piezoelectric parameters is crucial before selecting materials according to the application.

The piezoelectric constant is one of the most important piezoelectric coefficients, which describes the ratio of the linear response between the mechanical and electrical quantities of the piezoelectric material [52]. As a set of unique parameters to piezoelectric materials, it is a third-order tensor, which reflects the coupling relationship between the mechanical properties and dielectric properties of piezoelectric material. Four different piezoelectric

coefficients d, e, g and h can be obtained by different measuring boundary conditions during measurement as shown in Table 2-1, and the piezoelectric constant d is more commonly used. The first four sets of equation is for piezoelectric effect, while the second four sets of equation is for inverse piezoelectric effect [53].

Table 2-1 – Four Piezoelectric Coefficients.

Symbol	Equation	Unit
d_{ij}	$= \left(\frac{\partial D_i}{\partial T_j} \right)^E = \left(\frac{\partial S_j}{\partial E_i} \right)^T$	C/N or m/V
e_{ij}	$= \left(\frac{\partial D_i}{\partial S_j} \right)^E = - \left(\frac{\partial T_j}{\partial E_i} \right)^S$	N/Vm or C/m ²
g_{ij}	$= - \left(\frac{\partial E_i}{\partial T_j} \right)^D = \left(\frac{\partial S_j}{\partial D_i} \right)^T$	Vm/N or m ² /C
h_{ij}	$= - \left(\frac{\partial E_i}{\partial S_j} \right)^D = - \left(\frac{\partial T_j}{\partial D_i} \right)^S$	V/m or N/C

Where D is electric charge density displacement (also electric displacement); E is electric field strength; S is strain and T is stress.

As shown in Table 2-1, each piezoelectric coefficient has two subscripts, i and j, which represent two directions of both related quantities. The first number i in the subscript refers to the direction of the electric field, and the second number j refers to the direction of stress or strain. According to three directions for the x-axis, the y-axis and the z-axis, i is equal to 1, 2 and 3, and j is equal to 1 to 6 as shown in Figure 2.6. For example, d₃₁ means the polarization happens in electric field direction 3 when the stress or strain is applied in direction 1. D₁₅ means the polarization happens in electric field direction 5, and induced shear strain is applied in direction 2 [54].

Although the “33” power generation method has a higher piezoelectric coefficient and higher power generation efficiency, the piezoelectric energy harvesting device using the “31” power generation method is widely used for small PEHD because of its simple structure, low natural frequency, and easy acceptance of surrounding vibration energy, usually used in small piezoelectric energy harvesters [55].

Another key property of piezoelectric material is permittivity, and permittivity is used to measure the ability of a piezoelectric material to store an electric field in the process of dielectric polarization[56]. The permittivity is the product of the relative permittivity and the absolute permittivity in vacuum, usually represented by ϵ , in units of F/m. Also, as a device converting mechanical energy and electric energy, the efficiency of converting is an important factor for the material, which is the Electro-mechanical coupling factor. The factor is usually represented by k . For ϵ and k , they have the same format meaning subscript as piezoelectric coefficients.

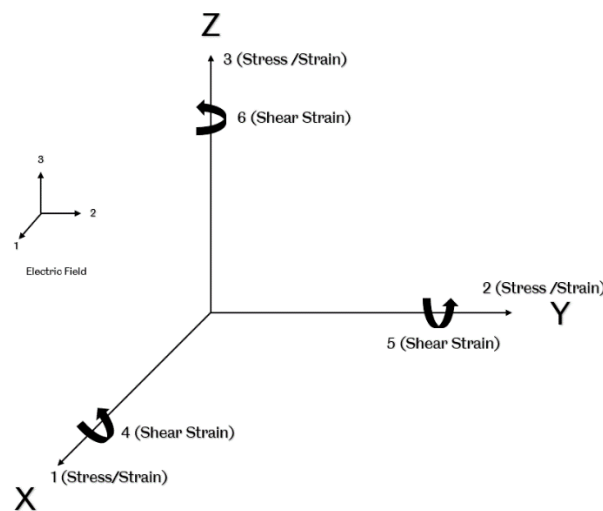


Figure 2.6 – Direction of Both Related Quantities for Piezoelectric Coefficients.

The behaviour of mechanical and electricity could be described by constitutive equations, and for a linear piezoelectric material, the equations are shown in Equation 2.4 and Equation 2.5, which show the relationship of strain and electric field. They could be rewritten to the relationship between stress and electric field as shown in Equation 2.6 and Equation 2.7 [55].

$$S = [S_E]T + [d^t]E \quad \text{Equation 2.4}$$

$$D = [d]T + [\epsilon_T]E \quad \text{Equation 2.5}$$

$$T = [c_E]S - [e^t]E \quad \text{Equation 2.6}$$

$$D = [e]S + [\epsilon^S]E \quad \text{Equation 2.7}$$

Where S_E is the compliance matrix in strain-Charge (m^2/N); d is piezoelectric coupling matrix (C/N); c_E is stiffness matrix (N/m^2) and e is piezoelectric coupling matrix is Stress-Charge (C/m^2).

And for the piezoelectric effect and inverse piezoelectric effect, the equations also could be rewritten to matrix equation, as shown in Equation 2.8 and Equation 2.9.

$$\begin{bmatrix} S_1 \\ S_2 \\ S_3 \\ S_4 \\ S_5 \\ S_6 \end{bmatrix} = \begin{bmatrix} S_{11}^E & S_{12}^E & S_{13}^E & 0 & 0 & 0 \\ S_{21}^E & S_{22}^E & S_{23}^E & 0 & 0 & 0 \\ S_{31}^E & S_{32}^E & S_{33}^E & 0 & 0 & 0 \\ 0 & 0 & 0 & S_{44}^E & 0 & 0 \\ 0 & 0 & 0 & 0 & S_{55}^E & 0 \\ 0 & 0 & 0 & 0 & 0 & S_{66}^E = 2(S_{11}^E - S_{12}^E) \end{bmatrix} \begin{bmatrix} T_1 \\ T_2 \\ T_3 \\ T_4 \\ T_5 \\ T_6 \end{bmatrix} + \begin{bmatrix} 0 & 0 & d_{31} \\ 0 & 0 & d_{32} \\ 0 & 0 & d_{33} \\ 0 & d_{24} & 0 \\ d_{15} & 0 & 0 \\ 0 & 0 & 0 \end{bmatrix} \begin{bmatrix} E_1 \\ E_2 \\ E_3 \end{bmatrix}$$

Equation 2.8

$$\begin{bmatrix} D_3 \\ D_2 \\ D_3 \end{bmatrix} = \begin{bmatrix} 0 & 0 & 0 & 0 & d_{15} & 0 \\ 0 & 0 & 0 & d_{24} & 0 & 0 \\ d_{31} & d_{32} & d_{33} & 0 & 0 & 0 \end{bmatrix} \begin{bmatrix} T_1 \\ T_2 \\ T_3 \\ T_4 \\ T_5 \\ T_6 \end{bmatrix} + \begin{bmatrix} \varepsilon_{11} & 0 & 0 \\ 0 & \varepsilon_{22} & 0 \\ 0 & 0 & \varepsilon_{33} \end{bmatrix} \begin{bmatrix} E_1 \\ E_2 \\ E_3 \end{bmatrix}$$

Equation 2.9

2.2.3.3 Piezoelectric Material

Piezoelectric materials are mainly divided into two categories, inorganic piezoelectric materials and organic piezoelectric materials are shown in Figure 2.7 [57],[58]. Inorganic piezoelectric materials include piezoelectric crystals and piezoelectric ceramics, and piezoelectric crystals generally refer to piezoelectric naturally occurring single crystals. Piezoelectric crystals are crystals grown in a long-range order of crystal lattices. This crystal structure has no symmetry centre and is therefore piezoelectric. Piezoelectric single crystals are common in nature, such as crystal (quartz crystal), lithium gallate, lithium niobite, titanium niobite and lithium transistor lithium niobite, lithium niobite and so on.

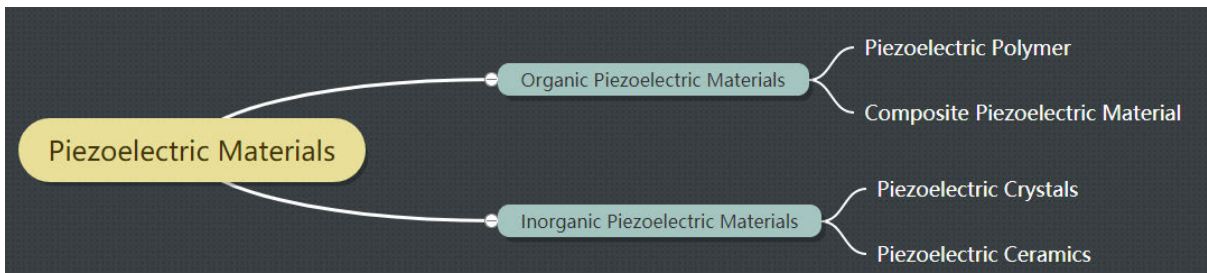


Figure 2.7 - Piezoelectric Material Classification.

Piezoelectric ceramics mainly mean piezoelectric polycrystals. Piezoelectric ceramics are synthesized polycrystals by irregular microcrystalline grains obtained by mixing, forming, high-temperature sintering with a raw material of a necessary component, a solid phase reaction of particle and a sintering process. Piezoelectric ceramics are also called ferroelectric ceramics. There are ferroelectric domains among the crystal grains of the ceramic, and the ferroelectric domains are composed of 180-degree domains that are antiparallel in the direction of spontaneous polarization and a 90-degree domain that is perpendicular to the spontaneous polarization direction. Under the condition of artificial polarization (application of a strong DC electric field), the spontaneous polarization is sufficiently aligned according to the direction of the external electric field and the residual polarization is maintained after the external electric field is cancelled. Therefore, the piezoelectric ceramics have macroscopic piezoelectricity and include barium titanite BT, lead zirconated titanite PZT, modified lead zirconated titanite, lead metasilicate, lead-bismuth citrate lithium PBLN, and modified lead titanite PT, etc [42],[43].

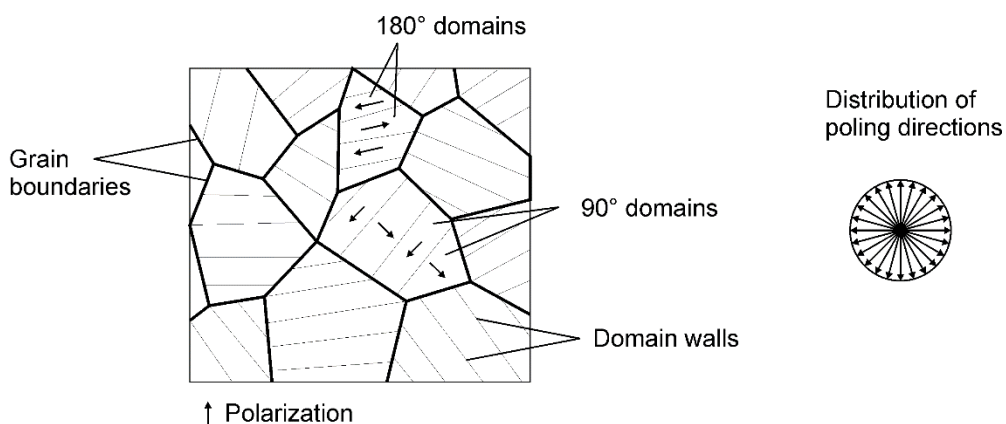


Figure 2.8 - Domain Direction of the Piezoelectric Ceramics.

The piezoelectric effect of piezoelectric ceramics is different from that of other piezoelectric materials. As shown in Figure 2.8, the internal grains of the piezoelectric ceramic material

have many spontaneously polarized domains. When there is no applied external electric field, the domains are randomly distributed in the grains, and their polarization effects are cancelled out for each other. Internal polarization of piezoelectric ceramics is zero, therefore, piezoelectric ceramic materials that are not polarized do not exhibit piezoelectric effects [61].

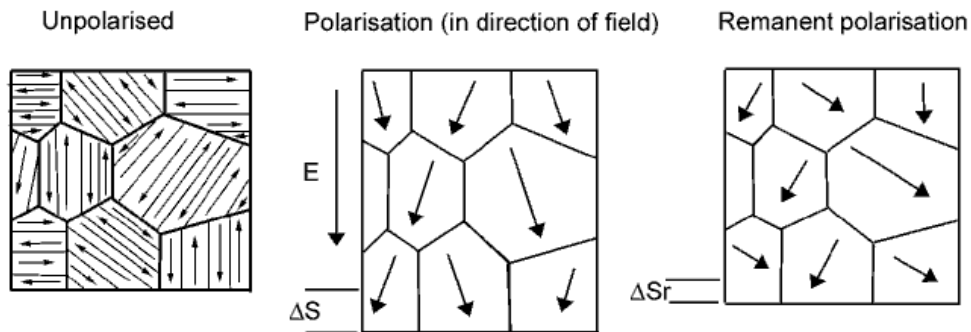


Figure 2.9 - Piezoelectric Ceramics Polarization Process.

When the piezoelectric ceramic is applied with an external electric field, the polarization direction of the domain is rotated according to the direction of the external electric field. The stronger the applied external electric field, the more the domains are more completely turned toward the direction of the external electric field. When all of the domain polarization directions are neatly aligned with the direction of the external electric field, the applied external electric field is referred to as saturation. At this time, when the external electric field is removed, the polarization direction of the domain is substantially unchanged, and the material at this time has piezoelectric characteristics as shown in Figure 2.9 [61].

Organic piezoelectric materials are also known as piezoelectric polymers, such as polyvinylidene fluoride (PVDF). These materials are widely used because of particularly soft, low density, low impedance, and high piezoelectric coefficient (g). In addition to this, piezoelectric materials also contain composite piezoelectric materials. This material is formed by embedding a sheet-like, rod-shaped, rod-shaped or powdered piezoelectric material in an organic polymer base material [62].

Different piezoelectric materials can be used in different applications depending on its mechanical and electrical property.

Table 2-2 gives the advantages and disadvantages of various materials and suitable applications [63].

Table 2-2 – Comparison of Different Piezoelectric Material.

Piezoelectric Material	Advantages	Disadvantages	Suitable Applications
Piezoelectric Ceramics	<ul style="list-style-type: none"> ● Strong piezoelectricity ● High permittivity ● Easy shape changeable 	<ul style="list-style-type: none"> ● High brittleness ● Large electrical loss ● Poor stability 	<ul style="list-style-type: none"> ● High power transducer ● Wideband filter
Piezoelectric Single Crystals	<ul style="list-style-type: none"> ● High stability ● High mechanical quality factor 	<ul style="list-style-type: none"> ● Lower piezoelectric coefficient ● Poor piezoelectricity ● Limit size 	<ul style="list-style-type: none"> ● Filter ● High frequency ultrasonic transducer ● Vibrator
Polymers	<ul style="list-style-type: none"> ● High flexibility ● Low density ● Low impedance ● High piezoelectric constant(g) ● light in mass ● High voltage output 	<ul style="list-style-type: none"> ● Low piezoelectric constant(d) 	<ul style="list-style-type: none"> ● Pressure sensor ● Underwater ultrasonic measurement
Composite Piezoelectric Materials	<ul style="list-style-type: none"> ● Impact resistance ● Not easily damaged ● High hydrostatic pressure corresponding rate 	<ul style="list-style-type: none"> ● Higher production costs 	<ul style="list-style-type: none"> ● Hydroacoustic transducer

The application of piezoelectric materials depends on the mechanical and electrical properties of the piezoelectric materials. Table 2-3 lists the properties of several commonly used materials. It should be noted that the Lead zirconium titanite (PZT) can be made in the form of sol-gel thin film and sputtered thin film in addition to polycrystalline.

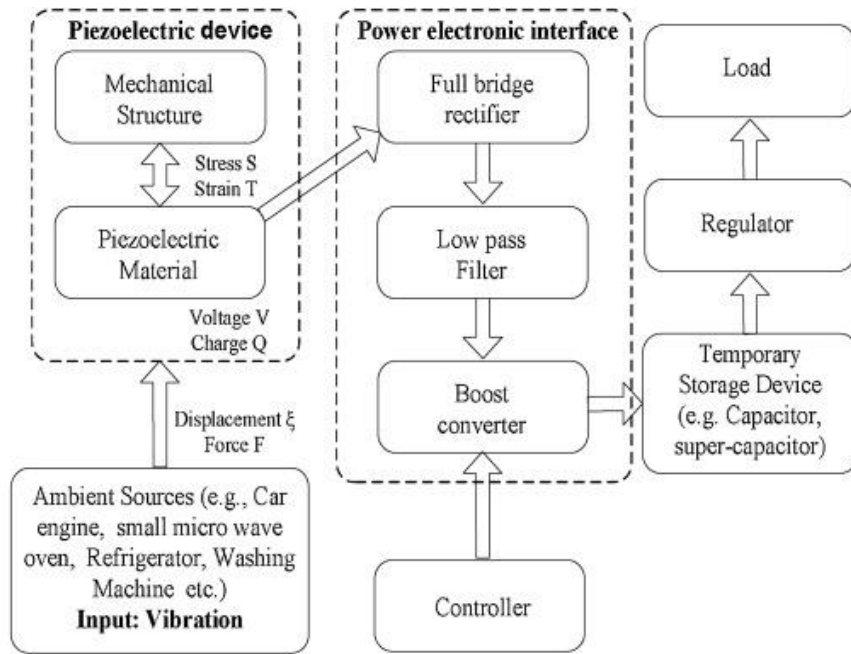
Table 2-3 – Properties of Commonly Used Materials [8].

Material	Chemical Formula	d_{31} C/N	$\epsilon_{33}/\epsilon_0^a$	k_{31}	$T_e (^{\circ}C)^b$ Temperature
Quartz	SiO ₂	2.3	4.4	-	-

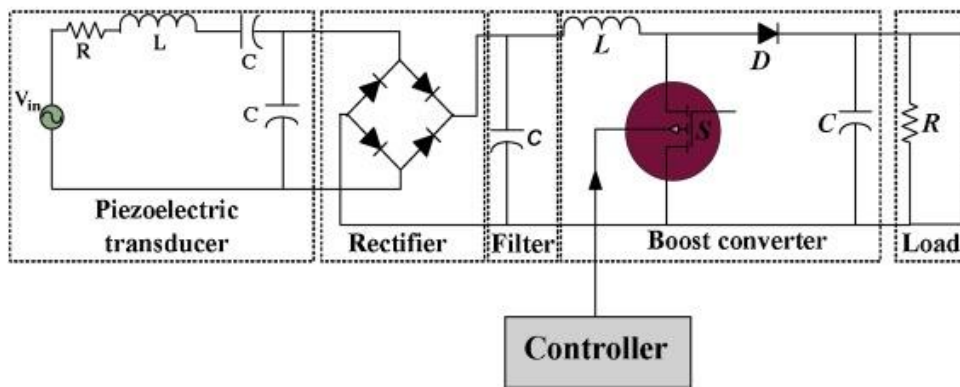
Bismuth Titanite (BTO)	$\text{Bi}_{12}\text{TiO}_{20}$	-79	1900	-	120
Lead Zirconated Titanite (PZT Polycrystalline)	$\text{Pb}[\text{Zr}_x\text{Ti}_{1-x}]\text{O}_3$	-190~-320	1800~3800	0.32~0.44	230~350
PZT Sol-gel Thin Film	$\text{Pb}[\text{Zr}_x\text{Ti}_{1-x}]\text{O}_3$	190~250	800~1100	-	-
PZT Sputtered Thin Film	$\text{Pb}[\text{Zr}_x\text{Ti}_{1-x}]\text{O}_3$	100	-	-	-
Polyvinylidene Fluoride (PVDF)	$-(\text{C}_2\text{H}_2\text{F}_2)_n-$	23	12~13	0.12	80~100
Zinc oxide (ZnO Sputtered Thin Film)	ZnO	10.5~11.5	10.8~11	-	-
Aluminium Nitride (AlN thin film)	AlN	-	8.6	-	-

2.2.3.4 Devices of Piezoelectric Vibration Energy Harvesting

The piezoelectric vibration energy harvesting system (PVEHS) normally consists of three sections, which are piezoelectric devices, power electronic interface and electric storage components as shown in Figure 2.10. The ambient vibration sources could be harvested by piezoelectric devices, and electric energy is obtained because of the piezoelectric effect. It is worth noting that due to the structure of the piezoelectric material, the electrical energy converted from mechanical energy will be alternating current (AC). AC frequency is related to piezoelectric material vibration frequency. Full bridge rectifier, low pass filter and boost converter are usually the main components of the power electronic interface, and the electricity through the power electronic interface will become more suitable for the load [64].



(a)



(b)

Figure 2.10 – The Diagram of PVEHS [3].

Piezoelectric Devices

Figure 2.11 shows the energy flow of the piezoelectric energy harvesting system [51]. Starting from external energy (ambient vibration source), the vibrational energy from the surrounding environment flows into the system from the A port, and then the energy flow is converted into three energy flows. One is converted into thermal energy through the path B-C, which corresponds to the mechanical loss of the piezoelectric energy collector itself. The other one uses the piezoelectric effect of the piezoelectric material to convert energy into electric energy through the path B-D-F. The last energy flow forms an energy loop along the path B-

D-E-K-L, which represents the mutual conversion between kinetic energy and elastic potential energy in a vibration cycle.

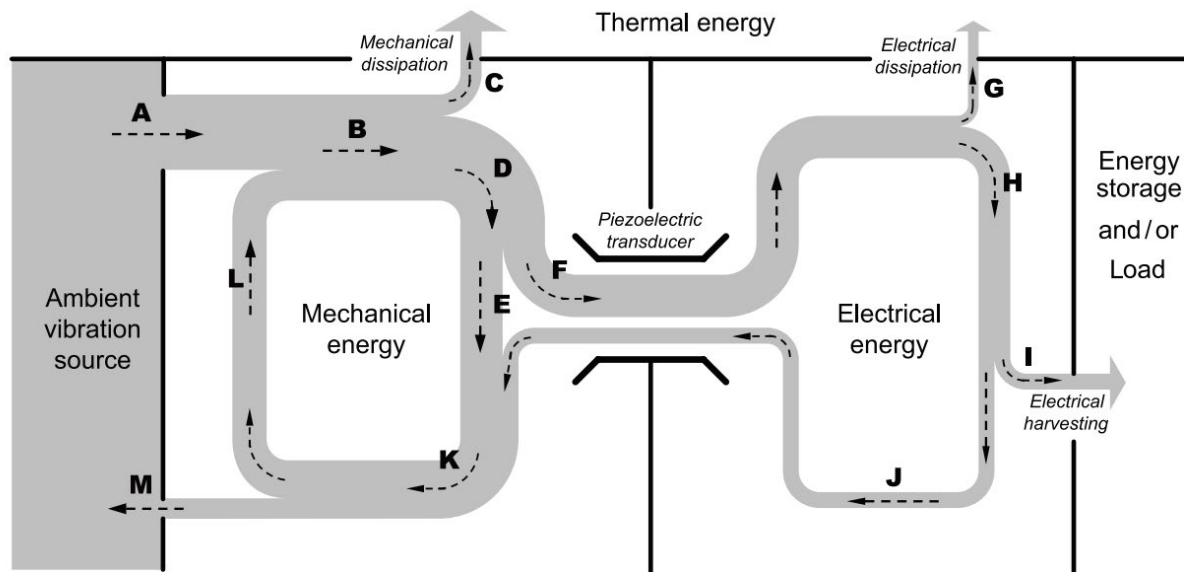


Figure 2.11 - Energy Flow of the Piezoelectric Energy Harvesting System [51].

Electrical energy after transduction is converted into three energy flows along energy flow F. One is converted into electrothermal energy along the energy flow G, and the other is converted into electric energy obtainable by the load through the path H-I. The last energy flow returns to the mechanical energy ring in the form of mechanical energy along the path J, so that "electronic damping" is introduced in the mechanical energy ring. If the entire mechanical structure of the piezoelectric energy harvester does not exactly match the excitation vibration source, part of the energy will return to the ambient source along the path M. The degree of matching is reflected by the phase difference between the acceleration of the external force and the speed of the relative displacement. Therefore, the piezoelectric vibration energy harvesting device should ensure the maximum collection of the current flowing along I under various vibration conditions and minimize the energy flowing along the C and G port.

The piezoelectric effect and inverse piezoelectric effect are used for different applications as shown in Figure 2.12. The technology development is necessary, in order to have better performance and lower costs. In the past, the researches mainly focus on piezoelectric materials and the running modes, instead of the dimensions of the piezoelectric energy harvesting device. The dimensions of the device could influence the efficiency significantly,

such as the shape, length, width and thickness. Therefore, future research could focus on the effect of changing dimensions according to different applications [65], [66].

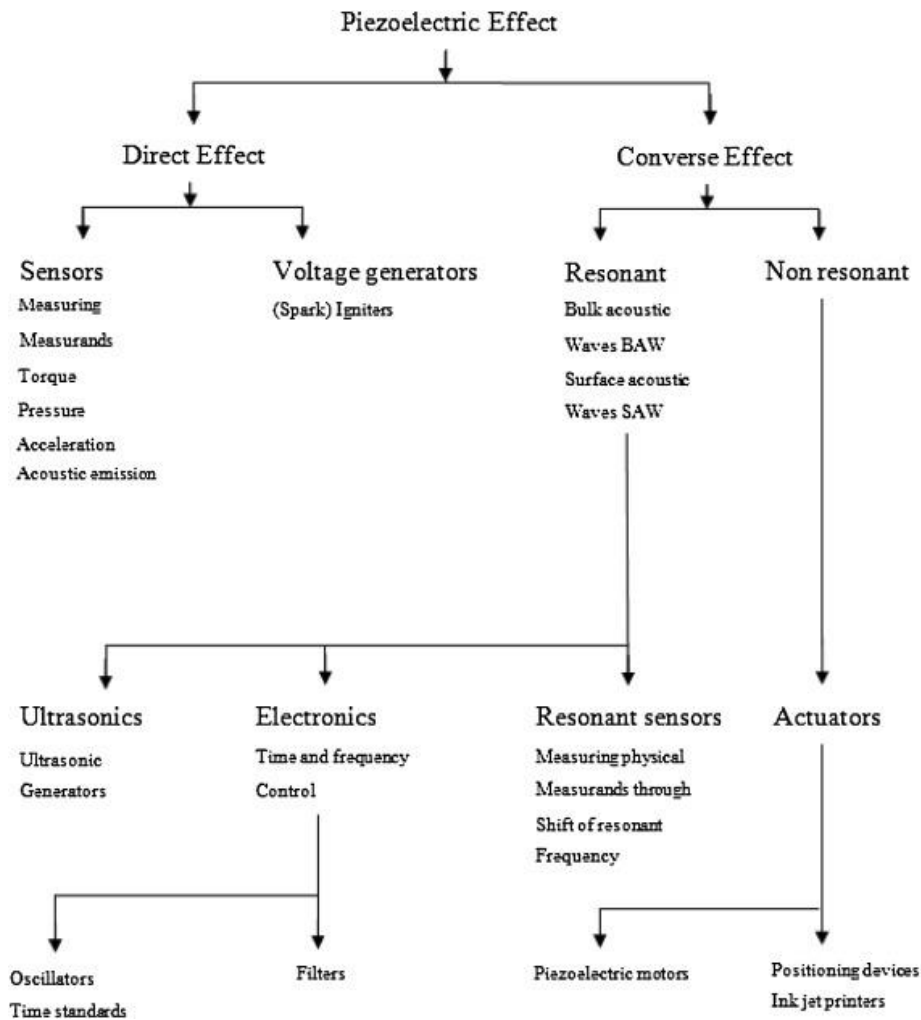


Figure 2.12 – Applications Based on Piezoelectric Effect [67], [68].

Power Electronic Interface

The full-bridge rectifier is also known as the AC-DC rectifier. For small-scale electric devices, DC power supply is necessary, and the output of PVDFS is AC, therefore, the full-bridge rectifier (a diode bridge rectifier) is usually used after the piezoelectric device, as shown in Figure 2.13 [69]. However, in recent research, after the rectifier is placed in the circuit, the output voltage is significantly reduced, which also reduces the overall efficiency of the system [70].

For some applications that require high voltage, the output voltage of the piezoelectric device is not sufficient to support the normal operation of the load. A boost converter is needed to

boost the voltage output. The boost converter can input DC power into the storage component first, and after a period of storage, output the power with a higher DC voltage to achieve the effect of boosting the voltage [71] – [73].

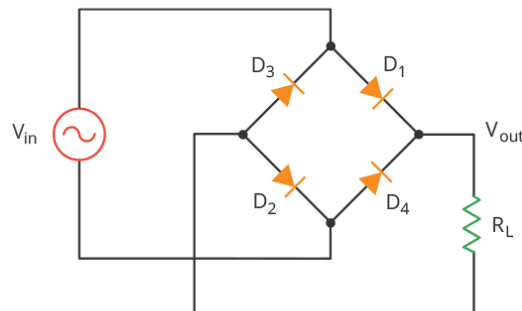


Figure 2.13 - A Diode Bridge Rectifier.

Electrical Energy Storage

As a piezoelectric vibration harvester that collects vibration energy, the vibration energy is generally intermittent. Therefore, in order to ensure that the load can work normally under a stable current and voltage, the energy storage element is an essential component in PVEHS. The most common energy storage element is a capacitor. The capacitor has the advantages of fast charging speed and a simple charging circuit. However, the charging and discharging efficiency of the capacitor is particularly low, also the charging takes a long time and the energy density is low [74], [75]. A supercapacitor has been recently researched. This kind of supercapacitor solves the shortcoming of the low energy density of ordinary capacitors. After improvement, the energy density of this supercapacitor can reach 10-100 times that of ordinary capacitors [75].

In addition, rechargeable batteries are also a type of energy storage element, such as nickel-metal hydride button batteries and lithium-ion batteries [76]. Compared to capacitors, rechargeable batteries have a wide energy density and can store energy for long periods of time. However, rechargeable batteries are susceptible to be damaged from external influences and may cause environmental pollution due to internal chemical substances.

2.2.4 Comparison of Three Methods

Three vibration energy harvesting methods are compared as shown in Table 2-4, which mainly includes mechanical-electrical conversion efficiency, advantages and disadvantages. Compared with other two methods, piezoelectric vibration energy harvester normally has higher efficiency, output voltage and faster conversion. Although the piezoelectric material is more expensive, it is more suitable for energy harvest, because it could generate enough power in same time for the device.

Table 2-4 – Comparison of Three Vibration Energy Harvester [8].

Vibration Energy Harvester Type	Excitation Source	Materials	Efficiency (%)	Attributes	Advantages	Disadvantages
Electromagnetic	Solar/Visible spectrum (Outdoor/Indoor)	Crystalline	10%-20%	-The high cost of materials	-High output currents -Long lifetime proved -Robustness	-Low output voltages
		Silicon	25%-30%			-Hard to develop MEMS devices
		GaAs	5%-9%	-The low light absorptivity of silicon		-May be expensive (material)
		Amorphous	~17%			-low efficiency in low frequencies and small sizes
		Silicon/CdTe				
CuInSe ₂		-Low power density				
Electrostatic	Vibrations	MEMS scale Capacitor	~13.33%	-An active system requiring a capacitor excitation voltage	- High-cost to build the systems - Adjusting the coupling coefficient is difficult -Size reduction increases capacitance	-Require high capacitance and its effect of increasing the cost -The high impact of parasitic capacitances -Need to control μm dimensions
Piezoelectric	Vibrations, Pressure variations	Ceramics, Single crystals, Polymer	~5-30%	-Depends on source excitation -Piezoelectric material property	-High output voltages -The conversion from mechanical to electrical is simple and faster -Life time and durability are long -The overall system efficiency is high	- Expensive (material) -Coupling coefficient linked to material properties

2.3 Flow-induced Vibration Energy Harvesting

Flow-induced vibration energy harvesting is a mainstream of the research on vibration energy harvesting. Because of its unique energy capture device, its research mainly aims to harvest micro-environment energy to power micro equipment or wireless devices (such as MEMs), unlike other energy harvesting. Flow-induced vibration energy harvesting extracts energy from flow, such as wind, wave, or tidal current, by utilizing aerodynamic instability phenomena. In the construction and aviation manufacturing industry, this vibration will be avoided as much as possible because it will cause a lot of losses. The 1.6 -kilometre Tacoma Narrows Bridge was one of the examples that aerodynamic instability causes the loss. Five months after opening to traffic due to insufficient thickness of the bridge deck, the bridge formed a Kamen Vortex Street under the blow of strong winds, and eventually, the bridge caused resonance and collapsed. However, flow-induced vibration energy harvester in the energy harvesting field has great potential because it is easy to form; moreover, most harvester designs have a long lifespan, lower maintenance cost and higher energy density [77]. Vibration is usually caused by the oscillator's elasticity, aerodynamic forces, and inertial force. Therefore, the vibration principle of different situations is important to improve the performance of the energy harvester.

For aerodynamic energy harvesting, Musavir et al. divide this type of vibration energy harvesting into three categories [78], as shown in Figure 2.14, motion-induced excitation energy harvesting (MIEEH), instability-induced excitation energy harvesting (IIEEH), and extraneously induced excitation energy harvesting (EIEEH). MIEEH, which includes a galloping energy harvester and a flutter energy harvester. IIEEH is an energy harvesting based on linear resonance, which includes vortex-induced vibration energy harvesting and buffeting energy harvesting. In addition, wake galloping caused by turbulence is usually classified into EIEEH. Apart from this, another way of classification divides the vibration into two categories, limit-cycle vibration (Galloping and Flutter) and forced response vibration (Vortex-induced vibration and Buffeting), respectively, which regards galloping and wake galloping as the same vibration form [77]. This section will review and analyse the existing designs of different categories of flow-induced energy harvestings.

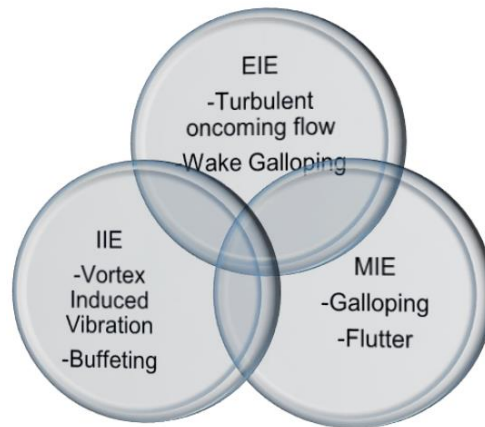


Figure 2.14 - Different Categories of Aeroelastic Energy Harvesters [78].

2.3.1 Vortex-induced vibration

Vortex-induced vibration (VIV) is one of the most common vibration phenomena in nature. When a fluid with a large Reynolds number passes through a bluff body, such as a cylinder, the fluid near the boundary layer will flow at a low speed and attach to the boundary layer due to the viscosity of the fluid. Then the boundary layer flow will be separated from the upper and lower surfaces of the object to form two shear layers flowing downstream. Because of the gradient pressure, discrete vortices will be generated downstream. The vortex will periodically fall out of the two sides of the object with opposite rotation and regular arrangement. This vortex generation process downstream of the bluff body is called vortex shedding, and the vortex is called Kármán vortex street.

Reynolds number (Re) is the ratio of inertial force to viscous force. Due to the difference in Re , the fluid flowing through the bluff body will have different effects. When Re is greater than about 90, vortex shedding will occur, as shown in Figure 2.15. Equation 2.10 shows the Reynolds number equation, where ρ and μ are fluid density and dynamic viscosity coefficients; and v and L are the characteristic velocity and characteristic length of the flow field respectively.

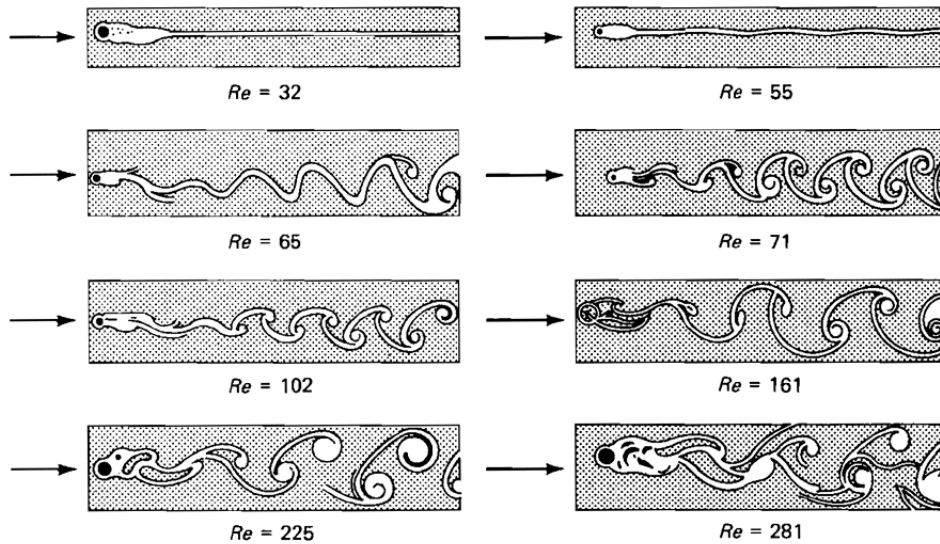


Figure 2.15 - The Effect of Reynolds Number on the Fluid Flowing through the Bluff Body [79].

Due to the vortex shedding, there will be a low-pressure zone in the vortex area. Therefore, periodic forces will be generated on both sides of the bluff body as the vortex shedding, causing the bluff body to produce periodic vibration consistent with the vortex shedding period, and this is called VIV[80] – [83]. The frequency of vortex shedding from the surface of the bluff body to the downstream (ω_f) can be defined as shown in Equation 2.11, where v and L are still the characteristic velocity and characteristic length of the flow field respectively; and St is Strouhal number; and the relationship between Re number and Strouhal number as shown in Figure 2.16 [84].

$$Re = \frac{\rho v L}{\mu}$$

Equation 2.10

$$\omega_f = 2\pi St \frac{v}{L}$$

Equation 2.11

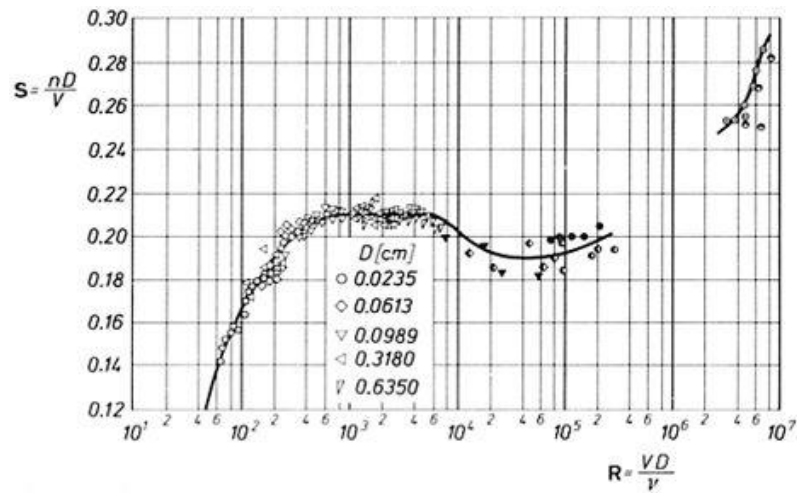


Figure 2.16 - The Relationship between Re Number and Strouhal Number [84].

The curve of vibration amplitude of VIV presents a parabolic shape with the increase of fluid velocity, as shown in Figure 2.17. Its vibration can be divided into three regions, pre-synchronization region, lock-in region, and post-synchronization region [85]. When the fluid velocity continues to increase, the amplitude of VIV gradually increases. When the fluid velocity reaches a certain range, it changes to a lock-in region, and the bluff body vibration frequency will be synchronized with the vortex shedding frequency. At this time, the vibration frequency of the bluff body is consistent with its natural frequency, forming resonance [84]. The bluff body has the largest vibration amplitude in this region. Once the fluid velocity exceeds this range, the vibration amplitude of the bluff body will gradually decrease.

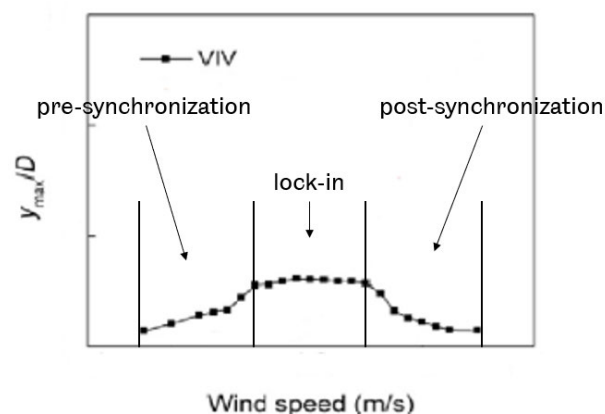


Figure 2.17 - The Three Regions for VIV [84].

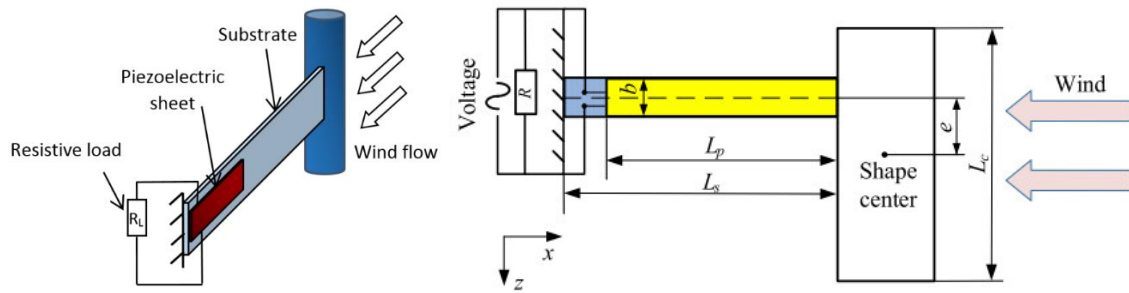


Figure 2.18 – (a) A Typical VIV Energy Harvester (b) A Bending and Torsion Piezoelectric Energy Harvester

[86].

VIV has always been one of the most important directions for researchers to study flow-induced vibration. A typical VIV energy harvester is shown in Figure 2.18(a). The cylinder is placed on the free end of the cantilever beam, and the vibration of the cylinder is transmitted to the piezoelectric material through the cantilever beam. Due to the unique nature of VIV, the mainstream research direction is concentrated in the following aspects.

- **Widen lock-in region range:** The vibration frequency enters the lock-in region when it is similar to the resonance frequency of the object. The current research tries to change the natural vibration frequency of the object to affect the lock-in region.
- **Hybrid VIV energy harvester:** Due to the limited conversion efficiency of vibration energy for single harvesting and VIV's maximum vibration frequency and amplitude are relatively fixed when it enters the lock-in region, therefore, several different vibration energy harvesting methods are designed in one design to increase its energy conversion efficiency and improve the output.
- **Improving post-synchronization region:** In post-synchronization region, the vibration amplitude decreases rapidly because the vortex shedding frequency is higher than the natural frequency of the object. To enable the harvester to continue to be used at high wind speeds, some design combines VIV and other vibration, such as galloping.

Single-degree-of-freedom (SDOF) VIV energy harvester is widely developed which harvests energy by a cantilever beam. Facchinetti et al. point out the basic mathematical model of SDOF VIV energy harvester, and Junlei et al. integrated the formula for the oscillator oscillating equation (Equation 2.12), wake oscillator equation (Equation 2.13) and circuit equation (Equation 2.14) [77], [87].

$$\begin{aligned}\ddot{\eta} + \left\{ 2\xi\omega + \left[\frac{1}{2} C_D \rho_0 D U_0 L_0 \left(\varphi(L_b) + \frac{D}{2} \varphi'(L_b) \right)^2 \right] \right\} \dot{\eta} + \omega^2 \eta + \theta V \\ = \frac{1}{4} C_{L_0} \rho_0 D U_0^2 L_0 \left[\varphi(L_b) + \frac{D}{2} \varphi'(L_b) \right] q\end{aligned}$$

Equation 2.12

$$\ddot{q} + \lambda \omega_{shed} [q^2 - 1] \dot{q} + \omega_{shed}^2 q = \frac{A}{D} \left[\varphi(L_b) + \frac{D}{2} \varphi'(L_b) \right] \dot{\eta}$$

Equation 2.13

$$\frac{V}{R_L} + C_p \dot{V} - \theta \dot{\eta} = 0$$

Equation 2.14

Where η is the displacement of oscillator; ω and ω_{shed} are natural frequency and the vortex shedding frequency; ρ_0 and U_0 are the density and flow rate of the flow; $\varphi(L_b)$ is the end displacement of cantilever beam; q is wake displacement; ξ , C_D and C_{L_0} are the coefficients of damping; drag and lift respectively and V , R_L , C_p and θ are circuit parameters.

Since the vibration of the bluff body will be consistent with its natural frequency when it is in the lock-in region, changing the bluff body's natural frequency is one of the main directions for improving VIV. In 2020, Jinda Jia et al. proposed a bending and torsion piezoelectric energy harvester that utilizes the asymmetry of the front-end cylinder, which was proved by numerical analysis and experiments. As shown in Figure 2.18(b), cylinder's shape centre and the cantilever beam's axis are not on the same horizontal line. Therefore, when the vortex falls off, the periodic force is applied to the shape centre of the cylinder. Thus, the design can simultaneously cause bending vibration and torsional vibration of the harvester. The result shows that due to the increase in eccentricity, the natural frequency of the bluff body decreases, and the minimum wind speed requirement for this harvester is 15% lower than the typical one [88]. This allows the harvester to operate at lower wind speeds. But the results prove that torsional strain does not contribute to energy harvesting, and the maximum power output of the harvester is not as good as the typical performance.

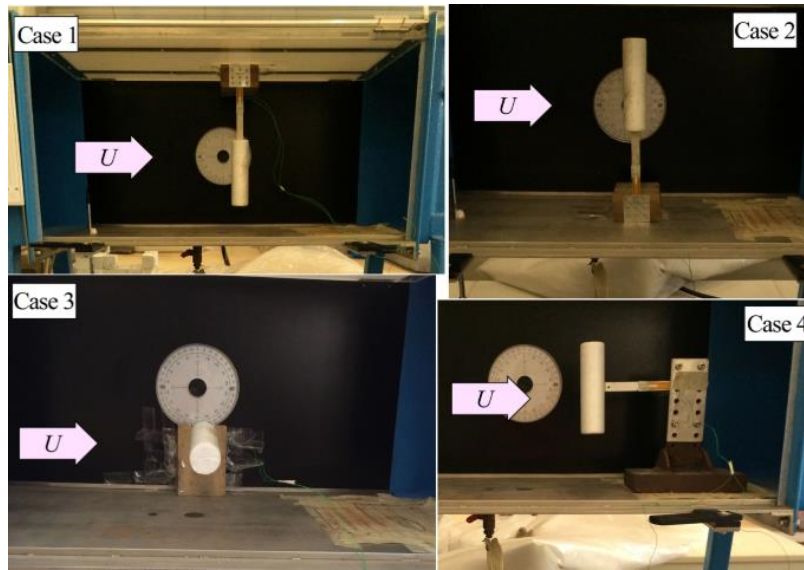


Figure 2.19 - Different Cantilever Configurations [89].

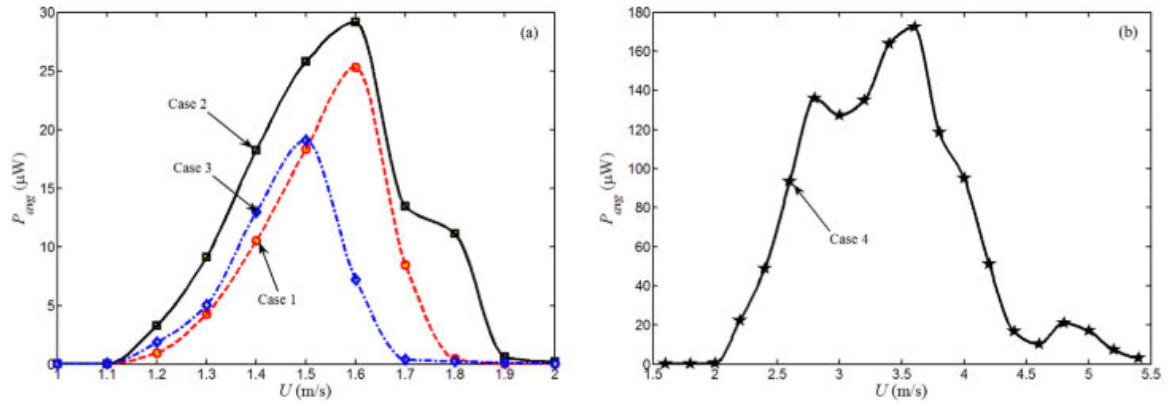


Figure 2.20 - Power Output for Four Cantilever Configurations [89].

H.L.Dai et al. did related research based on different cantilever configurations, as shown in Figure 2.19. In the free vibration experiment, Case 4 has the highest natural vibration frequency, which is almost twice that of the other three configurations. In the energy harvesting experiment, it was found that Case 2 has the best performance at low wind speeds of 1.3 to 1.8m/s, but Case 4 performs best at wind speeds of 2 to 5m/s, as shown in Figure 2.20 [89]. At higher wind speeds, due to the vibration characteristics of VIV, the energy harvested is minimal.

Improving the performance of the harvester by adding objects before or after the bluff body to adjust the natural frequency is another research direction of VIV, after adding objects, the vortex shedding and Reynolds number of the bluff body are affected, so a large

vibration can be obtained at low wind speeds. The most typical research recently is the double-cylinder energy harvester [90] and the three-cylinder harvester [91]. In the double-cylinder energy harvester, the diameter of the two cylinders is 32mm. Through CFD and experiments, the energy output of the two cylinders at intervals of 125mm, 250mm, and 375mm is analysed. When the two cylinders are separated by 125mm, for the effective wind speed range of energy harvesting, the two cylinders are respectively 150% and 267% of a single cylinder. The area of the power output of two cylinders is respectively 339 and 679 percent of a single cylinder. For a three-cylinder collector, at a wind speed of 1.2m/s, the total power output can reach 3.5 times the power output of a single cylinder.

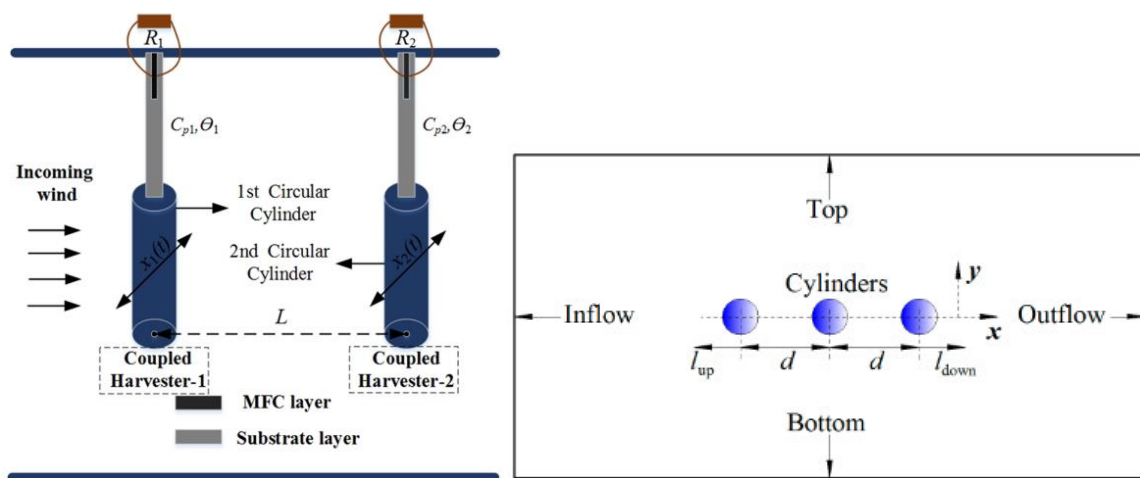


Figure 2.21 - Two-cylinder and Three-cylinder Energy Harvester [90], [91].

The second way to improve the performance of VIV energy harvesters widely used by researchers is to combine electrostatic energy harvesting or electromagnetic energy harvesting with piezoelectric energy harvesting. Zhihui Lai et al. developed a hybrid wind energy harvester that combines piezoelectric energy harvesting and electrostatic energy harvesting under VIV in 2021 [92]. The energy harvester removes the space of a capsule from the inside of the cylinder and places a small ball in the capsule. The piezoelectric material is still fixed at the end of the cantilever beam. In addition, dielectric elastomer (DE) materials are placed on the two ends of the capsule as shown in Figure 2.22. The harvester has a higher output power than a typical VIV piezoelectric energy harvester, but due to the addition of dielectric elastomer (DE) materials, the design cost also rises. In the design of hybrid energy harvesters, consideration should be given to whether different energy

harvesting methods in the design can positively influence each other, rather than simply combining them.

Another popular research direction for VIV is to transform VIV to galloping by changing the shape of the bluff body. J. Song et al. added two splitter plates behind the cylinder as shown in Figure 2.23(a). Due to the change in the symmetry of the cylinder, the power output increases with the increase in wind speed (characteristic of galloping). And the paper also pointed out that when the length of the splitter plate is equal to 0.65 times the diameter of the cylinder, the output power is maximum[93]. The design of the splitter plate provides a reliable design concept for this research direction. In 2020, J. Wang et al. combined square and circle to create a new bluff body shape as shown in Figure 2.23(b) [94]. The output power curves of these shapes combine the characteristics of the VIV and galloping output power curves. As the wind speed increases, the curve first gradually rises, then begins to decline briefly, and finally rises again. After comparison, "BB1 $\alpha = 0$ " has the best effect. Compared with VIV, the maximum output power is increased by 71.34%.

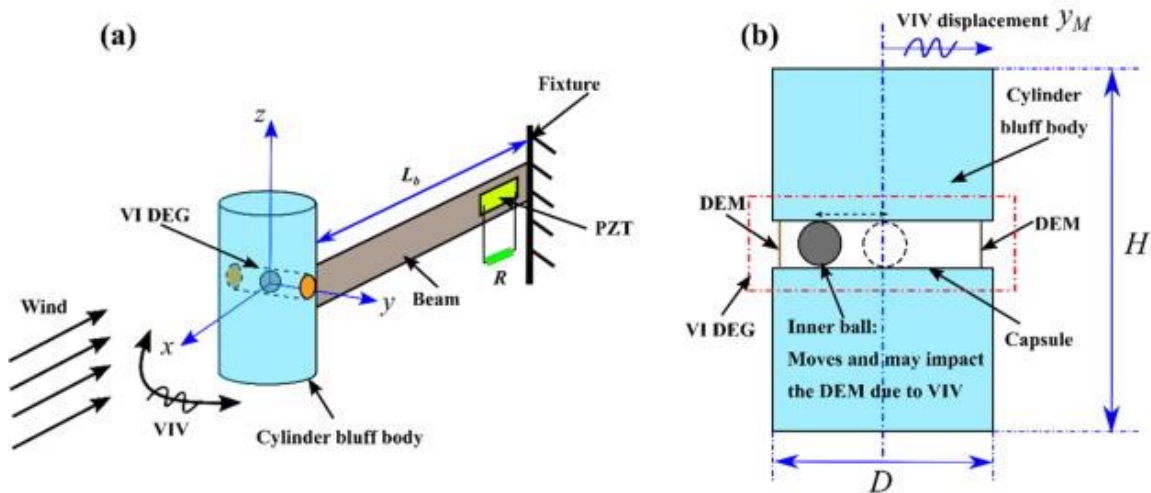


Figure 2.22 - Hybrid Wind Energy Harvester [92].

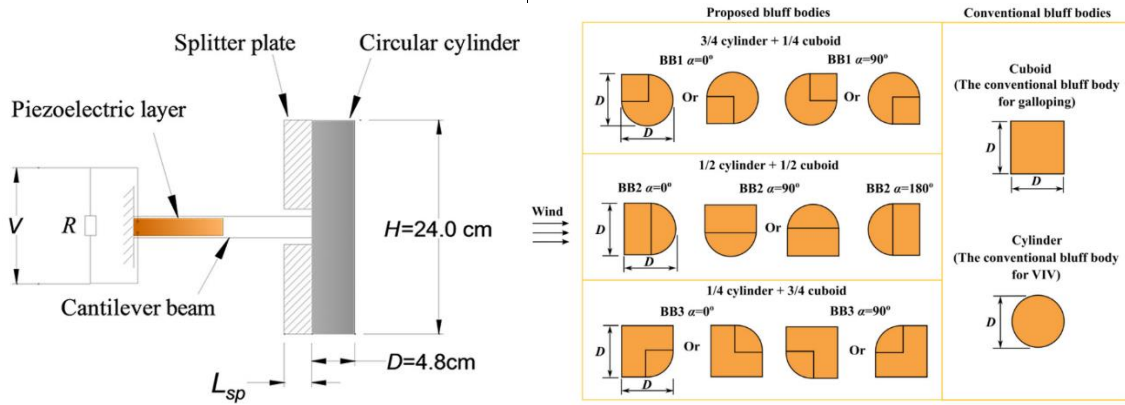


Figure 2.23 - (a) Cylinder with Splitter Plate (b) Cross-section of Bluff Bodies Created [94].

Overall, VIV harvester has better performance at lower wind speed, and the power output reach the maximum when the frequency of vortex shedding is similar to the natural frequency. The direction of future research can be from four aspects: Widen lock-in region range, combining other energy harvesting methods, and improving post-synchronization region.

2.3.2 Galloping

Galloping is a divergent bending self-excited vibration caused by the negative slope of the lift curve. This negative slope makes the displacement of the structure always consistent with the direction of the air force during the vibration process, and the structure continuously absorbs energy from the outside, thus forming unstable vibration. Galloping generally occurs in flexible lightweight structures with angular, non-streamlined cross-sections as shown in Figure 2.24(a), such as cubes. The difference with VIV is that the amplitude of galloping increases with the increase of fluid velocity, but the minimum operating fluid velocity is larger than VIV, the curve of typical galloping vibration amplitude and fluid velocity is shown in Figure 2.24(c). As shown in Figure 2.24(b), it is generally assumed that the non-cylindrical bluff body is fixed on the spring, and the fluid flows from right to left at the speed of U . The governing equation of galloping motion can be written as shown in Equation 2.15[86]. In addition, the lift force (F_L) and drag force (F_D) could be expressed as show in Equation 2.16

$$M\ddot{\omega} + C\dot{\omega} + K\omega = F_Z$$

Equation 2.15

$$F_L = \frac{1}{2} \rho U_{rel}^2 D C_L$$

$$F_D = \frac{1}{2} \rho U_{rel}^2 D C_D$$

Equation 2.16

where M , C , K are the mass of the bluff body; the damping coefficient, and the spring stiffness respectively; F_z and ω are the aerodynamic force and displacement distance of bluff body from the centre of gravity respectively; ρ and D are the density of the flow and characteristic dimension of the bluff body respectively; C_L and C_D are the coefficients of lift and drag.

In reality, the circuit load will generate electrical damping (C_e) and electrical stiffness (K_e) after the harvester is connected with a circuit, and they will also affect the aerodynamic force, thus, the governing equation could be written as show in Equation 2.17. Tabesh et al. use Laplace transform on Equation 2.15, and represent formula of electrical damping (C_e) and electrical stiffness (K_e) [95], where R_l is resistive load; C and θ represent electrical capacitance and coupling coefficient respectively; and ω_f is the frequency of the bluff body.

$$M\ddot{\omega} + (C + C_e)\dot{\omega} + (K + K_2)\omega = F_z$$

Equation 2.17

$$K_e = \frac{(R_l \omega_f \theta)^2 C^s}{1 + (R_l C^s \omega_f)^2}$$

$$C_e = \frac{R_l \theta^2}{1 + (R_l C^s \omega_f)^2}$$

Equation 2.18

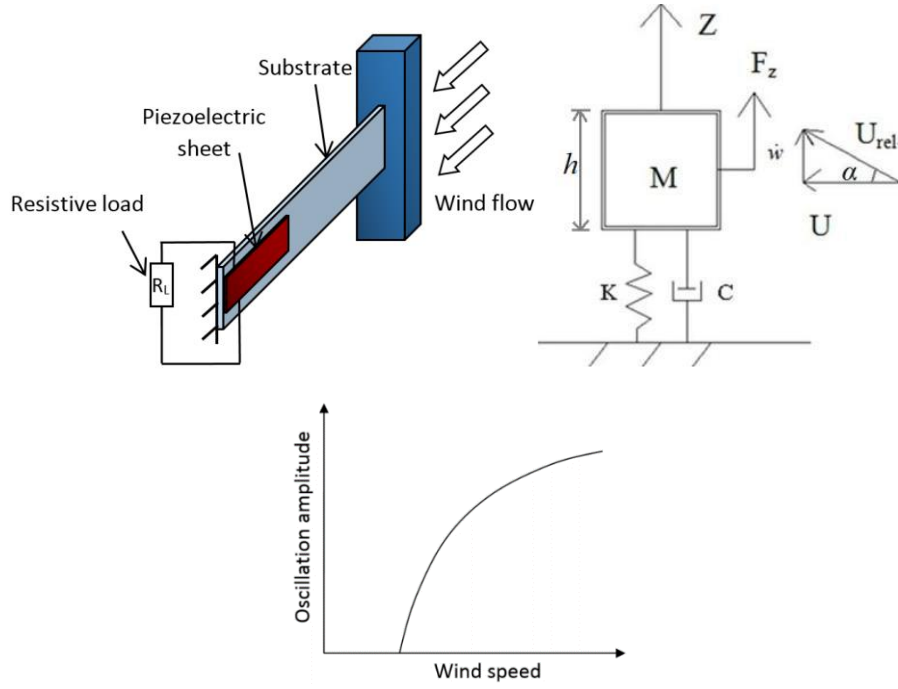


Figure 2.24 - (a) Typical Galloping Piezoelectric Energy Harvester (b) The Governing Equation of Galloping Motion (c) Typical Curve of Galloping Vibration Amplitude VS Fluid Velocity [86].

Not like VIV, the vortex shedding frequent D/U is much less than the bluff body's oscillations characteristics of the galloping $2\pi/\omega$ [96]. Therefore, the quasi-static theory can be applied to classical galloping study, which is the aerodynamic force on the bluff body is determined by relative instantaneous velocity only. The aerodynamic force F_Z can be expressed as

$$F_Z = \frac{1}{2} \rho U_{rel}^2 DH [a_1 \alpha + a_3 \alpha^3]$$

Equation 2.19

Where H is the height of bluff body; a_1 and a_3 are empirical coefficients defined by the geometry of the bluff body cross-section; and α is the angle of attack ($\alpha = \dot{\omega}/U_{rel}$). The Equation 2.15 can be rewritten as

$$M\ddot{\omega} + \left(C + \frac{R_l \theta^2}{1 + (R_l C^s \omega_f)^2} - \frac{1}{2} \rho U_{rel} DH a_1 - \frac{1}{2} \rho U_{rel} DH a_3 \left[\frac{\dot{\omega}}{U_{rel}} \right]^2 \right) \dot{\omega} + \left(K + \frac{(R_l \omega_f \theta)^2 C^s}{1 + (R_l C^s \omega_f)^2} \right) \omega = 0$$

Equation 2.20

The damping part in Equation 2.20 is composed of two parts, linear damping and non-linear damping. The linear damping part mainly determines the cut-in wind speed; at a relatively low wind speed, energy harvesting can be accomplished by modifying the device's structural characteristics and the oscillator's form structure. Non-linear damping part determine the maximum amplitude of the oscillator, which also has a significant impact on vibration reduction and stabilises system oscillation.

$$\text{Linear damping part: } C + \frac{R_l \theta^2}{1 + (R_l C^s \omega_f)^2} - \frac{1}{2} \rho U_{rel} D H a_1$$

$$\text{Non – linear damping part: } -\frac{1}{2} \rho U_{rel} D H a_3 \left[\frac{\dot{\omega}}{U_{rel}} \right]^2$$

Equation 2.21

The current improvements for galloping energy harvesters can be divided into three categories as following

- Optimizing the bluff body shape and structure: Oscillator's shape and structural parameters determine the frequency and amplitude of galloping. Unlike VIV energy harvester oscillator, most its oscillator are cylinders. It is more flexible for galloping energy harvester to obtain the better performance of the harvester by changing the shape of the bluff body.
- Widening operation range: The galloping is a low frequency and high amplitude vibration, but its cut-in speed is higher, meaning its performance may not be satisfied in lower flow speed. Reducing the cut-in speed by optimizing the design is another research aspect for galloping energy harvester.
- Hybrid galloping energy harvester: Galloping is usually coupled with other vibration and harvested energy together, such as combining with VIV. The energy output of this kind of energy harvester performs well in some applications.

For galloping, the conventional cross-sectional shapes are square, triangle, and D-shaped[97], [98]. For a square, the vortex is generated at the front vertices on both sides but reattaches to the boundary layer at the back vertices on both sides. Due to the reattachment of the vortex, pressure fluctuations appear on the upper and lower sides of the square, which affects the lift force of the bluff body as shown in Figure 2.25. So, the

researchers merged the upper and lower back vertices of the square to turn the square into a triangle. The triangle shape can effectively avoid the reattachment of the vortex and ensure the coordination of vortex shedding at the upper and lower sides. In recent years, many researchers have made some novel designs for square cross-sections based on the design concept of the square to the triangle. A funnel-shaped design was proposed in 2020 [99] (Figure 2.26(a)). This design not only prevents the vortex from re-attaching but also leaves space for the vortex to fall off. Experimental and simulation results show that the maximum output power of the design can reach $2.34\text{mW}/\text{cm}^3$, while the output power of the bluff body with square and triangular cross-sections is $0.207\text{mW}/\text{cm}^3$ and $1.56\text{mW}/\text{cm}^3$, respectively. At the same time, the design also reduces the minimum operating wind speed of the energy harvester. Similar to this design, some researchers pointed out a novel energy conversion system, which include a T-shaped bluff body (Figure 2.27). The T-shaped design is composed of four planes with a thickness of 0.01m . Two planes are perpendicular to each other to form a "T-shaped" structure. Two planes on both sides are used to reduce the influence of the boundary. This system has a maximum output power of 21.23W at a flow rate of $12.25\text{m}/\text{s}$ [100]. The fluid in this design is water. Due to the different viscosity of the fluid, the output power cannot be compared solely. But in the same environment, the design still shows a better performance than the rectangle. Later, Fengrui Liu et al. conducted a deeper study on the T-shape and designed a Y-shape energy harvester. The Y-shape consists of three planes, which are two front plates with a certain angle and a tailplane. The influence of the angle between the two front plates and the length of the tailplane for power output are analysed as shown in Figure 2.26 (b) [101]. The results show that when the angle between two front plates is between 60 degrees and 80 degrees, and the ratio of the length of the tailplane to the length of the two front plates is between $4/3$ and $5/3$, the output power is the highest. Compared with the T-shaped design, the Y-shaped design has better performance at low wind speeds, but the performance at relatively high wind speeds is not much different from the T-shaped design. There are many other designs of the bluff body for galloping, whose power outputs are considerable, as shown in Table 2-5.

Another novel design is to reduce the minimum operating wind speed of the energy harvester by adding other objects before and after the bluff body. The most typical design

recently is a comb-like beam design proposed by Guobiao Hu et al. in 2021 (Figure 2.28). This design fixes a number of parasitic beams parallel to the bluff body on the cantilever beam behind the bluff body in order to minimize the torsional vibration of the bluff body. This design can reduce the minimum operating wind speed by 12.5% compared to the rectangular design, and at 3m/s, the maximum power output of the design is 171.2% of the rectangular design[102]. Wan and Jongwon represented a removable cuboid design, which two sections of the cuboid body and the end of the cantilever beam are fixed through two springs, as shown in Figure 2.29. The cuboid will move backwards and vibrate because of the drag force when the flow passes it, and centrifugal force, elastic force, aerodynamic force and inertial force will be coupled. The result shows the design has a lower cut-in wind speed, and its mean power density improvement rate is 23.4% compared with the normal cuboid design[103].

VIV will be formed after the fluid passes through the circular cross -section object, but the bluff body of the non -circular cross section will also produce a vortex shedding phenomenon. Different from the circular cross -section object, the separation point of the boundary layer of the bluff body is fix and does not change with the Reynolds number. Therefore, the study of the coupling of galloping and VIV is also an important direction for galloping research, which improves the energy harvesting efficiency of the harvester through coupling [77].

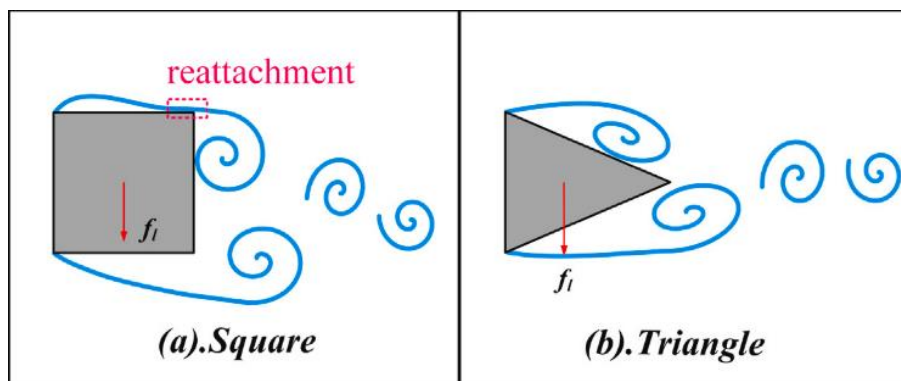


Figure 2.25 - Fluid Pass Square and Triangle Shape [99].

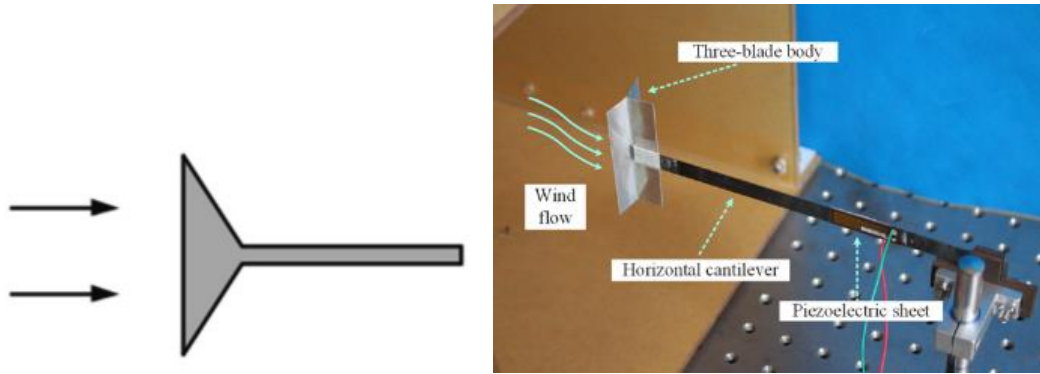


Figure 2.26 - (a) A Funnel-shape Design (b) T-shaped Structure [99].

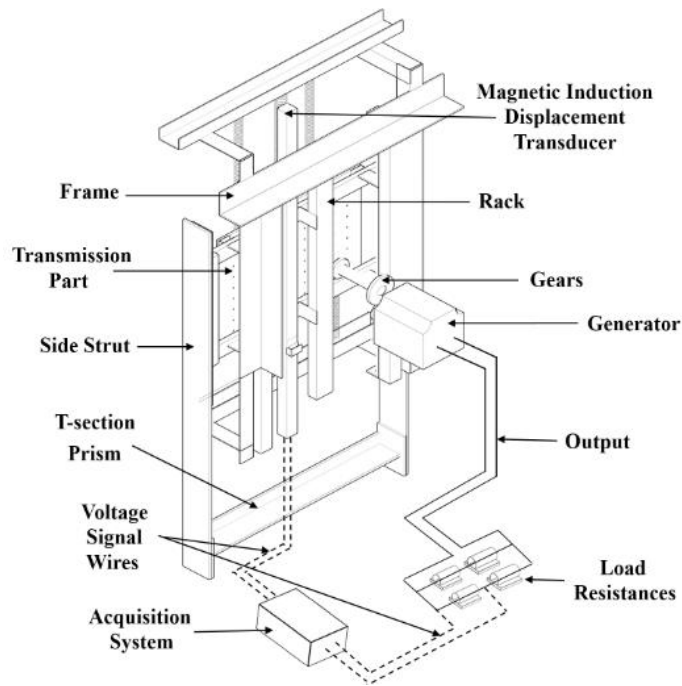


Figure 2.27 - T-shaped Energy Conversion System [100].

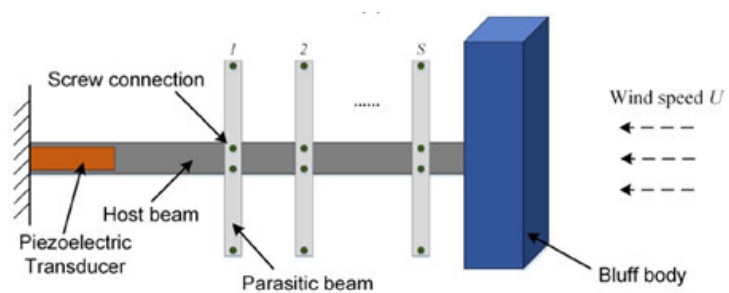


Figure 2.28 - A Comb-like Beam Design [102].

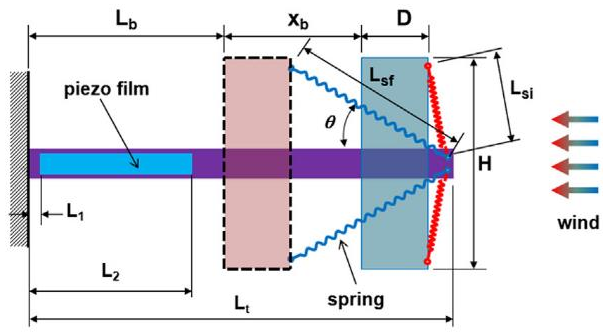
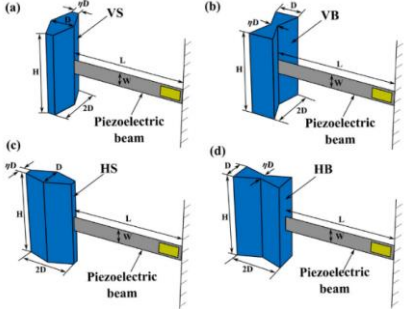
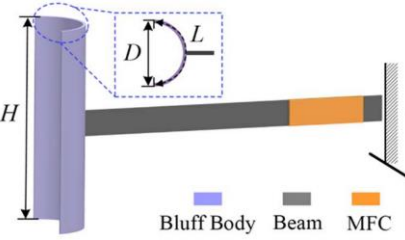
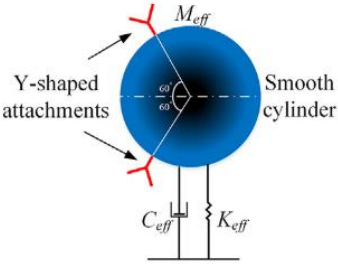


Figure 2.29 - Removable Cuboid Design [103].

Table 2-5 – Other Bluff Body Novel Design for Galloping in Recent Years

NO.	Novel design	Schematic diagram	Bluff body size(L*W*H)	Power output at the maximum wind speed in the experiment	Ref.
1	Spindle-like and butterfly-like design (2020)		33*66*117mm	8.02V at 2.92m/s	[104]
2	A curved plate design (2019)		35*35*100 mm ³	0.0356mW at 5m/s	[105]
3	Energy harvester with Y-shaped attachments (2019)		32*32*118 mm ³	0.576mW at 1.8m/s	[85]

2.3.3 Flutter

Flutter, similar to gallop, is a large-scale vibration that occurs due to the coupling of fluid dynamics, elastic forces, and inertial forces. Unlike gallop, flutter usually consists of two degrees of freedom, which are vertical movement and torsion. Flutter usually occurs in wing-shaped structures, as shown in Figure 2.30(a)[106]. In order to make the flutter instability tend to diverge, in the flutter of the wing-shaped structure, the aerodynamic centre and the centre of gravity must be respectively located on the front and back sides of the elastic shaft. Figure 2.30(b) shows the flutter of a typical wing-shaped movement. The wing moves in the vertical direction and twists at the same time [107].

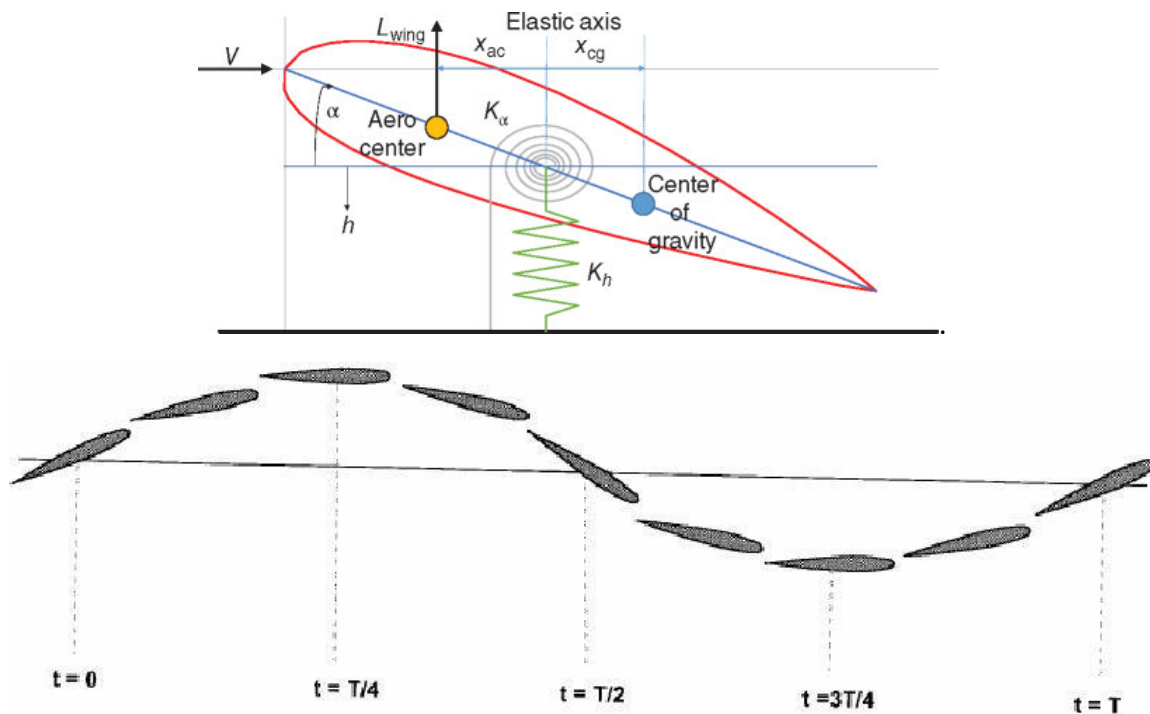


Figure 2.30 - (a)Wing-shaped Structure (b) A Typical Wing-shaped Movement [106], [107].

It is worth noting that flutter occurs when the fluid velocity reaches the critical flutter speed. The relationship between the critical flutter speed and flutter frequency is shown in Equation 2.22 [106], where V_c is the critical flutter speed; Y is Young's modulus of the beams; T is the beam thickness; and ρ and L are the fluid density and the beam length respectively.

$$V_c = \left(\frac{YT^3}{\rho L^3} \right)^{\frac{1}{2}}$$

Equation 2.22

When the fluid velocity is large, the energy of aerodynamic excitation will be greater than the natural damping of the system, and the vibration level will increase. When the fluid velocity continues to increase, this will usually cause the amplitude to continue to increase, which eventually leads to equipment damage. Depending on the parameters of the system, the flutter amplitude image is slightly different. A typical flutter amplitude image is that the amplitude continues to rise as the wind speed increases as shown in Figure 2.31 [108].

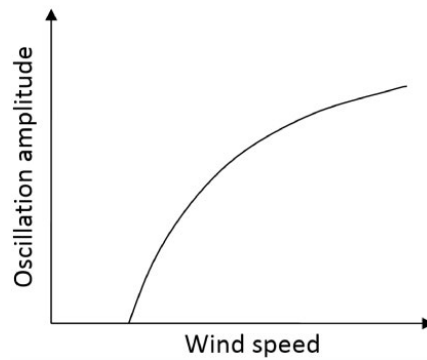


Figure 2.31 - A typical Flutter Amplitude [108].

The research on flutter in recent years has mainly focused on wing shape design, improving the performance of harvester by adjusting the stiffness of the structure, size of the wing, locations of the piezoelectric devices etc. For the locations of the piezoelectric devices, there are two places where the piezoelectric device is placed. (1) The first is to place the piezoelectric device at the constraint of the aerofoil section. In 2020, Xiaobiao Shan et al. proposed a novel flutter design[109]. As shown in Figure 2.32, the wing is fixed at the constraint of the aerofoil section through two flexible springs, and two main piezoelectric devices are placed on two flexible springs. In addition, to improve the flutter performance, a square prism was placed on the wing-shaped structure, and a cylinder, which is connected to the wing-shaped structure by a cantilever beam with a piezoelectric device, was placed at the end of the wing-shaped structure. When the fluid flows through the structure, the tail end cylinder undergoes vortex-induced vibration, which further increases the overall performance of the design. This design can produce a maximum voltage output of 17.94V

when the wind speed is 13.69m/s. (2) In addition, the other is to place a cantilever beam with a piezoelectric device at the end of the wing-shaped structure design. As shown in Figure 2.32, the maximum energy output in this design can reach 0.3233W [110].

Zhiyong Zhou et al. proposed a rectangular wing design in 2019 [111]. The rectangular wing is fixed by a cantilever beam with a piezoelectric device, and a magnet is fixed at the front end of the rectangular wing. The other two magnets are fixed on both sides of the front of the rectangular wing. Through the design of rectangular wings and magnets, the structure has a good voltage output. Through the design of rectangular wings and magnets, the structure has a good voltage output, and it also provides an alternative to the wing shape for the flutter design. Santos et al. represented a classical flutter energy harvester with larger attack angle, as shown Figure 2.33, the study showed that the position of the elastic axis and the inertia parameters significantly impact the structural response, while the stiffness of the structure has a minimal impact for flutter energy harvester. Another interesting study improved the efficiency of harvester by adding a moving part (slider) on cantilever beam, was pointed out by Hafezi et al., as shown in Figure 2.34. By changing the location of the slider, they could control the cut-in wind speed, and increase the power output [112].

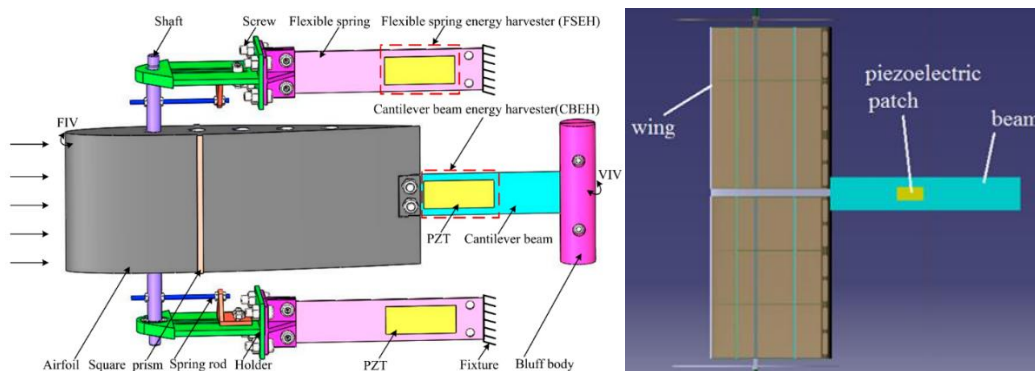


Figure 2.32 - Novel Flutter Energy Harvesting Design [109].

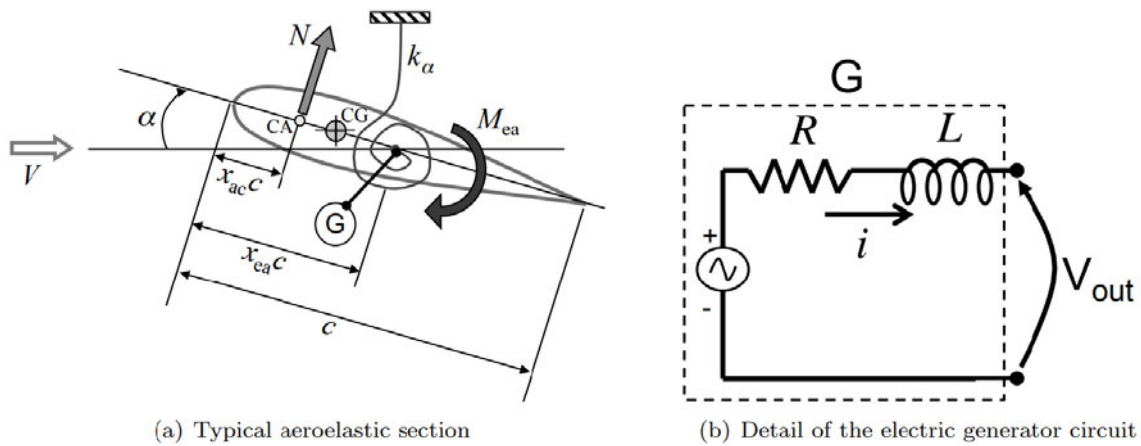


Figure 2.33 - Higher Attack Angel Flutter Energy Harvester [111].

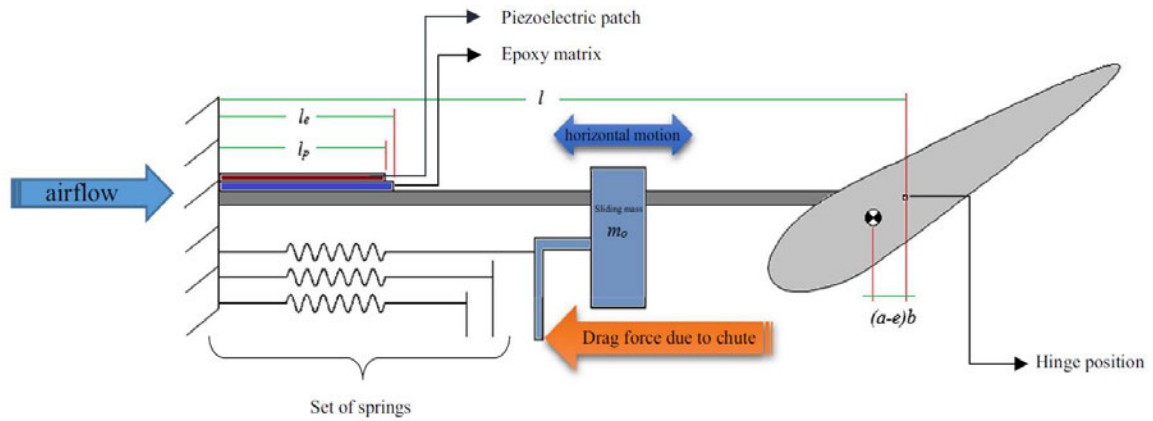


Figure 2.34 - Adaptive Flutter Piezoelectric Energy Harvester [113].

In general, for flutter energy harvesters, the main design direction is the wing-shaped structure, and stiffness of the structure, attack angle and locations of piezoelectric devices have largely influenced performance. It should be noted that proper structure can be added to the design to prevent equipment damage caused by excessive fluid velocity.

2.3.4 Buffeting

Buffeting is a kind of periodic vibration that results from wakes from upstream flow or naturally occurring turbulence and typically happens in unstable flow fields. In some studies, the buffeting and Wake-induced vibration (WIV) are usually separated into two vibration modes. WIV is usually a phenomenon in which the turbulence generated by the fluid flowing through the front object causes the rear object to vibrate. It can be seen from the vibration description that the condition of buffeting contains WIV and is wider than it;

therefore, WIV is a study aspect of buffeting. The governing equation of SDOF buffeting motion can be written as follows [77].

$$M\ddot{\omega} + C_{st}\dot{\omega} + K\omega = F_{MIM}(t) + F_{EIM}(t)$$

Equation 2.23

Where M stands for mass; C_{st} stands for system damping; K stands for spring stiffness; and F_{MIM} and F_{EIM} stand for fluid's unstable aerodynamic forces.

In recent years of research, a design using WIV to harvest energy has also appeared. There is no clear classification between VIV and WIV. For example, the vibration of the rear bluff body in [90] can be counted as WIV; however, the front cylinder vibrates as VIV; from the perspective of effect, it is not a complete VIV, because it has been affected by the rear cylinder. The main difference is whether the front bluff body is fixed; and in this section, only an energy harvester with the rear cylinder or other shape body as an oscillator is considered WIV (buffeting). Wang et al. showed a useful strategy for complex structural aerodynamic issues (muti-cylinder or muti-prism energy harvester) as shown in Figure 2.35. First, the lattice Boltzmann method is used to determine the external force f of the VIVs piezoelectric energy harvester. The electromechanical coupling equation is changed to force (f) to get the system response, which is then utilised as the starting point for the subsequent phase. The iterative process ends when the error precision satisfies the predetermined requirements (the system reaches a stable state) [112].

Daoli Zhao et al. proposed a WIV design in 2021 [114]. The design consists of two D-shaped cylinders, the front D-shaped cylinder is fixed, and the back D-shaped cylinder is fixed by a light cantilever beam with a piezoelectric device, as shown in Figure 2.36. The maximum power density of this design is 1074W/m³.

Another common type of buffeting design is to use flexible plates for energy harvesting. E. Binyet et al. placed the flexible board behind the rectangular bluff body and used the alternating vortex shedding generated by the fluid flowing through the bluff body to make the flexible board vibrate [115]. This design is a typical design. The future research direction can study the influence of the shape of the front bluff body on the power output, and the influence of the rigidity of the flexible board on the power output.

Jianjun Liu et al. proposed a design based on a bionic perspective in 2020, as shown in Figure 2.37 [116]. This design simulates the vibration of leaves and fixes a triangular sheet on a cantilever beam with a piezoelectric device. The maximum energy output is 0.55mW. Compared with other flutter designs, this design is simpler and less expensive, and more flexible.

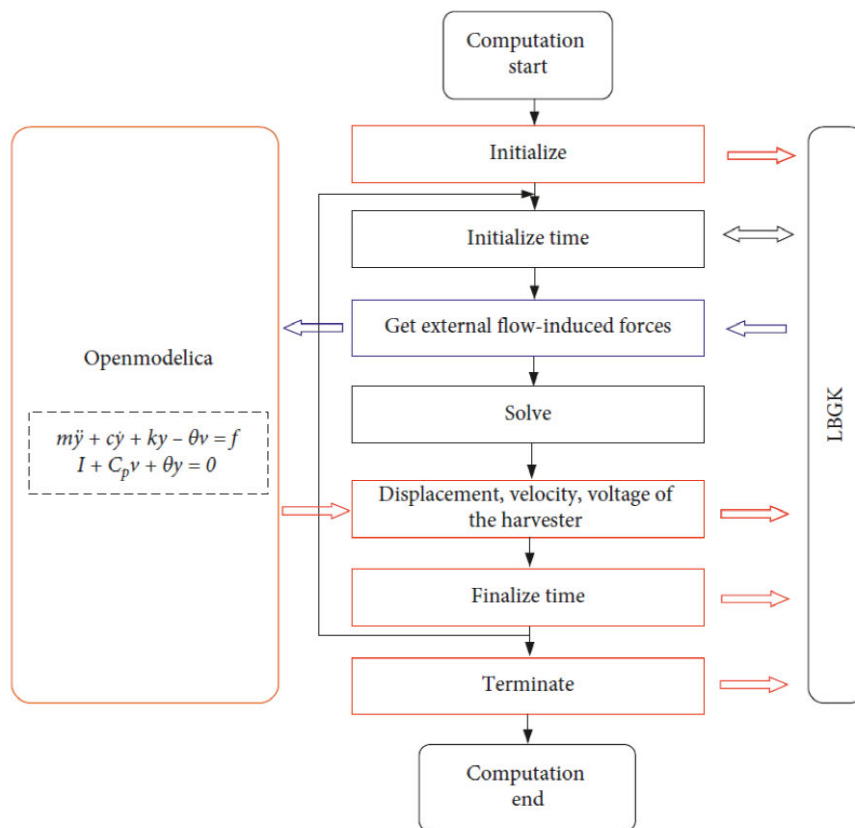


Figure 2.35 - Computational Process of Coupling [112].

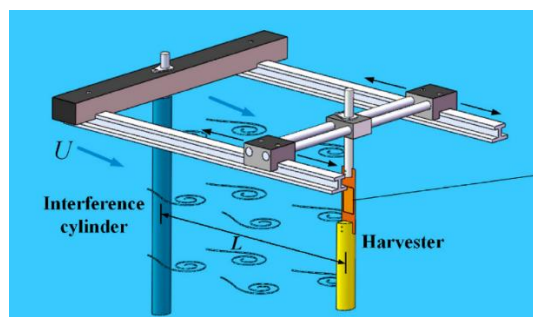


Figure 2.36 - D-shaped Cylinder WIV [114].

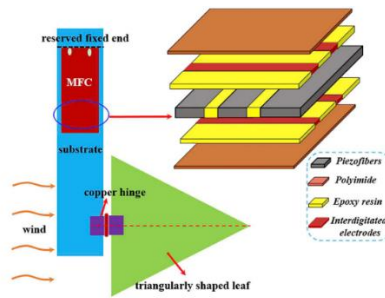


Figure 2.37 - Triangularly Shaped Leaf Fetter Design [116].

2.3.5 Summary of Flow-induced Energy Harvesting

This section compares various flow-induced vibrations and provides a summary of flow-induced energy harvesters that rely on piezoelectric technology. Different flow-induced vibration has their unique characteristics and restrictions, and compared with other vibrations, galloping has a broader development potential. Although the cut-in speed of galloping is generally high, with the development of novel design, its bandwidth has been greatly improved. Meanwhile, hybrid energy harvester, which is combined two or more kinds of vibration, has better performance.

Some energy harvesters in the Table 2-7 are relatively high, but it has a lower energy harvesting efficiency, which may be due to the multiple piezoelectric devices applied.

Table 2-6 Comparison of Flow-induced Vibration

	VIV	Buffeting	Galloping	Flutter
Category	<ul style="list-style-type: none"> ● Motion-induced excitation vibration (Forced response vibration) ● External excitation 		<ul style="list-style-type: none"> ● Instability-induced excitation vibration (Limit-cycle vibration) ● Self-excitation 	
Feature	<ul style="list-style-type: none"> ● Lower cut-in speed ● Limited operating bandwidth 		<ul style="list-style-type: none"> ● Higher cut-in speed ● Larger amplitude 	
	Flow goes through a circular cross-section object	Happening in unstable flow fields	Flow goes through a bluff body	Flow goes through a wing-

				shaped structures
Vibration trend	As the flow rate increases, the vibration rate increases first, and after reaching the maximum amplitude, it lasts for a period of time, and then decreases as the flow rate increases	Similar to VIV vibration, but due to complex turbulence impact, it generally only has a large amplitude during resonance.	After reaching the cut-in speed, the amplitude increases as the flow rate increases. Sometimes the characteristics of VIV are also displayed.	The vibration trend is similar to the galloping, but the vibration is a typical two-dimensional involving bend and twist vibrations
Limitation	Can't work at high flow speeds	Mathematical models are complicated and cannot be effectively analysed	The performance needs improvement in lower flow speed	Structural failure may happen caused large amplitude in higher flow speed

Table 2-7 - Summary of Recent Flow-induced Vibration Energy Harvesters

	Design	Body Size (L*W*H)mm	Bandwidth	Flow Velocity	Power Output	Reference
VIV	An asymmetric bending-torsional harvester	85*40*120	1.9 - 2.3m/s	2.1 m/s	405.9 μW	[88]
	Top and vertical cylinder design	90*30*120	1.3 – 1.8m/s (case 2) 2.2 – 4.4m/s (case 4)	1.4 m/s 3.7 m/s	30 μW 168 μW	[89]
	Double-cylinder energy harvester	200*20*20	2.84 – 4.46m/s	3.5 m/s	60 μW	[90]
	A hybrid piezo-dielectric harvester	70*70*25	0.8-1.1m/s	1.05 m/s	117 μW	[92]
	A cylinder with a splitter plate design	48*48*240	≥ 3 m/s	7 m/s	12 V	[93]
	Hybrid wind energy scavenging by coupling VIV and galloping	170*400*400	≥ 1 m/s	4.2 m/s	13.45 V	[94]

Gallop	Funnel-shaped design	72*50*160	≥ 7 m/s	7 m/s	4.3mW	[99]
	T-shaped design	20*20*90	≥ 4.8 m/s	12.25 m/s	21.23W	[100]
	Y-shaped design	17.6*30*70	≥ 1 m/s	5 m/s	1.5mW	[101]
	Spindle-like and butterfly-like design	33*66*117	≥ 1.5 m/s	2.92 m/s	8.02V	[104]
	A curved plate design	35*35*100	≥ 1.5 m/s	5m/s	35.6 μW	[105]
	Energy harvester with Y-shaped attachments	32*32*118	≥ 0.9 m/s	1.8 m/s	0.576mW	[85]
	A comb-like beam design	32*32*140	≥ 2 m/s	3 m/s	0.1245mW	[102]
	Removable cuboid design	60*60*120	≥ 1 m/s	12 m/s	10mW	[103]
Flutter	Concurrent flutter and VIV harvester	100*30*1	≥ 3 m/s	13.69 m/s	17.94 V	[109]
	Moving part flutter harvester	-	≥ 15 m/s	25m/s	50mW	[113]
Buffeting	Hydrokinetic piezoelectric energy harvesting	28*14*0.3	≥ 0.25 m/s	0.4 m/s	1074W/m ³	[114]

	The form of leaf design	500*500*0.1	≤ 20 m/s	12.9 m/s	184 V	[116]
--	-------------------------	-------------	---------------	----------	-------	-------

2.4 The Study of Cantilever Beam

The mainstream type of wind-induced piezoelectric energy harvesters design is to use aeroelasticity to generate vibration captured by cantilever beam. The typical structure of an aeroelastic energy harvester is shown in Figure 2.38. It consists of a cantilever beam and a vibrating body (oscillator), one end of the cantilever beam is fixed; the vibrating body is placed on the free end of the cantilever beam, and the piezoelectric device is placed on the surface of the cantilever beam. The cantilever beam as a mass-spring-damper system can transmit vibration, and can easily couple the mechanical collection structure with the electronic harvesting circuit [117]. The piezoelectric layer is fixed on the cantilever beam, and the piezoelectric layer harvests the stress and strain of the bending of the cantilever beam to generate the power output. The oscillator has a significant effect on energy harvesting; however, many studies show the geometry and parameter of the size of the cantilever beam are also relevant to power output. R. Hosseini and M. Hamedi proposed a triangular tapered cantilever beam, which has higher resonant frequency compared with the rectangular cantilever beam [118]. Hosseini et al introduced the strain distributed on various geometry beam (rectangle, triangle and trapezoidal beam), the result showed that triangle has the greatest strain distributed, and is two times than rectangular beam [119]. The existing research on cantilever beams is mainly concentrated on the two types: triangle and trapezoidal, and other irregular shapes remain to be studied. And the existing research shows that the shape of the cantilever beam has a small impact on the performance of the piezoelectric energy harvesters, but it has a greater impact on the vibration frequency and amplitude of the oscillator.

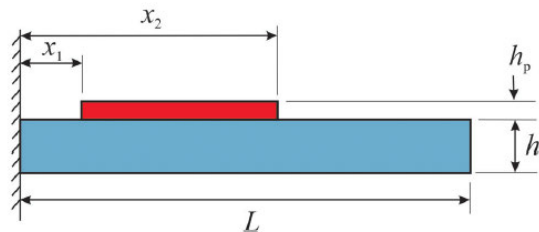


Figure 2.38 - A Typical Structure of the Aeroelastic Energy Harvester

As shown in Figure 2.38, h_p and h_s are the thickness of the piezoelectric layer and a cantilever beam (substrate); L is the length of a cantilever beam; x_1 and x_2 are the distance

from both the edge of the piezoelectric layer to the base. The natural frequency and the internal moment will be represented in this section. In the formula derivation process, some boundary conditions and assumptions need to be set and made; therefore, it is necessary to show derivation steps.

2.4.1 The Natural Frequency

The beam's stress (σ) and strain (ε) is represented by Equation 2.24, where M is the bending moment; I is the moment of inertia; y is the distance of neutral axis from the surface, and E is young's modulus.

$$\sigma = \frac{My}{I} = \frac{M}{I/y}$$

$$\varepsilon = \frac{\sigma}{E}$$

Equation 2.24

In general, the working bandwidth of vibration energy harvesters usually are designed around structural its first natural frequency, because first natural frequency is the lowest resonance frequency and often produces the greatest amplitude and output power [120]. According to the Rayleigh method for the beam [118], a rule of thumb of first natural frequency can be expressed as follows.

$$\omega_1 = \frac{0.5678}{L^2} \sqrt{\frac{\frac{E_s h_s^3}{12} + \frac{2E_p h_p^3}{3} + \frac{E_p h_p h_s^2}{2} + E_p h_s h_p^2}{\rho_s h_s + 2\rho_p h_p}}$$

Equation 2.25

Where E_s and E_p are young's modulus of substrate and the piezoelectric layer, and h_s and h_p are thickness of substrate and the piezoelectric layer. It's worthy to noticed that thickness of piezoelectric is well smaller than the thickness of substrate, therefore, the effect of piezoelectric layer on natural frequency and vibration behaviour can be ignored in the following equations. Also, along with the stiffness of the beam, it is also assumed that the mass is dispersed on the beam. The rule of thumb of first natural frequency can be rewritten as:

$$\omega_1 = 0.1639 \frac{h_s}{L^2} \sqrt{\frac{E_s}{\rho_s}}$$

Equation 2.26

S. Rao [121] represented another equation (k-th mode) for beam's first natural frequency as follows, where λ_k is eigenvalue calculated in Equation 2.28, and EI and m are beam's flexural rigidity and mass per length.

$$\omega_k = \lambda_k^2 \sqrt{\frac{EI}{mL^4}}$$

Equation 2.27

$$1 + \cos\lambda_k \cosh\lambda_k = 0$$

Equation 2.28

In the Equation 2.27, EI can be expressed as follows for rectangle cantilever beam, where B is the width of the beam.

$$EI = \frac{EBh_s^3}{12}$$

Equation 2.29

In the vibration energy harvester, the cantilever beam does not exist alone, and the oscillating object (e.g., a bluff body or a cylinder) is fixed at the free end. Khurmi and Gupta [122] defines the concept of effective mass of cantilever beams and pointed out the equation for whole oscillator. The effective mass of the cantilever beam (m_{eff}) means that the beam of effective mass can still maintain the same vibration frequency with the same stiffness of the original beam and no tip mass.

$$m_{eff} = \frac{3EI}{L^3 \omega_w^2}$$

Equation 2.30

Total mass M_T is equal to effective mass of cantilever beam plus the mass of the oscillating object. Therefore, the natural frequency of the whole oscillator (ω_w) can be obtained.

$$\omega_W = \sqrt{\frac{3EI}{L^3 M_T}}$$

Equation 2.31

2.4.2 The Internal Moment

The beam is assumed to meet the Euler–Bernoulli theory or thin beam theory before calculating. The beam is well thinner, only subjected to lateral loads, and the beam's shear deformation and rotatory inertia have been ignored. The governing equation of motion for a cantilever beam with only effect by the front vibrating body can be represented as follows.

$$\frac{\partial^2 M(x, t)}{\partial x^2} + m \frac{\partial^2 Z_{rel}(x, t)}{\partial t^2} = - \frac{\partial^2 Z_b(x, t)}{\partial t^2}$$

Equation 2.32

Where $M(x, t)$ represents the internal moment, $Z_b(x, t)$ and $Z_{rel}(x, t)$ are displacement at point x and time t of the base motion and transverse bending of neutral axis relative to its base respectively. The relationship between stress(σ), strain(ε) and electric field can be given by the piezoelectric constitutive relations for the substrate and piezoelectric layers as shown in Equation 2.33[117][123]. E_3 is the applied electrical field, which can be expressed as $E_3(t) = -v(t)/h_p$, where v is the voltage.

$$\begin{aligned}\sigma_1^P &= E_p(\varepsilon_1^P - d_{31}E_3) \\ \sigma_1^S &= E_s\varepsilon_1^S\end{aligned}$$

Equation 2.33

The width of the substrate and piezoelectric layer is assumed to be same, and the bending strain of the beam can be shown as $\varepsilon_1 = -y \frac{\partial^2 Z_{rel}(x, t)}{\partial x^2}$, therefore the internal moment can be rewritten shown in Equation 2.34. Then the equation can be reduced to by employing Equation 2.33 into Equation 2.34.

$$M(x, t) = - \int_{-(h_s/2)}^{(h_s/2)} \sigma_1^S B y dy - \int_{-(h_s/2)}^{(h_s/2)+h_p} \sigma_1^P B y dy$$

Equation 2.34

$$M(x, t) = EI \frac{\partial^2 Z_{rel}(x, t)}{\partial x^2} + \varpi v(t) [H(x - x_1) - H(x - x_2)]$$

Equation 2.35

Where ϖ is coupling term and can be expressed as $\varpi = -E_p B d_{31} (h_s + h_p)$. In the Equation 2.35, because the piezoelectric layer is not fully covered the substrate, the second term of the equation multiplied $H(x - x_1) - H(x - x_2)$ is the Heaviside function, which ensures the survival of this term when it is used in the governing equation of motion. Finally, the governing equation can be obtained by employing Equation 2.35 into Equation 2.32.

$$EI \frac{\partial^4 Z_{rel}(x, t)}{\partial x^2} + m \frac{\partial^2 Z_{rel}(x, t)}{\partial t^2} + \varpi v(t) \left[\frac{d\delta(x - x_1)}{dx} - \frac{d\delta(x - x_2)}{dx} \right] = -m \frac{\partial^2 Z_b(x, t)}{\partial t^2}$$

Equation 2.36

Where $\delta(x)$ is the Dirac delta function, can be calculated as follows[117]:

$$\int_{-\infty}^{\infty} \frac{d^{(n)}\delta(x - x_0)}{dx^{(n)}} f(x) dx = (-1)^n \frac{df^{(n)}(x_0)}{dx^{(n)}}$$

Equation 2.37

2.5 Conclusion and Research Gaps

This chapter reviews three aspects step-by-step, and the main findings of this review are as follows.

Firstly, different vibration energy harvesting methods are reviewed in Section 2.2. Through the review and comparison, it can be found that the building cost of electrostatic energy harvesters is relatively expensive, while the material cost of electromagnetic and piezoelectric energy harvesters is relatively expensive, although they do not require much building cost. In addition, in terms of energy conversion efficiency, the efficiency of electrostatic energy harvesters is relatively stable (13.33%), while the energy conversion efficiency of electromagnetic and piezoelectric energy harvesters mainly depends on the materials used. And also, in this section, a detailed review of the internal details of piezoelectric energy harvesters has been made in order to better understand the principle of piezoelectric kits and the operation of various components in piezoelectric energy harvesters.

Existing piezoelectric energy harvesters mainly rely on four different types of wind-induced vibrations to operate, so existing wind-induced vibrations are classified and compared in Section 2.3. The two most widely used vibrations are VIV and galloping. Relatively speaking, galloping has a wider wind speed operating range, while the energy harvesting efficiency of VIV will be reduced when the wind speed is too small or too large due to its different vibration principle. Therefore, galloping was determined as the research direction in subsequent studies. In addition, this section also determined the future development direction of various wind-induced vibrations, in which changing the front-end model of the piezoelectric energy harvester is an important future development direction of galloping, and a model that can vibrate in the galloping mode will be proposed in the subsequent chapters of this thesis. Finally, the research on cantilever beams can provide theoretical support for the future selection of cantilever beams and digital analysis. In Section 2.4, different calculation methods are integrated for the same parameters.

CHAPTER 3. METHODOLOGY

3.1 Introduction

In this chapter, a new design will be proposed, which is expected to be used as the front-end model of the piezoelectric energy harvester and can be vibrated in a galloping manner. In this chapter, the inspiration and of the prototype of the new design will be discussed first, which will be made by a 3D printer, and in order to study the different variables in this design, multiple prototypes of different sizes will be printed and introduced in this chapter.

In addition, the equipment and equipment used in the experiment will be introduced in this chapter, especially the two different piezoelectric kits that will be used in the following experiment to carry out comparative experiments. The introduction of the two piezoelectric kits and their related data will also be displayed in this chapter. In addition, unlike many other studies, in the following experiment, a force sensor will be used to record the force data of the model vibration process, so as to be able to more accurately compare the simulation results with each other. Other equipment used in the experiment will also be displayed, such as a wind tunnel and oscilloscope.

Before conducting experiments on the model, in order to ensure that materials and experimental equipment are not wasted unnecessarily, an initial simulation verification will also be performed in this chapter. The initial simulation verification will first roughly prove that the design has the potential for having a better performance. The process and results of the preliminary simulation verification will also be shown in this chapter. Finally, the coupling equations of mechanics and electricity will be derived.

3.2 Design

The current piezoelectric harvesting devices are mainly based on the above four vibration types (Vortex-Induced Vibration, Flutter, Galloping and Buffeting). The power output and cut-in wind speed of a galloping-based piezoelectric energy harvester has been improved in these years. In this study, a novel design based on galloping will be shown.

3.2.1 Novel Design Idea

Galloping generally occurs in the bluff body with angular and optimizing the body shape has become a mainstream study of galloping. The aim of optimizing the body shape is to create net lift force by generating the pressure difference between the upper and lower side to satisfy the galloping conditions. C. Zhou [105] proposed a curved plate shape design and analysed the effect of various lengths of the curved plate. In the experiment and simulation, the average power output of the structure of the curved plate, Square, Triangular, and D-Shaped are compared, and the average power of the Curved Plate is the highest. He pointed out that the design has better performance because of the bigger inner circulation, which forms below the shear layer of the curve plate's both sides. The inner circulation can generate a high-pressure area alternately at the upper and lower sides; therefore, the pressure difference of both sides leads to net lift force acting. Moreover, the net lift force is small when the curve length is short; Inner circulation will not generate, and the shear layer will adhere to the curve body, if the curve length is too large (like a cylinder). Another interesting design is adding two splitter plates behind a cylinder to change vibration from VIV to galloping[93]. The experiment showed the design can increase the pressure difference significantly between the upper and lower side and has larger vibration amplitude.

In this study, a reverse C shape with a tail design is proposed, and it is expected to have better performance by larger pressure difference between the upper and lower parts of the object. The tail structure is fixed in the middle of the C shape, and in this configuration, the vortex will not fall directly but will continue along the tail structure. It is expected to extend the time of the pressure difference to increase the power output. In addition, inner circulation will still generate because of the bluff body with angular, and the tail structure is expected to help inner circulation to generate higher pressure area.

3.2.2 Prototype

A reverse C shape with a tail design is shown in Figure 3.1. This structure consists of two parts. The front-end structure is a semi-circular structure with a diameter of D , and the back is a tail structure with a length of L . Due to the semi-circular design of the front end, the design is expected to generate a large drag force, and the material and the semi-circular

thickness of the design need to be considered. In this future study, various structure variables will be analysed, such as the diameter of the semi-circular, the length and width of the tail, etc. The design of the prototype is based on galloping, using the principle of galloping to collect energy in the case of a wider range of wind speeds. A cantilever beam will be connected to the end of the design; When the structure is vibrated, the energy harvest is achieved by the piezoelectric kit attached to the cantilever beam. The cantilever beam should vibrate as the first vibration mode in most conditions of piezoelectric energy harvesting; therefore, the piezoelectric kit will be placed at the fixed end to maximise power output. In addition, in order to avoid the impact of gravity, the direction of the wind is from left to right.

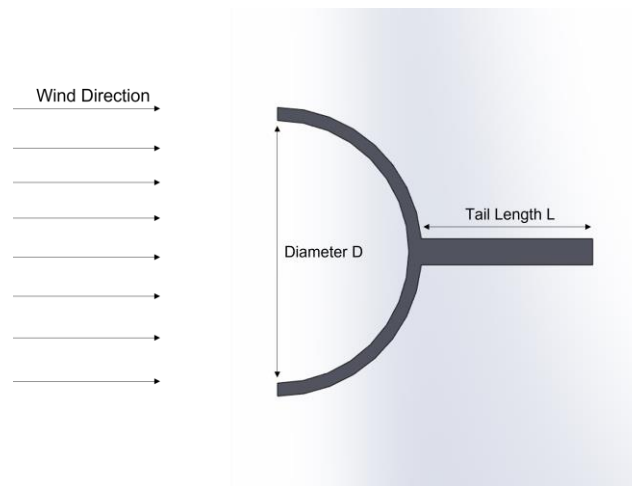


Figure 3.1 - Top View of the Prototype

3.2.3 Variables

Prototype variables include as follow

- Tail length
- Curve diameter (ratio of curve diameter and tail length)
- Curve thickness
- Prototype width
- Cantilever beam stiffness

To analyse the performance of the models in the real world, the 3D models was designed and printed by 3D printer (Prusa MK3S). In some other studies, some models are made of lighter metals, such as aluminium. In comparison, 3D printers can create models more

efficiently, and models created do not need to be assembled. Polylactic acid (PLA) as a material used in the 3D printer has better mechanical performance, and its young's module is around 2.7GPa, which is enough for the experimental requirements in this study.

The modules created by the 3D printer are divided into three series, T series, R series and A series (Figure 3.2). Firstly, the T series was created to verify the effect of the tail on energy harvesting. The size of the T1 is the same as that of the Curved Plate proposed by C. Zhou, and T2 adds a tail with a length of 22.75mm based on T1. A study on the splitter plates behind the cylindrical bodies by J. Song et al. shows that when the ratio of the cylindrical diameter and the splitter plates is equal to 0.65, the harvester has the best performance. Although the prototype is semi-circular instead of a cylinder in this study, the tail length of the T2 is still set as 22.75mm ($35\text{mm} \times 0.65$) in the comparison of the T series.

The A series is manufactured to analyse the impact of the length of the tail on the harvester's performance. It contains the five models of A1 to A5. For the convenience of future manufacturing, the value of the tail length should be an integer. Therefore, when designing the A series, the inter diameter of the five models is adjusted to 40mm. The tail length of this series is 10mm, 20mm, 26mm, 30mm, and 40mm, respectively, corresponding to the ratio of the diameter to the length of the tail 0.25, 0.5, 0.65, 0.75, and 1.

Before designing the A series, the R series was first designed. The R series was originally planned to be produced in a total of five models, and the length of the tail is the same as the five models of the A series. However, the curved thickness of the R series is only 0.5mm which is the same as the T series, and it is only a thin layer of material in 3D printing. In multiple printing, other models except R1 and R2 are printed failed or cannot maintain their structure due to too thin curve thickness. Therefore, the A series was adjusted from 0.5mm to 2mm on the thickness of the curve. The R1 and R2 can be compared with A4 and A5 to study the effects of the curve thickness on the performance of the harvester.

The prototype's width determines the model's windward cross-sectional area. In general, the longer the width, as the cross-sectional area increases, the larger the harvested energy and the greater the drag force to the model. In addition, a rear-mounted hole is attached to the back of models, which is used to connect a model and the cantilever beam. The

thickness of the model tail is set to 4mm to ensure the stability of the joint between the model and the cantilever beam. The three series model specifications are shown in Table 3-1.

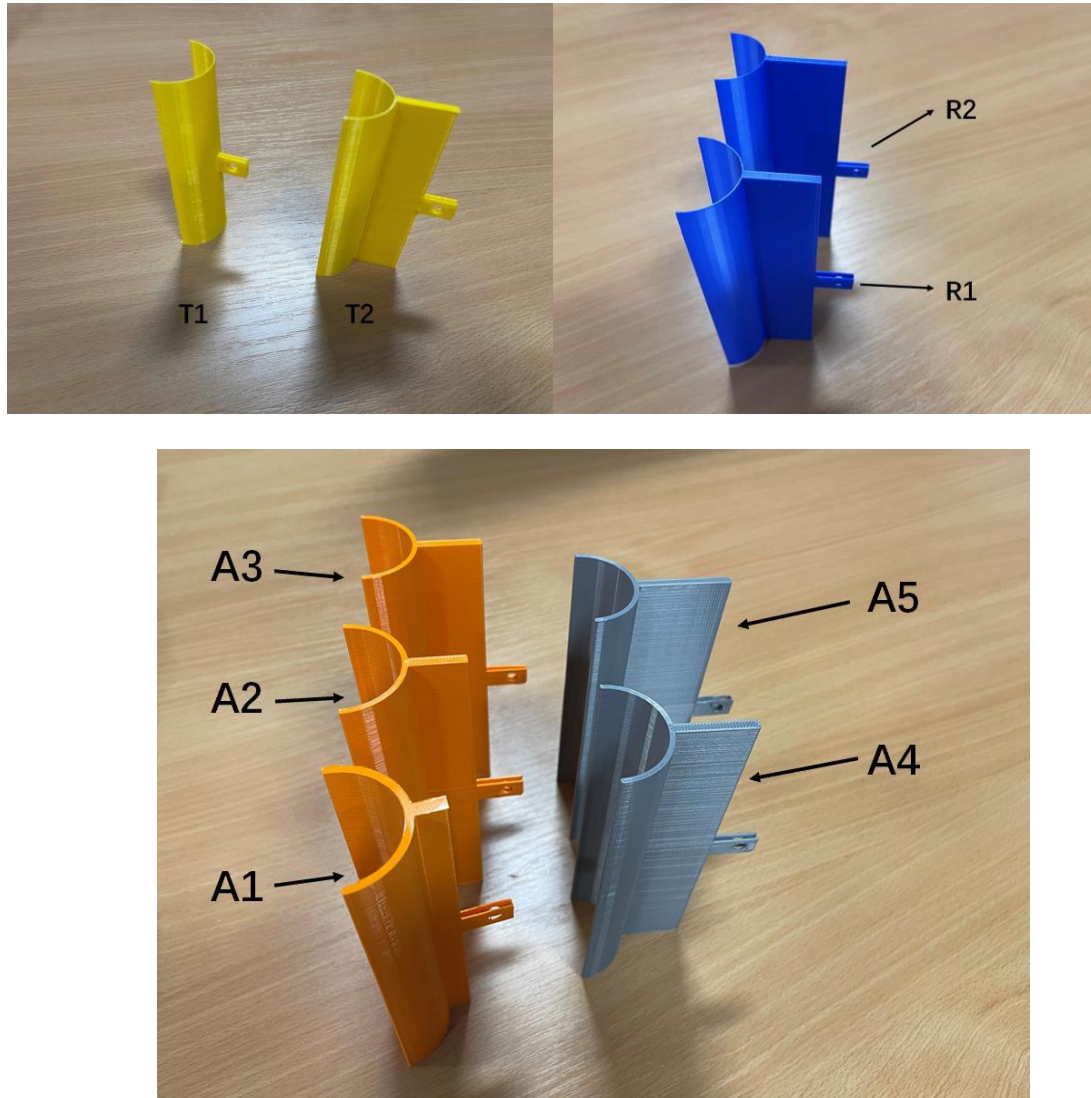


Figure 3.2 - Different Series Model for the Experiment

Table 3-1 - Experimental Models Specifications

Model Code	Curve (mm)	Thickness	Curve Inter Diameter (mm)	Tail Length (mm)	Width (mm)
T1	0.5		35	0	100
T2	0.5		35	22.75	100

R1	0.5	40	30.00	150
R2	0.5	40	40.00	150
A1	2	40	10.00	150
A2	2	40	20.00	150
A3	2	40	26.00	150
A4	2	40	30.00	150
A5	2	40	40.00	150

The cantilever beam plays a significant role in the piezoelectric energy harvester with a cantilever beam. The front-end model drives the cantilever beam vibration, and the cantilever beam will transmit vibration to the piezoelectric kits attached to it. The vibration of the piezoelectric energy harvesters is mainly based on the first mode of natural frequency, so the cantilever beams with a lower natural frequency of the first mode are usually selected. The vibration frequency of a cantilever beam is related to its mass and stiffness. In many other studies, metal cantilever beams, especially aluminium beams, have been used due to their low density and good ductility. In this study, two cantilever beams will be used for testing to study the impact of the stiffness of the cantilever beam on the energy harvester so as to select the most suitable cantilever beam. The specific parameters of the cantilever beam are shown in Table 3-2, where the plastic cantilever beam is printed by a 3D printer.

Table 3-2 - Cantilever Beams Specifications

Length	Width	Thickness
180 mm	10 mm	1.4 mm
Beam Material	Aluminium	Plastic (PLA)
Density	2.7 g/cm ³	1.25 g/cm ³
Young's module	70 GPa	2.7 GPa

3.3 Experiment

3.3.1 Piezoelectric Layer

In this study, there is two piezoelectric kits are chosen to be compared, TE connectivity (LDT0-028K) and Smart Material (M-2807-P2). LDT0-028K piezoelectric kit is made of Polyvinylidene fluoride (PVDF), and the piezoelectric film of the kit is covered by mylar and acrylic coating. A report written by Orrego et al.[124] showed the cross-section of another similar piezoelectric film (LDT4-028K/L) by light microscope and tested the relationship between stress and strain as shown in Figure 3.3. PVDF is covered by laminated Ag-ink electrodes and polyester substrate (PET). According to the piezo film sensors technical manual of the manufacturer [125] (Table 3.1), both kits are the same except for the dimension of each layer. Therefore, the property data of LDT4 can be referenced for this study, in order to understand the microstructure better. The manufacturer also gave the relationship between tip deflection and voltage (see Figure 3.4). It shows that the voltage could be generated 7V by 2mm of the tip deflection. And manufacturer points out that the maximum voltage is above 70V when the bending angle achieves 90 degrees.

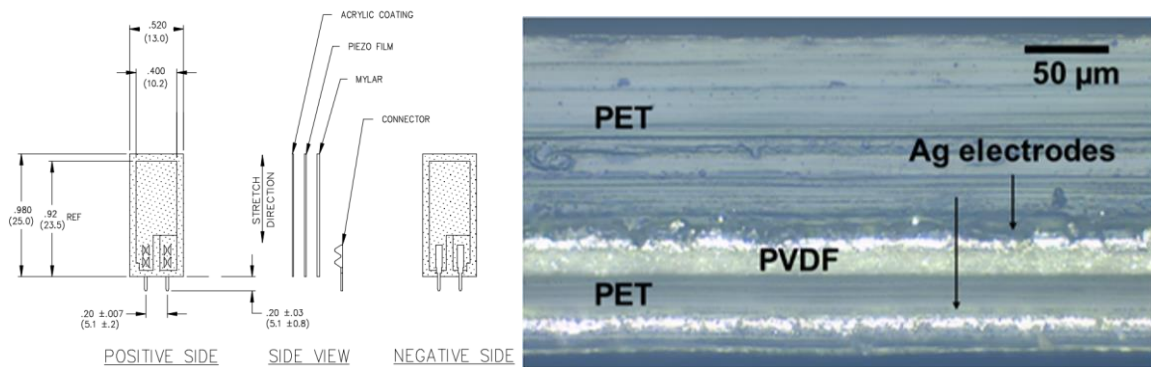


Figure 3.3 - LDT0-028K Structure [125].

Table 3-3 - The Dimension Comparison of LDT0 and LDT4 [125].

Model Number	Dimension of PVDF Film (L×W×H)	Dimension of Electrode (L×W)	Total Thickness
LDT0-028K	25mm×13mm×28μm	23.5mm×10.2mm	0.2mm
LDT4-028K	171mm×22mm×28μm	156mm×19mm	0.2mm

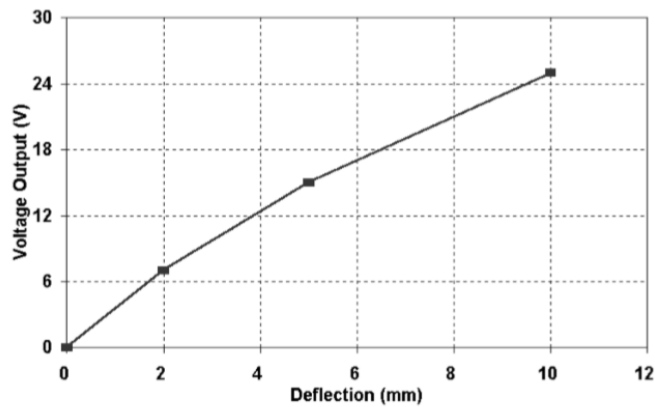


Figure 3.4 - Relationship of Tip Deflection and Voltage (LDT0-0.28K) [125].

M-2807-P2 is made of Lead zirconate titanate (PZT), the covering is polyimide film, and the piezoceramic fibres are fixed in the middle of the device. The piezoelectric kit comprises polyimide film, electrodes, and rectangular piezo ceramic rods sandwiched between adhesive layers. Because of the interdigitated design of the electrodes attached to the film, the applied voltage is transferred directly to and from the ribbon-shaped rods as shown in Figure 3.5 [126]. Connecting wires to the electrodes of the kit is a challenge because a composite made of plastic is below the electrodes. If the soldering process is too long or too hot, the electrode will fall off due to the plastic becoming soft and failing to bind with the substance of the sputtering electrode.

According to the datasheet of both piezoelectric kits, some key parameter is shown in Table 3-4, and it clearly shows that the piezoelectric kit based on the PZT piezoelectric kit (M-2807-P2) have better performance in an electric field, which has Strong piezoelectricity and higher capacitance. However, in actual use, in addition to having excellent piezoelectric performance, piezoelectric materials also need to have certain bending resistance and stiffness in order to be able to withstand the repeated high-frequency vibration of the structure. Therefore, it can be seen that the PVDF piezoelectric kit (LDT0-028K) is more prominent in mechanical performance. In the following experiments, the performance of the two piezoelectric materials will also be evaluated.

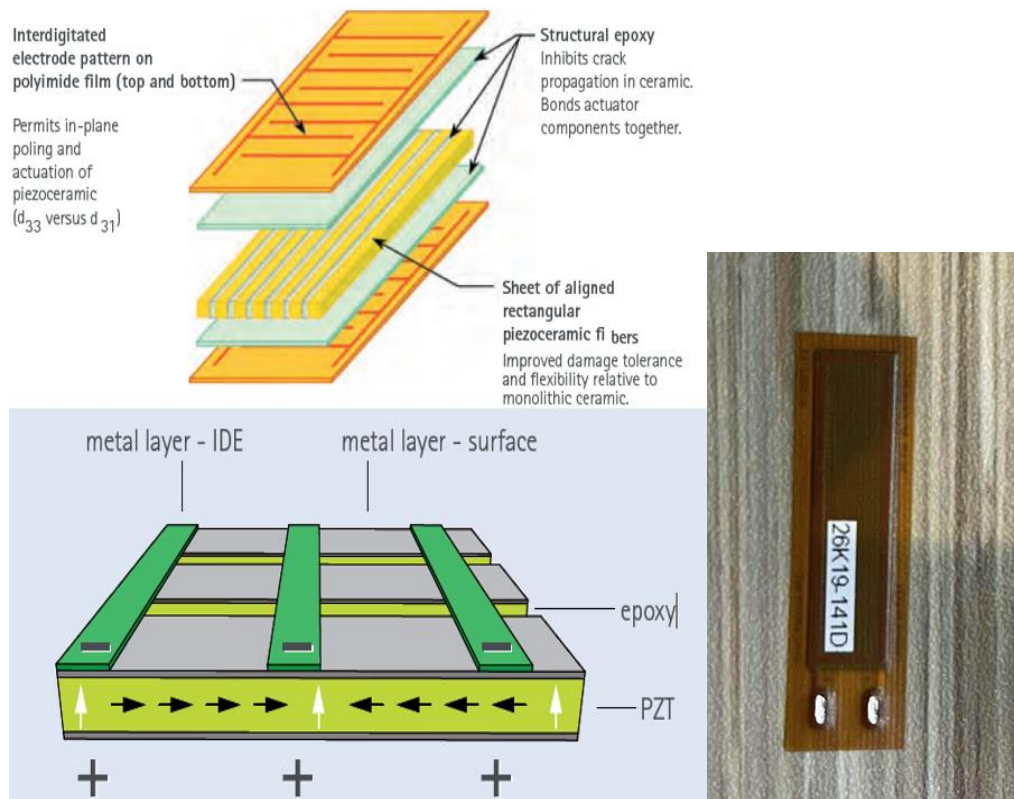


Figure 3.5 - M-2807-P2 Structure [126].

Table 3-4 - Parameters of Two Piezoelectric Kits [126].

Piezoelectric Kits NO.	LDT0-028K	M-2807-P2
Dimensions (mm)	25 × 13 × 0.2	37 × 10 × 0.3
Density (kg/m)	1780.00	114.24
Yield Strength (GPa)	50.0	30.3
Poisson's Ratio	0.34	0.31
Capacitance (ρF)	500	15110
Piezo Strain Constant d_{31} ($\rho C/N$)	23	-170
Piezo Strain Constant d_{33} ($\rho C/N$)	-33	400

The main difference between the piezoelectric kits used in the experiments is the piezoelectric material, PVDF and PZT. The experiment will compare the performance of both kits, and the one with high power output will be chosen. On the other side, although

the output power of the two piezoelectric kits is different, the output power trend at different wind speeds should be roughly similar. Therefore, using two different piezoelectric kits to harvest energy respectively in the experiment can also reduce the experimental error to avoid incorrect results caused by the failure of the piezoelectric material.

3.3.2 Wind Tunnel

The experiment carried out in the wind tunnel laboratory of the Heart Space building at the University of Sheffield. As shown in the Figure 3.6, the wind tunnel laboratory generates high-speed wind by rotating the rotor at high speed. In theory, the highest wind speed can reach 22m/s, but because it is not a closed-loop wind tunnel, factors such as site restrictions are considered when using it. The test wind speed in the study will be from 2m/s to 10m/s. For the United Kingdom, the annual average wind speed at sea level is about 4.3m/s [107]. This test range can cover wind speed in most areas. The working section of the wind tunnel is in the middle, and its dimension is 1.2×1.2×3 m³. There are a ‘doors’ of the working section in the back, which allow to place the experimental device inside. Besides, an adjustable mounting point is in the middle, and the models can be fixed at the point. Other parameters of the wind tunnel can be seen in Table 3-5.

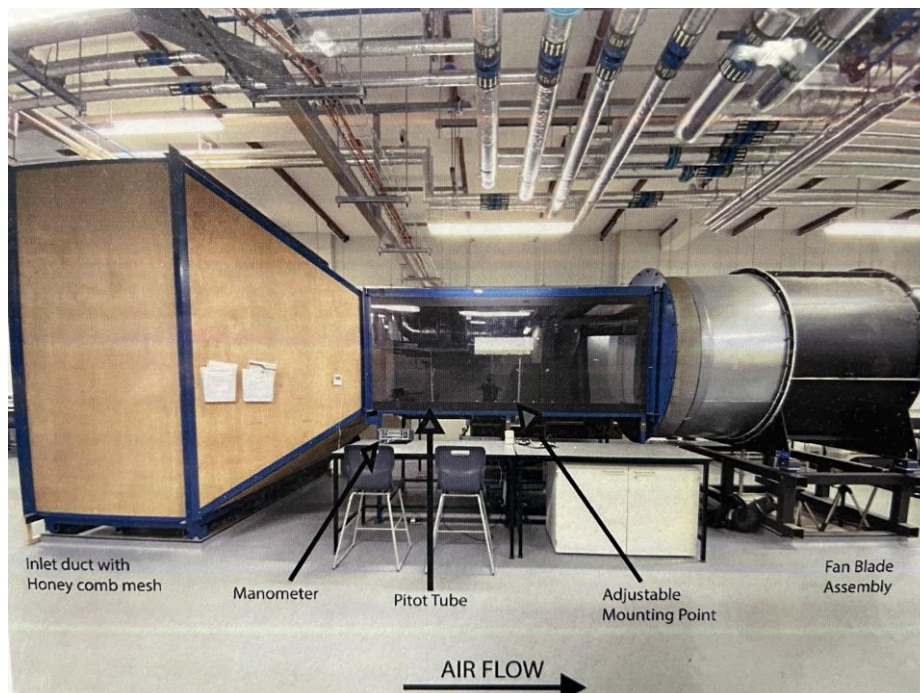


Figure 3.6 - Wind Tunnel

Table 3-5 - Specifications of Axial Flow Fan and Wind Tunnel

Minimum Velocity	3 m/s or 130 rpm
Maximum Velocity	12 m/s or 500 rpm
Contraction Ratio	6:1
Turbulence intensity	0.5% (can be increased if required)
Reynolds Number / m	1,200,000
Unsteady gust generation	+/-15% at 10m/s at 2Hz
Fan diameter	1850 mm
Volume	31.1 m ³ /sec
Pressure	505 Pa
Fan abs. Power	27.2 Kw

Its operating process is as follows:

- Make sure no loose things are present by looking inside the wind tunnel.
- Verify that the thumb screw has been used to secure the sting in the proper location. The pitch angle may be changed using the black handwheel located below the wind tunnel.
- Make that the test model is securely fastened to the multi-axis transducer plate using bolts or Araldite, as the multi-axis transducer is highly delicate.
- Before shutting the door and turning on the fan, a visual check of the interior through the glass will be done to ensure nobody is inside. Lock the latch on the wind tunnel door and close it.
- Verify that the Manometer is connected to the Pitot tubes. Turn it on by pressing the red button.
- Verify that no one is positioned in front of the fan.
- Isolator on and wait for the inverter to start up.
- press the green button to start.

- The motor's speed may be adjusted with the Up and Down Arrows.
- Reduce the motor speed before the ultimate switch-off, as the Isolator will restart at the previous speed setting.
- Press the Red button to stop the Wind Tunnel motor.
- Turn off the Isolator, Manometer, and lights and shut down the computer.

3.3.3 Measure Devices

A digital oscilloscope (TBS 1072B) is selected to measure and record piezoelectric kit power output as shown in Figure 3.7. A digital oscilloscope can build a waveform by digitizing the signal, which has the function of recording and storing the signals. It can be used to observe and compare the single process signals, low-frequency signals, and signals observed at different times and different places at different times. The key performance specifications are shown in Table 3-6. The vibration frequency of models is predicted below 10Hz. According to the sampling theory, aliasing will not happen when the sample rate is more than two times higher than the high-frequency component of the signal. Therefore, the oscilloscope is suitable for measurement in this study, because the bandwidth models and sample rate are much higher than the vibration frequency predicted.

Electrodes of piezoelectric kits can be connected with the oscilloscope's two-channel by probes. In the original plan, a passive voltage probe (50 MHz) and a current probe will be connected to two channels. The current probe is replaced with an external resistance load due to the expensive cost of the current probe, and the overall power output will be calculated by the voltage drop and resistance load. Cheng-Feng Zhou et al. studied the effect of an external resistance load on power output, showing power output is almost steady after the load is over 820k Ω [105]. In order to facilitate subsequent calculations and analysis, the external resistance of 1M Ω will be used in this study.

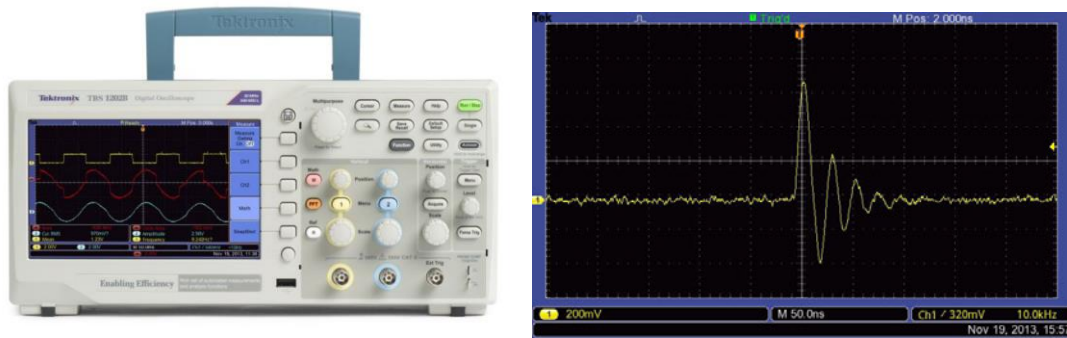


Figure 3.7 - Digital Oscilloscope and Screen

Table 3-6 - Key Performance Specifications for TBS 1072B Oscilloscope

Bandwidth models	70 MHz
Channel	2-channel
Sample rate	2 GS/s
Record length	2.5k point

In addition, a pitot tube connected to the manometer was placed in the wind tunnel, as shown in Figure 3.6. The wind speed of the wind tunnel can be changed by adjusting its fan rotation speed. Although the look-up table of fan rotation speed and wind speed is given, it can more accurately verify whether the wind speed reaches the expected wind speed.

A multi-axis transducer (ATI: nano 43) is placed on an adjustable mounting point of the wind tunnel, and the transducer can measure force and torque on all six-axis. A transducer, high-flex cable insulated, and intelligent data acquisition system make up the whole transducer system (Ethernet/Device Net interface or F/T controller), as shown in Figure 3.8.

In most piezoelectric energy harvesters' experiments, the vibration frequency, voltage output and power output of the harvester are used as important conditions to measure whether the harvester's performance is excellent. The vibration frequency of the harvester can be determined according to the change of voltage output, or it is determined by a high-speed camera. The electrical data can be collected by a corresponding device, like an oscilloscope. Generally speaking, in order to better determine the performance of a piezoelectric energy harvester design, simulation software is usually used to observe the

fluid state when the fluid flows across the model. After the simulation, the result can show the value of the lift force or lift coefficient over time, and the vibration frequency can be determined according to the change in the lift force. However, the value of the lift during the vibration of the harvester is difficult to determine in the experiment. Overall, the vibration frequency and voltage output can only be obtained in the experiment, and only the lift value and vibration frequency can be obtained in the simulation. Except for vibration frequency, it is difficult to verify the result of experiments and simulations through more parameters. In addition, when designing the piezoelectric energy harvesters, the lift force should also be measured in the experiment as an important indicator in order to find the appropriate material to avoid damage caused by insufficient structural strength. Therefore, the transducer used can provide great help to this study.

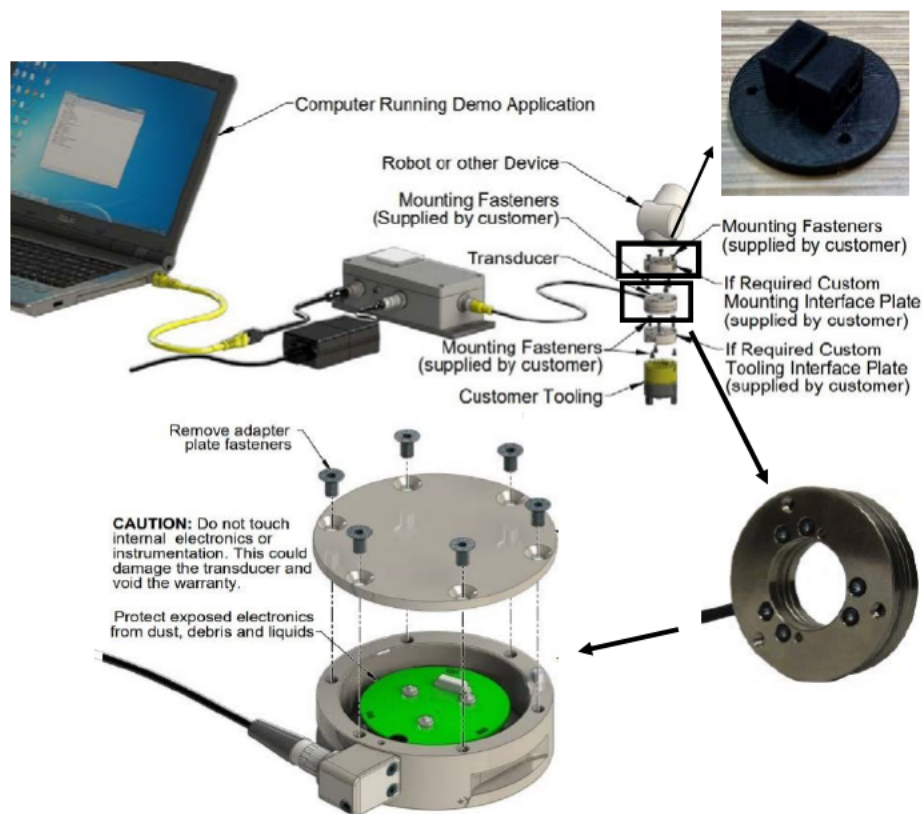


Figure 3.8 - Nano43 Transducer System.

The resonant frequency of the transducer is much larger than the prototype frequency expected, and other parameters in Table 3-7 also show that the transducer is suitable for this study. The adjustable mounting point in the wind tunnel is a vertical steel pipe that can be adjusted height, and the transducer is installed on the top of the steel pipe. However,

in the experiment, the model of the energy harvester is expected to vibrate in the horizontal direction, which means that the cantilever beam is vertical. Therefore, the mounting interface plate needs to be designed to fix the one end of vertical cantilever beam to the horizontal transducer. A mounting interface plate is made by 3D printer as shown in Figure 3.8.

Table 3-7 - Nano43 Transducer Specifications.

Single-Axis Overload (F_{xy})	± 300 N
Single-Axis Overload (F_z)	± 380 N
Single-Axis Overload (T_{xy})	± 3.2 Nm
Single-Axis Overload (T_z)	± 4.6 Nm
Resonant Frequency (F_x, F_y, T_z)	2800 Hz
Resonant Frequency (F_z, T_x, T_y)	2300 Hz
Weight	0.0387 kg
Diameter	43 mm
Height	11.5 mm

The operation screen of the whole transducer system is shown in Figure 3.9, and its operating process is as follows

- After installing the model, check whether the data acquisition box connected to the computer is FT12384, and check whether the indicator light of the system box is green (green represents normal power supply).
- Check whether the screws of data acquisition box and cable are tightened.
- Open the Lab view (Lift, Drag, Torque) program on the computer and check whether the "Calibration File" value is also FT12384.
- Select the output folder.
- Run the program and set zero scale.
- Before running the wind tunnel, stop the program running and select the output sample number.

- Run the program again and collect data.

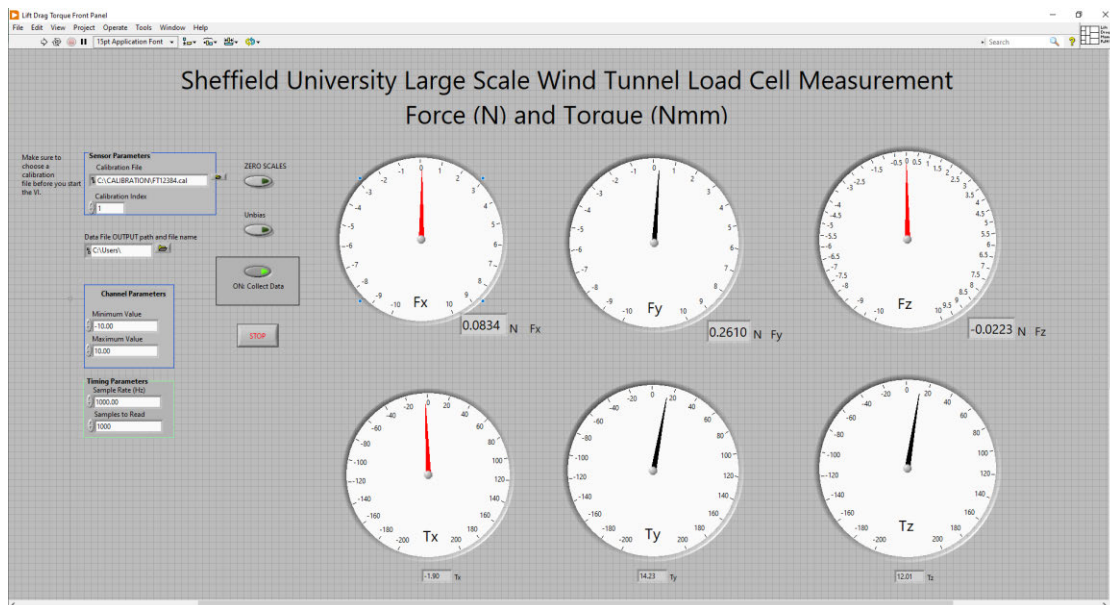


Figure 3.9 - The Operation Screen of the Transducer System.

3.4 `Modelling

Before the start of the following study, in order to verify the feasibility of new design and avoid waste experimental time and equipment, the initial simulation verification will be performed. The initial simulation verification will compare the three existing models (square, cylinder and curve plate) and new models under the same conditions in order to determine that the study has research value. The four model configurations were created in 2D to compare the improvement and were established and analysed using computational fluid dynamics (CFD). Ansys 2021R2 Fluent was used for the process.

3.4.1 Geometry

In the initial simulation verification, the performance of the four models in the fluid will be compared in the fluid, namely the cubic, cylindrical, curve plate and curved body with tail. cubic and cylinder are typical models of galloping and VIV respectively, and a curve plate has been pointed out that has better performance. Through initial simulation verification, on the one hand, the performance of the design of the curve plate can be verified, and on the other hand, it can be preliminary verification whether the design of a curved body with tail design has the potential for research. The main body (Square, Circle, Curve and Curve

with tail) was enclosed within a rectangle of dimensions 200 x 100cm, and the centre of the curve was set at a rectangular horizontal middle line and had a 50cm distance from the left side of the rectangle, as shown in Figure 3.10. The geometry size allowed the dominant flow features to be enough to capture and avoid the air streamlining near the wall affecting the bluff body.

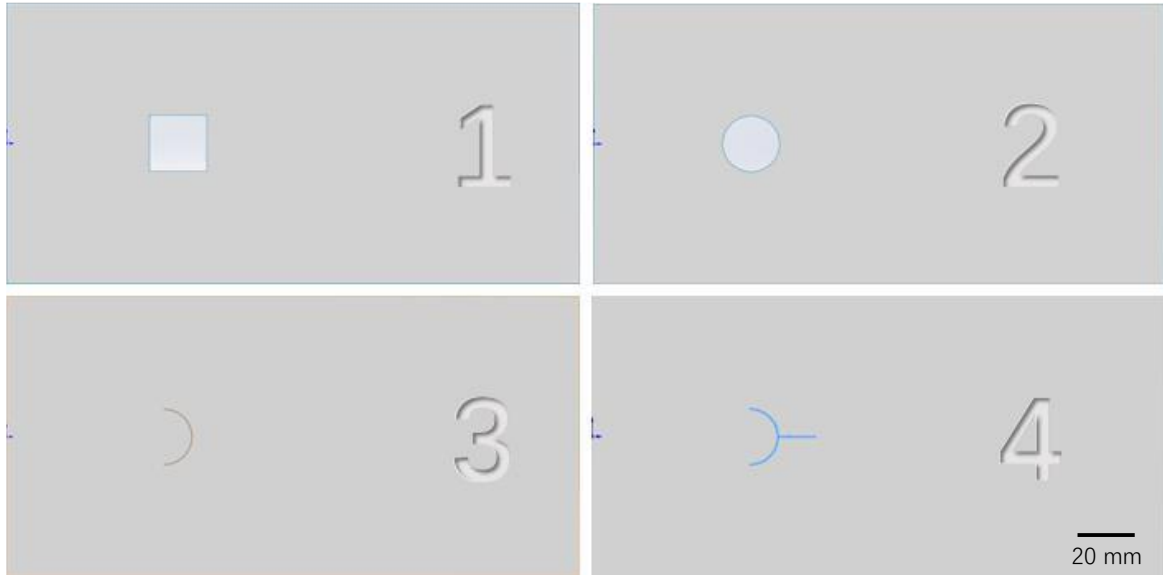


Figure 3.10 - Four Design of Initial Simulation Verification.

In the simulation, in order to ensure that the four designs can be effectively compared, their feature length is set to the same value (square edge length, circular diameter, semi-circular diameter). Model 3 and Model 4 are composed of semi-circular with a thickness of 1mm. The ratio of the semi-circular diameter and the tail length is 0.65, according to the study of the splitter plates of the cylinder. The parameters of the model and fluid in the simulation are shown in Table 1.

Table 3-8 - Parameter of Simulation Models and Fluid.

Parameter	Value	Unit
Feature Length	20	mm
Tail Length	13	mm
Enclosed Rectangle Length	200	mm

Enclosed Rectangle Width	100	mm
Fluid Density	1.225	kg/m ³
Fluid Viscosity	1.79E-05	kg/m-s

3.4.2 Mesh Generation

The triangles method was used for the rectangular fluid domain. Because the initial simulation verification could indicate whether the study has future research value, the priority was to ensure the results' accuracy. As shown in Figure 3.11, in order to ensure that the average unit quality is higher than 0.95, the overall mesh number was intensive. The number of mesh elements around the main body was increased as a better display of fluid performance.

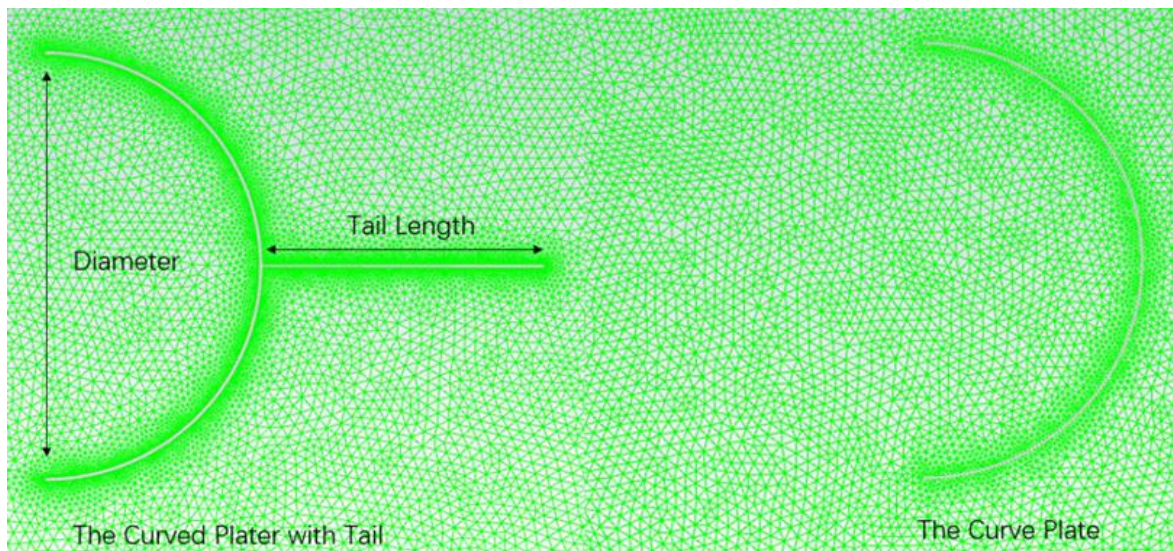


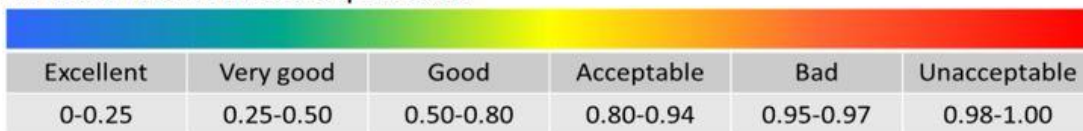
Figure 3.11 - The 2D Simulation Models.

The top and bottom boundaries of the rectangle were set as a fixed wall, and the airflow direction was perpendicular to the inlet boundary. The left and right boundaries of the rectangle were set as velocity inlet and pressure outlet respectively.

Before the subsequent simulation, the mesh quality was evaluated. As the mesh-created procedure is similar for the four models, the following evaluation takes the curve plate model as an example.

- The aspect ratio of the model is 1.2. The aspect ratio is essential for measuring the mesh's quality. It shows the ratio of the triangle's longest and shortest edges, and mesh quality is the best when it's equal to 1.
- Jacobian Ratio (Corner Nodes) is 1. Its range is from -0.1 to 1. It is used to judge the high curvature and distortions of the elements. The value is better to close to 1. It will lead to a severe mesh division failure if the value is near to 0 or negative.
- The value of skewness is also one of the primary evaluations of the quality of the mesh in the mesh structure. The skewness indicates the proportion of mesh structures resembling their ideal form or shape. In the simulation, the value is excellent (0.05), according to Figure 3.12.
- Moreover, orthogonal quality was also excellent for the mesh quality evaluation (0.97).
- The number of mesh elements is 169275.
- The average element quality is 0.97.

Skewness mesh metrics spectrum



Orthogonal Quality mesh metrics spectrum

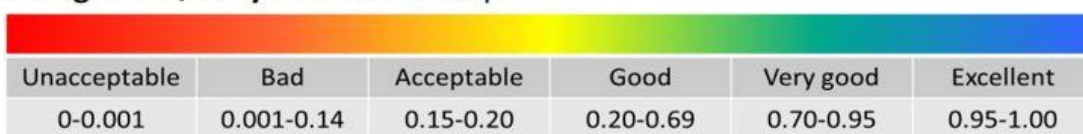


Figure 3.12 - Important Criteria Spectrum (Skewness and Orthogonality).

3.4.3 Solver Settings

Compared with several viscosity models, although the time consumption of the Spalart-Allmaras model is relatively small, it's not accurate. The average wind speed in the UK is about 4-6m/s, and the Reynold number obtained by the wind speed is about 50,000. The k-omega model is not suitable for this simulation because of the larger Reynold number. Although Reynolds Stress equation model is more accurate, the time cost is too high for the simulation of 2D geometry. Finally, for the three k-epsilon, the standard K-Epsilon model was selected, because of its computational accuracy and time consumption. The comparison and description of various viscous models are shown in Table 3-9.

The turbulence intensity was 5%, and the turbulent viscosity ratio was 10. Two monitors (lift coefficient and drag coefficient) were applied to the body. Two models were simulated within the same conditions with 4m/s of inlet boundary velocity.

Table 3-9 - Comparison of Various Viscous Models.

Viscous Model	Description	Characteristic
Spalart-Allmaras	This model is often used in aviation fluid calculations. It is extremely effective for the simple fluid flow with a relatively simple geometry, and because the model is a unilateral model, it can save computing resources.	<ul style="list-style-type: none"> ● Less amount of calculation ● Has a good effect on simple boundary problems ● Calculation results are not widely tested, and the lack of sub-models
Standard k-ε	k-epsilon is the most widely used turbulence model especially in industrial flow computing. It includes three forms: standards k-epsilon model, RNG k-epsilon model, and Realizable k-epsilon model.	<ul style="list-style-type: none"> ● More applications ● Moderate amount of calculation ● Accumulated a lot of data and is very accurate ● The result of complicated flowing simulation such as large curvature is not good
RNG k-ε		<ul style="list-style-type: none"> ● Simulate moderate complex flows such as separation flow, rotation flow, and jet-flow ● Limited by the eddy-viscosity hypothesis
Realizable k-ε		<ul style="list-style-type: none"> ● Similar with RNG k-epsilon ● Better simulate the problem of jet-flow

		<ul style="list-style-type: none"> ● Limited by the eddy-viscosity hypothesis
Standard k- ω	<p>This model is also a two - equation model, which includes two types, standard k-omega and SST k-omega. In the flow computing, it is usually compared with the SA model.</p>	<ul style="list-style-type: none"> ● Better performance for flow of lower Reynolds number ● Suitable for flow with boundary layer separation in reverse pressure gradient ● More amount of calculation
SST k- ω		<ul style="list-style-type: none"> ● Similar with standard k-omega ● Not suitable for free shear flow
Reynolds Stress	<p>It is the typical turbulent model. The eddy-viscosity hypothesis is avoided.</p>	<ul style="list-style-type: none"> ● Higher CPU and time utilization ● Suitable for complex 3D flow

The other simulation solution method setting is set because of balancing the accuracy and saving computational resource, which is shown in Table 3-10.

Table 3-10 - The Simulation Solution Method

Solution Catalogue	Solution Method Used
Pressure-Velocity Coupling	Simple Scheme
Spatial Discretization	Second Order Pressure and Momentum
	First Order Upwind Turbulent Kinetic Energy
	First Order Upwind Turbulent Dissipation Rate
Transient Formulation	Second Order Implicit Option

3.4.4 Validation

Four models are simulated at 4m/s, and their lift coefficients will be compared. The following Figure 3.13 shows the comparison of three models: rectangular, semi cycle and curved plate. The Figure shows the lift coefficient of the three models when the vibrated becomes stable so that it can have a better comparison of the vibration amplitude. It clearly

shows that the curved plate design (yellow line) has a higher lift coefficient. This result is in line with the previous C. Zhou's research results, which also verifies the results of research on the curved plate.

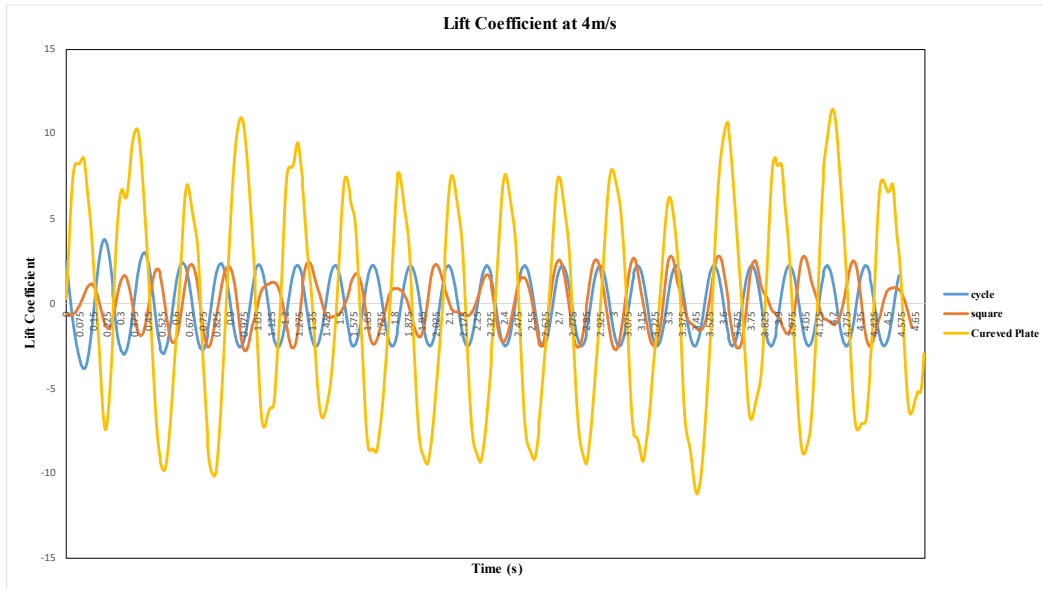


Figure 3.13 - Lift Coefficient of Rectangular, Cycle and Curved Plate at 4m/s.

For better observation, the comparison of the new design (a reverse C shape with a tail) and the curved plate design is shown in Figure 3.14. The blue line represents the lift coefficient of the curved plate, and the orange line is for the new design. The design shows a better response time and has a more significant lift coefficient than the curved plate design at 4m/s. This verification proves that the new design may have better performance and has the value and potential of continuing research. Further detailed simulation research will continue in Chapter 5.

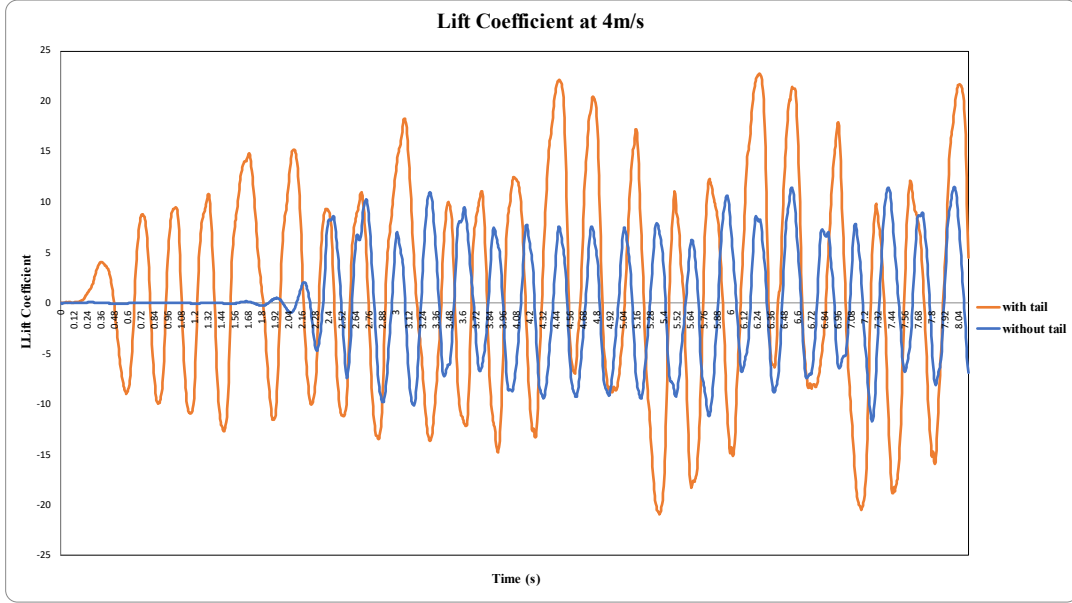


Figure 3.14 - Lift Coefficient of Curved Plate and New Design at 4m/s.

3.5 Mechanical and Electrical Circuit Coupling Equation

The following piezoelectric constitutive equation (Equation 3.1) is utilised to construct the mechanical and electrical circuit coupling equation. where D_3 is the electrical displacement and ε_{33}^T is the permittivity at constant stress.

$$D_3 = d_{31}\sigma_1 + \varepsilon_{33}^T E_3$$

Equation 3.1

The permittivity at a constant strain can be obtained by $\varepsilon_{33}^T = \varepsilon_{33}^S + d_{31}E_p$, and it needs to be used to replace the permittivity at a constant stress when expressing the electrical parameters equation. The voltage across the piezoelectric kit is calculated by $E_3(t) = -v(t)/h_p$. Therefore, the equation of electrical and the permittivity at constant strain can be rewritten as follows.

$$D_3 = d_{31}E_p \varepsilon_1(x, t) - \varepsilon_{33}^S \frac{v(t)}{h_p}$$

Equation 3.2

The following equation (Equation 3.3) can be used to express the average bending strain at time t and position x . After combining Equation 3.2 and Equation 3.3, the piezoelectric constitutive equation can be rewritten, as shown in Equation 3.4.

$$\varepsilon_1(x, t) = -\left(\frac{h_s}{2} + h_p\right) \frac{\partial^2 Z_{rel}(x, t)}{\partial x^2}$$

Equation 3.3

$$D_3 = -d_{31}E_p \left(\frac{h_s}{2} + h_p\right) \frac{\partial^2 Z_{rel}(x, t)}{\partial x^2} - \varepsilon_{33}^S \frac{v(t)}{h_p}$$

Equation 3.4

By integrating the electrical displacement over the piezoelectric area from x_1 to x_2 , the electric charge in the piezoelectric kit can be expressed.

$$q(t) = \int \vec{D}_3 \cdot \tilde{n} dA = - \int_{x=x_1}^{x=x_2} \left(d_{31}E_p \left(\frac{h_s}{2} + h_p\right) B \frac{\partial^2 Z_{rel}(x, t)}{\partial x^2} + \varepsilon_{33}^S B \frac{v(t)}{h_p} \right) dx$$

Equation 3.5

where D_3 is the vector of electric displacement and \tilde{n} is the unit outward normal. And the following equation shows the current generated by the piezoelectric kit.

$$i(t) = \frac{dq(t)}{dt} = - \int_{x=x_1}^{x=x_2} \left(d_{31} \left(\frac{h_s}{2} + h_p\right) E_p B \frac{\partial^3 Z_{rel}(x, t)}{\partial x^2 \partial t} \right) dx - \frac{\varepsilon_{33}^S B (x_2 - x_1)}{h_p} \frac{dv(t)}{dt}$$

Equation 3.6

It can be seen from the above equation that the formula of the current generated by the piezoelectric kit is composed of two parts. The first part is related to the vibration of the cantilever beam, and the second part is related to the voltage across the piezoelectric film. In the second part, the decisive part $(\varepsilon_{33}^S B (x_2 - x_1) / h_p)$ is called the capacitance of the piezoelectric kit, which is connected to the resistance load. So, the second part is related to the performance of the piezoelectric kit itself. The equation of voltage output is expressed as follows, according to Equation 3.6.

$$v(t) = R_L i(t) = -R_L \left[\int_{x=x_1}^{x=x_2} \left(d_{31} \left(\frac{h_s}{2} + h_p\right) E_p B \frac{\partial^3 Z_{rel}(x, t)}{\partial x^2 \partial t} \right) dx + \frac{\varepsilon_{33}^S B (x_2 - x_1)}{h_p} \frac{dv(t)}{dt} \right]$$

Equation 3.7

The above equation can be rewritten as follows.

$$\frac{dv(t)}{dt} + \frac{h_p}{\varepsilon_{33}^S B(x_2 - x_1) R_L} v(t) = - \frac{d_{31} \left(\frac{h_s}{2} + h_p \right) E_p h_p}{\varepsilon_{33}^S B(x_2 - x_1)} \int_{x=x_1}^{x=x_2} \frac{\partial^3 Z_{rel}(x, t)}{\partial x^2 \partial t} dx$$

Equation 3.8

The general mechanical and electrical circuit coupling equation (Equation 3.8) for a cantilevered piezoelectric harvester under transverse vibrations is applicable to the harvesters that are partially or completely coated by piezoelectric films.

3.6 Considerations and Market Analysis

This section provides a multi-faceted analysis of the practicality of the design in this thesis, including considerations of lifespan, cost, and potential competitors.

The design incorporates basic mechanical components and piezoelectric kits with a lifespan of up to 12 years for the piezoelectric kits [127]. However, during the energy harvesting process, the basic structure of the design undergoes continuous vibration. In the experimental phase discussed in Chapter Four, there were instances of fracture in the cantilever beams due to metal fatigue. In practical applications, more robust cantilever beams such as brass or plastic can be used to extend the lifespan of the structure. Additionally, the cantilever beams in the design are easily replaceable as they are fixed to the front structure and piezoelectric kits using screws and adhesives. Therefore, the overall estimated lifespan of the design is 12 years or more.

The cost of typical energy harvesting devices consists of construction and maintenance expenses. For this design, the construction cost mainly includes the structural cost and the cost of the piezoelectric kits. The M-2807-P2 piezoelectric kit used in this thesis has an individual cost of approximately £40, while the LDT0-28K piezoelectric kit cost is cheaper, around £2 per unit [126],[125]. The structural cost, including the circuitry, is approximately £10. Apart from the potential need to replace the cantilever beams in case of fracture, this design has minimal additional maintenance costs. The price of a single cantilever beam is approximately £2 per year.

Lastly, small-scale solar photovoltaic panels appear to be potential competitors. However, solar panels are ineffective during nighttime or in low-light conditions, and typically a combination of wind and solar energy is employed to ensure continuous functionality. The cost of the design is lower than that of small-scale wind turbines, and its structure allows for easy disassembly. The output power of small-scale wind turbines is proportional to the surface area of their rotor [128], and therefore, there is potential for this design to serve as a supplementary energy source to solar photovoltaic panels, replacing small-scale wind turbines.

CHAPTER 4. EXPERIMENT

4.1 Introduction

The reverse C Shape with a tail design model are composed of three aspects: the model's shape, the cantilever beam and the energy collection device (piezoelectric kit). Although the initial simulation verification (chapter 3.4) proves that the design (curved body with tail) may have better performance than other designs, the result still requires experimental verification. And the research on the shape of the design model is also another new direction worthy of research, such as the length of the tail, and the thickness of the curved body. In most energy harvesters' research, selecting cantilever beams is single or fixed. Generally, aluminium cantilever or brass cantilever beams are always selected. But in fact, the material of the cantilever beams has an important effect on the performance of the energy harvester, so the research should also be carried out in the experiment. Finally, as an important part of an energy harvester, the piezoelectric kit transforms mechanical kinetic energy into electrical energy.

In this chapter, the performance of the design will be verified through experiments and optimizing the model based on the performance. The study of the shape of energy harvesters is divided into three parts. First, the effect of the tail will be tested using T series models; after that, the A Series will be used to test the effect of the tail length; finally, the R series models will be tested to verify the effect of the thickness of the curved body. Three series models will be tested in the wind tunnel, respectively. In addition, in this chapter, the experiment will be planned to study the cantilever beam of the energy harvester to verify the effect of the cantilever beams of different materials on the energy harvester. Finally, the energy harvester relies on the piezoelectric kits on the cantilever beam to harvest energy. Therefore, the selection of the piezoelectric kits is also critical. At the end of this chapter, different piezoelectric sheet will be studied, so that the most suitable piezoelectric kits will be determined through this study.

4.2 Effect of Tail

4.2.1 Experimental purpose and requirements

The main difference between new design and existing design is to add tails to the curved body. This section will verify the effectiveness of the new design and analyse the performance of new design through experiments. As the first experiment, the T series model will be used for experiments. The parameters of two models (T1 and T2) of the T series are similar. Except for the T2 model, the tail structure of 22.75mm is added behind the curve body. The comparison of the T1 and T2 models mainly evaluates through the three aspects of lift force, vibration frequency and voltage output. The experiment's main purpose is to verify whether the new design can improve the performance of the energy harvester at different wind speeds in order to prepare for subsequent experiments.

4.2.2 Experimental Device and Setup

The lift force data of the experiment will be collected by the force sensor, and the voltage output data will be collected by an oscilloscope. After the experiment, the parameters of new design models will be further studied. Therefore, in this experiment, only the voltage output of the T series models is collected and analysed, and the energy output of the models will be studied in the subsequent section.

The initial plan was to test the model at a wind speed of 1-10m/s, but in the experiment, it was found that because the front curved body surface of the T series models was very thin, only 1mm. The experiment at a higher wind speed can easily cause the model structure to break, thereby damaging the wind tunnel. The average wind speed of the UK is about 4-6m/s, so in this and subsequent experiments, the experimental wind speed is set to 3m/s-7m/s. In addition, in order to fix the cantilever beam on the transducer, a mounting interface plate has been designed and made by a 3D printer (Figure 4.1). However, due to the limitation of the transducer below, a screw hole for fixing the mounting interface plate and transducer is located below the cantilever beam. Therefore, it has to be checked before the experiment to prevent experimental error caused by the connection between the screw and cantilever beam due to gravity reasons.

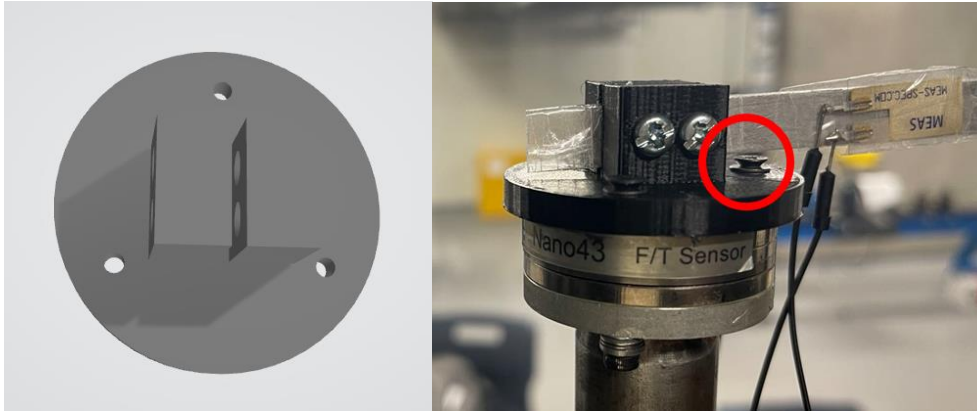


Figure 4.1 - A Mounting Interface Plate for Connecting Transducer and Cantilever Beam.

The experimental setup steps are listed as follows.

- Fix a mounting interface plate on the Nano 43 transducer.
- place and glue the piezoelectric kit (LDT0-028K) on the end of an aluminium cantilever beam.
- Use two screws to fix the end of the cantilever beam to A mounting interface plate to ensure the cantilever beam's fixing.
- Use a screw to fix the model to the other end of the cantilever beam.
- Connect the piezoelectric kit with two oscilloscope probes.

4.2.3 Experimental Steps

- Make sure the model is in a stable state, and the cantilever beam is not contacted with a mounting interface plate except for two screw fix points.
- Open the wind tunnel and set the wind speed to 3m/s.
- After 10-20 seconds, wait for the vibration amplitude to stabilize, open the Nano 43 sensor and the oscilloscope, and record the force data.
- Record the data for 10 seconds and stop recording.
- Turn off the wind tunnel, save the data, repeat the first step of the operation, and adjust the wind speed to 4ms, 5m/s, 6m/s, and 7m/s respectively in the following repeat experiments.
- Process data to obtain the frequency of vibration, the average lift force, and the voltage output of each model.

4.2.4 Experimental results and Phenomenon

The T series models were placed at a 3m/s-7m/s of wind speed for experiments. The figure below (Figure 4.2) is the lift force curve chart of the T series models at the wind speed of 5m/s. The lift force curve of the T1 and T2 models is roughly a sine wave shape, but there are some minor fluctuations in the curve. On the one hand, these fluctuations may be caused by turbulence in the airflow, on the other hand, the T1 model is more unstable during vibration because of its lighter weight. When calculating the lift force value of each model, multiple peak points will be selected to calculate the average lift force of its model. The vibration frequency of the models can also be calculated through the lift force curve. At a wind speed of 5m/s, although the peak lift force of T2 is higher than the T1 model, its frequency is slightly smaller than the T1 model.

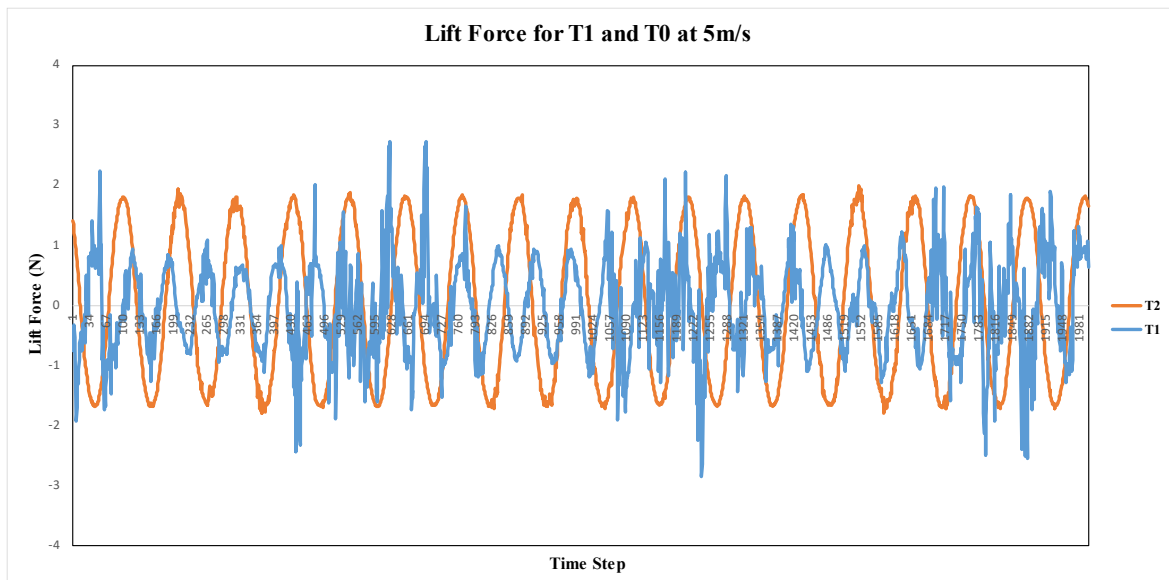


Figure 4.2 - Lift Force for T1 and T0 at 5m/s.

Compared with the T1 model, the T2 model has a 22.75mm tail structure. The ratio of the tail length and the diameter of the curved surface is 0.65. It can be seen from Figure 4.3 that the peak lift force of the T2 model has been higher than the T1 model within the range of 3m/s to 7m/s. Figure 4.4 shows the RMS voltage generated by the two models under the test wind speed. Although the vibration frequency of the T1 model is higher than the T2 model, due to the huge gap between the vibration amplitude, the voltage generated by the T2 model is much higher than the T1 model. It is worth noting that as the wind speed increases, the slope of the voltage generation curve for the T2 model is greater than the

slope of its lift force curve. This is since the rate of frequency decrease for the T2 model is smaller than for the T1 model. From the results of the test wind speed, it can be predicted that as the wind speed increases, the voltage gap between the T2 model and the T1 model will become larger and larger.

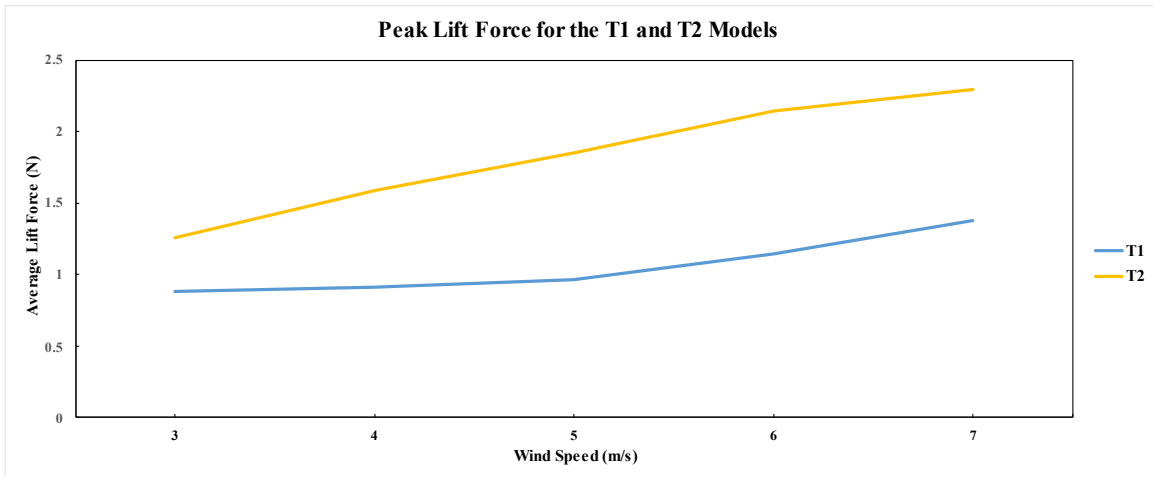


Figure 4.3 - Peak Lift Force for the T1 and T2 Models.

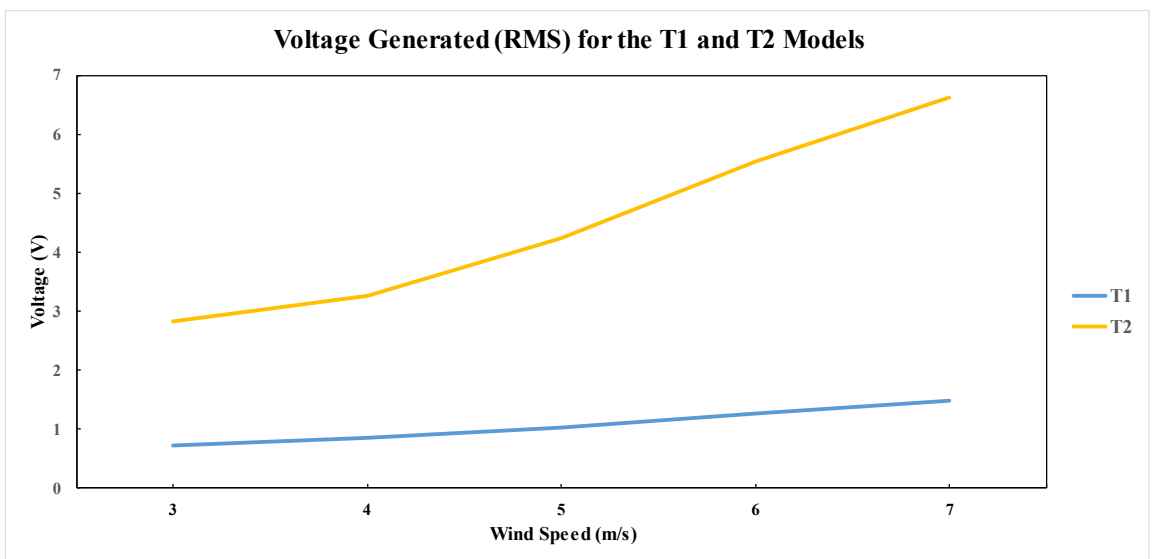


Figure 4.4 - Voltage Generated (RMS) for the T1 and T2 Models.

4.2.5 Conclusion

The new models have shown good performance from the voltage generated and lift force values. Especially at the wind speed of 7m/s, the lift force of the T2 model is about twice the T1 model, and the voltage generated by the T2 model is almost 5 times the T1 model. In addition, it can be seen from Figure 4.2 that although the lift force curve of the T1 model

basically presents a sine wave shape trend, there are obvious fluctuations in the curve compared with the T2 model. The experimental observation also shows the T1 model is accompanied by more small-range vibration in the vibration process, and the T2 model is more stable.

The lift curve is recorded by the force sensor. The larger the vibration amplitude (bending angle), the larger the sensor displays the lift. The piezoelectric kit is placed on the cantilever beam, and its voltage generated is directly related to the amplitude and frequency of vibration. Although the vibration frequency of the T2 model is lower than the T1 model, and the lift of the T2 model is higher than the T1 model in the experiment, the T2 voltage generated by the model is much higher than the T1 model. Therefore, it can be concluded that in this model, the vibration amplitude has a greater impact on the voltage.

Finally, by comparing the voltage-generated curve in this experiment with the previous research data, although the two experiments use different piezoelectric kits, which causes the voltage generated to be different, the voltage-generated curve trend is roughly the same. In summary, through this experiment, the effectiveness of the model is proved.

4.3 Effect of Varies Tail Length

4.3.1 Experimental Purpose and Requirements

After verifying the effect of tail design on the performance of design, the effect of tail length on performance will be studied. The experiment aims to study the relationship between tail length and the performance of the piezoelectric energy harvester design. The performance can be determined by lift force and power output. The initial plan was to lengthen the tail of the model, and after printing through a 3D printer, the effect of the tail of different lengths was tested respectively. So, the R series was designed according to the experiment demand. In order to better observe, the inter diameter of the front curved surface of the R series model has been increased from 35mm to 40mm; the model width has been increased from 100mm to 150mm, and other parameters remain unchanged compared with the T series. The R series is planned to design five models. Their tail length (L) is set to 10mm, 20mm, 26mm, 30mm, and 40mm, which correspond to the ratio of tail length to the curve inter diameter (0.25, 0.5, 0.65, 0.75 and 1) as shown in Figure 4.5.

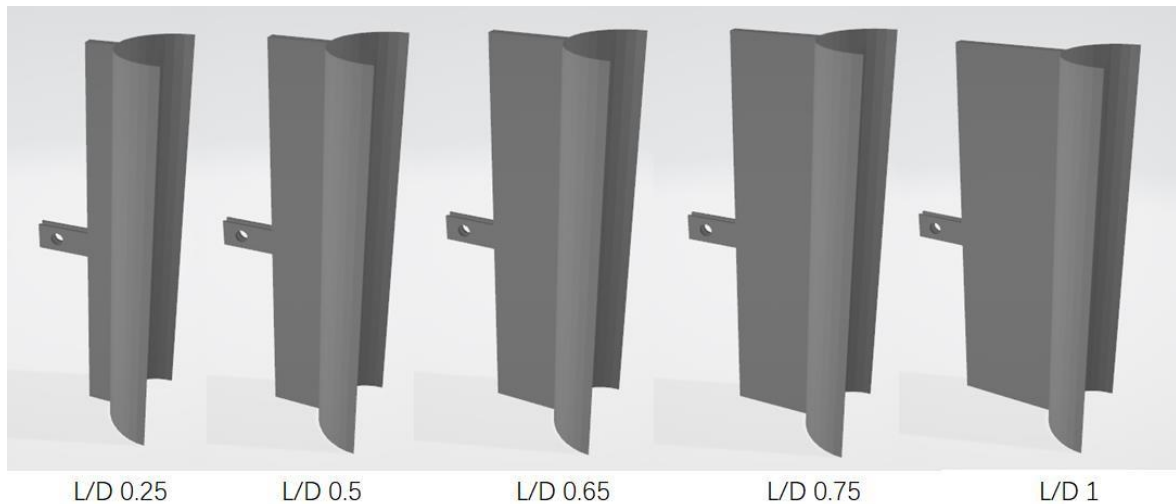


Figure 4.5 - R Series Models Design.

R series was printed by a 3D printer; however, several models of the R series were not successful in being printed due to the thickness of their front curved being too thin. The 3D printer is printed layer by layer by melting plastic. The thickness of the front curve surface of the model is only 0.5mm, so it could only print a layer of materials when it was printed. This leads to the low strength of the curved part. In addition, if the thickness is large enough, even if an error occurs when printing a certain layer, the structural impact by error will be relatively small as other layers continue to cover. However, an error will affect the entire structure if the thickness is only a layer. Eventually, the three models of the R series were broken or damaged, etc., and could not continue the experiment as shown in Figure 4.6. There were only the R1 (L/D 0.75) and R2 (L/D 1) models survived.

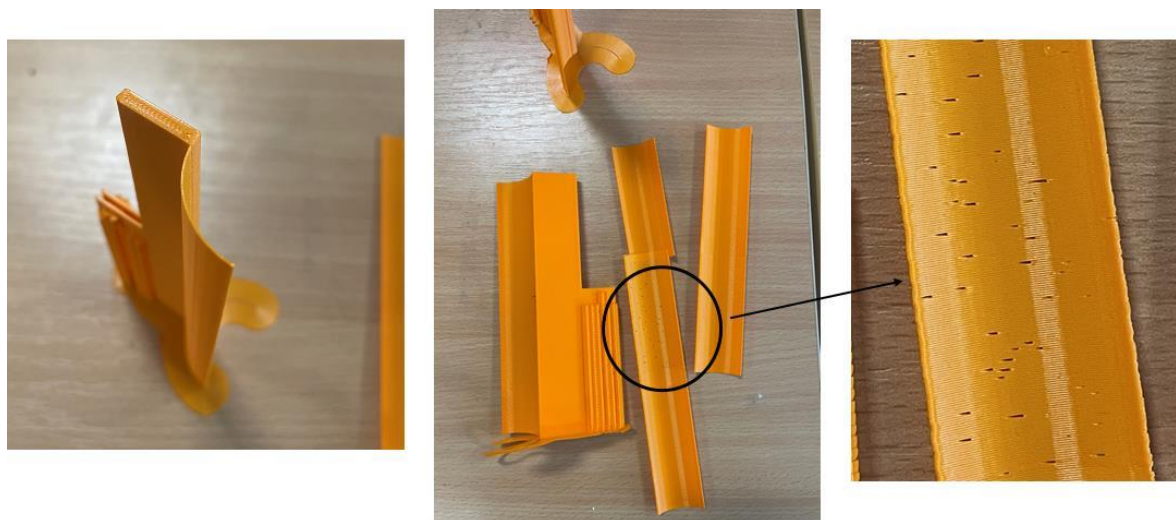


Figure 4.6 - The Broken R Series Models.

Therefore, the A series has been designed and made according to the parameter of the R series except for increasing the thickness of the front curve. The curve's inter diameter is the same as the R series; the outer diameter increased from 41mm to 44mm. Compared with other series, its structure is very stable, as shown in Figure 3.2.

4.3.2 Experimental Device and Setup

The performance of the energy harvester will be evaluated by the lift force and power output. In order to reduce the error caused by the model's weight, the model will be vertically fixed at a mountain point. The model was expected to swing left and right when the wind passed through it. The lift will be collected through the Nano 43 sensor. In terms of power output, the oscilloscope will be used for energy harvest. However, the voltage probe and external resistance will be used due to the high price of the current probe. The two voltage probes can be collected the voltage drop through external resistance, and the power output data is obtained after calculating. The experimental setup steps are listed as follows.

- Fix a mounting interface plate on the Nano 43 transducer.
- place and glue the piezoelectric kit (LDT0-028K) on the end of an aluminium cantilever beam.
- Use two screws to fix the end of the cantilever beam to A mounting interface plate to ensure the cantilever beam's fixing.
- Use a screw to fix the model to the other end of the cantilever beam.
- Connect the piezoelectric kit with two oscilloscope probes.

Experimental setups are shown as follows in Figure 4.7.

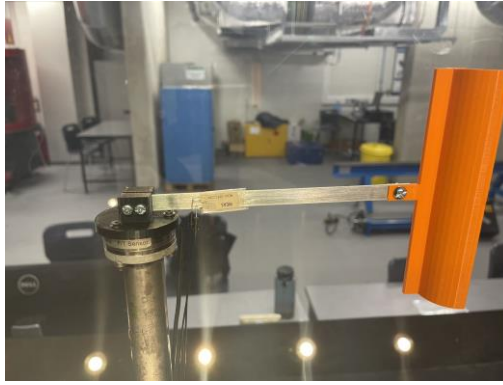


Figure 4.7 - Experimental Setups for A Series Models.

4.3.3 Experimental Steps

The experiments are divided into three stages. Testing the lift force of each model in the first stage. Testing the response time of each model in the second stage. In the last stage, the power output of each model was tested. These three stages of testing will be carried out in order, and the test results of three stages can be verified with each other to reduce experimental errors. In addition, data analysis will be performed after the experiments at each stage. If the data has obvious errors, the experiments can be adjusted in time to avoid waste of time and experimental equipment.

4.3.3.1 First Stage: The Lift Force

- Make sure the model is in a stable state, and the cantilever beam is not contacted with a mounting interface plate except for two screw fix points.
- Open the wind tunnel and set the wind speed to 3m/s.
- After 10-20 seconds, wait for the vibration amplitude to stabilize, open the Nano 43 sensor, and record the force data.
- Record the data for 10 seconds and stop recording.
- Turn off the wind tunnel, save the data, repeat the first step of the operation, and adjust the wind speed to 4ms, 5m/s, 6m/s, and 7m/s respectively in the following repeat experiments.
- Process data to obtain the frequency of vibration, and the average lift force of each model.

4.3.3.2 Second Stage: The Power Output

- Make sure the model is in a stable state, and the cantilever beam is not contacted with a mounting interface plate except for two screw fix points.
- Check the connection between the oscilloscope and the piezoelectric sheet and the external resistance
- Open the wind tunnel and set the wind speed to 3m/s.
- After 10-20 seconds, wait for the vibration amplitude to stabilize, open the oscilloscope, and record the voltage data.
- Record the data for 5 seconds and stop recording.
- Turn off the wind tunnel, save the data, repeat the first step of the operation, and adjust the wind speed to 4ms, 5m/s, 6m/s, and 7m/s respectively in the following repeat experiments.
- Calculate the data of the two probes and calculate the power output through voltage drop and resistance.

4.3.4 Experimental Results and Phenomenon of the A Series Models

The first stage of the A series (the lift force test) was performed at the wind speed of 3m/s, 4m/s, 5m/s, 6m/s, and 7m/s, respectively. The experimental results of it at 6m/s are shown in the Figure 4.8 below. The lift curve is not smooth at some points, because the force sensor (Nano 43) is very sensitive. It is also worth noting that the positive and negative of the force sensor value represents the different directions, but the curve does not keep it symmetrically on both sides of the X-axis. For example, the A3 model in this figure (Gray line) has an average minimum value of 0.986 and an average maximum value of 12.794. The minimum value of its lift force is still positive. If the value is accurate, this means that when the A3 model is tested, it always only bends to one side, which cannot happen obviously in reality.

It can be found that the five curves show a downward trend when comparing the peak lift force of all A series models at different wind speeds. The values of all five models go down at 7m/s. VIV phenomenon always occurs at cylindrical objects, and the amplitude and lift force will go down after the wind speed exceed the "Lock-in region". The design is a typical

galloping structure (with a sharp angle); however, its curve is not a normal galloping phenomenon.

In addition, the peak lift force of the A1 model is relatively high at different wind speeds, but the long-tail model, A4 and A5 models show lower peak lift force at different wind speeds.

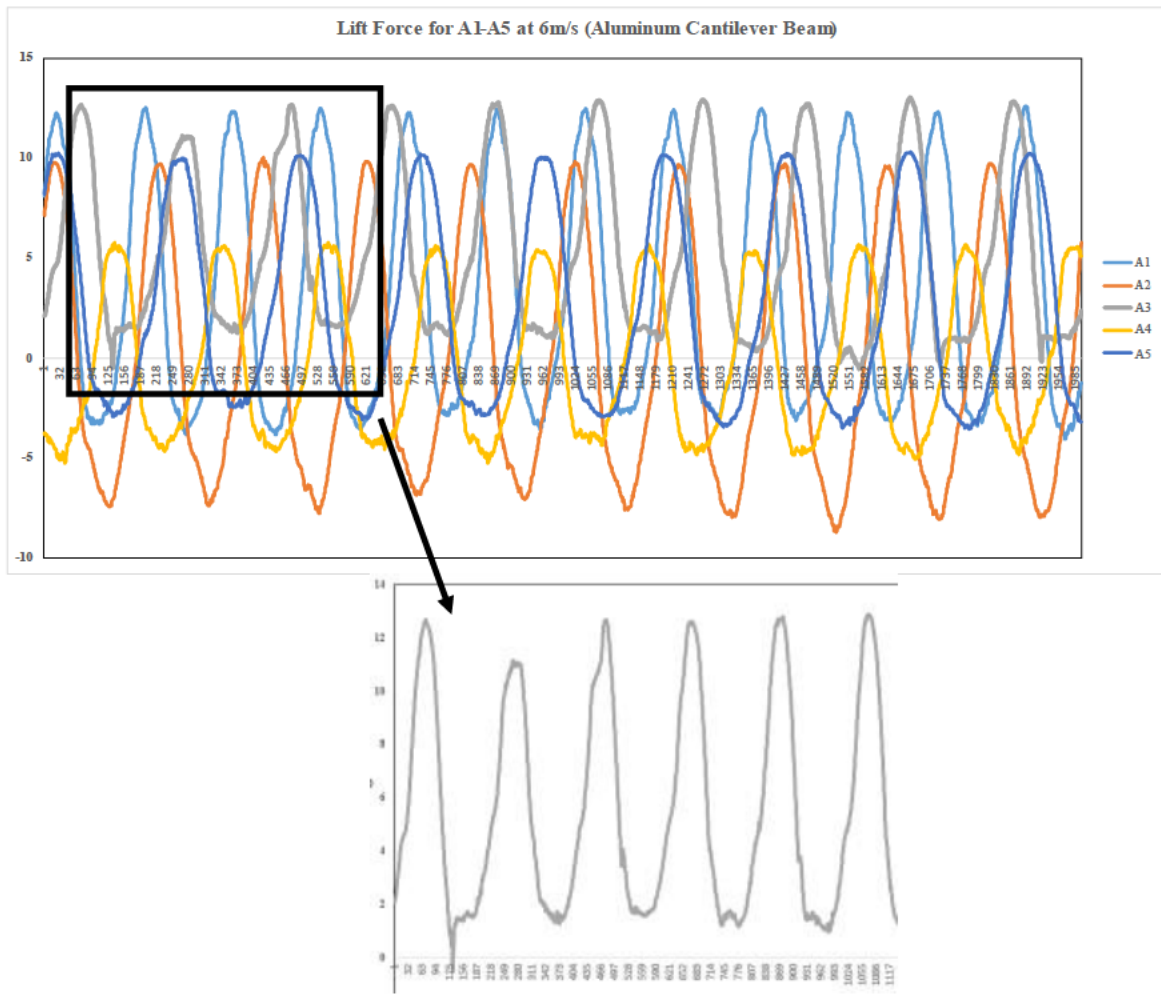


Figure 4.8 - Lift Force for A1-A5 at 6m/s.

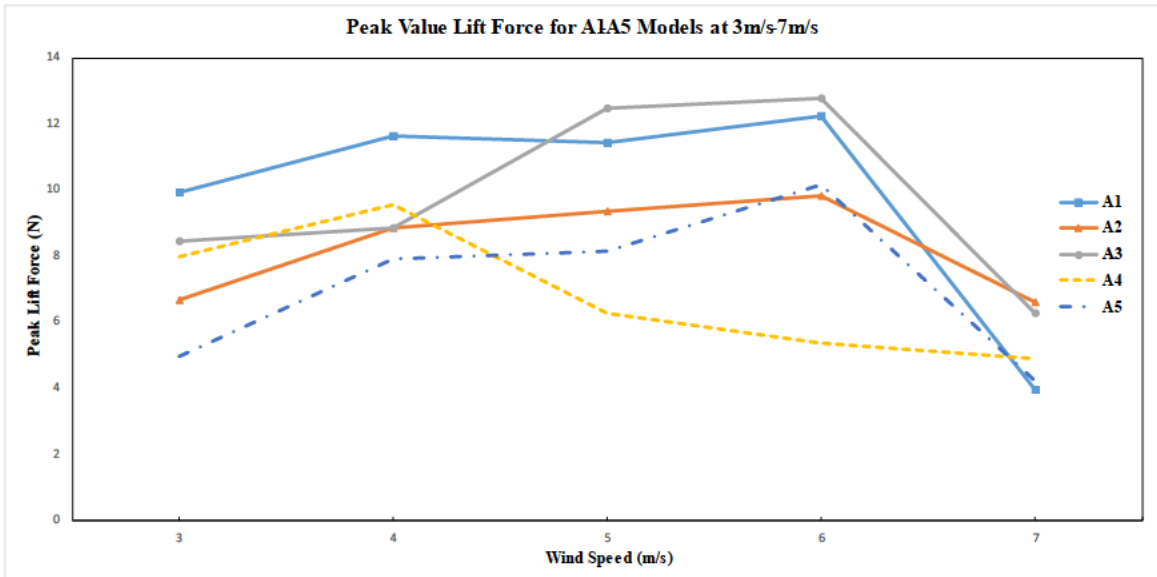


Figure 4.9 - Peak Value of Lift Force for A1-A5 Models at 3m/s-7m/s.

In order to exclude the error of direction determination caused by the force sensor, the force data of five models has been re-analysed. By adding the average peak value and the average deepest value of each model, the average lift force of each model at different wind speeds is calculated as shown in Figure 4.10.

The average lift force diagram of the A series models at different wind speeds (Figure 4.10) does not show visible differences with the peak value of the lift force. It can be seen that at 7m/s, the five curves still show a downward trend. Even if the data of 7m/s is removed, compared to other models, the A1 and A3 models are relatively higher at 3-6m/s at 3-6m/s, but their curves have always displayed fluctuations. The A2 model has shown a rising trend with the period, and the A4 and A5 models still maintain a lower lift force at various wind speeds.

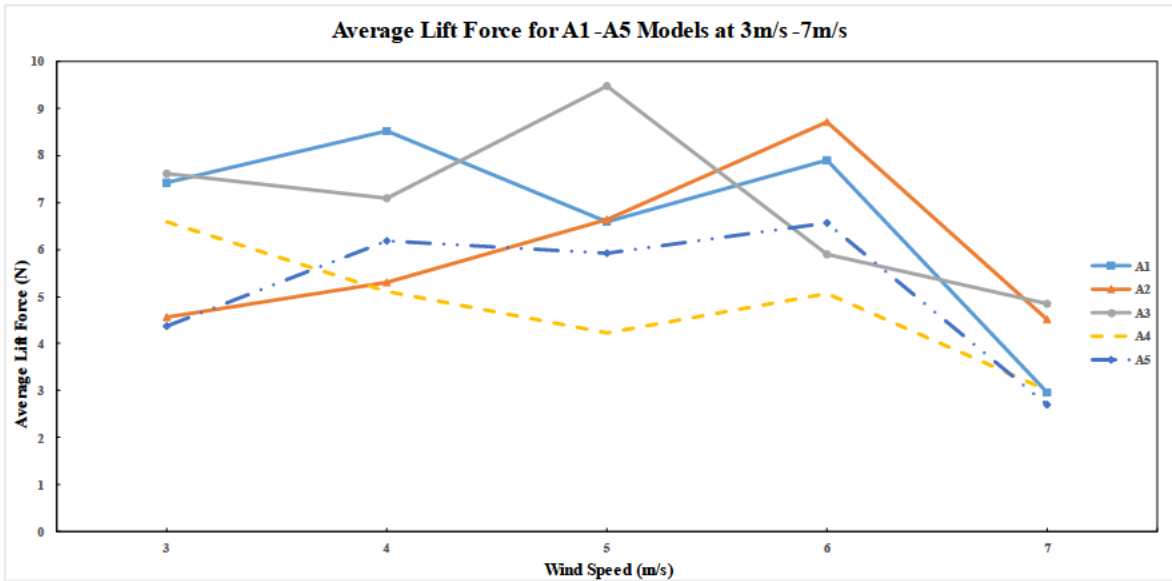


Figure 4.10 - Average Lift Force for A1-A5 Models at 3m/s-7m/s.

Due to the gravity of the front models and the continuous vibration, the cantilever beam finally broke at the end, as shown in Figure 4.11 a below. For obtaining accurate experimental results, in the experiment of the A series models, the experimental order was to test the five models under the same wind speed first, then adjust the wind speed, and test again. It ensures that the state of cantilever beams is roughly consistent when testing each model at the same wind speed. Therefore, in the subsequent tests, especially at the wind speed of 7m/s, the cantilever beam broke, so the lift force declined. And the cantilever beam is in contact with the screw of a mounting interface plate after the cantilever is broken, resulting in an asymmetric lift force curve of the model.

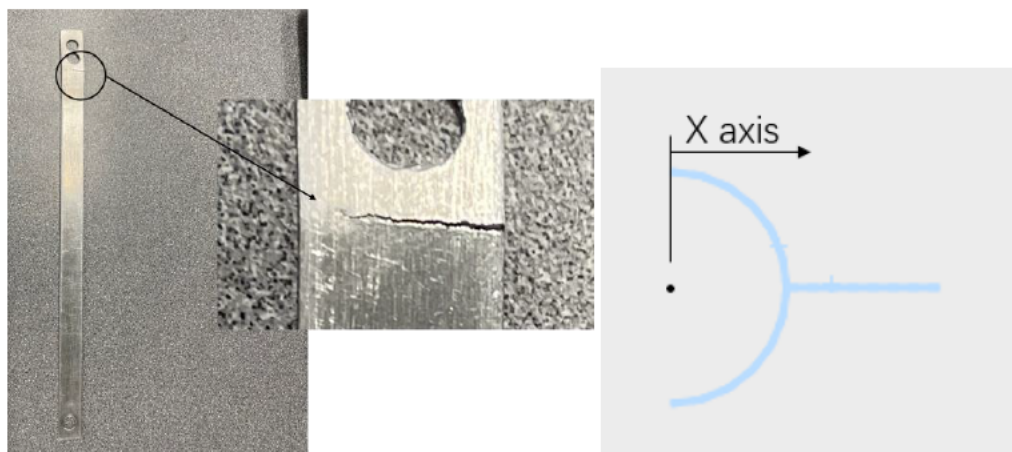


Figure 4.11 – (a) Broken Cantilever Beam (b) The A Series Model X Axis Schematic Diagram.

Due to the abnormal data when the wind speed is 7m/s, a broken cantilever beam is found in the inspection experimental equipment. Although in the experiment with a wind speed of 3-6m/s, a small break may have already happened in the cantilever beam, the general trend of the lift force of each model should not be greatly affected. Compared with the A4 and A5 models, the A1-A3 models have a relatively large lift force; however, it was observed that the vibration amplitude of the A5 model was significantly larger than the others during the experiment. The Nano 43 force sensor will show higher lift force when the bending angle is larger for the same model. The A series models have been re-analysed, because of the problem of inconsistency between phenomena of observation and obtained data.

One end of the cantilever beam was connected to the front model, and the other end was connected to the Nano 43 force sensor. Therefore, the force of the front-end model is transmitted to the Nano 43 force sensor through the cantilever beam, and the sensor will decompose the torque into the force in all directions. According to the equation of moment of force, under the action of the same force, the longer the distance between the front-end model and the sensor, the greater the torque obtained by the sensor. The fixed point of the A series models, and the cantilever beam is behind the tail, which means that the longer the tail, the longer the length of the torque distance. However, in the actual situation, the torque distance should be the length from the centre of gravity of the front-end model to the force sensor.

Solidworks could be used to check the parameters of the models, and the gravity point of the A series models are shown in Table 4-1 below.

Table 4-1 - Gravity Point of the A Series Models.

Model No.	Gravity Point: X axis (mm)
A1	20.573
A2	26.005
A3	29.145
A4	31.213
A5	36.336

The high value of gravity points means that the model's centre of gravity is more backward, which means a shorter torque distance as shown in Figure 4.11 b. It is clearly seen that the torque distance of the A5 model is about 16mm shorter than the A1 model. If the same force is applied horizontally at the front-end of the A1 and A5 models, the force sensor will display that the force applied for the A5 model is smaller than the A1 model. This is why the A1 model's lift at different wind speeds is greater than that of the A5 model.

4.3.5 Experimental Results and Phenomenon of the S Series Models

In order to be able to compare the effect of the tail length on the model performance more clearly, the A series model needs to be improved. The main problem of the existing A-series models is that the connection point with the cantilever beam is located behind the tail, which means that the overall length of the model with a longer tail is also longer. And for the model tail part, its weight is heavier than the front-end model, so its centre of gravity point will be moved a lot for the model with the longer tail. In order to improve the problem of the A series model, the S series model was designed as shown below based on the A series model (Figure 4.12).

The S series models were improved according to the A series model, so their parameters are roughly the same. The curved diameter and width of the two series models are the same, and the tail length of the S1-S5 model is the same as the tail length of the A1-A5 model. At the same time, in order to better verify the effect of the design on the experiment, the S0 model without a tail is added to the S series model. The curved diameter and width of the model are consistent with other S series models. The S series model mainly improved the position of the connection point with the cantilever beam and moves the connection point from behind the tail to the curved surface. This means the models of this series are the same in total length, regardless of the length of the tail. And due to the existence of cantilever beams, the cantilever beams will be filled in the vacancy in the middle of the S3, S4 and S5 model tails, so the vacancy will not have a great impact on the aerodynamic force of the structure as shown in Figure 4.13.

In addition, the aluminium cantilever beam was produced. In order to prevent the cantilever fracture again, the overall equipment would be checked after every five experiments to ensure that each experimental piece of equipment was in good condition.

At the same time, the lift force data of the Nano 43 force sensor would also be checked to determine whether the image is symmetrical on both sides of the x-coordinate axis.



Figure 4.12 - The S Series Models.



Figure 4.13 - Experimental Setup for S Series Models (Aluminium Cantilever Beam).

The S series was tested in the wind tunnel. At 3m/s, the curve of the S2-S5 model is a sine wave shape symmetrical in the X-coordinate axis. However, the S0 and S1 models have always maintained a small vibration in the test, and the vibration phenomenon is similar to buffeting vibration.

Taking the S0 model and the S5 model at 3m/s as an example as shown in Figure 4.14, the S0 model has maintained a small vibration, and it can be seen from the lift curve. Although its vibration is not a sine wave shape, it can still be seen that the curve can be divided into several stages. In each stage of the vibration of the S0 model at 3m/s, the vibration starts with a small amplitude vibration, and then the vibration becomes a large high-frequency vibration. The time of high-frequency vibration is about twice the small vibration, and then, the small vibration is repeated again. The lift curve of the S0 model shows this shape within the experimental wind speed (3m/s - 7m/s), except the curve fluctuations continue to increase. The lift curve of the S1 model is similar to the S0 model, but after the wind speed exceeds 5m/s, the curve gradually becomes a sine wave shape. The lift force curve of the S0 and S1 models are different from the lift curve of the T0 and T1 models, and the result will be discussed in the next section.

Compared with the S1 model, the lift curve of the A5 model is obviously a standard sine wave shape. Although the lift curve is not completely smooth at some points, it may be caused by the excessive sensitivity of the Nano 43 force sensor and the turbulence in the fluid. S2, S3, and A4 model curves are also similar to the S5 model, which is a sine wave.

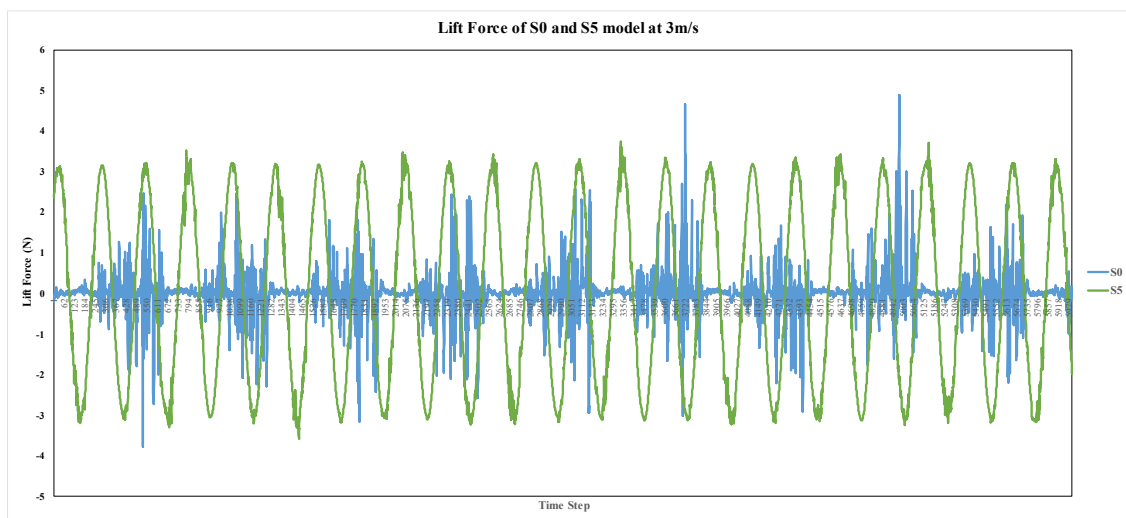


Figure 4.14 - The Lift Force of the S0 and S5 Model at 3m/s.

The peak lift force of the S series model is calculated, as shown in the figure below. It can be clearly seen that the lift force curve is roughly consistent with the observation results. The S5 model has been found that it had a large vibration amplitude in the observation, and the force sensor displayed that the S5 model has the highest lift force value at the

experimental wind speed. The lift force of other models of the S series is reduced in turn according to the length of the tail. The S0 model's lift force is the lowest.

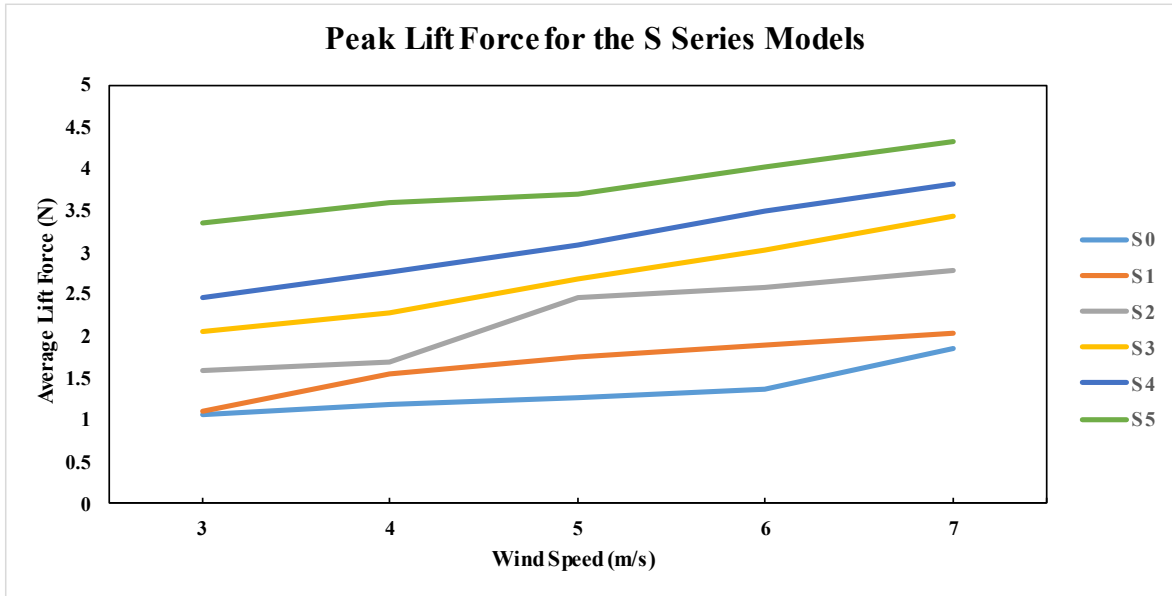


Figure 4.15 - Peak Lift Force for S Series Models.

The piezoelectric kit is fixed on the cantilever beam, and in addition to the vibration amplitude that affects the power output, the vibration frequency can also affect the power output of the piezoelectric kit. The average vibration frequency of the S series models can be obtained from the data of the force sensor. It can be clearly seen that the vibration frequency is generally inversely proportional to the tail length, except for the S1 and S0 models, as shown in Figure 4.16. The frequency of the S1 model rises significantly after the wind speed reaches 5m/s, which also corresponds to the lift force curve of the S1 model. When the wind speed is 6m/s, the vibration frequency of the S1 model exceeds the S2 model, and its vibration frequency becomes the highest in the S model. The S0 model has always maintained a lower vibration frequency under the wind speed of testing. The frequency of the S0 and S1 models differs from that of the T0 and T1 models. This phenomenon will be discussed in the next section.

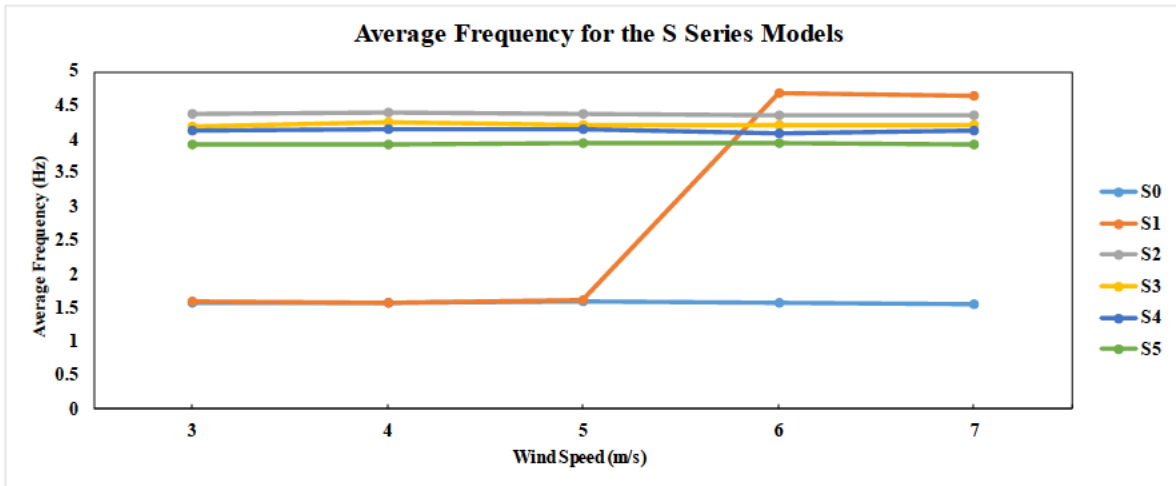


Figure 4.16 - Average Frequency for S Series Models.

In this experiment, the following phenomena can be found through observation:

- At the same wind speed, the model with a long tail length has a shorter response time and can start a stable vibration with consistent amplitude faster.
- For the same model, the larger the wind speed, the faster the model starts to have consistent amplitude.

Due to the limitation of the experimental equipment, the phenomena will also be examined through the simulation results of the subsequent Chapter 5.

The S series model is tested for the voltage output by the oscilloscope. It can be seen from the voltage output chart that the voltage output curve is similar to the lift force curve, where the S5, S4, S3 and S2 models are similar to their lift force curve trends. In addition, the voltage output curve of the S1 model is very different from the lift curve. After 4m/s, it gradually increases, and it can be seen that the growth rate is higher than the other S series. Finally, due to its lower lift force and vibration frequency, the S0 model's voltage output is the lowest in the S series model at the entire experimental wind speed. It is worth noting that in the section of the effect of the length of the tail on the energy harvester, the LDT0-028K piezoelectric kit was selected to be used, so the voltage output value is lower. The research on the effect of different piezoelectric kits will be discussed in section 4.6.

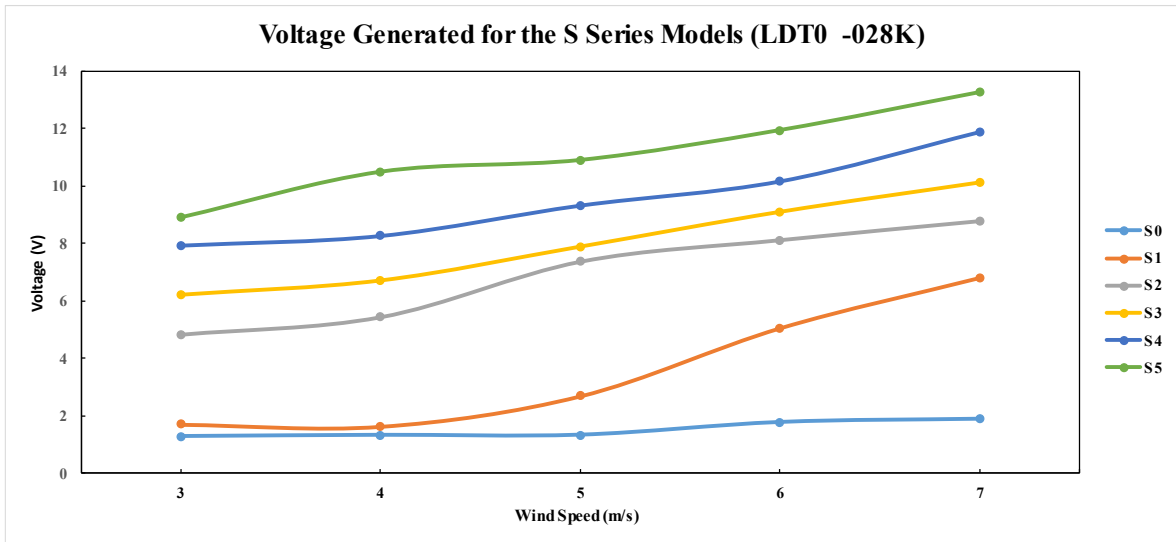


Figure 4.17 - Voltage Generated for the S Series Models.

Due to the expensive price of the oscilloscope current probe, the two voltage probes and an external resistance are used in this experiment. The voltage drop at both ends of the resistance is to calculate the circuit current, thereby calculating the power output of the piezoelectric kit. C-F Zhou etc., have studied the effect of external resistance on circuit power output[105]. The article proposed that when the external resistance value is greater than 820K ohms, the power output of the circuit becomes stable and is no longer affected by wind speed changes. Therefore, in this experiment, 1M Ohm external resistance was used. As shown in Figure 4.18, the external resistance is placed in a white box and connected to the piezoelectric kit, and the other end is connected to the two voltage probes.

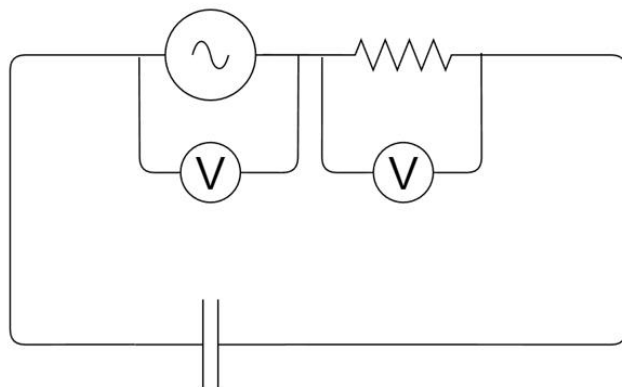
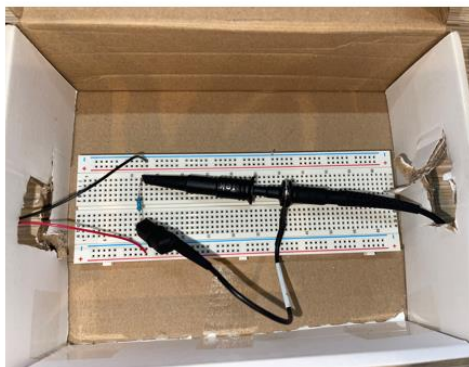


Figure 4.18 - The External Resistance Box.

The output power curve and the voltage generated curve trend is roughly the same. After calculation, as shown in the table below, the maximum output power of the A5 model can reach 175.48 μ W at a wind speed of 7m/s. Compared with previous studies, the power output of the A0 model is less than previous studies; however, the piezoelectric kit used is different. The power output of A0 will be compared in the subsequent section by using the same piezoelectric kit.

Table 4-2 - Power Output for S Series Models with Aluminium Cantilever Beam and LDT0-28K Piezoelectric Kit.

Power output (μ W)					
	3m/s +/- 0.01	4m/s +/- 0.01	5m/s +/- 0.01	6m/s +/- 0.01	7m/s +/- 0.01
A0	1.62	1.73	1.75	3.13	3.54
A1	2.86	2.63	7.18	25.50	46.32
A2	23.18	29.44	54.21	65.86	77.10
A3	38.74	45.15	62.31	82.78	102.37
A4	62.79	68.20	86.72	103.07	140.83
A5	79.35	109.97	118.70	142.36	175.48

4.3.6 Discussion

The experiment was initially used in the A-series models. Because the torque distance of the A series models was significantly different, the data collected by the force sensor did not have comparativeness. Therefore, the S series was designed on the basis of the A series models, and the S0 model with a tail length of 0 was added to the S series models. There are two models of T1 and T2 in the T series models. The tail length and the curved body's diameter are 0 and 0.65, respectively. This ratio corresponds to the S0 and S3 models in the S series models. Although the cross-sectional area of the S series model is larger than the T series, the lift curve trend of the two series models can still be compared.

Compared with the S3 model, the lift force and voltage output of the T2 model in the experimental wind speed are less than the S3 model. This should be caused by the cross-section area of the T2 model being less than the S3 model. However, it is worth noting that in the T-series model experiments, the frequency of the T1 model is greater than the T2 model. This phenomenon can also be found in the experiment of the S series model. For the S2-S5 model, as the length of the tail increases, the vibration frequency is decreased, whereas the S0 and S1 models are different. The S1 model's frequency is rapidly rising and higher than the S2 model when 6m/s of the wind speed. The vibration frequency of the S0 model has always been the lowest model in the S series model.

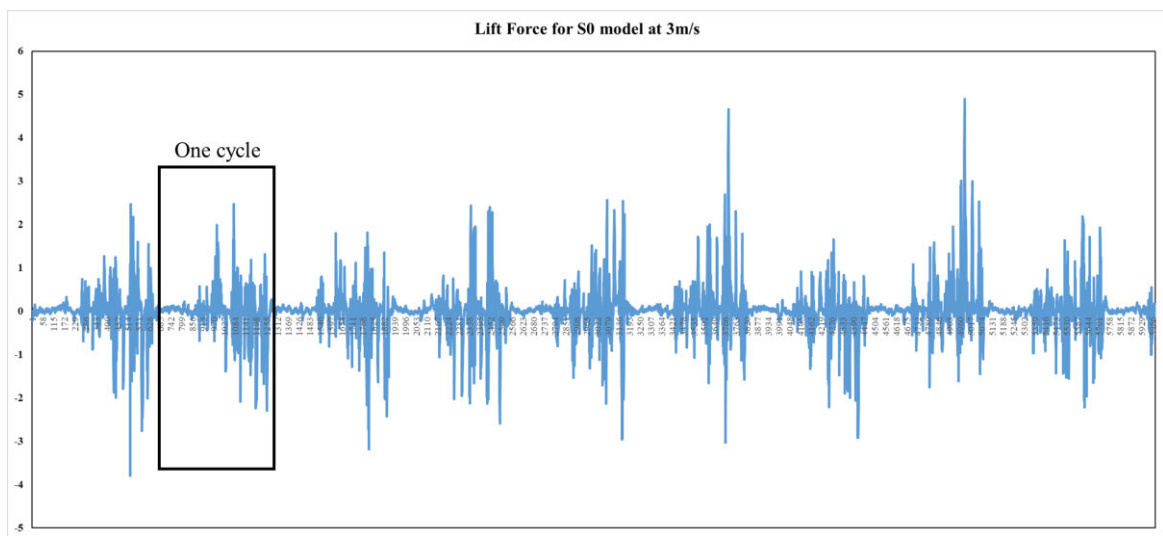


Figure 4.19 - Lift Force for S0 model at 3m/s.

By observing the lift force data of the S0 and S1 models (Figure 4.19), it can be found that the lift force curve of other models presents a sine wave shape trend, as is the same as the lift force curve of the T1 and T2 models. However, the lift curve of the S0 model shows a small vibration trend, as shown in Figure 1. The vibration of the S0 model consists of several cycles. Each cycle can be divided into two stages. The first stage is a small high-frequency vibration, and the S0 model saves energy in this stage. Then it enters the second stage and starts to consume energy to vibrate with a larger amplitude.

Compared with the T1 and S0 models, the T1 model has a smaller cross-sectional area and curved body thickness, which causes the T1 model to be lighter than the S0 model, which means that the T1 model is closer to its natural frequency, and it is easier to make a stable same amplitude vibration. Because the S0 model presents cyclical vibration, its frequency

can only be calculated by cyclical. Therefore, the calculated frequency is lower than the other models.

4.3.7 Conclusion

In general, the effectiveness of model design has been further verified through experiments in this section. And in the case of the ratio of tail length and curved body diameter from 0 to 1, the longer the length of the tail, the higher the voltage output and power output of the model, and the higher the lift, but the lower the vibration frequency. At the wind speed of 7m/s, the power output of the model (S5 model) is 175.48 μ W, while the S0 model is only 3.54 μ W. And through observation, the model with a larger tail length has a shorter response time, which means it can start to maintain the same amplitude stable vibration more quickly. However, the impact of the response time on power output needs to be future studied.

And through the experiments in this section, it can also provide suggestions for the selection of the cantilever beams of the design. The selection of cantilever beams should consider their material strength. Once the cantilever is broken due to fatigue, it will greatly affect the energy output. The power output can be used to determine the status of a cantilever beam in a future test.

4.4 Effect of Thickness of the Curved Body

4.4.1 Experimental Purpose and Requirements

The R series models were originally designed to compare with the T series models, but because their curved body is thinner, three models of the five models have not been printed successfully. The remaining two models, R1 and R2, their curved body thickness is different, but the ratio of the tail length and the diameter of the curved body is the same as the S4 and S5 models. Therefore, the R1 and R2 models can be tested and compared with the S4 and S5 models to study the effects of curved body thickness on energy output.

However, the connection between the two models (the R series models) and the cantilever beam is at the back end of the tail, and the connection point for improved S series models is located at the curved body back end. Therefore, the force sensor cannot be effectively

used to compare the two sets of data. The models' voltage and power output will be compared in this experiment.

4.4.2 Experimental Device and Setup

The selection of experimental devices and the experimental setup are similar to section 4.3. In this experiment, the voltage output and power output data of the R1 and R2 models will be compared with the S4 and S5 models, respectively. The experimental setup steps are listed as follows.

- Fix a mounting interface plate on the Nano 43 transducer.
- place and glue the piezoelectric kit (M-2807-P2) on the end of a plastic cantilever beam.
- Use two screws to fix the end of the cantilever beam to A mounting interface plate to ensure the cantilever beam's fixing.
- Use a screw to fix the R1 and R2 models to the other end of the cantilever beam.
- Connect the piezoelectric kit with two oscilloscope probes.

4.4.3 Experimental results and Phenomenon

Figure 4.20 shows the voltage output data of the R1 and R2 models. At the same time, for the convenience of comparison, the curves of the S4 and S5 models have also been added to the chart. It can be seen that under the same tail length, the voltage output of the R series models is slightly higher than the S series model at the experimental wind speed due to the thinner curved body. The power output is calculated as shown in Table 4-3, and although the gap between the R series and S series models is not huge, under the experimental wind speed, the power output of the R series models is basically higher than the models of S series with the same tail length.

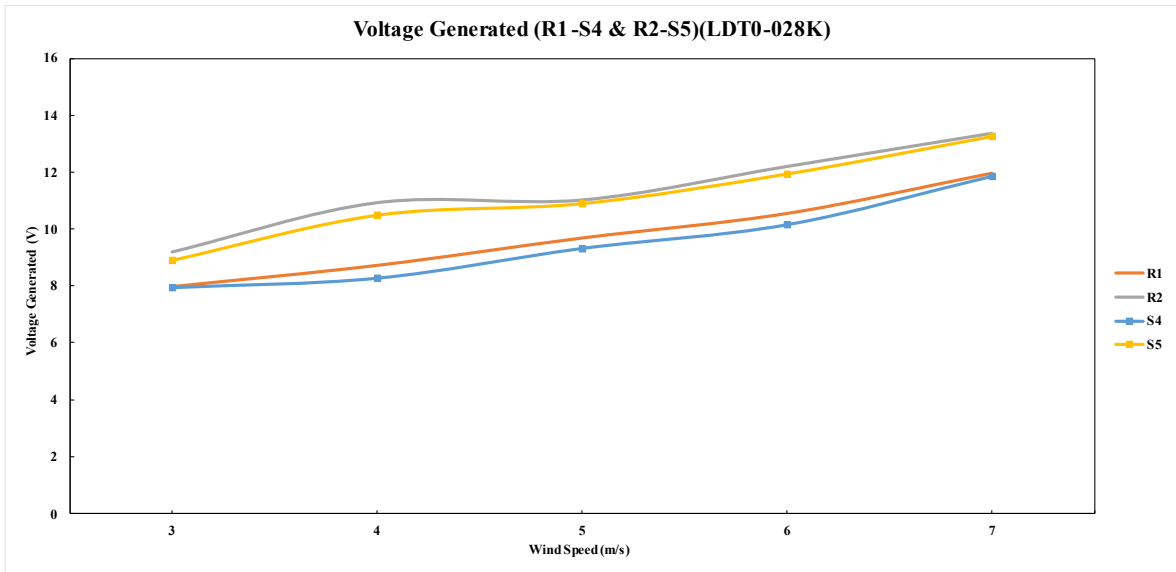


Figure 4.20 - Voltage Generated Comparison (R1-S4 & R2-S5) (LDT0-028K).

Table 4-3 - Power Output for R1 and R2 Models (mW).

	3m/s	4m/s	5m/s	6m/s	7m/s
R1	0.063802	0.076314	0.094069	0.111595	0.143535
R2	0.084164	0.119212	0.121335	0.148872	0.178910

Compared with the vibration frequency of the two models, it can be found that the vibration frequency of the R series model is slightly higher than the S series model. The curve does not clearly show the relationship between frequency and wind speed. When the wind speed increases, the frequency of each model is basically stable, which is consistent with the frequency data obtained when testing the S model.

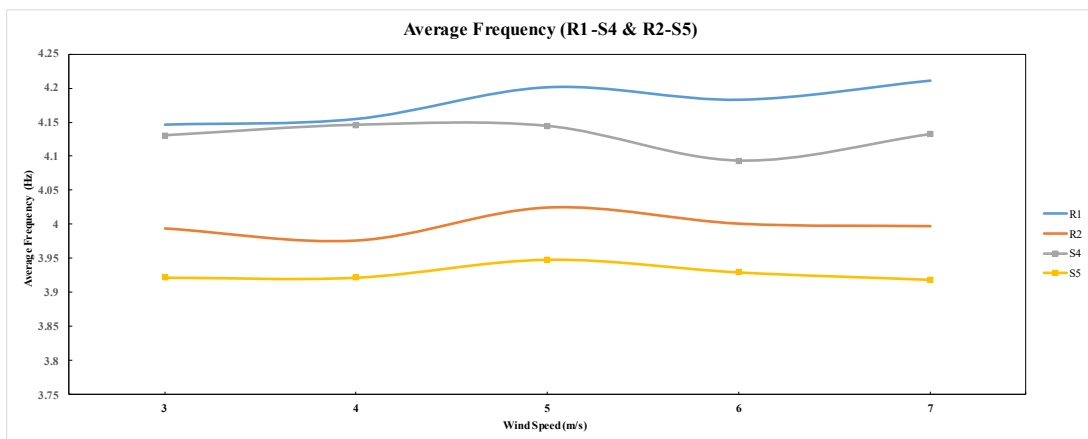


Figure 4.21 - Average Frequency Comparison (R1-S4 & R2-S5).

4.4.4 Conclusion

It can be seen through this experiment that the thin curved body is more conducive to energy harvest. When the air flows across the tip of the curved surface, the thicker curved thickness will cause the airflow to lose energy due to the reattachment, as shown in Figure 2.25, which will cause the energy harvest efficiency to decrease.

In general, the curved body's thickness can affect the energy harvesting efficiency, and the thinner the curved body, the higher the energy harvesting efficiency. However, in the manufacturing and usage process, the thinner curved surface is easily damaged. Therefore, in the subsequent design, it is necessary to make the curved surface as thin as possible under the condition that the structure is not damaged so that it can have higher energy harvesting efficiency.

4.5 Effect of Cantilever Beam Material

4.5.1 Experimental Purpose and Requirements

In the previous studies of many piezoelectric energy harvesters with cantilever beam, only a kind of cantilever beam was used to connect models in the experiment, but for the energy harvesters, the cantilever beam is also an important part of it. Therefore, the research on the cantilever beam is also important. In this section, the materials of the cantilever beam will be experimentally studied, and two materials of the cantilever beams (aluminium and plastic) will be selected and tested in the wind tunnel in order to compare the performance and select the best suitable cantilever beam for the energy harvester. The size of the two cantilever beams is completely consistent ($180 \times 10 \times 1.4\text{mm}$). The plastic cantilever beams are made of 3D printers, and the material is PLA plastic. In section 4.3, aluminium cantilever beams are used in the experiment, in order to save experimental time, plastic cantilever will be connected and tested with the S series models in this experiment.

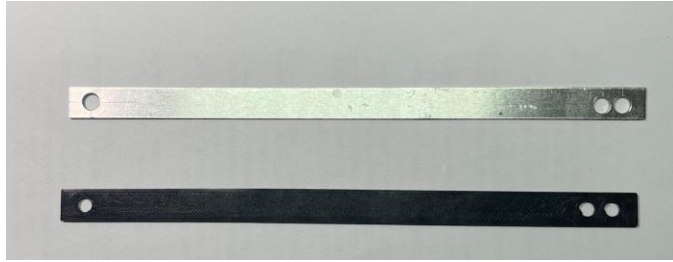


Figure 4.22 - The Cantilever Beams Used in the Experiment.

4.5.2 Experimental Device and Setup

The selection of experimental devices and the experimental setup are similar to section 4.3, except for the selection of cantilever beams. The experimental setup steps are listed as follows.

- Fix a mounting interface plate on the Nano 43 transducer.
- place and glue the piezoelectric kit (LDT0-028K) on the end of a plastic cantilever beam.
- Use two screws to fix the end of the cantilever beam to A mounting interface plate to ensure the cantilever beam's fixing.
- Use a screw to fix the model to the other end of the cantilever beam.
- Connect the piezoelectric kit with two oscilloscope probes.

4.5.3 Experimental results and Phenomenon

This section will show the results of the experiment with a plastic cantilever beam. First of all, lift force data is collected through the force sensor. The following figure shows the lift force data of the S0 and S5 models at 3m/S wind speed. It can be seen that the data is similar to the data of the lift force curve in the 4.3 section. The lift force curve of the S5 model is a sine wave shape, but the lift force curve of the S0 model shows a regular small vibration. The data analysis proves that in this experiment, the lift force curve of all models is symmetrical at the X coordinate axis, which means that the condition of experimental equipment is fine.

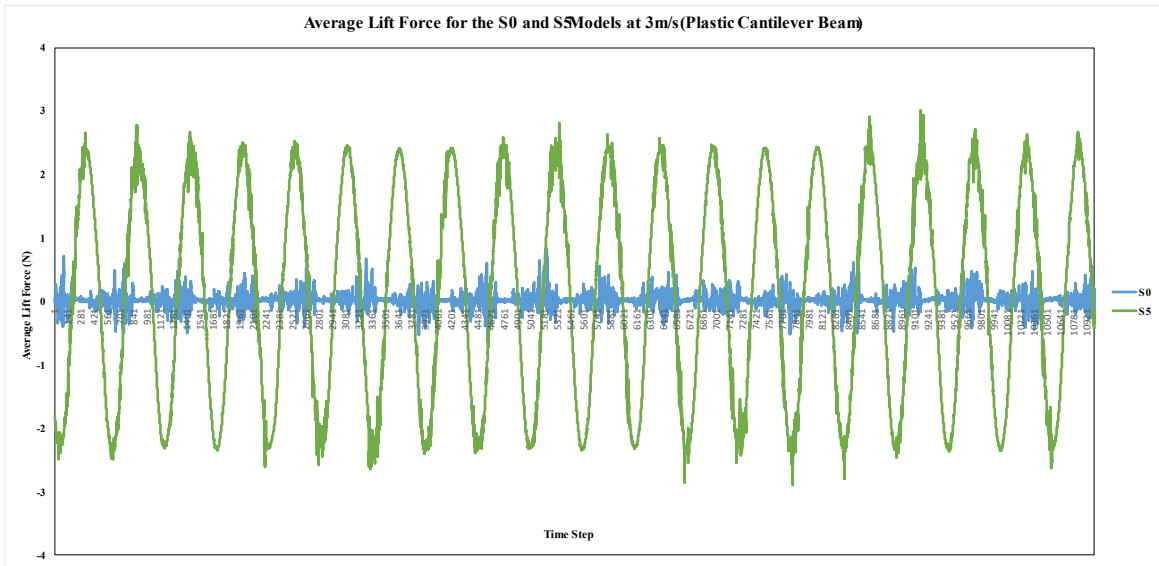


Figure 4.23 - Average Lift Force for the S0 and S5 Models at 3m/s (Plastic Cantilever Beam).

After testing under experimental wind speed (3m/s-7m/s), each model's average lift force data is calculated after data analysis, as shown in Figure 4.24. The S0 model still maintains the lowest lift force in the experimental wind speed but compared with the data in Section 4.3, the lift of the S0 model after 5m/s has a relatively large rise trend. The lift force of the S1 model rises rapidly after 3m/s of wind speed. The lift force of the S1 model becomes the highest in the S series model at 5m/s. The remaining four models of the S series maintain a trend of steady increase, but it is worth noting that, unlike the testing with aluminium cantilever beams, the tail length of the S2-S5 models with a plastic cantilever beam is inversely proportional to its lift force.

When comparing the lift force results of the model with an aluminium cantilever beam and with a plastic cantilever beam, it has been found some differences in average lift force. Compared with the model with an aluminium cantilever beam, the average lift force values of the S5 and S4 models have decreased at different wind speeds. The value of the S3 model is slightly lower than the previous experiment at 3m/s; however, the lift value is higher within 4m/s - 7m/s. The S2, S1 and S0 models are higher than the previous values in whole experimental wind speeds.

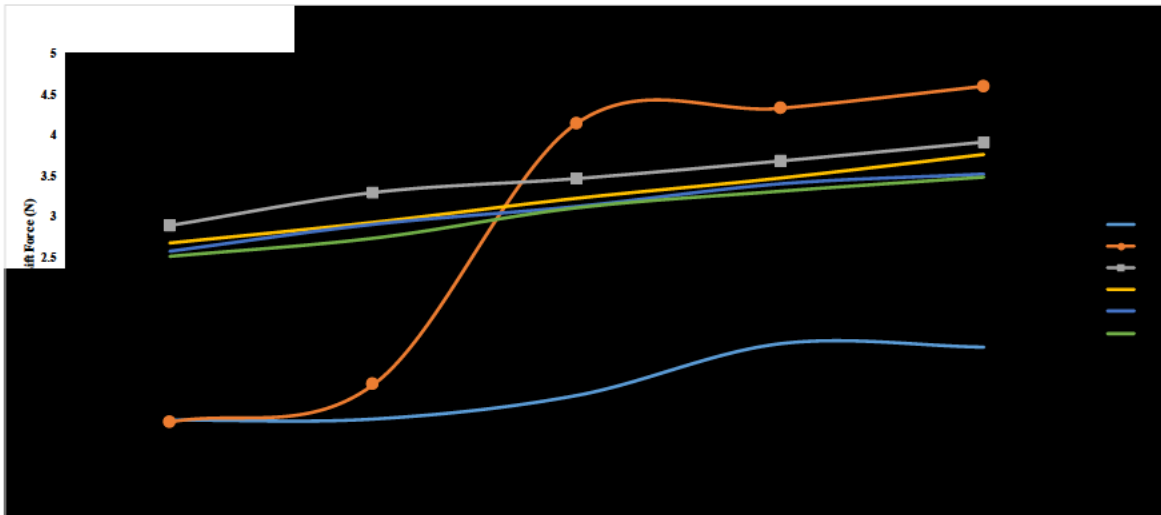


Figure 4.24 - Peak Lift Force for the S Series Models (Plastic Cantilever Beam).

The vibration frequency is analysed through the force sensor's lift force data, as shown in Figure 4.25. The vibration frequency of the model with an aluminium cantilever beam has basically remained stable in the entire experimental wind speed, except that the S1 model rose sharply at 6m/s. However, in this experiment, the vibration frequency of all models of the S series has a significant decline, and the figure shows that the relationship between vibration frequency and the tail length of the model shows an inverse proportion.

Finally, for voltage output, the figure is similar to the figure of the lift force curve (Figure 4.26). The voltage output of the S1 model at 3m/s and 4m/s is similar to the S0 model, but its voltage output rose rapidly at 5m/s, becoming the model with the highest voltage output value. The voltage output value of the S2-S5 model decreases in order. Although the voltage output of the S0 model has improved compared with the previous experiments, it is still the model with the lowest voltage output in the S series model.

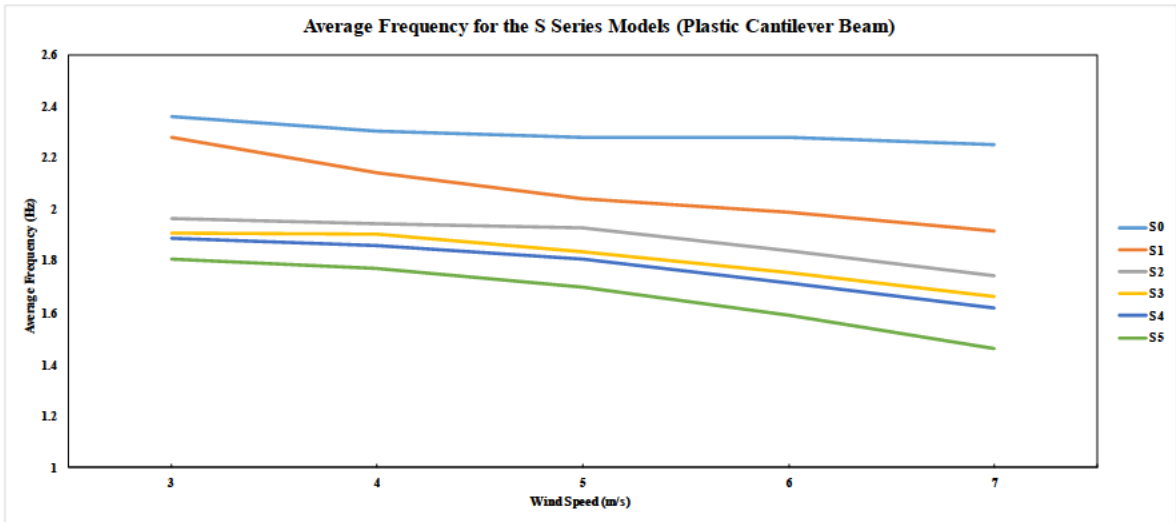


Figure 4.25 - Average Frequency for the S Series Models (Plastic Cantilever Beam).

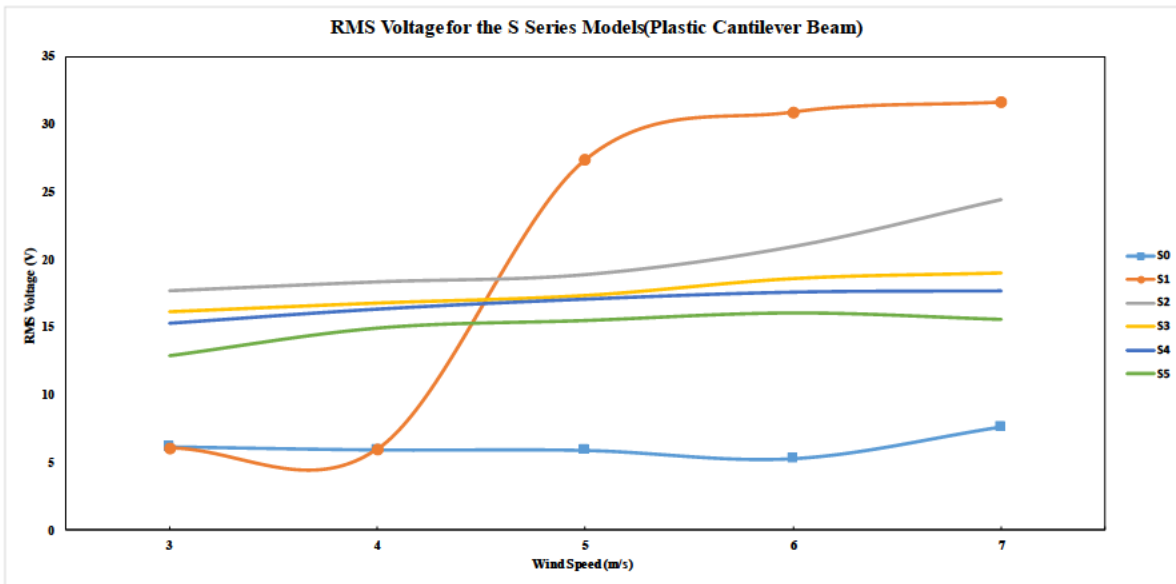


Figure 4.26 - RMS Voltage for the S Series Models (Plastic Cantilever Beam).

4.5.4 Discussion

The experiment of the S series models with a plastic cantilever beam shows different phenomena, especially in the aspect of lift force and voltage output. Both experiments use a series of models. The only difference is that the cantilever beams are different. One is an aluminium cantilever beam, and the other is a plastic cantilever beam. From the experimental results, it can be seen that although the S0 model had different values in the lift force and voltage output within the two experiments, it was still the model with the

lowest value of the S series models. Therefore, the effectiveness of the design will not change due to changing the material of the cantilever beams.

The role of the cantilever beam is to connect the front model and transmit vibration to the piezoelectric kit at the end of its tail. Different materials for the two cantilever beams will lead to different hardness, which will affect the experimental performance. According to the lift data of the forcer sensor, a higher lift force value means that the vibration amplitude of the model is very large. When the vibration frequency of an object is close to its natural frequency, the vibration amplitude of the object will increase. The formula for natural frequencies is shown in Equation 2.27. Therefore, the first natural frequency could be calculated as follows [129].

Table 4-4 - The First Natural Frequency Parameter for Two Beams (S3 model).

	Aluminium	Plastic
Modulus of Elasticity [E] (GPa)	70	4.8
Area Moment of Inertia [I] (mm ⁴)	2.287	
Beam length [L] (mm)	220	
Uniform load per unit length [w] (N/mm)	0.0025	
First natural frequency [f1] (Hz)	9-10	2-3

On the other hand, the cantilever beam plays the role of damping in the process of vibration. The stiffness of the plastic cantilever beam is far less than the aluminium cantilever beam, which means that the aluminium cantilever beam has a higher damping coefficient, which means that the vibration frequency with models with an aluminium cantilever beam will be higher. It can be seen from the table below that the vibration frequency of models with an aluminium cantilever beam does not change much at the experimental wind speed, and their frequency is between 1.5-4.7Hz. However, the vibration frequency of the models with a plastic cantilever beam decreases as the wind speed increases. Among them, the vibration frequency of the S0 and S1 models exceeds 2Hz or close to 2Hz, while the vibration frequency of the S5 model is minimal at the same wind speed, only 1.46Hz at 7m/s.

Table 4-5 - Frequency of Models with an Aluminium Cantilever Beam.

	3m/s (Hz) +/- 0.0001	4m/s (Hz) +/- 0.0001	5m/s (Hz) +/- 0.0001	6m/s (Hz) +/- 0.0001	7m/s (Hz) +/- 0.0001
S0	1.5701	1.5679	1.5843	1.5610	1.5497
S1	1.5871	1.5638	1.6026	4.6904	4.6339
S2	4.3649	4.3898	4.3649	4.3440	4.3478
S3	4.1771	4.2463	4.2123	4.2159	4.2017
S4	4.1305	4.1459	4.1442	4.0933	4.1322
S5	3.9216	3.9216	3.9479	3.9293	3.9185

Table 4-6 - Frequency of Models with a Plastic Cantilever Beam.

	3m/s (Hz) +/- 0.0001	4m/s (Hz) +/- 0.0001	5m/s (Hz) +/- 0.0001	6m/s (Hz) +/- 0.0001	7m/s (Hz) +/- 0.0001
S0	2.3585	2.3041	2.2805	2.2779	2.2523
S1	2.2779	2.1413	2.0408	1.9877	1.9146
S2	1.9646	1.9433	1.9294	1.8406	1.7443
S3	1.9084	1.9062	1.8362	1.7550	1.6609
S4	1.8868	1.8587	1.8060	1.7144	1.6160
S5	1.8083	1.7718	1.6975	1.5913	1.4618

Models with an aluminium cantilever beam are not affected by their natural frequency of models in the vibration because their vibration frequency is much lower than their natural frequency. For models with a plastic cantilever beam, the vibration frequency of the S series model is similar to the models' natural frequency (2-3 Hz). Therefore, models whose vibration frequency is similar to its natural frequency show a larger vibration amplitude, and show a larger lift force and voltage output. This is why different cantilever beams cause different results.

4.5.5 Conclusion

This section has proved the difference between models with an aluminium cantilever beam and models with a plastic cantilever beam. In general, if the plastic cantilever beam is used in the experiment, the S1 model does have a good voltage output at the larger wind speed (over 5m/s). However, once the wind speed is less than 5m/s, the S1 model will do a small vibration motion, and the voltage output will be significantly reduced compared with other models. Therefore, the S2 model with a plastic cantilever beam can show a more stable performance.

But it should be noted that the result is only applicable to the S series model. If the model changes, such as increasing the diameter of the front semicircle or replacing the model material, the weight of the model will change, resulting in the vibration frequency of the model is not close to its natural frequency and the voltage output will be reduced. Therefore, if the model changes, the S5 model will still be the best choice based on ignoring the impact of its natural frequency.

4.6 Effect of Different Piezoelectric Layer

4.6.1 Experimental Purpose and Requirements

Two different pieces of piezoelectric kits in the experiment are used, namely LDT0-28K and M-2807-P2. The price of LDT0-28K pieces of pieces is cheaper, about 2 pounds, and this kit is made of Polyvinylidene Fluoride and can bend at an angle of 90 degrees. But the other is about 35 pounds, and it could be easily damaged if the banding angle is too larger because it is made of lead zirconate titanate. Therefore, in the early experiments, due to the unclear performance of the model, in order to prevent the experimental results error caused by the piezoelectric kit damage (a larger bending angle), the LDT0-28K piezoelectric kit was used in the early experiments. However, in many previous studies, the M-2807-P2 piezoelectric kit was used for energy harvest. In order to better compare the experimental results, in this section experiment, the M-2807-P2 piezoelectric sheet will be used to test the S series Model. After testing, the results can be compared with previous studies, and the performance of two different piezoelectric kits can be compared.

4.6.2 Experimental Device and Setup

The selection of experimental devices and the experimental setup are similar to section 4.3, except for the selection of piezoelectric kit. The experimental setup steps are listed as follows.

- Fix a mounting interface plate on the Nano 43 transducer.
- place and glue the piezoelectric kit (M-2807-P2) on the end of a plastic cantilever beam.
- Use two screws to fix the end of the cantilever beam to A mounting interface plate to ensure the cantilever beam's fixing.
- Use a screw to fix the S series models to the other end of the cantilever beam.
- Connect the piezoelectric kit with two oscilloscope probes.

4.6.3 Experimental results and Phenomenon

The model of this experiment is the same as the model used in Section 4.3, all of which are S series models, so the lift curve is consistent with Figure 4.15. The voltage output and the power output are different due to the different selections of piezoelectric kits. It can be seen from the figure below that the trend is roughly the same as before, and the S5 model still maintains a higher voltage output. In addition, it is worth noting that when the wind speed is improved, because the models present a larger vibration range, the M-2807-- P2 piezoelectric kit is more sensitive to bending, so the voltage output curve rising rate of the models has a significantly higher than the result of using LDT0-28K.

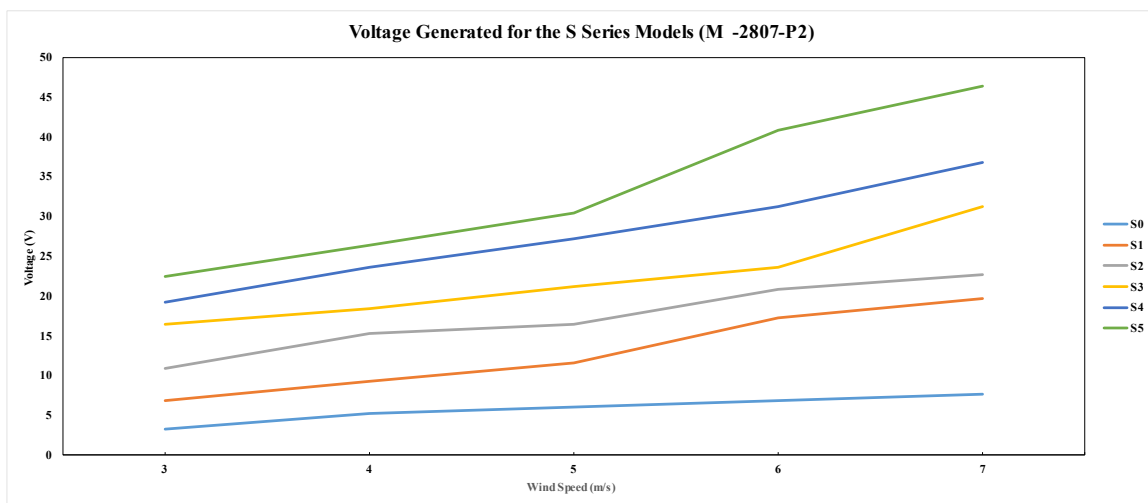


Figure 4.27 - Voltage Generated for the S Series Models (M-2807-P2).

It can be clearly seen from the table below that the power output data of S0 is slightly greater than the previous research. This is because the cross-sectional area of the model used in the experiment is larger. Compared with the LDT0-028K piezoelectric sheet in Section 4.3, the M-2807-P2 piezoelectric sheet has higher energy conversion efficiency, and the power output has been increased by several times.

Table 4-7 - Power Output for S Series Models with Aluminium Cantilever Beam and M-2807-P2 Piezoelectric Kit.

Power output mW					
	3m/s	4m/s	5m/s	6m/s	7m/s
S0	0.010	0.027	0.030	0.046	0.057
S1	0.046	0.084	0.134	0.295	0.384
S2	0.116	0.231	0.268	0.432	0.510
S3	0.268	0.338	0.449	0.556	0.973
S4	0.368	0.556	0.739	0.973	1.354
S5	0.501	0.696	0.924	1.664	2.152

4.6.4 Conclusion

Although M-2807-P2 is more expensive, its price is about ten times that of LDT0-28K, but its energy harvest efficiency is much greater than LDT0-28K. In addition, in this experiment, the voltage generated and power output of the S0 model are compared with previous studies. Both experiments use the same piezoelectric kit, and the data is basically the same. This experiment can also prove that the design has better performance; for example, at the wind speed of 7M/S, the maximum output power of the S5 model can reach 2.15MW.

4.7 Conclusion

This chapter has studied and analysed the new design through experiments. The effectiveness of the design was first proved by the experiment. The voltage output of the design T2 model is about four times that of the T1 model (original design). After determining the effectiveness of the model, some key parameter of the design was tested

to understand its impact on power output. The tail length, curved body thickness and cantilever beam materials were considered. It can be seen through experiments that the length of the tail length has the greatest effect on energy harvest. When the ratio of the diameter of the curved body and the tail length is 1 (S5 model), the power output reaches $175.48 \mu\text{W}$ at a wind speed of 7m/s. The effects of the thickness of the curved body are not obvious on the power output, but it can also be seen that the thinner the curved body part, the greater the power output. In addition, the material of the cantilever beam can also affect the power output through the resonance frequency of the structure. Therefore, the effect of resonance frequency should be considered in the future design to choose the appropriate cantilever beam. Finally, the two types of piezoelectric kits were compared, and the M-2807-P2 piezoelectric kit was more sensitive and had high energy output. However, the price of this type of piezoelectric kit is relatively expensive, and the price and power output should be balanced when used.

In general, the experimental analysis of models was made, and the results of each experiment were discussed. In the subsequent chapters, the model will be simulated under a wider set of conditions after verification by comparison with experimental results.

CHAPTER 5. SIMULATION

5.1 Introduction

In order to understand the fluid flow around the design, the computational fluid dynamics (CFD) simulation needs to be used. Through simulation, it is possible to obtain data on lift force, frequency, and other parameters under ideal conditions. While there may be discrepancies between ideal condition data and experimental data, the overall trends in the data should remain similar, making it still valuable as a reference. Additionally, simulation allows for observing fluid trajectories around the model, providing a theoretical basis for future model improvements. CFD is a numerical simulation technology that simulates complex fluid movements. Ansys 2021R2 Fluent was used for meshing and simulating the design in this study.

Initial simulation verification was performed in Chapter 3, and the effectiveness of the design was preliminarily verified. In this chapter, the S series models are first simulated at different wind speeds to compare with the experimental results. At the same time, it can observe how the fluid flow changes are different between the curved body and the design model. In addition, more simulation studies will be conducted on the length of the tail, the thickness of the front curved body diameter of the design will be changed, while the length of the tail will be further increased. It can show whether the simulation results can be consistent with the previous simulation results through this simulation research. Finally, the thickness of the curved body will be studied. In the experiment of Chapter 4, the thickness of the curved body can affect the model performance. In this chapter, the two groups with different curved body thickness models will be simulated to observe how the curved body thickness affects the fluid flow and the model performance.

This chapter verifies the model's effectiveness through the CFD simulation. The simulation results can be compared with the experimental results of Chapter 4. At the same time, this chapter will select models with different curved body diameters for simulation, which can ensure the accuracy of the simulation result.

5.2 Simulation of the S Series Models

5.2.1 Geometry

In this section, the S series model will be simulated at the experimental wind speed (3m/s-7m/s), and the lift coefficient will be recorded for verification with the experimental results. The S series models tested in this section include six models (S0, S1, S2, S3, S4 and S5) enclosed by a rectangular shape of 400×200cm. The centre of the curved body of the models is located on the horizontal middle line and 100cm from the left side of the rectangular, as shown in Figure 1. The geometry size allowed the dominant flow features to be enough to capture and avoid the air streamlining near the wall affecting the bluff body.

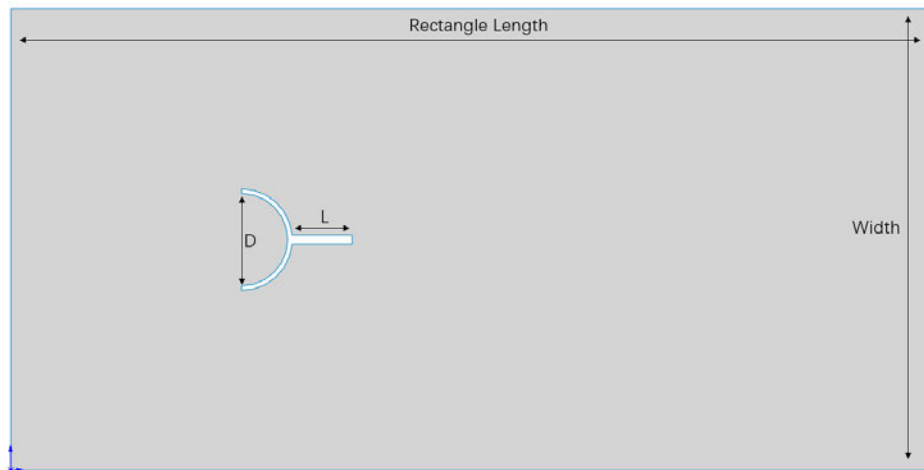


Figure 5.1 - The Simulation Geometry for the S Series Models.

The parameters of the simulation models and the fluid are shown in the table below. The curved body diameter of the S series model is the same, and the length of the tail is different. The tail length (l) of the S series models is 0cm, 10cm, 20cm, 26cm, 30cm, and 40cm, which correspond to the ratio of tail length to the curved body diameter is 0, 0.25, 0.5, 0.65, 0.75 and 1, respectively.

Table 5-1 - The Parameters of the Simulation Models and the Fluid.

Parameter	Value	Unit
Inter Diameter of Curved Body	40	mm

Thickness of Curved Body	2	mm
Thickness of Tail	4	mm
Rectangle Length	400	mm
Rectangle Width	200	mm
Fluid Density	1.225	kg/m ³
Fluid Viscosity	1.79E-05	kg/m-s

5.2.2 Mesh Generation

After the geometric shape was created, the mesh was generated in the geometric shape. The triangles method was used for the rectangular fluid domain with the default meshing parameters. The mesh around the bluff body was further refined in order to better reflect the fluid flow around the bluff body. The initial mesh of the S0 model is shown in Figure 5.2, and the image also shows the refined mesh around the bluff body. The mesh around the tail structure of the S1-S5 models has also conducted the same refined grid as the bluff body.

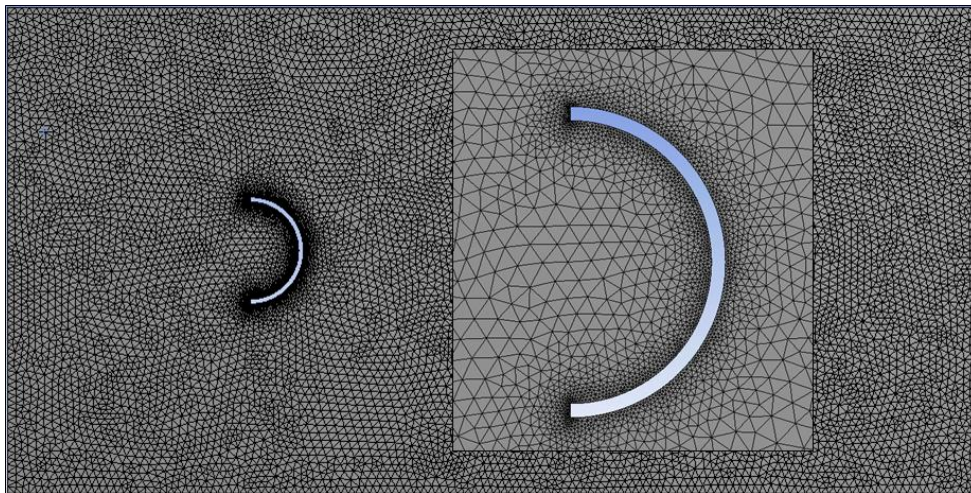


Figure 5.2 - Mesh Generated for S0 Model.

In the simulation, a static grid is used, which means that the grid will remain static, and relative motion is generated by the action of the fluid. The airflow direction was perpendicular to the velocity inlet boundary, while the rectangle's left and right edges were

designated as the velocity inlet and pressure outlet respectively. The top and bottom bounds of the rectangle were fixed walls.

The quality of the mesh will directly affect the simulation results, so the evaluation of the mesh quality is an important condition to determine whether the grid is excellent. In the table below, the five criteria of mesh quality were mainly evaluated, and the significance of their representatives has been discussed in Chapter 3.4. It can be seen from the table below that the evaluation result of the mesh is excellent. The mesh quality of another five models (S1-S5 models) was also evaluated, and the evaluation results were similar to the S0 models.

Table 5-2 - Evaluation of Mesh Quality for S0 Model.

Quality Metric	Target	Average Value
Element Quality	1	0.964
Aspect Ratio	1	1.197
Jacobian Ratio (Corner Nodes)	1	1.000
Skewness	0	0.054
Orthogonal quality	1	0.966

Although the mesh quality evaluation is very good, the mesh density greatly impacts the simulation results. In general, the more refinement mesh will represent more accurate results, but the more time consumption will be. In this simulation, six models need to be simulated, and each model needs to be simulated once at the five different wind speeds; thus, the simulation needs to be considered the time cost under the premise of considering the accuracy of the simulation result. Mesh independent study can show whether the number of meshes can provide more accurate simulation results. Five meshes have been compared in the study, M1 5874 (coarse), M2 16421, M3 22652 (medium), M4 54679 and M5 87865 (fine).

The peak lift coefficient corresponding to the amount of mesh for the S0 model at 7m/s is shown in Figure 1. When the number of meshes increases from M1 to M2 and from M2 to M3, the peak lift coefficient changes by more than 40%; when it changes from M3 to M4

and M4 to M5, the changes in the peak lift coefficient tends to be slow, only less than 5%. When the number of grids is M3, the lift coefficient begins to stabilize. Although increasing the number of meshes will make the simulation result more accurate, to balance the accuracy of time consumption and results, the number of M3 (medium) meshes was selected in subsequent fluid flow simulation. S1-S5 models' mesh number is similar to S0, so similar mesh settings were used.

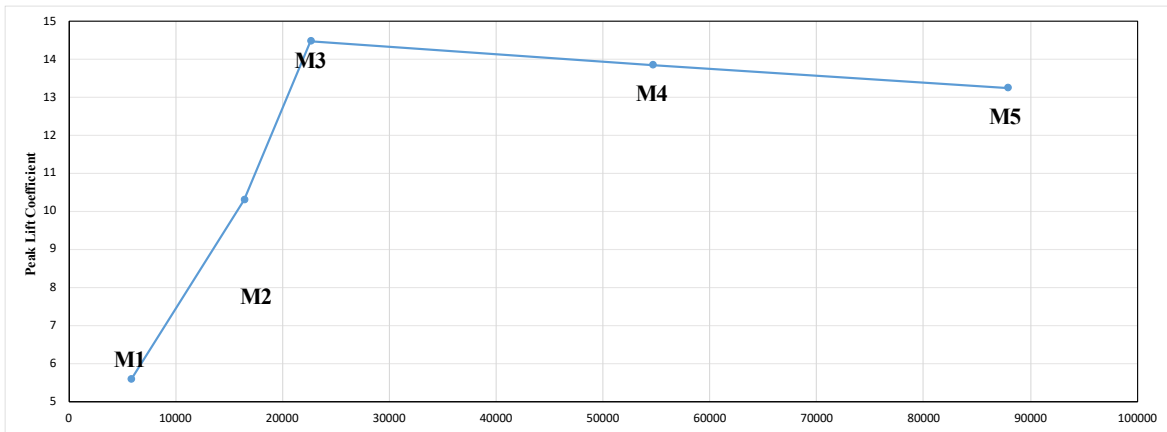


Figure 5.3 - Mesh Independent Study for the S Series Models.

5.2.3 Solver Setting

The standard K-Epsilon model was selected, because of its computational accuracy and time consumption. The turbulence intensity was 5%, and the turbulent viscosity ratio was 10. Two monitors (lift coefficient and drag coefficient) were applied to the body. The S series models were simulated within the same conditions with 3m/s - 7m/s of inlet boundary velocity. The other simulation solution method setting is same as the initial simulation validation because of balancing the accuracy and saving computational resource, which is shown in Table 3-10.

5.2.4 Result

5.2.4.1 Fluid Movement Analysis

The time steps were selected as 0.001s to ensure the accuracy of the results. In this section, the S0 model and S1 model will be compared firstly to determine the impact of the tail structure on fluid flow. The lift coefficient curve of the S0 model is shown in Figure 5.4. After starting with a small oscillation, a fixed amplitude vibration was started at about 0.26s.

In order to be more intuitive to represent the motion of the fluid through the bluff body, the three representative cycles were selected in the lift coefficient data of the S0 model when the lift coefficient curve presents a fixed amplitude periodic vibration, as shown in Figure 5.5. The peak values of the first cycle (0.46s) and the peak negative of the third cycle (0.539s) were selected, respectively, to show the state of the corresponding fluid flow. The time selection of the peak and bottom points of other models was the same way as the S0 model, which was selected when the curve presents a fixed amplitude periodic motion.

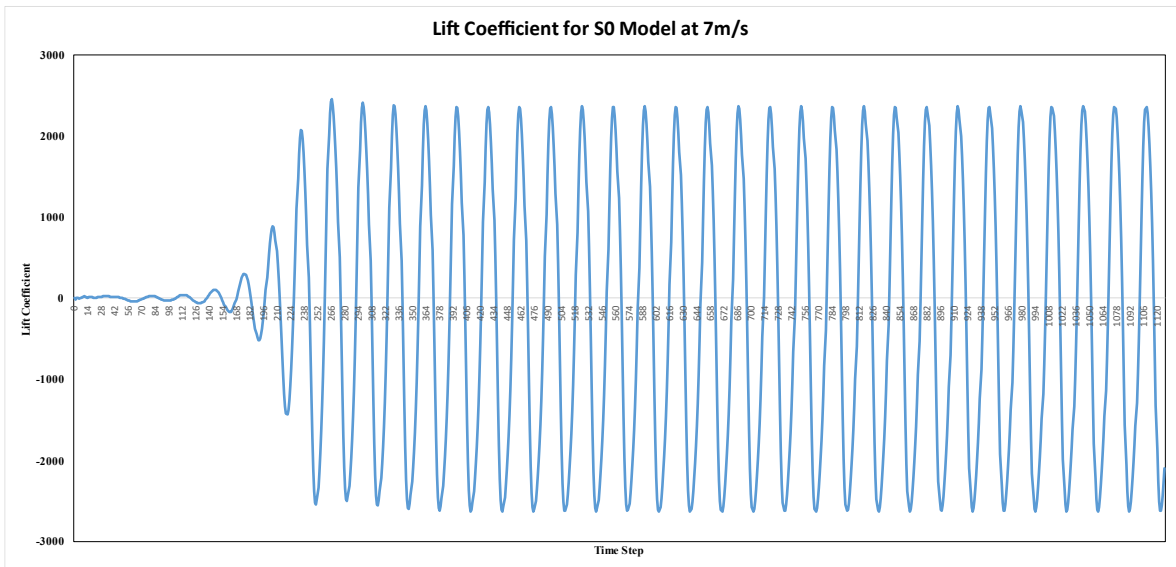


Figure 5.4 - Lift Coefficient for S0 Model at 7m/s.

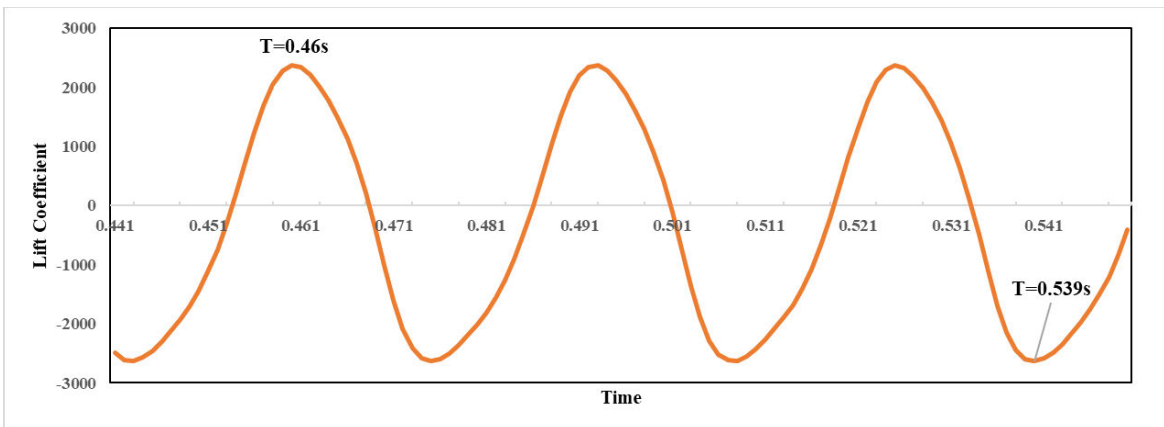


Figure 5.5 - Representative Lift Coefficient Cycle for the S0 Model.

The plots of the S0 model (vector and contour plots) of the peak and bottom lift coefficient point has been shown in Figure 5.6. The figure clearly illustrates the galloping principle of the bluff body. When the fluid flows past the bluff body, the front end of the body blocks

its flow, causing inner circulation will form alternately on the upper and lower surfaces of the body, with the rotation direction being opposite. Due to the generation of inner circulation, negative pressure occurs in the inner circulation, which leads to the generation of the net lift force of the bluff body.

In addition, the velocity of the shear layer is affected by the inner circulation, which causes the fluid to accelerate as it moves around the inner circulation. The acceleration of the fluid can lead to a decrease in pressure, which is known as the Bernoulli effect. Therefore, the symmetry of the shear layer on both sides of the bluff body is broken, resulting in the dynamic instability of the bluff body, which will generate more net lift force. Finally, the vortex of the inner circulation falls off, and the inner circulation forms on the other side. This process enables the bluff body to maintain a fixed amplitude periodic motion.

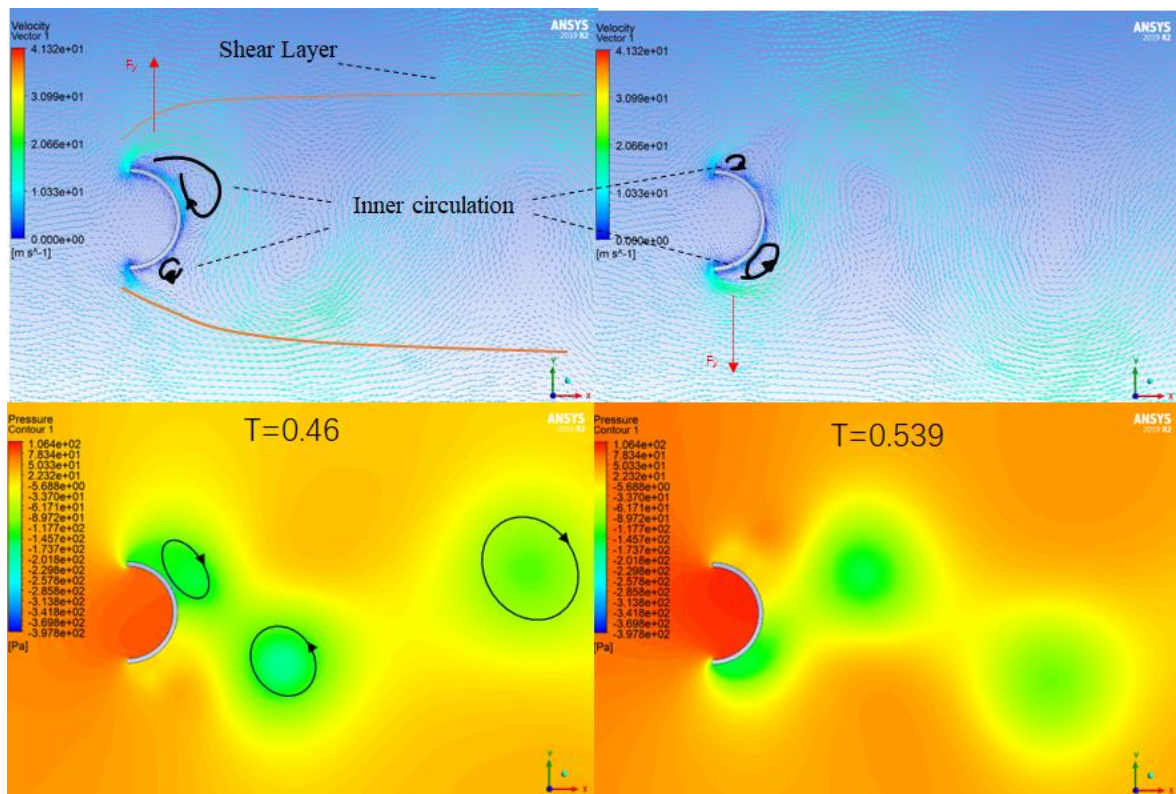


Figure 5.6 - Vector and Contour Plots for S0 Model at Key Points.

To more effectively analyse the impact of the tail structure on fluid flow, the S1 model, which is most similar to the S0 model, was selected for analysis. The Figure 5.7 shows the vector and contour plots of the S1 model, and, like the S0 model, the peak and bottom points of the lift coefficient at a fixed amplitude periodic motion are selected for

comparison. Taking 1.526s as an example, it can be seen from the vector diagram that the upper part of the separated shear layer is close to the centreline of the tail flow, while the lower part of the shear layer has just left, which causes the upper surface pressure on the body to be lower than on the lower part. After the fluid flows downward past the centreline, it will return and hit the tail structure from bottom to top at a faster speed. Due to the tail structure of the S1 model, a larger inner circulation area is formed, which can be seen from the contour plot.

Compared with the S0 model, the tail structure of the S1 model causes the shear layer to pass around the tail structure with a larger radius of inner circulation and close to the centreline of the tail flow, forming a larger internal circulation, and net lift force is generated due to the pressure difference. In addition, the fluid passing around the centreline of the tail flow will also hit the tail structure upwards, and the direction of this force is consistent with the direction of net lift generated by the body, so the body obtains more net lift.

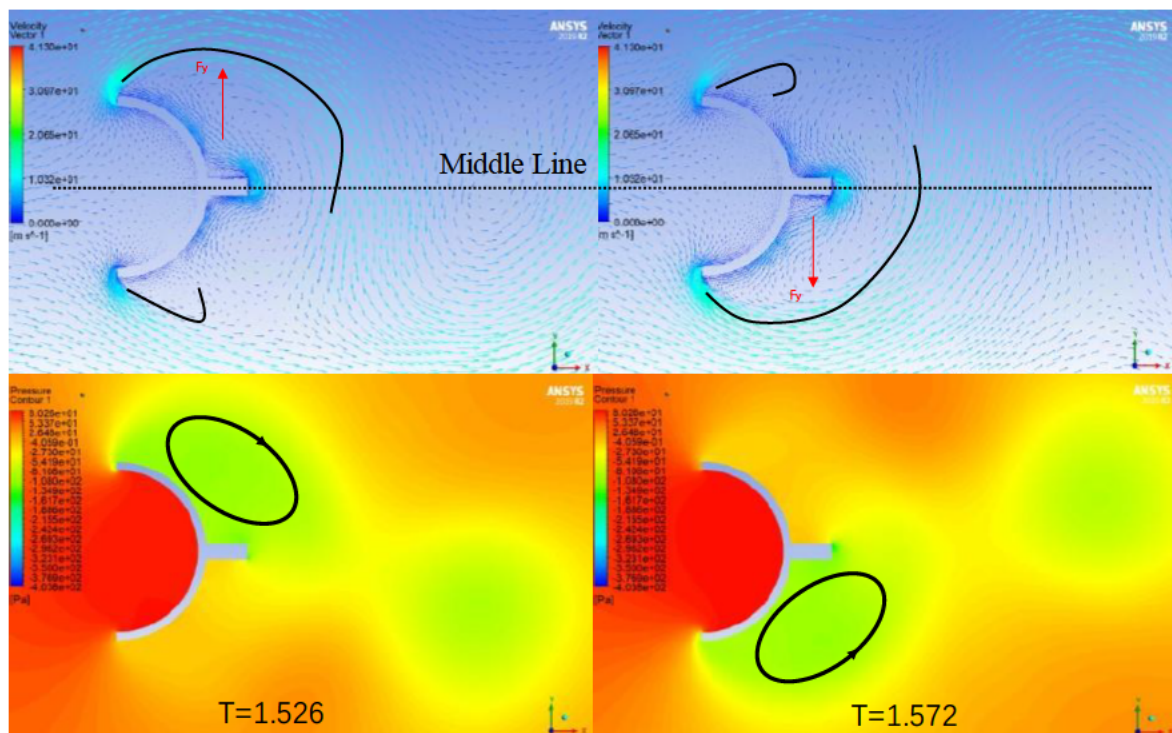


Figure 5.7 - Vector and Contour Plots for S1 Model at Key Points.

Below is the velocity streamline diagram of the S1 model at 1.572s. Through this figure, it can be seen more clearly that when an internal circulation is formed in the lower part of

the body, the flow speed of the surrounding boundary layer obviously increases, causing negative pressure to occur. In addition, the vortex will affect the subsequent boundary layer, and the vortex shedding hits the upper boundary layer, causing the upper part of the fluid to flow upwards instead of flowing around the bluff body, thereby causing the pressure difference between the upper and lower parts to increase, ultimately causing the body to move downward.

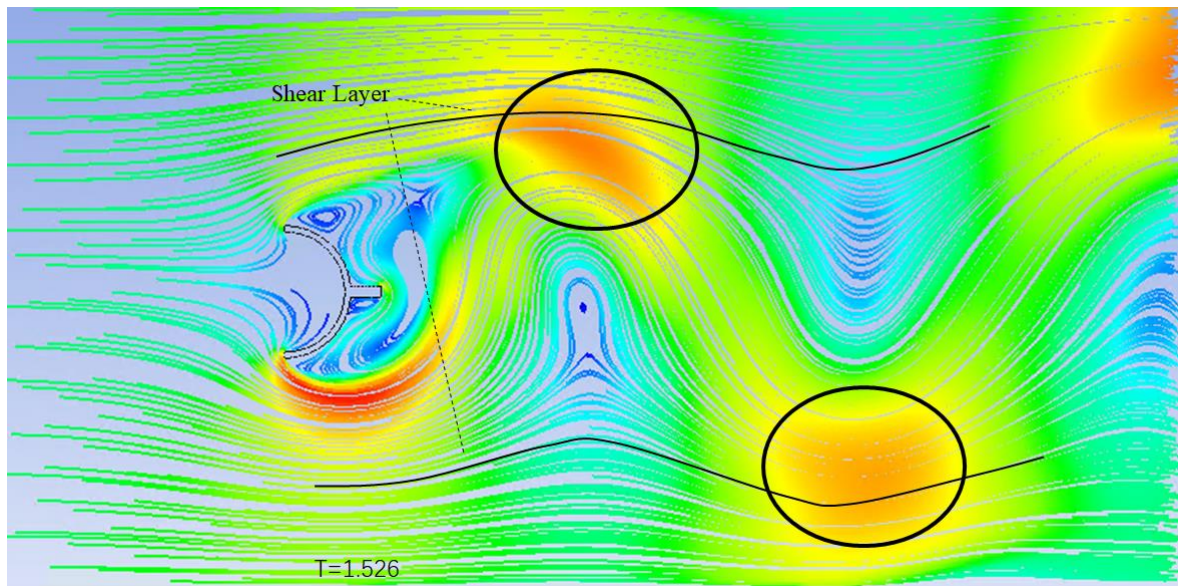


Figure 5.8 - Velocity Streamline Diagram of the S1 Model at 1.526s.

5.2.4.2 Lift Coefficient Curve Analysis

In the simulation of the S series models, a lift coefficient monitor was added. The lift coefficient curve of the S1 model and the S0 model are both after a short period of small-amplitude vibration, the lift coefficient peak gradually increases, and finally begins to vibrate with a stable amplitude, as shown in Figure 5.9 for the S1 model. However, the lift coefficient curve of the S3-S5 models is slightly different from that of the S0 and S1 models. Taking the lift coefficient curve of the S5 model as an example, as shown in Figure 5.10, the peak of the lift coefficient curve gradually increases at the beginning, and the peak of the curve reaches the highest point at 0.274s, but then the peak of the curve begins to decrease, and finally begins to vibrate with a stable amplitude. Figure 5.11 shows two different cycles of the S5 model, with the blue curve being the cycle at 0.274s and the orange curve being the cycle when fixed amplitude periodic motion begins (selected when

the time is 1.395s). Comparing the two cycles, the peak of the blue cycle has decreased by about 20% compared to the orange cycle. The difference between the S1 model and the S5 model is that the length of the tail structure is different, but the peak of the lift coefficient curve of the S5 model has obviously decreased when it begins to vibrate with a fixed amplitude periodic. Therefore, it is necessary to study the S5 model in order to understand how the length of the tail causes the peak of the lift coefficient curve to decrease.

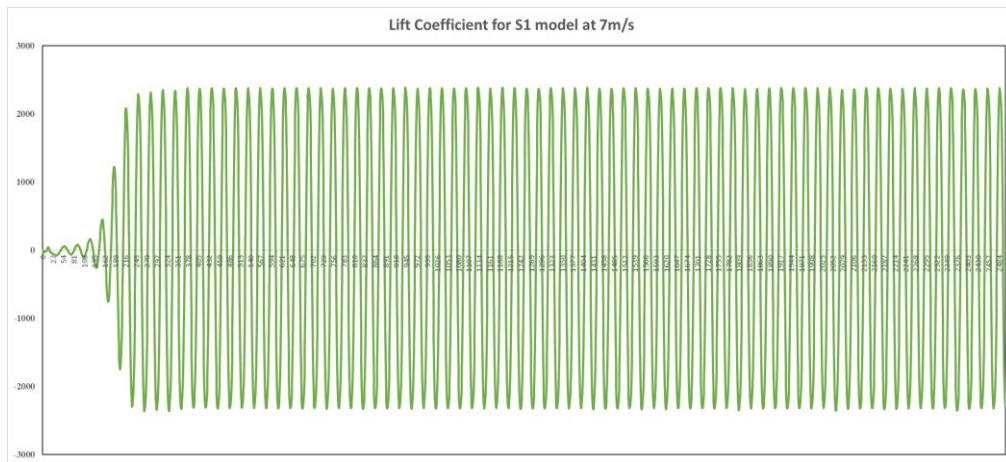


Figure 5.9 - Lift Coefficient for S1 Model at 7m/s.

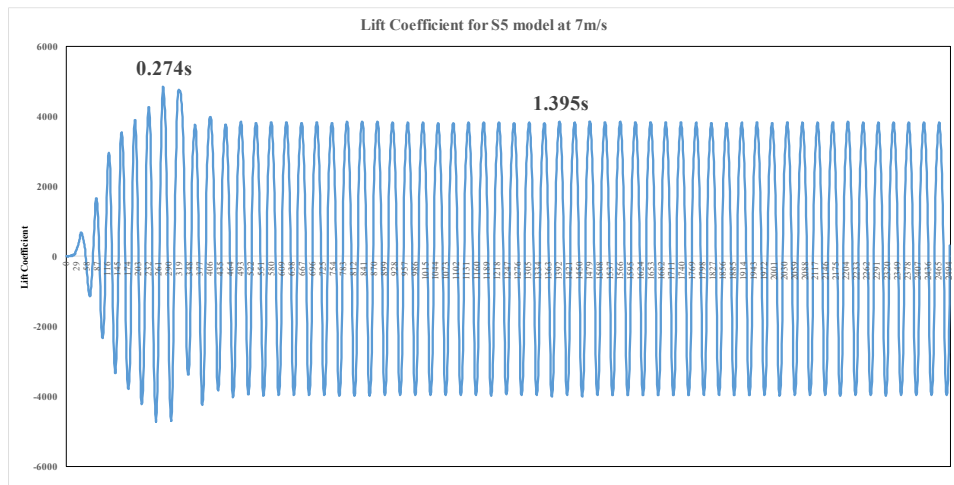


Figure 5.10 - Lift Coefficient for S5 Model at 7m/s.

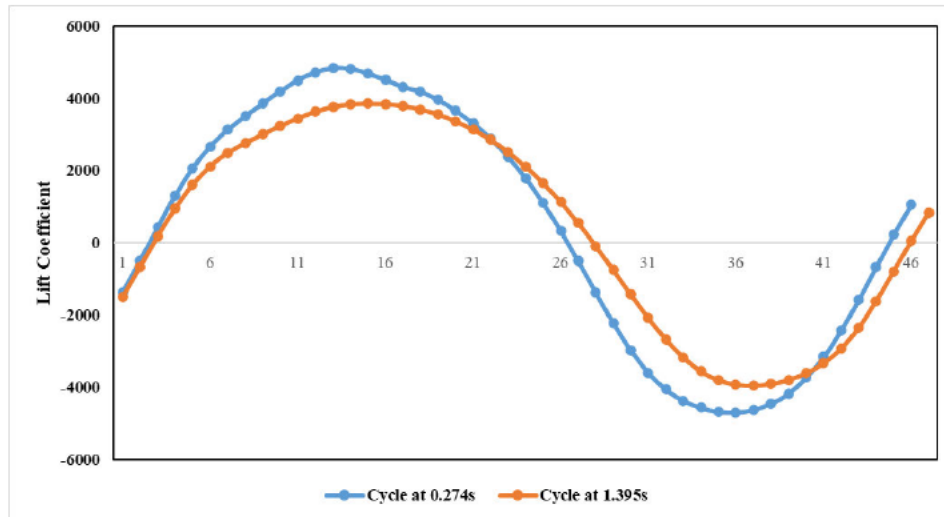


Figure 5.11 - Representative Cycles of S5 Model.

Figure 5.12 shows the velocity streamlines diagram of the S5 model at 0.274s and 1.395 seconds, respectively. From the two figures, it can be compared that, firstly, in Area 2, it is clear that the boundary layer of the fluid flow in Cycle 2 flows upwards along the rear end of the tail structure, while the boundary layer of the fluid flow in Cycle 1 does not exceed the centreline of the tail end of the bluff body, but instead hits the tail structure of the bluff body. This gives the body additional lift in the same direction as its movement. In addition, in Area 1, compared with Cycle 2, the red area (higher speed flow) of the flow line of Cycle 1 has a higher density and a larger area. Therefore, Cycle 1 generates a larger negative pressure in this area. Finally, comparing Area 3, it can be seen that the velocity flow line of the inner circulation of Cycle 2 is denser and has a larger area, which causes the pressure difference between the upper and lower surfaces of the body to be lower, resulting in a lower net lift than Cycle 1.

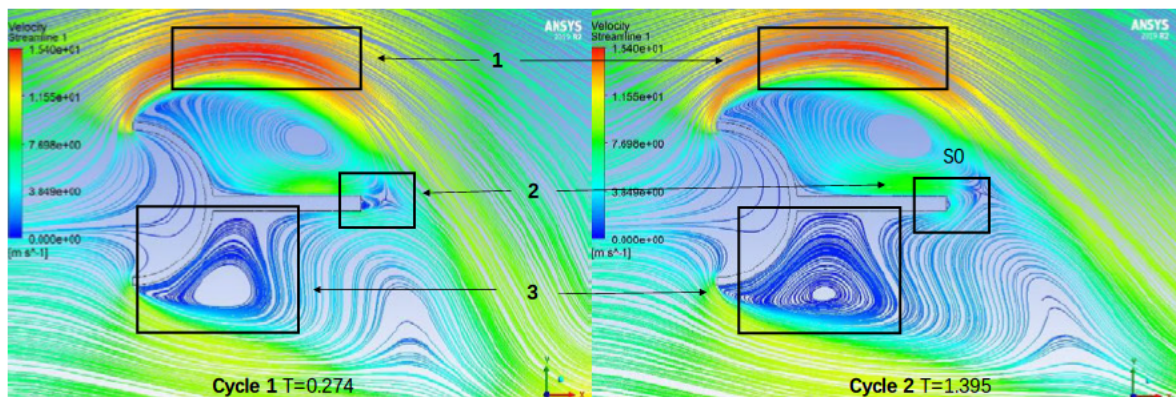


Figure 5.12 - Streamline Plot for S5 Model at Key Points.

From the vector diagram of the S5 model, it is clear to observe the changes in the inner circulation, as shown in Figure 5.13. At the end of the bluff body tail structure, the fluid flow in Cycle 2 flows upwards along the rear end of the tail structure from below, resulting in the centre point of the inner circulation on the upper side rising compared to Cycle 1, thus reducing the impact of the inner circulation on the upper part of the bluff structure. On the other hand, compared to Cycle 1, in Cycle 2, due to the internal circulation being generated in the lower half of the bluff body becoming larger, it can be seen that the inner circulation that has already separated from the lower half is farther from the bluff body.

In general, the decrease in the lift coefficient of Cycle 2 is primarily due to the inner circulation of the upper half being farther from the bluff body, resulting in lower negative pressure and, thus, lower net lift. On the other hand, the inner circulation of the lower half of Cycle 2 is generated earlier and has a larger area, further reducing the pressure difference between the upper and lower surfaces of the bluff body.

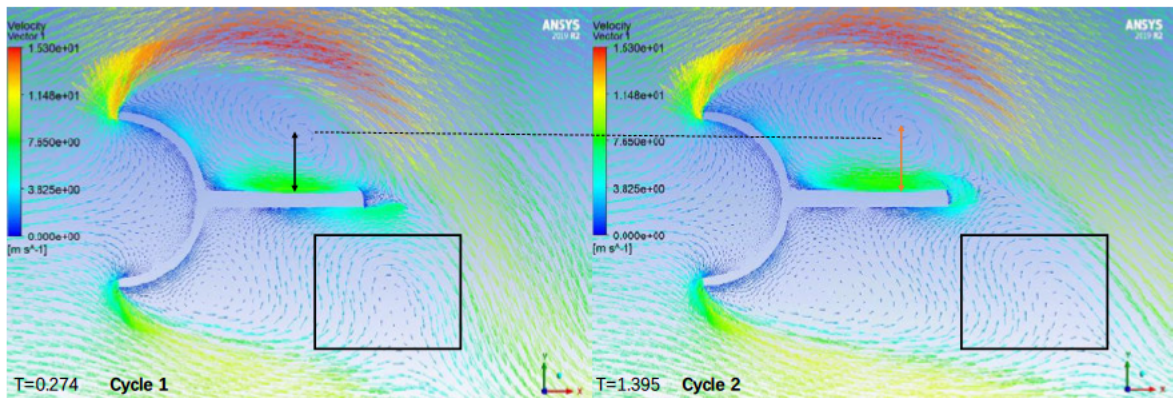


Figure 5.13 - Vector Plot for S5 Model at Key Points.

5.2.4.3 S Series Model Comparison Analysis

The S series models were simulated at wind speeds ranging from 3m/s to 7m/s, and the simulation results of each model will be compared in this section. The lift coefficient was selected for comparison when the model began to vibrate at a fixed amplitude, and the vibration frequency of each model was obtained through the lift coefficient curve. The lift coefficient determines the size of the lift the model receives from wind and is also directly proportional to the vibration amplitude of the model. The vibration frequency can also affect the output power of the piezoelectric energy harvester. The figure below is the lift

coefficient curve for the S series models, and it can be seen that as the length of the model's tail increases, the lift coefficient increases at different wind speeds. At a wind speed of 7m/s, the lift coefficient of the S5 model increased by about 57% compared to the S0 model. This lift coefficient curve also conforms to the principle of galloping vibration, where the lift coefficient of a model increases as the fluid speed increases as shown in Figure 5.14.

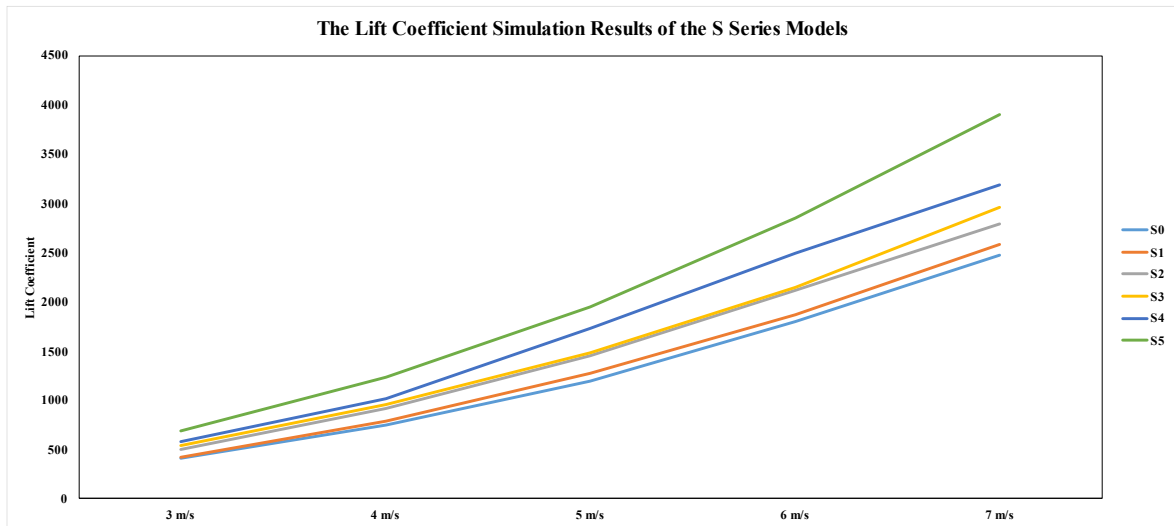


Figure 5.14 - The Peak Lift Coefficient Simulation Results of the S Series Models.

Although the S5 model performed well in the lift coefficient simulation results of the S-series models, it can be seen from Figure 5.15 that, at the same wind speed, the vibration frequency of the model decreases as the length of the bluff body's tail increases. As the wind speed increases, the vibration frequency of the same model also increases, but it can be seen from the figure that the distance between the five curves increases from 3 m/s to 7 m/s, which suggests that the model with a shorter tail structure or no tail structure seems to have a greater rate of increase in frequency as the wind speed increases.

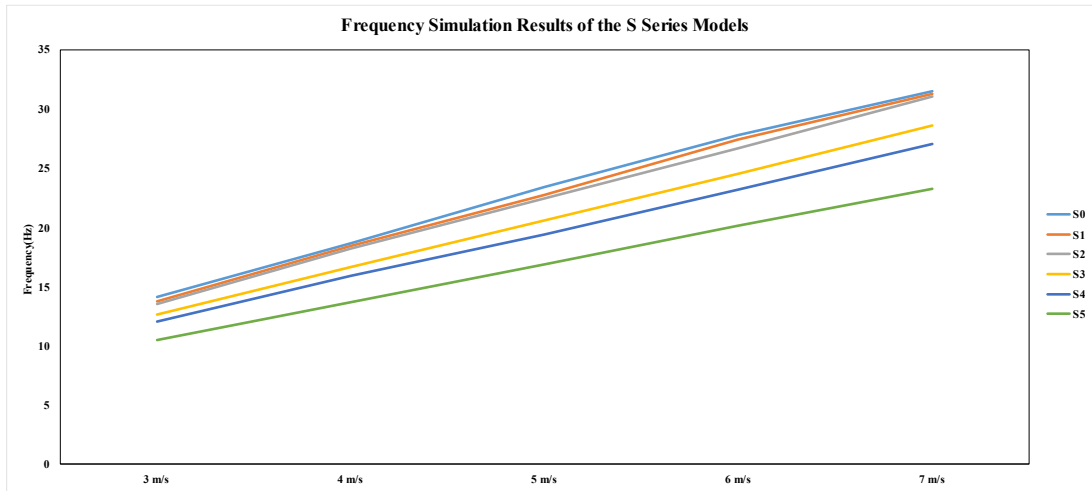


Figure 5.15 - Frequency Simulation Results of the S Series Models.

5.2.4.4 Responding time Analysis

From the lift coefficient curves of the S series models, it can also be found that the response time of the various models is not the same. Figure 5.16 compares the response time of the S0, S3, and S5 models. It can be seen from the figure that the curve of the S5 model has a noticeable fluctuation around 0.02s, the curve of the S3 model begins to fluctuate around 0.05s, and the curve of the S0 model begins to fluctuate around 0.1s.

Response time represents how quickly the model can start to vibrate, and the faster the response time, the faster the piezoelectric energy harvester can start to harvest energy. From the analysis, it can be concluded that the models with a longer tail structure have a shorter response time.

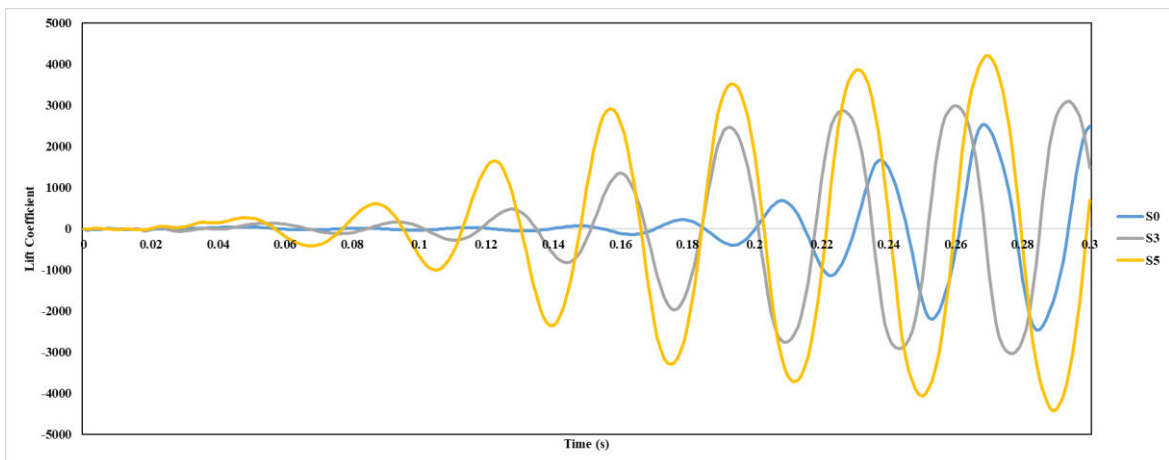


Figure 5.16 - Response Time Analysis.

5.2.5 Discussion and Conclusion

In this section, simulations of the S-series models were carried out, and as the length of the tail increased, the lift coefficient of the model also increased. However, the vibration frequency of the model decreased as the length of the tail increased, which can also be concluded from the analysis in Section 5.2.4.2. As the length of the tail increases, the area of the inner circulation produced becomes larger and larger, and as the boundary layer of the fluid flows around to the other side of the centreline of the tail structure, inner circulation causes the formation of a negative pressure region. However, as the area becomes larger and larger, the time required to form an inner circulation also becomes longer, so the frequency becomes lower and lower.

Another point worth noting is that the S1 model, like the S5 model, has a tail structure, but the length of the tail structure is different. However, there is no noticeable drop in the lift coefficient peak in the lift coefficient graph of the S1 model. It can be seen from Figure 5.7 that the reason for this may be that the tail of the S1 model is too short, and it is easy for the boundary layer of the fluid to flow across the centreline of the rear of the tail. Therefore, this occurs during the rising period of the lift coefficient, so there is no noticeable drop in the lift coefficient peak in the lift coefficient graph of the S1 model.

Additionally, the situation where the lift coefficient decreases for models with longer tails may be avoided in the future by adjusting the tail structure of the model. For example, by setting two symmetrical grooves on the upper and lower sides of the rear of the tail, the fluid can flow directly to the rear after passing through the groove instead of flowing to the other side across the centreline of the rear of the tail.

Since the S-series models are used for vibration energy harvesting, piezoelectric kits are placed at the end of a fixed cantilever beam at the rear of the model, so both the amplitude and frequency of the model's vibration can affect the total power output. Therefore, the lift coefficient and frequency simulation results cannot effectively determine which model will have a higher power output. In the next chapter, the results of the simulation and experiments will be compared.

5.3 Study of Tail

5.3.1 Geometry and Other Setting

In order to compare with the experimental results, the S series models used in the previous section were the same as the models used in the experiment. This section will change the geometric shape of the models and change the length of the tail structure to observe whether the trend of the lift coefficient change is consistent as in the previous section. In addition, the maximum ratio of the tail length to the diameter of the front curved body of the S series models is 1 (i.e. The S5 model). In this section, the ratio will be increased at the same wind speed to investigate the effect of longer tails on the bluff body structure. Ten models with different tail structure lengths were simulated at 5m/s of wind speed, and Table 5-3 shows the geometric parameters of the 2D model which like Figure 5.1, and the tail lengths of each model.

Table 5-3 - The Geometric Parameters for the P Series Models Simulation.

Parameter	Value	Unit
Inter Diameter of Curved Body	20	cm
Thickness of Curved Body	0.1	cm
Thickness of Tail	0.1	cm
Rectangle Length	200	cm
Rectangle Width	100	cm
Model Number	Tail Length (cm)	Ratio of L/D
P1	5	0.25
P2	10	0.5
P3	13	0.65
P4	15	0.75
P5	20	1

P6	25	1.25
P7	30	1.5
P8	40	2
P9	50	2.5
P10	60	3

The generation of mesh was similar to Section 5.2, and the quality of the mesh was also checked, moreover the solver setting was the same as in Section 5.2.

5.3.2 Result

Being selected the P10 model with the longest and most representative tail length from among the ten models for analysis, its vector and contour plots are shown in Figure 5.17. Cycle 1 and cycle 2 represent the peak and bottom values of the lift coefficient curve when the model starts to fix amplitude vibration. The vector plot shows that inner circulation appears at the top and bottom ends of the P10 model, and the shear layer flows to the other side of the middle line of the tail structure along the inner circulation. When one side of the inner circulation is formed, the other side is also forming due to the longer tail length. Although the inner circulation on the other side is also formed and negative pressure is generated, the negative pressure generated is less than the inner circulation that has been formed. By comparing with the S5 model, it can be seen that the model with a longer tail length also generates a larger area of inner circulation, and the negative pressure produced by the inner circulation is also greater.

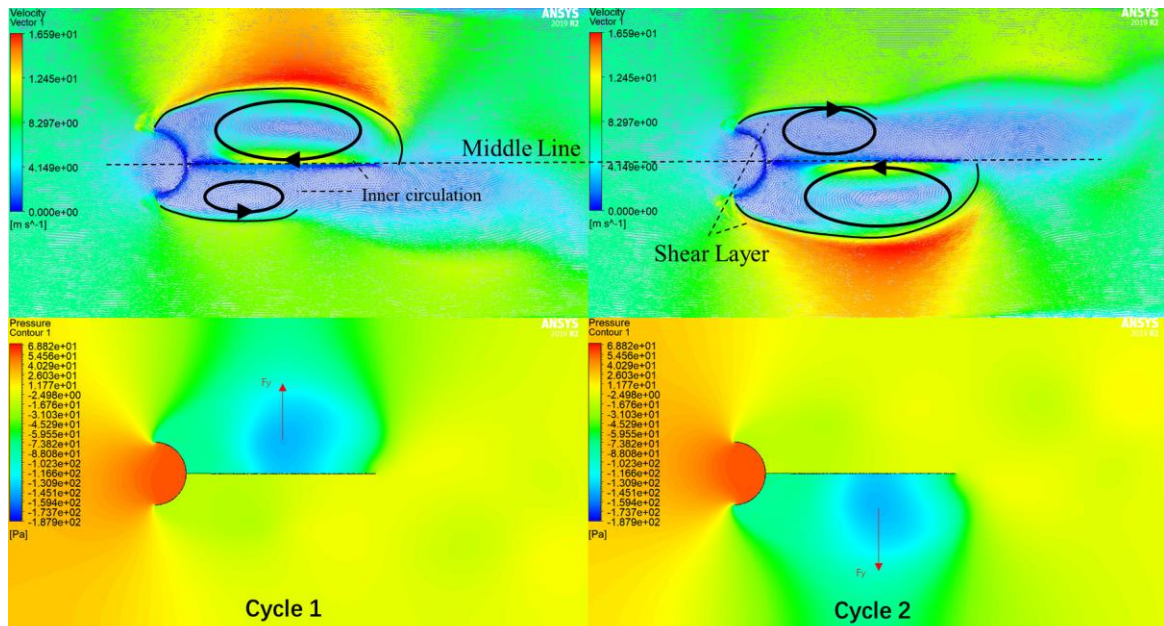


Figure 5.17 - Vector and Contour Plots for P10 Model at Key Points.

The peak lift coefficient curves of the P series model have been selected and summarized in Figure 5.18. The simulation results of the influence of tail structure length on the lift coefficient are similar to those in Section 5.2, with the lift coefficient increasing continuously as the tail length increases. Compared to the P1 model (tail length 5cm), the lift coefficient of the P10 model increased approximately five times. It is worth noting that a reference area was set during the simulation of the lift coefficient in Section 5.2, so the lift coefficient values simulated for the S series models are higher.

Figure 5.19 shows the influence of tail structure length on vibration frequency, again verifying that as the tail length increases, the vibration frequency becomes lower. Although the lift coefficient of the P10 model is high, its vibration frequency is 70% lower than that of the P1 model.

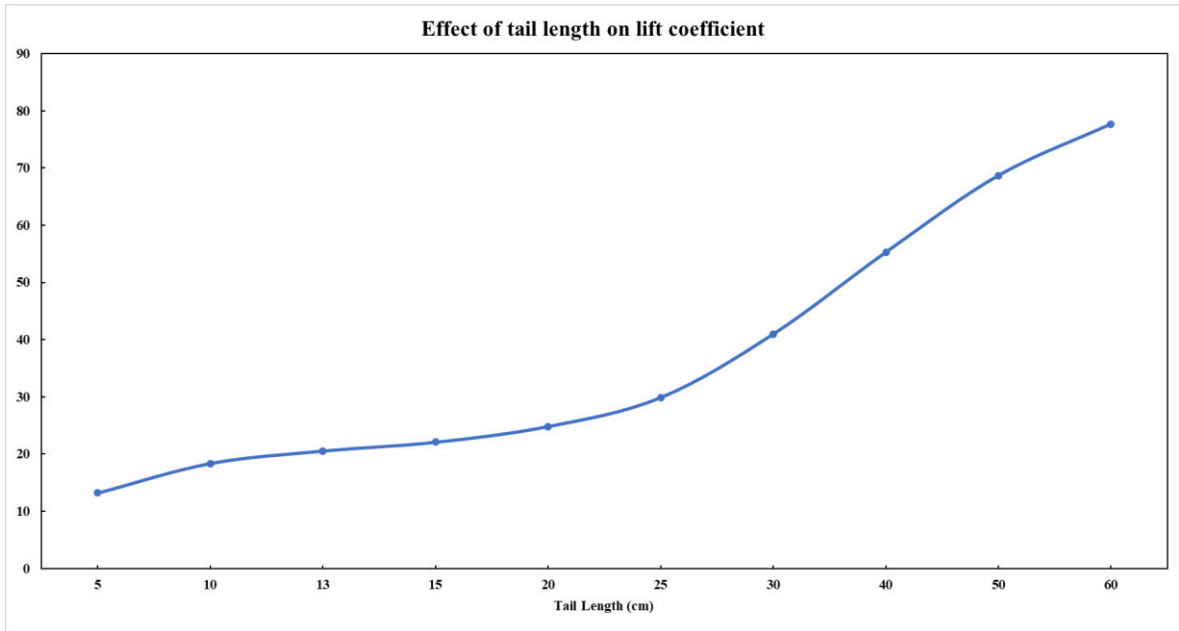


Figure 5.18 - Effect of Tail Length on Lift Coefficient (The P Series Models).

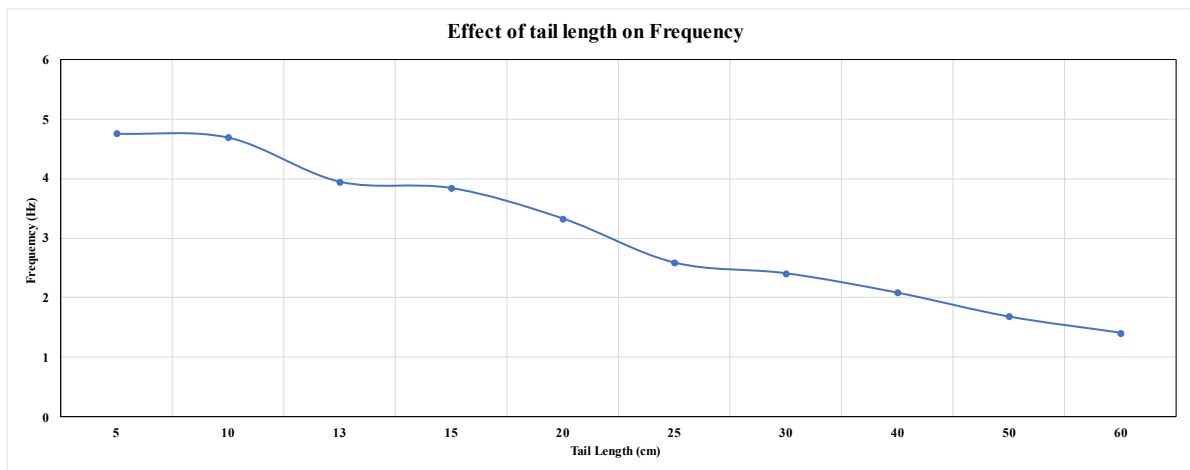


Figure 5.19 - Effect of Tail Length on Frequency (The P Series Models).

5.3.3 Discussion and Conclusion

Through the simulations in this section, the results in Section 5.2 have been verified, and analysis has also been performed on models with particularly long tail lengths. Although the lift coefficient has been increasing as the tail length increases, the vibration frequency has been decreasing. It can be expected that as the tail length continues to increase, there will be a certain length at which, due to its lower vibration frequency, its power output will no longer increase and will begin to decrease as the tail length further increases. Therefore, an optimum length of the tail can be determined by the simulations for different model

configurations without needing to build and experimentally test different solid model geometries.

5.4 Effect of Thickness of Curved Body

In this section, the thickness of the curved body of the model will be simulated and studied. Generally speaking, for a bluff body at galloping vibration, the longer the hydraulic diameter, the more energy that can be harvested from the fluid. For the design, the thicker the body, the longer the hydraulic diameter, and the higher the lift coefficient should be obtained when the same inner diameter is given. However, as shown in the experimental result of Chapter 4, the power output increases when the curved body's thickness is reduced. Therefore, this study aims to understand how the change in thickness of the curved body of the model affects the fluid flow and how lift coefficient and vibration frequency change when the thickness is reduced.

5.4.1 Geometry and Other Setting

In this section, two groups of models will be compared. The first group compares the R2 and S5 models, with the parameters of the R2 model and the simulation setup being the same as those of the S series models simulated in Section 5.2, except for the thickness. The second group will be changed the simulation time step, and the S4 model and the R1 model with different thicknesses of the curved body under a different time step than the previous simulation will be tested. Through these two groups of tests, not only can the effect of thickness on lift coefficient and frequency be tested, but also the effect of time step on the simulation results. The parameters of the four models are given in Table 5-4.

Table 5-4 - The Parameters of the Models Geometry and Simulation.

Parameter	Value	Unit
Thickness of Tail	4	mm
Rectangle Length	400	mm
Rectangle Width	200	mm

Model Number	Tail Length (mm)	Curved Body Thickness (mm)	Simulation Time Step (s)
S5	40	2	0.001
R2	40	0.5	0.001
S4	30	2	0.005
R1	30	0.5	0.005

The mesh generation setting and simulation solver setting was the same as in Section 5.2, and the quality of the mesh was also checked.

5.4.2 Result

The comparison curve of lift coefficient for the first group (S5&R2 models) is shown in Figure 5.20, where the blue curve represents the R2 model (thickness 0.5mm) and the orange curve represents the S5 model (thickness 2mm). Compared to the orange curve, the blue curve has a faster response time. As can be seen in the figure, when the peak of the blue curve reaches the highest point, it is 0.246s, while the orange curve is 0.397s. In addition, when the model starts fixed-amplitude motion, the peak of the blue curve is slightly larger than that of the orange curve, whereas the vibration frequency of the orange curve is greater than that of the blue curve.

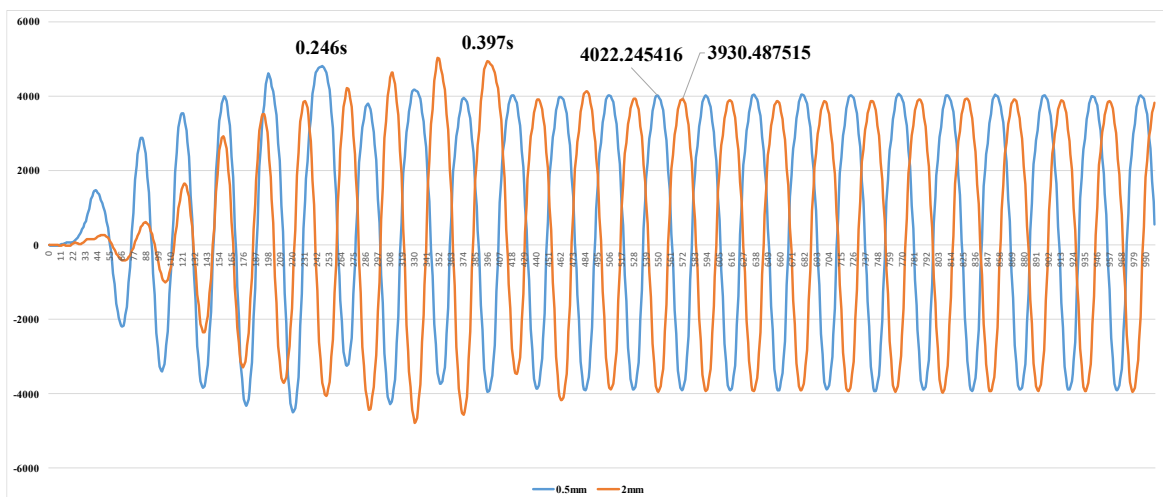


Figure 5.20 - Lift Coefficient Comparison for First Group (S5&R2).

Theoretically speaking, the larger the hydraulic diameter of a bluff body, the more energy it can harvest. The following images show the vector plots of the peak points for the S5 model and the R2 model when the model starts fixed-amplitude motion. From the comparison of the vector plots (Figure 5.21), it can be seen that when the inner diameter of the front curved body is the same, the reduction of thickness makes the boundary layer flowing through the front curved body lower, thus making the centre of the inner circulation formed at the top of the tail structure lower, which means that the inner circulation formed is closer to the tail structure. As a result, the negative pressure area formed is closer to the model, making the net lift of the model higher. For cycle 2, due to the influence of fluid viscosity, the generated inner circulation is closer to the tail structure, causing the vortex shedding to be slightly slower than cycle 1. Therefore, although the net lift of cycle 2 is greater than that of cycle 1, the frequency is smaller than that of cycle 1.

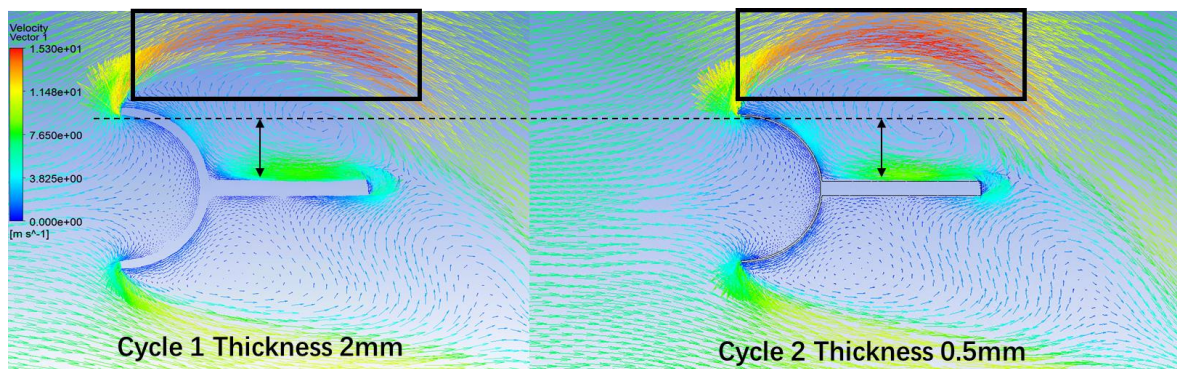


Figure 5.21 - Vector plot Comparison for First Group (S5&R2).

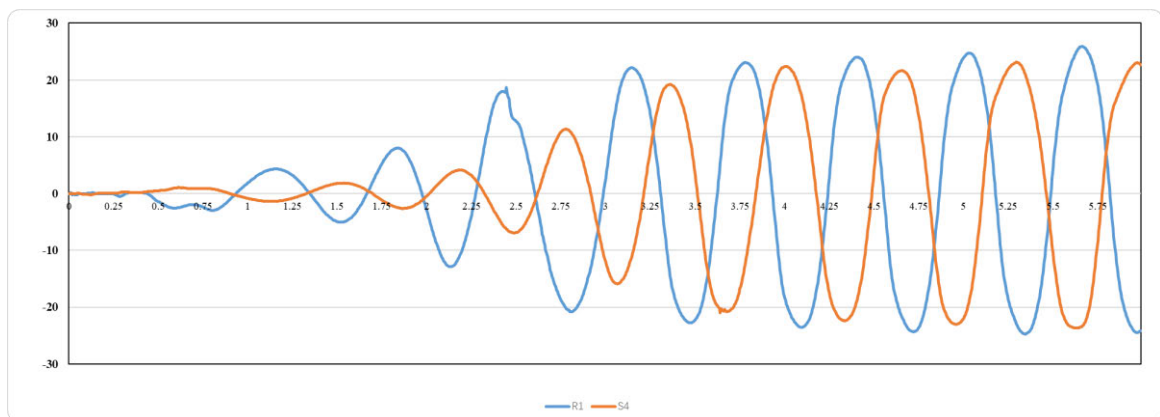


Figure 5.22 - Lift Coefficient Comparison for Second Group (S4&R1).

The second group of models (S4&R1 models) shows the same trend as the first group, with the R1 model (thickness 0.5mm) having a higher lift coefficient and faster response time, but a slightly lower frequency than the S4 model, as shown as Figure 5.22. It is worth noting that, due to the adjustment of the time step, the frequency of the second group of models is far lower than that of the first group of models. The time step of the second group is increased from 0.001s to 0.005s, while the frequency of the S4 model is about 1.6Hz, and the frequency of the S5 model is about 23Hz.

5.4.3 Discussion and Conclusion

In this section, the effect of the thickness of the curved body on the lift and frequency of the model was simulated and studied. From the results, it can be seen that although the amount of thickness change is not large (from 2mm to 0.5mm), it can still be found that the reduction of thickness increases lift and reduces frequency. In the real piezoelectric energy harvesting, the thickness of the model should be determined according to the properties of the piezoelectric kit used. If the piezoelectric kit is very sensitive to the stress applied to its surface, the thickness of the curved body should be minimized as much as possible in order to increase lift and improve the vibration amplitude. In addition, from the result in the second group, it can be seen that the simulation time step affects the frequency of the result curve. Under the same time step setting, the curve frequency can be compared to obtain the trend of change, but the calculated frequency in simulation cannot be verified with experimental data.

5.5 Conclusion

In this chapter, a simulation study of the design was conducted. First, in order to compare with the experimental results of Chapter 4, the S series models used in the experiment were studied. Then, the geometric shape of the model was changed, and the length of the tail structure was studied in more depth, exploring the performance of the model when the ratio of tail length to the diameter curved body was 3. Finally, the thickness of the curved body was studied. Through the simulation study in this chapter, it can be determined how different models perform in fluids and the state of the fluid when it flows through the models and the principle of how the lift and frequency of the model change.

When the fluid flows through the design model, the inner circulation formed on both sides at the model's tail is the main cause of the negative pressure generated. This chapter also demonstrated the effectiveness of the design. The lift coefficient of the S5 model increased by about 57% compared to the S0 model without a tail structure when the wind speed was 7m/s.

A new piezoelectric energy harvester design (a reverse C shape with a tail) has been proposed in this work. The design has a more significant lift coefficient and has the potential to have a larger energy output than the conventional designs. For the simulation study of the effect of tail length, the effect on lift coefficient and frequency has been obtained, and the experimental results will be verified with the simulation results from this study. The study has identified an opportunity for enhanced device efficiency by design and deployment that could contribute to tackling climate change.

CHAPTER 6. SIMULATION/EXPERIMENT VALIDATION

6.1 Introduction

In this chapter, the experimental results will be compared with the simulation results in order to study whether the simulation results can accurately predict the experimental results, and the results will be discussed in this context. If the simulation results can predict the experimental results, in the future improvement of the model, the initial validation can be done through simulation without the need to create a model through a 3D printer in order to reduce costs of experimentation and waste. In addition, this chapter will also discuss the power output of the piezoelectric energy harvester. The design of the model will affect the vibration amplitude and frequency of the harvester, but the harvester needs to use the piezoelectric kit to harvest energy during vibration, so it is important to explore the factors that affect the power output of the piezoelectric energy harvester. Finally, although this thesis presents a model of a piezoelectric energy harvester, there are many restrictions in its actual application. This chapter will also discuss the design of a piezoelectric energy harvester in real application.

6.2 Comparison the Result

6.2.1 Lift Force

In the experiments and simulations, the lift force of the S series models was tested, and data was collected. The differences between the lift force data in the experimental and simulation results can be observed by comparing them. In the simulation, the lift coefficient monitor was set up, and to make the data clearer and easier to compare, the reference area was also set up before the simulation. Therefore, the lift coefficient needs to be divided by the reference area in order to obtain an accurate lift coefficient. According to Equation 6.1, the lift force data simulated for the S series models can be calculated as shown in Table 6-1.

$$C_L = \frac{F_L}{\frac{1}{2}\rho V_\infty^2 l}$$

Equation 6.1

Where C_L is the lift coefficient, ρ is the fluid density, V_∞ is the velocity of fluid, l is the characteristic length and F_L is the lift force.

Table 6-1 - Lift Force (N) of Simulation Result for S Series Models.

	3 m/s (N) +/- 0.01	4 m/s (N) +/- 0.01	5 m/s (N) +/- 0.01	6 m/s (N) +/- 0.01	7 m/s (N) +/- 0.01
S0	0.22	0.41	0.64	0.97	1.34
S1	0.23	0.43	0.69	1.01	1.40
S2	0.27	0.49	0.79	1.14	1.51
S3	0.29	0.52	0.80	1.16	1.60
S4	0.31	0.55	0.94	1.35	1.73
S5	0.37	0.67	1.05	1.54	2.11

The experimental results of the lift force data were measured by a force sensor, and the force sensor was connected to the model through a cantilever beam. The force sensor measures torque and converts it into different forces in different directions. When comparing the experimental data with the simulated data, what is being compared is the lift force experienced by the model, so the experimental data needs to consider the length of the cantilever beam in order to calculate the lift force experienced by the front model. The lift force data for the experimental results of the S series models is shown in Table 6-2.

Table 6-2 - Lift Force (N) of Experiment Result for S Series Models (Aluminium).

	3m/s (N) +/- 0.01	4m/s (N) +/- 0.01	5m/s (N) +/- 0.01	6m/s (N) +/- 0.01	7m/s (N) +/- 0.01
S0	0.59	0.66	0.70	0.76	1.03
S1	0.61	0.85	0.97	1.05	1.13
S2	0.88	0.94	1.36	1.44	1.54
S3	1.13	1.27	1.49	1.68	1.90

S4	1.36	1.53	1.71	1.95	2.12
S5	1.86	2.00	2.06	2.24	2.40

For ease of comparison, the ratio of experimental results to simulation results for the S series models is shown in Figure 6.1. From the figure, the following three points of difference can be observed.

- Firstly, although the curves intersect at some points in the graph, the trend of the curves shows that, at the same wind speed, in most cases the longer-tailed models (such as the S5 model) have a larger difference between experimental and simulation results.
- Secondly, the ratio of experimental results to simulation results for the S series models increases as the wind speed increases, and the ratio of the two results is approximately 1 at a wind speed of 7m/s (the results are similar), while at low wind speeds, the simulation results are much lower than the experimental results.
- Finally, at a wind speed of 7m/s, the ratios for the S2-S5 models are all close to 1, but slightly less than 1. However, the simulation results for the S0 and S1 models at 7m/s are greater than their experimental results.

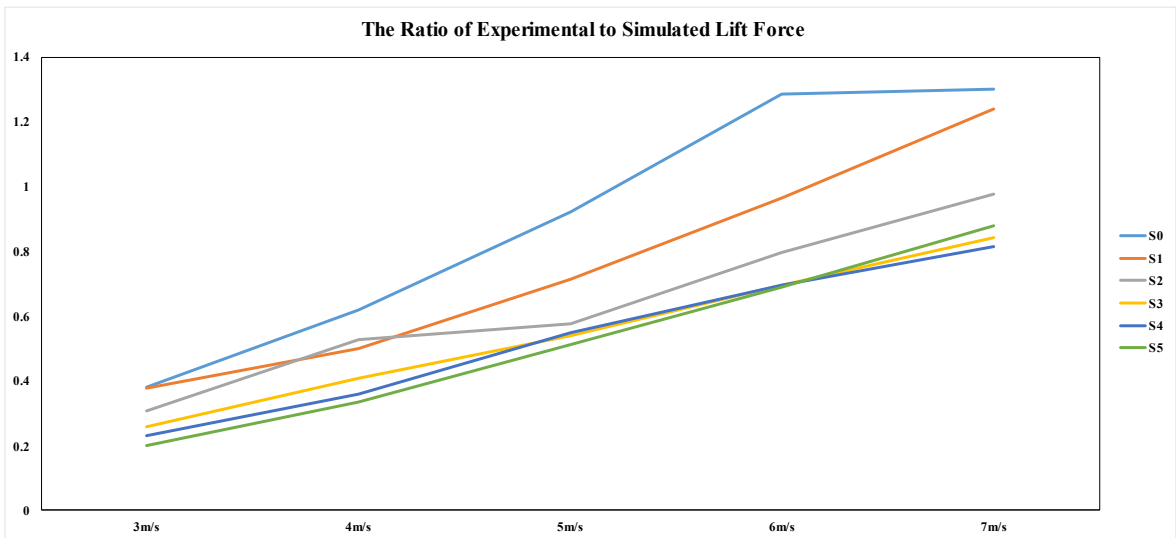


Figure 6.1 - The Ratio of Experimental to Simulated Lift Force.

Before comparing the experimental and simulation results, it is necessary to first describe the basis of the two results. The simulation results are obtained through static simulation, which means that the model remains stationary during static simulation, while the fluid

flows through the model to achieve relative motion. The experimental results are tested in a wind tunnel, where the model vibrates from left to right with the flow of the wind, and the larger the vibration amplitude of the model, the larger the data displayed by the force sensor.

First, the difference between the experimental and simulation results for the model with the longer tail is bigger. Using the S5 model and the S0 model as examples, the difference between the two models is the length of the tail. In the simulation, since the model is stationary, the model is only subjected to the lift force caused by the change in the fluid. However, as shown in Figure 6.2, when the S5 model starts to vibrate, a negative pressure appears on the left side of the model, and then the model tilts to the left side. However, with the tilt of the model, the wind at the front gives the model a drag force in the direction of deflection, causing the model to deflect over a larger range. The longer tail structure means that the drag force to the model's deflection is larger, so the difference in the results for the S5 model will be larger than the difference in the S0 model.

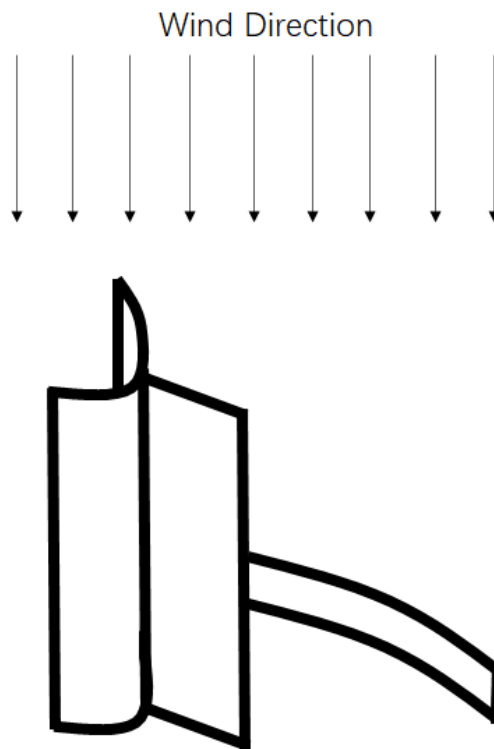


Figure 6.2 - Model Deflection Simulation Diagram.

Therefore, in general, in the experiment, the initial drag force of the model does not affect its vibration. However, once the vibration starts, the drag force increases the vibration

amplitude of the model. Because the model is fixed with the cantilever beam, when the vibration amplitude of the model reaches the maximum, the elastic potential energy of the cantilever beam will bring the model back to its original position.

Therefore, for the experimental results, the data received by the force sensor is composed of two parts, one part is the lift force caused by the shape of the model, and the other part is the drag force caused by wind. When the wind speed increases, the lift force of the model significantly increases, but due to the design of the model, the influence of the wind drag force on the model decreases, and the lift force of the model dominates. Therefore, in the experiments of the S series models, when the wind speed increases, the experimental results of the model approach the simulation results.

According to this theory, as the wind speed increases, the experimental results should approach and never exceed the simulation results. However, as can be seen in the graph, when the wind speed is 7m/s, the simulation results of the S0 and S1 models are greater than their experimental results. This is guessed to be related to the tail structure of the model. When the model deflects, the wind drag force at the front acts on the tail structure of the model for the model with a longer tail, causing the model to deflect further. However, for the S0 and S1 models, they do not have a tail, or the tail structure is too short, so there is no drag force acting on the tail structure when they deflect, but rather all the drag force acts on the curved body at the front, and that suppress their vibration. Finally, this resulted in the experimental results of the S0 and S1 models being smaller than their simulation results. There may be another reason for the abnormal lift force results of the S0 and S1 models, which will be discussed in the next section.

6.2.2 Frequency

The frequency of the simulation results is related to the time steps set in the simulation, but the trend of the frequency should be consistent with the experimental results. However, by comparing the simulation results with the experimental results, it can be found that the trend of the frequency of S0 and S1 in the experimental results is different from that in the simulation results as shown in Table 6-3 and Table 6-4.

Table 6-3 - Frequency (Hz) of Simulation Result for S Series Models.

	3 m/s (Hz) +/- 0.0001	4 m/s (Hz) +/- 0.0001	5 m/s (Hz) +/- 0.0001	6 m/s (Hz) +/- 0.0001	7 m/s (Hz) +/- 0.0001
S0	14.0845	18.6672	23.3918	27.7778	31.4961
S1	13.7457	18.4162	22.7273	27.3973	31.2500
S2	13.5135	18.1818	22.4215	26.6667	31.0559
S3	12.6183	16.6667	20.5761	24.4756	28.5714
S4	12.0482	15.8730	19.4175	23.1793	27.0270
S5	10.4932	13.6986	16.8776	20.1613	23.2558

Table 6-4 - Frequency (Hz) of Experiment Result for S Series Models.

	3m/s (Hz) +/- 0.0001	4m/s (Hz) +/- 0.0001	5m/s (Hz) +/- 0.0001	6m/s (Hz) +/- 0.0001	7m/s (Hz) +/- 0.0001
S0	1.5701	1.5679	1.5843	1.5610	1.5497
S1	1.5871	1.5637	1.6026	4.6904	4.6339
S2	4.3649	4.3898	4.3649	4.3440	4.3478
S3	4.1771	4.2463	4.2123	4.2159	4.2017
S4	4.1305	4.1459	4.1442	4.0933	4.1322
S5	3.9216	3.9216	3.9479	3.9293	3.9185

According to the simulation results, the longer the tail length, the lower the vibration frequency, while in the experimental results, the frequency of the S1 model suddenly rises and exceeds other models when the wind speed is 6m/s. The S0 model has the lowest frequency among all models at all experimental wind speeds. This is related to the statistics of the experimental results, which can be seen in Figure 6.3; the lift coefficient curve of the S0 model is not a simple sine wave shape, but a periodicity high-frequency small-amplitude

vibration. The curve of the S1 model before the wind speed is 6m/s is similar to that of the S0 model, but when the wind speed is 6m/s, its waveform becomes a sine wave shape.

Since the vibration of the S0 model can be observed to have a clear periodicity, the frequency of such periodic small-amplitude vibrations is assumed to be the periodic frequency. Comparison with the simulation result shows that the vibration frequencies of the S0 and S1 models are theoretically higher than those of the other models. However, due to their vibration process in the experiment, it is difficult to determine their vibration frequencies, which ultimately leads to the inconsistency between the experimental results and the simulation results.

Overall, the reason for the inconsistency between the experimental results and the simulation results is due to the different statistical methods used for the experimental results. If the frequency is calculated based on the small-amplitude vibrations of the S0 and S1 models, their frequencies are indeed higher than those of the other models, which is consistent with the trend of the simulation results.

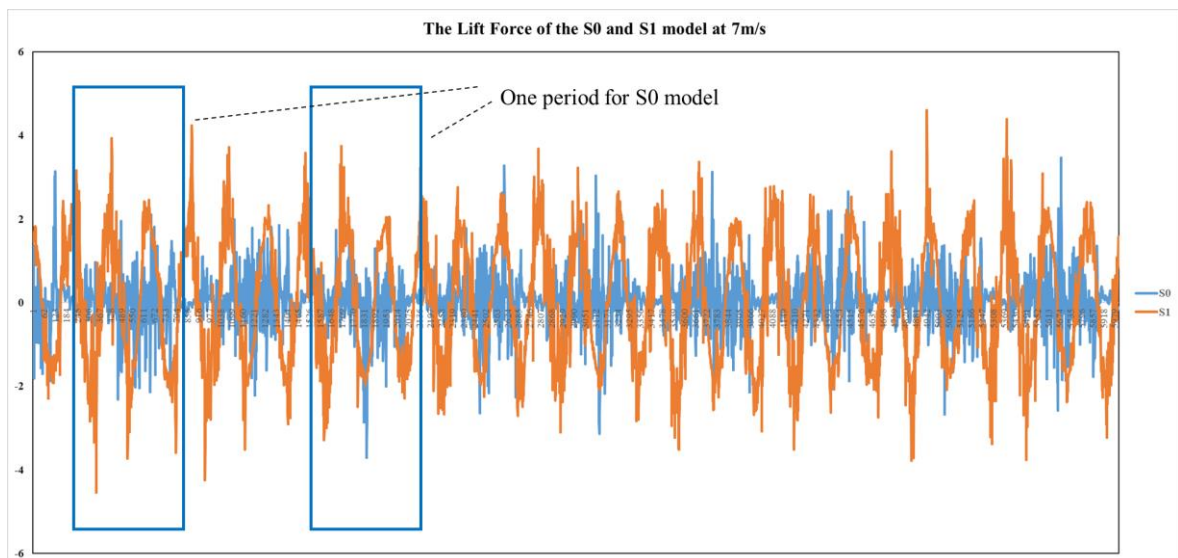


Figure 6.3 - The Lift Force of the S0 and S1 Model at 7m/s (Aluminium).

Similarly, the difference between the lift coefficient result of the S0 and S1 models in the experiment and the simulation result may also be due to the fact that they are not sine wave shapes, so their peak lift coefficient can only be calculated by calculating the average of the peak values of the small-amplitude vibrations, which leads to errors.

Regarding the experimental results of the vibration frequency of the S series model, it can be seen from Figure 4.16 (aluminium cantilever beam) and Figure 4.25 (plastic cantilever beam), the frequency of the S series model decreases with increasing wind speed. But the simulation results show that as the wind speed increases, the inner circulation falls off faster, so the frequency increases. This difference should also be related to the drag force of the wind to the model. As the wind speed increases, although the influence of the drag force on the maximum vibration amplitude becomes smaller, the drag force prevents the model from returning to the starting point, thus increasing the model's vibration period time. So the experimental results will show that the vibration amplitude of the model is lower when the wind speed is higher.

Therefore, by comparing, it can be basically proved that the simulation results are effective. When evaluating the impact of the bluff body structure on the piezoelectric energy harvester, simulation can be used for analysis. Although factors such as the drag force need to be considered in the experiment, the general trend can be effectively analysed by simulation.

6.3 Power Output Analysis

The piezoelectric kit is placed on the cantilever beam at the rear of the model, and the application of stress to the surface of the piezoelectric kit will cause it to produce the power output. Therefore, in the experiment, the bending of the cantilever beam causes the piezoelectric kit to bend, thereby producing power output. In the experiment, the high lift force results mean that its angle of deflection is greater, and the models with high lift force results also have higher power output in the experiment. In addition, it can be found from the comparison between Figure 4.16 and Figure 4.17 that the increasing rate of lift force curve of the S series models is roughly the same, but the output voltage curve of the S1 model rises significantly when the wind speed is 5m/s, and it is also at 5m/s that the frequency of the S1 model starts to rise. Therefore, it can be proved that the power output of the piezoelectric kit is positively correlated with the vibration and lift force of the model. As two important parameters (vibration frequency and lift force) affecting the power output of the piezoelectric kit, it is difficult to determine which factor has a greater impact on power output based on experimental results. However, according to simulation results,

as the tail length continues to increase, the lift coefficient will continue to rise, while the vibration frequency will continue to decrease. Therefore, with the increase in tail length, the drag force the model receives will further increase, meaning that the model's vibration frequency will be lower than the simulation results. So, it can be expected that as the model's tail length continues to increase to a certain critical point, the model's voltage generated and power output will begin to decrease due to its too-low vibration frequency as shown in Figure 6.4.

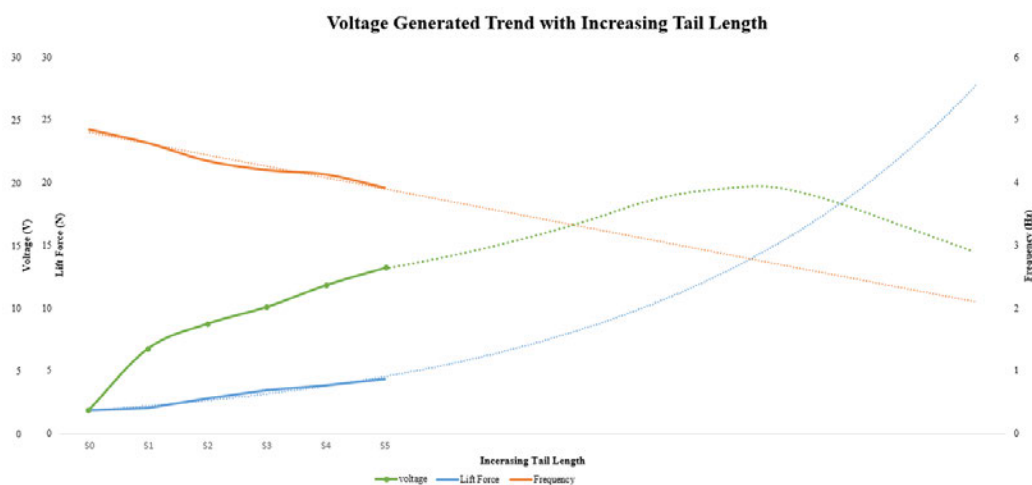


Figure 6.4 - Power Output Trend with Increased Tail Length.

6.4 Piezoelectric Energy Harvesters in Real Application

It can be seen from the experimental results that there are some differences of the vibration data (lift force etc.) and power output of the model between the experimental result and the simulation result. For example, in simulation, the thinner the thickness of the front curved body of the model, the greater the lift force will be, but in the actual experiments, the model with a thin curved body is easy to fail in production and easily damaged in experiments, especially in the case of high wind speeds. Therefore, in this section, the design of the novel piezoelectric energy harvester will be considered and analysed from a practical perspective, combining experimental results and simulation results. The analysis will be divided into three aspects: firstly, analysing the design of the front model; secondly, analysing the selection of the cantilever beam; and finally, analysing the piezoelectric film.

Firstly, for the front-end model, in this article's experiment, the front-end model uses a 3D printer for printing. Using a 3D printer has the advantage of making the model more convenient and with lower production costs. However, because the model is made of plastic, it results in the overall weight of the model being lighter, and because the 3D printer will print the model layer by layer, in some thinner structures, the printed model is prone to breaking or defects. When the vibration frequency of an object is close to its natural frequency, the vibration amplitude of the object will increase. Therefore, in the design of piezoelectric energy harvesters, the vibration frequency of the model and cantilever beam should be as close as possible to their natural frequency. Generally, the greater the mass, the lower the natural frequency. And because plastic models are prone to damage, it is possible to use a 3D printer to make models during the experiment to determine the performance of the model, but in practical applications, models can be made of aluminium or other metals so that the model's surface body thickness can be thinner, the model more robust, and its natural frequency also lower. Additionally, mass blocks can be added to the end of the cantilever beam to increase the overall weight and adjust the overall natural frequency while ensuring the model remains unchanged as shown in Figure 6.5.

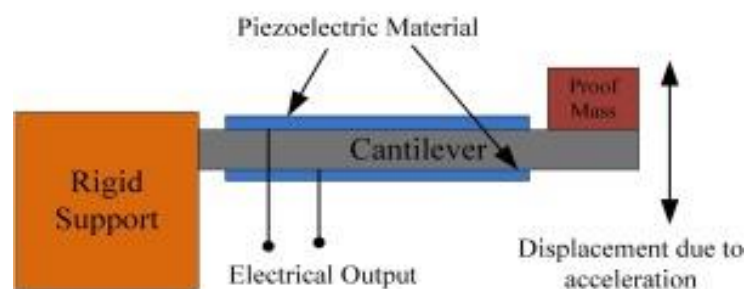


Figure 6.5 - Cantilever Beam with Mass Block [8].

The selection of the cantilever beam has long been an important indicator that affects the piezoelectric energy harvester, which has been overlooked in many kinds of research. Through the comparison of the experiment results of different cantilever beams, it can be

seen that different cantilever beams can not only affect the vibration performance of the front-end model but also affect the power output of the entire piezoelectric energy harvester. In this article, two different cantilever beams, aluminium cantilever beams and plastic cantilever beams, were used. Although the plastic cantilever beam has better results in some model experiments because it is closer to its natural frequency, the performance of the model with a plastic cantilever beam is not stable, and it depends on the larger wind speed. At low wind speeds, its performance is not as good as the aluminium cantilever beam. If the weight of the front-end model is adjusted so that the model with the aluminium cantilever beam is also close to its natural frequency, the performance of the aluminium cantilever beam should be better than that of the plastic cantilever beam. Aluminium cantilever beams are widely used in most piezoelectric energy harvesting research, but as the front-end model continues to improve, the amplitude and frequency of vibrations also increase.

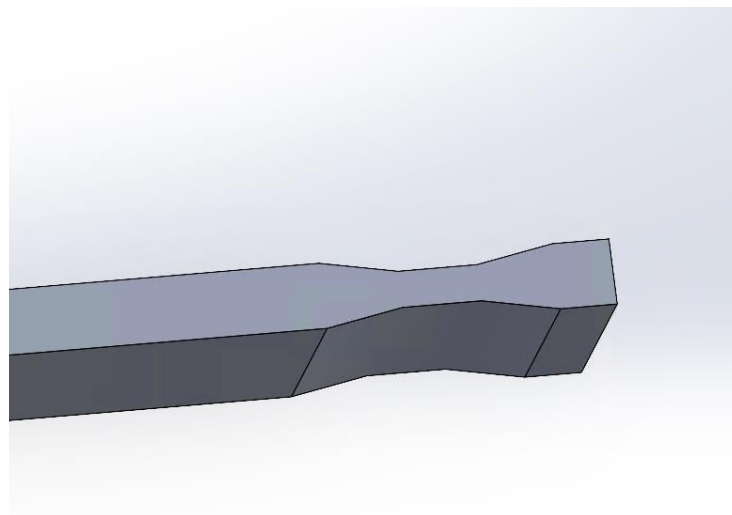


Figure 6.6 – Tail Structure with Grooves.

In the experiments conducted of this thesis, two aluminium cantilever beams have broken due to metal fatigue. In the future design of piezoelectric energy harvesters, the metal fatigue of the cantilever beam should be taken into consideration.

According to the flow trend of the fluid in the simulation results of this thesis, adding two grooves on both sides of the end of the tail structure, as shown in Figure 6.6, may further increase the performance of the piezoelectric energy harvester.

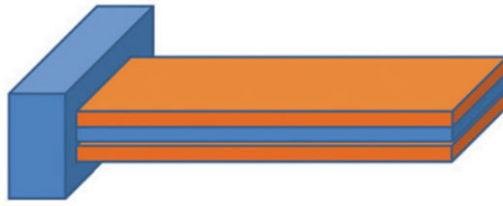


Figure 6.7 - Illustration of a Cantilever Beam Covered with Piezoelectric Films on Both Sides.

Finally, the piezoelectric kit is the most important component in the entire piezoelectric energy harvester, and its function is to convert vibration into power output. In the experiment, only one piezoelectric kit was placed on one side of the cantilever beam, but in practical applications, piezoelectric kits can be placed on both sides of the cantilever beam, and the number of placed piezoelectric films can be increased. Under ideal conditions, a whole piezoelectric film is placed on both sides of the cantilever beam as shown in Figure 6.7, so as to maximize the power output of the entire piezoelectric energy harvester. In the comparison of the two different piezoelectric kits, it can be seen that the M-2807-P2 piezoelectric kit although more expensive, is roughly ten times the cost of the LDT0-28K piezoelectric film (about 40 pounds), but its voltage output is also nearly ten times higher than LDT0-28K. Because the surface space of the cantilever beam is limited, LDT0-28K piezoelectric film is a better choice for piezoelectric film selection.

6.5 Conclusion

In this chapter, through the comparison of experimental results and simulation results, it is proven that simulation can be used in the design model stage to determine the effectiveness of the innovative design. And there are some differences between the experimental results and the simulation results, which also conforms to the principle of galloping. Galloping, as a widely used vibration in piezoelectric energy harvesters, is mainly characterized by the fact that the object's vibration is enhanced due to the force direction and its motion direction being the same. And the amplitude of galloping will increase with the increase of wind speed, unlike VIV.

This chapter also provides a brief analysis of energy output and gives the direction that needs to be taken into account when designing piezoelectric energy harvesters in real

application in the end. Overall, through this chapter, the validity of experimental results and simulation results can be basically determined.

CHAPTER 7. CONCLUSION

7.1 Experimental Findings

7.1.1 Conclusion

During the experimental phase, three series of models were mainly used for comparative experiments, and two different materials of cantilever beams (aluminium and plastic cantilever beams) were also selected to be compared with the S series models. Finally, a comparison was also made between the two widely used piezoelectric kits. The experimental data came from the force sensors placed at the end of the cantilever beam and the oscilloscope connected to the piezoelectric kit on the surface of the cantilever beam.

Specific findings are as follows:

- Adding a tail structure behind the traditional curved body structure was observed to improve the model's performance effectively. The T2 model has another 22.75mm tail structure than the T1 model, but when the wind speed is 7m/s, the lift coefficient of the T2 model is twice that of the T1 model, and the voltage output is about five times that of the T1 model.
- The originally planned A series models were redesigned as S series models due to the problem of different models' centre of gravity. The S series models consist of six models with increasing tail lengths, where the tail length of the S5 model is 40mm, and the S0 is a curved body structure without a tail. It was observed that the peak lift of the S5 model was approximately 2.5 times that of the S0 model under the experimental wind speed. At a wind speed of 7m/s, the power output of the model (S5 model) was $175.48 \mu W$, while that of the S0 model was only $3.54 \mu W$. This verified that the model is more effective and improves.
- The R series models were mainly used to study the effect of the front curved body thickness of the model on the model performance. When the thickness becomes thinner, both lift and voltage output will have a small increase.
- The experimental comparison of the two cantilever beams shows that the natural frequency of the model and the cantilever beam has a great impact on the vibration

performance of the model. Although plastic cantilever beams have a larger power output at a specific wind speed, the power output of aluminium cantilever beams is more stable at all wind speeds.

- Finally, the experiments for different piezoelectric films show that the M-2807-P2 piezoelectric film has excellent performance, and once again verifies the excellent power output of the S5 model. When the M-2807-P2 piezoelectric film is used, the S5 model can reach a power output of 2.152mw at 7m/s, while the S0 model is only 0.057mw.

7.1.2 Suggestions for Future Work

In the experiments of the A series models, due to the significant change in the centre of gravity of each model of the A series, the data recorded by the force sensor fixed at the end of the cantilever beam cannot be effectively analysed for this series of models. And in the test of the A series models, there were two breaks of the aluminium cantilever beam, which also increased the duration of the experiment. However, the centre of gravity of the S series models also changes, but the change is small and can be ignored in the calculation. Although the performance of the model can be observed through the results of voltage output and power output, the lift results of the model can be compared with the simulated lift force results. Therefore, in subsequent research, the tail structure can be separately made with lightweight materials and then pasted on the back of the curved body, so that more accurate lift force results can be obtained through the force sensor.

Additionally, in the experiments of this thesis, the research on cantilever beams is limited to the study of their materials due to time constraints. In subsequent research, the length, width, and thickness of the cantilever beams can be further studied. The position of the piezoelectric kit on the cantilever beam can also be studied in the future. Theoretically, the more piezoelectric kits are placed, the greater the overall energy output will be. However, considering the price of the piezoelectric kits, the most suitable position for placing the piezoelectric films should be found in order to maximize power output.

Finally, this paper presents a model, but other parameters of the model can also be studied in the future, such as the length of the model's curved surface, the thickness of the model's

tail, and other factors, so that the performance of the model can be further improved based on the research in this thesis.

7.2 Simulated Findings

7.2.1 Conclusion

In the simulation stage, in addition to simulating the S series models and R series models used in the experiment in 2D, further simulation research was also conducted on the length of the tail. In this study, the longest model's tail length was increased to three times the diameter of the front curved body.

The main findings in the simulation are as follows:

- The formation of inner circulation at the back of the curved body is one of the main reasons for the lift generated by the model. For models without a tail structure, inner circulation also forms, but the area is smaller, so the area of the negative pressure region is smaller, and the lift is smaller eventually. In contrast, for the model, due to the obstruction of the tail structure, the area of the inner circulation generated on both sides will increase as the tail length increases. Although this will cause the frequency of vortex shedding to decrease, it will greatly increase the lift of the model.
- Additionally, it can be seen from the flow of fluid that when vibration first starts, the lift force will reach a peak, and afterwards the lift force peak value will slightly decrease and remain stable. This is due to the fluid flowing through the end of the tail structure at one side flowing towards the other side. If this situation can be avoided, the lift force will be further enhanced.
- It is undeniable that as the length of the tail structure increases, the lift force will be greater, but the vibration frequency of the model will decrease. Because power output is affected by both the vibration amplitude and frequency, when the tail length increases to a certain critical point, power output will begin to decrease, and the power output and tail length curve is expected to be a parabolic shape.
- Finally, it has been proven that the front end of the curved body becoming thinner will indeed increase lift force; this is due to the inner circulation generated on one side of

the tail structure being closer to the model surface. This will make the negative pressure on the model surface lower, and thus obtaining greater lift force.

7.2.2 Suggestions for Future Work

Through simulation, it can be seen that the inner circulation formed at the tail is the main reason for the lift force generated, so in future research, the model design can be appropriately changed to increase the inner circulation area. Additionally, in order to obtain higher lift force, in the future one can try to add a groove on the ends of the tail structure on both sides, so that the fluid can flow along the groove instead of flowing to the other end of the tail structure.

In subsequent simulations, further research can also be done on the thickness of the tail structure. According to existing research theory, the thinner the tail structure, the greater the lift will be. But this theory still needs to be verified by subsequent simulations.

It is worth noting that the simulation used in this article is a static 2D model, so only changes in fluid flow through the model can be observed. In subsequent research, a dynamic 3D model can be used for simulation to obtain more accurate results.

7.3 Validating Findings

7.3.1 Conclusion

In comparing the experimental and simulation results, the main comparison was of the lift and frequency results. And based on these two results, suggestions were given for improvements in energy output and the application of piezoelectric energy harvesters in real application.

The main findings of the validation are as follows:

- By comparing the experimental results with the simulation results, the effectiveness of the model was verified, and it was observed that the difference between the simulation and experimental results increases as the tail structure of the model becomes longer.
- The cause of this difference is considered to be the combined effect of the lift force and the drag force that the model receives. The drag force that the model receives is

in the same direction as the movement of the model, which allows the model to obtain a greater amplitude, which is consistent with the principle of the galloping motion.

- The larger the experimental wind speed is, the closer the simulation results are to the experimental results. This is considered to be due to the fact that under high wind speeds, the lift force is the main driving force for the model's vibration. Therefore, the proportion of interference from the drag force the model receives is reduced, thus making the two results closer.
- However, it is also due to the drag force that the model receives that the vibration period time of the model becomes longer, thereby reducing the vibration frequency. This makes the vibration frequency of the model increase with wind speed in the simulation, but in the experiment, the frequency of the same model remains unchanged at different wind speeds.

7.3.2 Suggestions for Future Work

From the comparison, it can be seen that the difference between the simulation and experimental results can be explained and accepted. Therefore, in subsequent designs, initial research and validation can be performed through simulation in order to reduce experimental consumption. Experimentation is also necessary due to the drag force, especially if the initial validation uses 2D static simulation.

Since only lift force and frequency results can be given in the simulation, while power output is related to both parameters, in future experiments, models with longer tail lengths should be made and tested in experiments, and the power output of different tail length models should be recorded in order to find the best tail length size.

In the future, the production of experimental models should calculate the natural frequency of the model and cantilever beam, and by changing materials, adding counterweights and other methods, so that the produced model can approach its natural frequency, and achieve better results.

In general, the design of the front-end model is one aspect of improving the efficiency of the piezoelectric energy harvester. The selection of the cantilever beam and the selection of the piezoelectric kit will also greatly affect the power output of the harvester. When

designing the front-end model, it is also necessary to consider whether it can match the piezoelectric kit used. Some piezoelectric kits have a maximum bending angle, if exceeded, it may damage the piezoelectric kit. Therefore, in the design of future practical applications, if the design of the front-end model, the selection of the cantilever beam, and the selection of the piezoelectric kit can be matched, the piezoelectric energy harvester will have higher power output and more widely used.

REFERENCES

- [1] S. Sharma, R. Kiran, P. Azad, and R. Vaish, "A review of piezoelectric energy harvesting tiles: Available designs and future perspective," *Energy Convers. Manag.*, vol. 254, no. January, p. 115272, 2022, doi: 10.1016/j.enconman.2022.115272.
- [2] X. Zheng, L. He, S. Wang, X. Liu, R. Liu, and G. Cheng, "A review of piezoelectric energy harvesters for harvesting wind energy," *Sensors Actuators A Phys.*, vol. 352, no. October 2022, p. 114190, 2023, doi: 10.1016/j.sna.2023.114190.
- [3] M. R. Sarker, S. Julai, M. F. M. Sabri, S. M. Said, M. M. Islam, and M. Tahir, "Review of piezoelectric energy harvesting system and application of optimization techniques to enhance the performance of the harvesting system," *Sensors Actuators, A Phys.*, vol. 300, p. 111634, 2019, doi: 10.1016/j.sna.2019.111634.
- [4] A. A. Babayo, M. H. Anisi, and I. Ali, "A Review on energy management schemes in energy harvesting wireless sensor networks," *Renew. Sustain. Energy Rev.*, vol. 76, no. October 2016, pp. 1176–1184, 2017, doi: 10.1016/j.rser.2017.03.124.
- [5] S. M. Bozorgi, A. Shokouhi Rostami, A. A. R. Hosseinabadi, and V. E. Balas, "A new clustering protocol for energy harvesting-wireless sensor networks," *Comput. Electr. Eng.*, vol. 64, pp. 233–247, 2017, doi: 10.1016/j.compeleceng.2017.08.022.
- [6] S. Panda *et al.*, "Piezoelectric energy harvesting systems for biomedical applications," *Nano Energy*, vol. 100, no. April, p. 107514, 2022, doi: 10.1016/j.nanoen.2022.107514.
- [7] Yole Developpement, "Examples of bioMEMS-enabled systems," *Glass & silicon for BioMEMS The heart of tomorrow's medical devices*. http://www.yole.fr/iso_upload/News/2020/PR_BIOMEMS_TELEDYNE_YOLEGROUP_Nov2020.pdf.
- [8] M. R. Sarker, S. Julai, M. F. M. Sabri, S. M. Said, M. M. Islam, and M. Tahir, "Review of piezoelectric energy harvesting system and application of optimization techniques to enhance the performance of the harvesting system," *Sensors Actuators A Phys.*, p. 111634, 2019, doi: 10.1016/j.sna.2019.111634.
- [9] J. P. Thomas, M. A. Qidwai, and J. C. Kellogg, "Energy scavenging for small-scale unmanned systems," *J. Power Sources*, vol. 159, no. 2, pp. 1494–1509, 2006, doi: 10.1016/j.jpowsour.2005.12.084.
- [10] P. Harrop and R. Das, "Energy Harvesting and Storage for Electronic Devices 2010–2020," *IDTechEx*, vol. (n.d.), 2020.
- [11] M. Gaynor and J. Waterman, "Design framework for sensors and RFID tags with healthcare applications," *Heal. Policy Technol.* 5, pp. 357–369, 2016.
- [12] SFH 7741-Z OSRAM Opto Semiconductors Inc. Sensors, "Transducers," *DigiKey*, 2010.
- [13] "SFH 5711-2/3-Z by OSRAM Opto Semiconductors | Ambient Light Sensor," 2019. (n.d.) Arrow.com.
- [14] P. Stanley-Marbell and D. Marculescu, "An 0.9 x 1.2" Low power, energy-harvesting system with custom multi-channel communication interface, 2007 Des. Autom. Test Eur. Conf. Exhib.," *IEEE*, pp. 1–6, 2007.

- [15] J. Ryckaert *et al.*, "Ultra-wide-band transmitter for low-power wireless body area networks: design and evaluation," *IEEE Trans, IEEE Trans. Circuits Syst. I Regul. Pap.*, vol. 52, pp. 2515–2525, 2005.
- [16] iMEMS®ADXL103, "ADXL203 And ADXL204 - Analog Devices Inc. -Accelerometers Online Catalog, 2004–2018, DigiKey Electronics, 2018."
- [17] J. A. Paradiso and M. Feldmeier, "A. Compact, Wireless, Self-Powered Pushbutton Controller, Springer, Berlin, Heidelberg, 2001, pp. 299–304."
- [18] S. Grady, "Zero Power Wireless Sensors Using Energy Processing, 2011."
- [19] S. Roundy and P.K. Wright, "A Piezoelectric Vibration Based Generator for Wireless Electronics, 2004."
- [20] M. Ferrari, V. Ferrari, M. Guizzetti, and D. Marioli, "An autonomous battery-less sensor module powered by piezoelectric energy harvesting with RF transmission of multiple measurement signals, *Smart Mater. Struct.* 18(2009), 085023."
- [21] X. Jiang, J. Polastre, and D. Culler, "Perpetual environmentally powered sensor networks, in: IPSN 2005. Fourth Int. Symp. Inf. Process. Sens. Networks, IEEE, 2005, pp. 463–468."
- [22] "Best Research-Cell Efficiencies," *National Renewable Energy Laboratory (NREL) [Public domain]*, 2019. <https://www.nrel.gov/pv/cell-efficiency.html> (accessed Dec. 25, 2019).
- [23] Z. K. Chou SK, Yang WM, Chua KJ, Li J, "Development of micro power generators – a review," *Appl Energy*, vol. 88, pp. 1–16, 2011.
- [24] G. M., "Solar energy conversion by dye-sensitized photovoltaic cells," *Inorg Chem*, vol. 44, no. 68, pp. 41–51, 2005.
- [25] E. Y. Danick Briand and S. Roundy, *Micro Energy Harvesting*. 2015.
- [26] C. Forman, I. K. Muritala, R. Pardemann, and B. Meyer, "Estimating the global waste heat potential," *Renew. Sustain. Energy Rev.*, vol. 57, pp. 1568–1579, 2016, doi: 10.1016/j.rser.2015.12.192.
- [27] A. A. Sebald G, Guyomar D, "On thermoelectric and pyroelectric energy harvesting," *Smart Mater Struct*, vol. 18:125006, 2009.
- [28] L. C. Lu Z, Zhang H, Mao C, "Silk fabric-based wearable thermoelectric generator for energy harvesting from the human body," *Appl Energy*, vol. 164, pp. 57–63, 2016.
- [29] Renewable Energy Enquiries Bureau, "The UK wind energy resource (Wind Energy Fact Sheet 8)," 2001. <http://webarchive.nationalarchives.gov.uk/http://www.berr.gov.uk/files/file17789.pdf> (accessed Dec. 27, 2017).
- [30] J. Zhang, Z. Fang, C. Shu, J. Zhang, Q. Zhang, and C. Li, "A rotational piezoelectric energy harvester for efficient wind energy harvesting," *Sensors Actuators, A Phys.*, vol. 262, pp. 123–129, 2017, doi: 10.1016/j.sna.2017.05.027.
- [31] Z. Xie, C. A. Kitio Kwuimy, Z. Wang, and W. Huang, "A piezoelectric energy harvester for broadband rotational excitation using buckled beam," *AIP Adv.*, vol. 8, no. 1, 2018, doi: 10.1063/1.5018077.
- [32] Z. Xie, J. Xiong, D. Zhang, T. Wang, Y. Shao, and W. Huang, "Design and experimental investigation of a piezoelectric rotation energy harvester using bistable and frequency up-conversion mechanisms," *Appl. Sci.*, vol. 8, no. 9, 2018, doi: 10.3390/app8091418.

- [33] X. Cui, M. Teng, and J. Hu, "PSPICE-based analyses of the vibration energy harvester system with multiple piezoelectric units, *Can. J. Electr. Comput.*," *Comput. Eng.*, vol. 38, pp. 246–250, 2015.
- [34] M. Rezaeisaray, M. El Gowini, D. Sameoto, D. Raboud, and W. Moussa, "Low frequency piezoelectric energy harvesting at multi vibration mode shapes," *Sensors Actuators, A Phys.*, vol. 228, pp. 104–111, 2015, doi: 10.1016/j.sna.2015.02.036.
- [35] P. Panthongsy, D. Isarakorn, P. Janphuang, and K. Hamamoto, "Fabrication and evaluation of energy harvesting floor using piezoelectric frequency up-converting mechanism," *Sensors Actuators, A Phys.*, vol. 279, pp. 321–330, 2018, doi: 10.1016/j.sna.2018.06.035.
- [36] A. Karami, Di. Galayko, and P. Basset, "A Novel Characterization Method for Accurate Lumped Parameter Modeling of Electret Electrostatic Vibration Energy Harvesters," *IEEE Electron Device Lett.*, vol. 38, no. 5, pp. 665–668, 2017, doi: 10.1109/LED.2017.2682232.
- [37] Z. Zhang, H. Xiang, Z. Shi, and J. Zhan, "Experimental investigation on piezoelectric energy harvesting from vehicle-bridge coupling vibration," *Energy Convers. Manag.*, vol. 163, no. January, pp. 169–179, 2018, doi: 10.1016/j.enconman.2018.02.054.
- [38] Y. Pei, Y. Liu, and L. Zuo, "Multi-resonant electromagnetic shunt in base isolation for vibration damping and energy harvesting," *J. Sound Vib.*, vol. 423, pp. 1–17, 2018, doi: 10.1016/j.jsv.2018.02.041.
- [39] J. Leicht and Y. Manoli, "A 2.6 μ w-1.2 mW Autonomous Electromagnetic Vibration Energy Harvester Interface IC with Conduction-Angle-Controlled MPPT and up to 95% Efficiency," *IEEE J. Solid-State Circuits*, vol. 52, no. 9, pp. 2448–2462, 2017, doi: 10.1109/JSSC.2017.2702667.
- [40] R. Bolt, M. Magno, T. Burger, A. Romani, and L. Benini, "Kinetic AC/DC Converter for Electromagnetic Energy Harvesting in Autonomous Wearable Devices," *IEEE Trans. Circuits Syst. II Express Briefs*, vol. 64, no. 12, pp. 1422–1426, 2017, doi: 10.1109/TCSII.2017.2768391.
- [41] J. He *et al.*, "Triboelectric-piezoelectric-electromagnetic hybrid nanogenerator for high-efficient vibration energy harvesting and self-powered wireless monitoring system," *Nano Energy*, vol. 43, no. August 2017, pp. 326–339, 2018, doi: 10.1016/j.nanoen.2017.11.039.
- [42] V. Dragunov and V. Dorzhiev, "Electrostatic vibration energy harvester with increased charging current," *J. Phys. Conf. Ser.*, vol. 476, no. 1, pp. 0–5, 2013, doi: 10.1088/1742-6596/476/1/012115.
- [43] F. U. Khan and M. U. Qadir, "State-of-the-art in vibration-based electrostatic energy harvesting," *J. Micromechanics Microengineering*, vol. 26, no. 10, 2016, doi: 10.1088/0960-1317/26/10/103001.
- [44] F. Cerini *et al.*, "Electro-mechanical modelling and experimental characterization of a high-aspect-ratio electrostatic-capacitive MEMS device," *Sensors Actuators, A Phys.*, vol. 266, pp. 219–231, 2017, doi: 10.1016/j.sna.2017.07.048.
- [45] H. Hayashi, M. Suzuki, A. Mori, T. Sugiyama, and G. Hashiguchi, "Electrostatic micro transformer using potassium ion electret forming on a comb-drive actuator," *2013 Transducers Eurosensors XXVII 17th Int. Conf. Solid-State Sensors, Actuators*

- Microsystems, TRANSDUCERS EUROSENSORS 2013*, vol. 100, no. June, pp. 442–445, 2013, doi: 10.1109/Transducers.2013.6626798.
- [46] N. G. Elvin, N. Lajnef, and A. A. Elvin, “Feasibility of structural monitoring with vibration powered sensors,” *Smart Mater. Struct.*, vol. 15, pp. 977–986, 2006.
- [47] F. Duck, “The electrical expansion of quartz ’by Jacques and pierre curie,” *Ultrasound*, vol. 17, pp. 197–203, 2019.
- [48] H. Krautkrämer, J. & Krautkrämer, “Ultrasonic Testing of Materials,” *Springer*, 1990.
- [49] R. S. C. Manbachi, A. & Cobbold, “Development and Application of Piezoelectric Materials for Ultrasound Generation and Detection,” *Ultrasound*, vol. 19, no. 4, pp. 187–196, 2011, doi: 10.1258/ult.2011.011027.
- [50] K. A. Cook-Chennault, N. Thambi, and A. M. Sastry, “Powering MEMS portable devices-a review of non-regenerative and regenerative power supply systems with special emphasis on piezoelectric energy harvesting systems,” *Smart Mater. Struct.*, vol. 17, no. 4, p. 043001, 2008.
- [51] J. Liang and W.-H. Liao, “Energy flow in piezoelectric energy harvesting systems,” *Smart Mater. Struct.*, vol. 20, no. 1, p. 015005, 2011.
- [52] M. Akizuki, M. S. Hampar, and J. Zussman, “An explanation of anomalous optical properties of topaz,” *Mineral. Mag.*, vol. 43, no. 326, pp. 237–241, 1379, doi: 10.1180/minmag.1979.043.326.05.
- [53] S. V. Kalinin, A. N. Morozovska, and L. Qing, “Reports on Progress in Physics Related content Ferroelectric , dielectric and piezoelectric properties of ferroelectric thin films and ceramics,” 1998.
- [54] Morgan Technical Ceramics, *Physical Basis*. 2013.
- [55] W. Liao, X. Do, and L. SG, “A self-power and optimal SSHI circuit integrated with an active rectifier for piezoelectric energy harvesting,” *IEEE Trans. Circuits Syst. I Regul. Pap.*, vol. 64, no. 3, pp. 537–549, 2017.
- [56] L. D. Landau, E. M. Lifshitz, and L. P. Pitaevskii, *Electrodynamics of continuous media*. Elsevier Butterworth-Heinemann.
- [57] C. Radusinović, Dušan & Markov, “Macedonite – lead titanate: a new mineral,” *Am. Mineral.*, vol. 56, pp. 387–394, 1971.
- [58] E. A. J. Burke and C. Kieft, “Second occurrence of makedonite, PbTiO₃, Långban, Sweden,” *Lithos*, vol. 4, pp. 101–104, 1971, doi: 10.1016/0024-4937(71)90102-2.
- [59] S. R. Anton and H. A. Sodano, “A review of power harvesting using piezoelectric materials (2003-2006),” *Smart Mater. Struct.*, vol. 16, no. 3, 2007, doi: 10.1088/0964-1726/16/3/R01.
- [60] L. J. H. and K. S. K. Lee C S, Joo J, Han S, “Poly(vinylidene fluoride) transducers with highly conducting poly(3,4-ethylenedioxythiophene) electrodes Proc. Int.,” *Sci. Technol. Synth. Met.*, vol. 152, pp. 49–52, 2005.
- [61] P. Paufler, “Fundamentals of Piezoelectricity,” *Zeitschrift für Krist.*, vol. 199, no. 1–2, pp. 158–158, 1992, doi: 10.1524/zkri.1992.199.1-2.158.
- [62] C S Lee, Joo J, Han S, and Koh S K, “Multifunctional transducer using poly(vinylidene fluoride) active layer and highly conducting poly(3,4-ethylenedioxythiophene) electrode: actuator and generator,” *Appl. Phys. Lett.*, vol. 85, no. 10, 2004, doi: 10.1063/1.1784890.
- [63] D. Z. Li H, Tian C, “Energy harvesting from low frequency applications using piezoelectric materials,” *Appl Phys Rev*, vol. 1:41301, 2014.

- [64] F. Huet, F. Formosa, A. Badel, J. F. Capsal, and M. Lallart, "Vibration energy harvesting device using P(VDF-TrFE) hybrid fluid diaphragm," *Sensors Actuators, A Phys.*, vol. 247, pp. 12–23, 2016, doi: 10.1016/j.sna.2016.05.029.
- [65] M. Ferrari, M. Baù, F. Cerini, and V. Ferrari, "Impact-enhanced multi-beam piezoelectric converter for energy harvesting in autonomous sensors," *Procedia Eng.*, vol. 47, pp. 418–421, 2012, doi: 10.1016/j.proeng.2012.09.173.
- [66] S. Kumar, R. Srivastava, and R. K. Srivastava, "Design and analysis of smart piezo cantilever beam for energy harvesting," *Ferroelectrics*, vol. 505, no. 1, pp. 159–183, 2016, doi: 10.1080/00150193.2016.1255848.
- [67] H. A. Sodano, D. J. Inman, and G. Park, "A review of power harvesting from vibration using piezoelectric materials," *Shock Vib. Dig.*, vol. 36, no. 3, pp. 197–205, 2004, doi: 10.1177/0583102404043275.
- [68] E. M. Nia, N. A. W. A. Zawawi, and B. S. M. Singh, "A review of walking energy harvesting using piezoelectric materials," *IOP Conf. Ser. Mater. Sci. Eng.*, vol. 291, no. 1, 2018, doi: 10.1088/1757-899X/291/1/012026.
- [69] C. Lan, L. Tang, and R. L. Harne, "Comparative methods to assess harmonic response of nonlinear piezoelectric energy harvesters interfaced with AC and DC circuits," *J. Sound Vib.*, vol. 421, pp. 61–78, 2018, doi: 10.1016/j.jsv.2017.11.019.
- [70] T. S. Shakthivel and R. G. Burela, "Vibration Based Piezoelectric Energy Harvesting," *Appl. Mech. Mater.*, vol. 852, pp. 846–851, 2016, doi: 10.4028/www.scientific.net/amm.852.846.
- [71] Z. J. Chew and M. Zhu, "Adaptive Maximum Power Point Finding Using Direct VOC/2 Tracking Method with Microwatt Power Consumption for Energy Harvesting," *IEEE Trans. Power Electron.*, vol. 33, no. 9, pp. 8164–8173, 2018, doi: 10.1109/TPEL.2017.2774102.
- [72] Y. Zhao, K. Wang, and M. Guan, "An adaptive boost converter for low voltage piezoelectric energy harvesting," *Ferroelectrics*, vol. 502, no. 1, pp. 107–118, 2016, doi: 10.1080/00150193.2016.1234912.
- [73] J. Kang, Y. Kim, J. Yoo, and L. Hwang, "Piezoelectric Energy Harvesting Using PMW-PNN-PZT Ceramics for DC-DC Converter Application," *Ferroelectr. Lett. Sect.*, vol. 42, no. 4–6, pp. 87–96, 2015, doi: 10.1080/07315171.2015.1068505.
- [74] B. Lin *et al.*, "Surface intercalated spherical MoS₂: XSe₂(1-x) nanocatalysts for highly efficient and durable hydrogen evolution reactions," *Dalt. Trans.*, vol. 48, no. 23, pp. 8279–8287, 2019, doi: 10.1039/c9dt01218d.
- [75] E. P. Gilshteyn *et al.*, "Flexible self-powered piezo-supercapacitor system for wearable electronics," *Nanotechnology*, vol. 29, no. 32, 2018, doi: 10.1088/1361-6528/aac658.
- [76] P. Yang *et al.*, "Anchoring carbon nanotubes and post-hydroxylation treatment enhanced Ni nanofiber catalysts towards efficient hydrous hydrazine decomposition for effective hydrogen generation," *Chem. Commun.*, vol. 55, no. 61, pp. 9011–9014, 2019, doi: 10.1039/c9cc04559g.
- [77] J. Wang, L. Geng, L. Ding, H. Zhu, and D. Yurchenko, "The state-of-the-art review on energy harvesting from flow-induced vibrations," *Appl. Energy*, vol. 267, 2020, doi: 10.1016/j.apenergy.2020.114902.

- [78] M. Bashir, P. Rajendran, and S. A. Khan, "Energy Harvesting from Aerodynamic Instabilities: Current prospect and Future Trends," *IOP Conf. Ser. Mater. Sci. Eng.*, vol. 290, no. 1, 2018, doi: 10.1088/1757-899X/290/1/012054.
- [79] F. M. White, *Viscous Fluid Flow*. New York: NY, McGraw-Hill.
- [80] F. Facchinetti, M.L., De Langre, E. and Biolley, "Coupling of structure and wake oscillators in vortex-induced vibrations," *JFS*, vol. 19(2), pp. 123–140, 2004.
- [81] F. Facchinetti, M.L., De Langre, E. and Biolley, "Vortex shedding modeling using diffusive van der Pol oscillators," *Comptes Rendus Mec.*, vol. 330(7), pp. 451–456, 2002.
- [82] E. Païdoussis, M.P., Price, S.J. and De Langre, *Fluidstructure interactions: Cross-flow-induced instabilities*. New York: Cambridge University Press, 2010.
- [83] C. H. Williamson, "Vortex dynamics in the cylinder wake," *AnRFM*, vol. 28(1), pp. 477–539, 1996.
- [84] R. D. Blevins, *Flow-induced vibration*, 2nd ed. New York: Van Nostrand Reinhold, 2000.
- [85] J. Wang, S. Zhou, Z. Zhang, and D. Yurchenko, "High-performance piezoelectric wind energy harvester with Y-shaped attachments," *Energy Convers. Manag.*, vol. 181, no. September 2018, pp. 645–652, 2019, doi: 10.1016/j.enconman.2018.12.034.
- [86] L. Zhao and Y. Yang, "On the modeling methods of small-scale piezoelectric wind energy harvesting," *Smart Struct. Syst.*, vol. 19, no. 1, pp. 67–90, 2017, doi: 10.12989/sss.2017.19.1.067.
- [87] M. L. Facchinetti, E. de Langre, and F. Biolley, "Coupling of structure and wake oscillators in vortex-induced vibrations," *J. Fluids Struct.*, vol. 19, no. 2, pp. 123–140, 2004, doi: 10.1016/j.jfluidstructs.2003.12.004.
- [88] J. Jia, X. Shan, D. Upadrashta, T. Xie, Y. Yang, and R. Song, "An asymmetric bending-torsional piezoelectric energy harvester at low wind speed," *Energy*, vol. 198, p. 117287, 2020, doi: 10.1016/j.energy.2020.117287.
- [89] H. L. Dai, A. Abdelkefi, Y. Yang, and L. Wang, "Orientation of bluff body for designing efficient energy harvesters from vortex-induced vibrations," *Appl. Phys. Lett.*, vol. 108, no. 5, pp. 1–6, 2016, doi: 10.1063/1.4941546.
- [90] S. Zhou and J. Wang, "Dual serial vortex-induced energy harvesting system for enhanced energy harvesting," *AIP Adv.*, vol. 8, no. 7, 2018, doi: 10.1063/1.5038884.
- [91] L. Ding, Q. Zou, L. Zhang, and H. Wang, "Research on Flow-Induced Vibration and Energy Harvesting of Three Circular Cylinders with Roughness Strips in Tandem," *Energies*, vol. 11, no. 11, 2018, doi: 10.3390/en11112977.
- [92] Z. Lai *et al.*, "A hybrid piezo-dielectric wind energy harvester for high-performance vortex-induced vibration energy harvesting," *Mech. Syst. Signal Process.*, vol. 150, p. 107212, 2021, doi: 10.1016/j.ymsp.2020.107212.
- [93] J. Song, G. Hu, K. T. Tse, S. W. Li, and K. C. S. Kwok, "Performance of a circular cylinder piezoelectric wind energy harvester fitted with a splitter plate," *Appl. Phys. Lett.*, vol. 111, no. 22, pp. 1–5, 2017, doi: 10.1063/1.5008918.
- [94] J. Wang *et al.*, "Hybrid wind energy scavenging by coupling vortex-induced vibrations and galloping," *Energy Convers. Manag.*, vol. 213, no. April, p. 112835, 2020, doi: 10.1016/j.enconman.2020.112835.

- [95] M. Eng, "on the Concepts of Electrical Damping and Stiffness in the Design of a Piezoelectric Bending Beam Energy Harvester," no. January, pp. 1–4, 2009.
- [96] A. Abdelkefi, M. R. Hajj, and A. H. Nayfeh, "Power harvesting from transverse galloping of square cylinder," *Nonlinear Dyn.*, vol. 70, no. 2, pp. 1355–1363, 2012, doi: 10.1007/s11071-012-0538-4.
- [97] C. B. Ewere F., Wang G., "Experimental investigation of galloping piezoelectric energy harvesters with square bluff bodies," *Smart Mater Struct*, vol. 23 (10), 2014, doi: 10.1088/0964-1726/23/10/104012.
- [98] Z. L. Y. and Z. Z. E. Wang J L, Tang L H, "Efficiency investigation on energy harvesting from airflows in HVAC system based on galloping of isosceles triangle sectioned bluff bodies," *Energy*, vol. 172, no. 1066–78, 2019.
- [99] D. Zhao, X. Hu, T. Tan, Z. Yan, and W. Zhang, "Piezoelectric galloping energy harvesting enhanced by topological equivalent aerodynamic design," *Energy Convers. Manag.*, vol. 222, no. April, p. 113260, 2020, doi: 10.1016/j.enconman.2020.113260.
- [100] N. Shao *et al.*, "Experimental investigation of flow-induced motion and energy conversion of a T-section prism," *Energies*, vol. 11, no. 8, pp. 1–23, 2018, doi: 10.3390/en11082035.
- [101] F. R. Liu, H. X. Zou, W. M. Zhang, Z. K. Peng, and G. Meng, "Y-type three-blade bluff body for wind energy harvesting," *Appl. Phys. Lett.*, vol. 112, no. 23, pp. 1–6, 2018, doi: 10.1063/1.5029415.
- [102] G. Hu, J. Wang, and L. Tang, "A comb-like beam based piezoelectric system for galloping energy harvesting," *Mech. Syst. Signal Process.*, vol. 150, p. 107301, 2021, doi: 10.1016/j.ymsp.2020.107301.
- [103] W. Sun and J. Seok, "Novel galloping-based piezoelectric energy harvester adaptable to external wind velocity," *Mech. Syst. Signal Process.*, vol. 152, p. 107477, 2021, doi: 10.1016/j.ymsp.2020.107477.
- [104] J. Wang *et al.*, "Enhancement of low-speed piezoelectric wind energy harvesting by bluff body shapes: Spindle-like and butterfly-like cross-sections," *Aerosp. Sci. Technol.*, vol. 103, p. 105898, 2020, doi: 10.1016/j.ast.2020.105898.
- [105] C. F. Zhou, H. X. Zou, K. X. Wei, and J. G. Liu, "Enhanced performance of piezoelectric wind energy harvester by a curved plate," *Smart Mater. Struct.*, vol. 28, no. 12, 2019, doi: 10.1088/1361-665X/ab525a.
- [106] L. Argentina, M.; Mahadevan, "Fluid-flow-induced flutter of a flag," *Proc. Natl. Acad. Sci. USA*, vol. 102, pp. 1829–1834, 2005.
- [107] S. Nabavi and L. Zhang, "Portable wind energy harvesters for low-power applications: A survey," *Sensors (Switzerland)*, vol. 16, no. 7, 2016, doi: 10.3390/s16071101.
- [108] E. Bryant, M., Shafer, M.W. and Garcia, "Power and efficiency analysis of a flapping wing wind energy harvester," *Proc. SPIE*, vol. 83410E, 2012.
- [109] X. Shan, H. Tian, H. Cao, and T. Xie, "Enhancing performance of a piezoelectric energy harvester system for concurrent flutter and vortex-induced vibration," *Energies*, vol. 13, no. 12, 2020, doi: 10.3390/en13123101.
- [110] C. Bao, Y. Dai, P. Wang, and G. Tang, "A piezoelectric energy harvesting scheme based on stall flutter of airfoil section," *Eur. J. Mech. B/Fluids*, vol. 75, pp. 119–132, 2019, doi: 10.1016/j.euromechflu.2018.11.019.

- [111] Z. Zhou, W. Qin, P. Zhu, W. Du, W. Deng, and J. Pan, "Scavenging wind energy by a dynamic-stable flutter energy harvester with rectangular wing," *Appl. Phys. Lett.*, vol. 114, no. 24, 2019, doi: 10.1063/1.5100598.
- [112] J. Wang *et al.*, "Broadening band of wind speed for aeroelastic energy scavenging of a cylinder through buffeting in the wakes of a squared prism," *Shock Vib.*, vol. 2018, 2018, doi: 10.1155/2018/2039561.
- [113] M. Hafezi and H. R. Mirdamadi, "A novel design for an adaptive aeroelastic energy harvesting system: flutter and power analysis," *J. Brazilian Soc. Mech. Sci. Eng.*, vol. 41, no. 1, 2019, doi: 10.1007/s40430-018-1509-6.
- [114] D. Zhao *et al.*, "Hydrokinetic piezoelectric energy harvesting by wake induced vibration," *Energy*, vol. 220, p. 119722, 2021, doi: 10.1016/j.energy.2020.119722.
- [115] E. M. Binyet, J. Y. Chang, and C. Y. Huang, "Flexible plate in the wake of a square cylinder for piezoelectric energy harvesting-parametric study using fluid-structure interaction modeling," *Energies*, vol. 13, no. 10, 2020, doi: 10.3390/en13102645.
- [116] J. Liu *et al.*, "Wind energy harvesting using piezoelectric macro fiber composites based on flutter mode," *Microelectron. Eng.*, vol. 231, no. January, p. 111333, 2020, doi: 10.1016/j.mee.2020.111333.
- [117] A. Erturk and D. J. Inman, "A distributed parameter electromechanical model for cantilevered piezoelectric energy harvesters," *J. Vib. Acoust. Trans. ASME*, vol. 130, no. 4, pp. 1–15, 2008, doi: 10.1115/1.2890402.
- [118] R. Hosseini and M. Hamed, "Study of the Resonant Frequency of Unimorph Triangular V-shaped Piezoelectric Cantilever Energy Harvester," *J. Comput. Appl. Res. Mech. Eng.*, vol. 6, no. 1, pp. 65–73, 2016.
- [119] R. Hosseini, O. Zargar, and M. Hamed, "Improving power density of piezoelectric vibration-based energy scavengers," *J. Solid Mech.*, vol. 10, no. 1, pp. 98–109, 2018.
- [120] R. Hosseini and M. Hamed, "An investigation into resonant frequency of triangular V-shaped cantilever piezoelectric vibration energy harvester," *J. Solid Mech.*, vol. 8, no. 3, pp. 560–567, 2016.
- [121] S. S. Rao, *Vibration of Continuous Systems*. John Wiley & Sons, 2007.
- [122] G. J. Khurmi RS, *Theory of machines*. New Delhi: Eurasia Publishing House, 2005.
- [123] R. Hosseini, M. Hamed, J. Im, J. Kim, and J. Dayou, "Analytical and experimental investigation of partially covered piezoelectric cantilever energy harvester," *Int. J. Precis. Eng. Manuf.*, vol. 18, no. 3, pp. 415–424, 2017, doi: 10.1007/s12541-017-0050-3.
- [124] Santiago Orrego *et al.*, "Microstructural and Mechanical Characterization of Flag," Baltimore, 2017.
- [125] M. Specialties, "Piezo Film Sensors Technical Manual," *Measurement*, no. March, p. 57, 2006, [Online]. Available: www.msiusa.com.
- [126] Smart Material, "Macro Fiber Composite (MFC) Datasheet," p. 8, 2017, [Online]. Available: https://www.smart-material.com/media/Datasheets/MFC_V2.3-Web-full-brochure.pdf.
- [127] KDP, "How long do piezoelectric sensors last?" <https://www.kdpes.co.uk/faq-items/how-long-do-piezoelectric-sensors-last/> (accessed Jun. 01, 2023).

- [128] UPS Battery Center, "Factors Affecting Wind Power Output."
<https://www.upsbatterycenter.com/blog/factors-affecting-wind-power-output/>
(accessed Jun. 01, 2023).
- [129] V. C. Pinto *et al.*, "Comparative Failure Analysis of PLA, PLA/GNP and PLA/CNT-COOH Biodegradable Nanocomposites thin Films," *Procedia Eng.*, vol. 114, pp. 635–642, 2015, doi: 10.1016/j.proeng.2015.08.004.

APPENDICES

THE UNIVERSITY OF SHEFFIELD: COVID-19 IMPACT FORM

This form is not compulsory but is intended to be a helpful note to examiners. You may submit this form alongside (not in) your thesis. The purpose of the form is to detail how your thesis has been impacted by the Covid-19 disruption.

STUDENT'S DETAILS	
Name: Zongyou ZUO	Registration Number: ██████████
Department: Mechanical Engineering	Faculty: Engineering
Please provide a brief summary of the work you were planning to complete before covid-19 restrictions were implemented (max 300 words)	
<p>In the initial research plan, experimentation was an important aspect of the research. The plan involved first creating a model, then placing it in a wind tunnel laboratory for comparison, and then improving the model design based on its performance and recreating the model. By continuously optimizing the model design, the final model performance was able to achieve the best results.</p> <p>Additionally, in order to investigate the model's performance under different wind speeds, the original plan was to test each model 20 times at wind speeds of 1-10m/s (increasing by 0.5m/s each time) in order to make the data more accurate. For the cantilever beam material, more hardness different cantilever beams were planned to be tested, such as brass cantilever beams, in order to explore the impact of cantilever beam selection on the performance of the novel design model.</p> <p>Finally, experiments with various materials of piezoelectric kits were also planned in order to compare their performance and cost to find the most suitable piezoelectric kit.</p>	

Please provide a summary of plans for specific studies you were intending to conduct in the future (see note 1) (max 300 words)
<p>Due to the impact of the COVID-19 pandemic, the wind tunnel laboratory was closed, so the experimental plan had to be reduced in order to complete the experiments within a short period of time after the laboratory reopens. And the model can only be made in iforge, after the laboratory reopens; the number of people in iforge is still controlled by the COVID-19 pandemic, so the time to make a set of models is greatly extended, probably two weeks to make a set of models.</p> <p>Therefore, the experimental process had to be changed to adapt to the reduced experimental time. Each model was changed from originally planned to test 20 times at different wind speeds to testing five times at wind speeds of 3m/s-7m/s. Only aluminium and plastic cantilever beams were selected for the experiment, and only two different types of piezoelectric thin films were selected for comparison. In the limited time, the model was optimized only once.</p>
Where relevant, please provide details of changes to your personal circumstances (see note 2) (max 150 words)
No
If your thesis includes Covid-related research, please include a brief statement of how it relates to your overall research aims (see note 3) (max 150 words)
NA
Please provide details of any previous funded extension, tuition-free extension or non-medical Covid-related leave of absence approved since March 2020
NA

Note 1. This information could form a basis for discussion at the viva examination and give Examiners additional means to assess the volume and standard of the work completed. Detailed information could be included in a future work section in the thesis itself.

Note 2. For example, ill health or additional caring responsibilities. additional difficulty related to an underlying disability, returned to clinical service, or has worked in a voluntary capacity for Covid-related research. These data could contextualise the judgement made by Examiners as to the most appropriate outcome.

Note 3. If in doubt, consult with your supervisor and Departmental PGR Lead.